

FINAL REPORT
NASA Project NAG5-1790-21

***Meso-Beta Scale Numerical Simulation Studies of Terrain-
Induced Jet Streak Mass/Momentum Perturbations***

prepared for the

*Mesoscale Processes Research Program
Atmospheric Dynamics and Radiation Branch
Earth Science and Applications Division
Office of Space Science and Applications
NASA Headquarters
Washington, D. C. 20546*

Attention: Dr. Ramesh Kakar, Program Manager

by

Yuh-Lang Lin and Michael L. Kaplan

Department of Marine, Earth, and Atmospheric Sciences
North Carolina State University
Raleigh, North Carolina 27695-8208

May 1995

Acknowledgments

We would like to thank Dr. Ramesh Kakar at NASA Headquarters for his generous financial support of the research supported by this project. We sincerely would like to thank Dr. Steven E. Koch for discussions concerning the CCOPE severe weather/gravity wave event of 11-12 July 1981 which provided the motivation for the proposed research, and for diligent collaboration concerning the interpretation and analysis of the model simulation results. Drs. Ahmet Aksakal and John Manobianco of NASA/GSFC as well as Drs. John Zack and Kenneth Waight of MESO, Inc. provided assistance with questions concerning data ingestion and various subroutines in the GMASS model. Computations were performed on the North Carolina Supercomputing Center's Cray Y-MP/E, and we acknowledge Dr. Bruce Loftis for providing the resources necessary to perform the computationally demanding numerical simulations. Mr. Robert A. Rozumalski provided expert technical assistance for some of the simulation experiments by ordering and decoding the raw data sets which were used to provide the initial conditions. Special thanks go to Heather Bowden for the efficiency and expertise with which she provided expert graphical support in redrafting many of the figures presented in this report. Finally, we would like to thank Dr. Ronald P. Weglarz for providing portions of his doctoral dissertation, which became the material presented in Part IV of this report, for implementing the GMASS model on the NCSC Cray Y-MP/E, performing all of the numerical simulations throughout the course of this research project, and for diligently preparing the numerous technical reports, conference preprints, and journal articles which have resulted from this project. Postprocessing of model data was performed on DEC Alpha workstations belonging to the Mesoscale Dynamics Group and on RISC 6000 workstations belonging to North Carolina State University's Facility for Ocean/Atmosphere Modeling and Visualization, which is funded by an equipment grant from IBM.

Table of Contents

Part I. 3-D Numerical Modeling of Meso-Beta Scale Terrain-Induced Jet Streak Mass/Momentum Adjustments

Executive Summary (Part I).....	i
1. Introduction.....	1
2. Numerical Model and Experiments	4
3. Early Observed Synoptic Conditions	11
<i>a) Mid-Upper Tropospheric Rawinsonde Data</i>	11
<i>b) Lower-Tropospheric/Surface Data</i>	19
<i>c) Satellite Observations</i>	21
<i>d) Summary of Synoptic Observations</i>	24
4. Comparison of Synoptic Scale QG Simulation to Standard Observations ...	25
5. Diagnoses of Simulated Mesoscale Background Adjustment Processes.....	31
<i>a) Stage I: Primary Mid-Upper Tropospheric Wind Adjustment</i>	32
<i>b) Stage II: Primary Mid-Upper Tropospheric Mass Adjustment and Frontogenesis</i>	39
<i>c) Stage III: Secondary Mid-Upper Tropospheric Wind Adjustment</i>	44
<i>d) Stage IV: Development of the Secondary Mesoscale Low-Level Jet Over the WGR</i>	50
<i>e) Terrain-Induced Thermal Perturbations Diagnosed from the LRT and HRT Simulations.....</i>	54
6. Summary and Conclusions	62

Part II. The Role of a Mountain-Plains Solenoidal Circulation in Jet Streak Geostrophic Adjustment Processes During CCOPE

Executive Summary (Part II).....	68
1. Introduction.....	70
2. Terrain Geometry.....	71
3. Observations of a Mountain-Plains Solenoid	73
4. Numerical Model and Experiments	79
5. Numerically Simulated MPS Circulation	79
<i>a) Stage I: Presolenoidal Structure</i>	79
<i>b) Stage II: Development of the MPS.....</i>	82
<i>c) Stage III: Mature MPS Circulation/Jet Streak Interaction.....</i>	85
<i>d) Stage IV: Geostrophic Adjustment and the Generation of Internal Gravity Waves.....</i>	88
6. Summary and Conclusions	90

Part III. The Role of Latent Heating in Modifying the Terrain-Induced Jet Streak Mass/Momentum Perturbations.....	93
Part IV. Linear Geostrophic Adjustment and Jetogenesis Forced by Impulsive and Propagating Zonal Momentum Sources in a Stratified Atmosphere	
Executive Summary (Part IV)	98
1. Introduction.....	100
2. Linear Theory for the Initial-Value Problem.....	103
3. Linear Theory for the Forced Problem.....	130
4. Summary and Conclusions	161
References.....	165

**Part I. 3-D Numerical Modeling of Meso-Beta
Scale Terrain-Induced Jet Streak
Mass/Momentum Adjustments**

Executive Summary (Part I)

Mesoscale model simulations provide insight into the complex jet streak adjustments on 11-12 July 1981 that preceded the first of two significant gravity wave events shown by Koch and Golus (1988) to have been generated over the Rocky Mountains in Montana. Simulations employing a variety of terrain treatments indicate that prior to wave formation, geostrophic adjustment processes modified the structure of the mid-upper tropospheric jet streak by creating secondary jetlets to the southeast of the polar jet streak in proximity to the gravity wave generation region.

This simulated restructuring of the mid-upper tropospheric jet streak is the result of a four-stage process. During stage I, the wind adjusts to the mass field as the jet streak exit region propagates into the inflection point between the upstream trough and downstream ridge in the height field. A streamwise inertial-advection acceleration occurs in response to a cross-stream component of the accelerating wind field that is the result of an intensifying pressure gradient force in the *unbalanced* jet streak exit region. Thus, descent (ascent) within the middle troposphere in the left (right) exit region occurs in association with a thermally direct circulation. This stage ends as a cross-stream thermally indirect circulation develops in the right exit region, thus producing a new *balanced* mesoscale wind maximum (or jetlet) to the southeast of the primary jet streak core.

Stage II is initiated as the mass field is forced to adjust to the new ageostrophic wind field created during stage I. The cross-stream pattern of balanced vertical motion in the exit region of the primary jet streak becomes complicated by the development of a thermally indirect circulation in the exit region of the newly formed mid-upper tropospheric mesoscale jetlet. These adjustments produce multiple cellular structure in the vertical motion fields. Adiabatic cooling and warming within the new thermally indirect circulation result in both frontogenesis and a rightward shift in the midtropospheric pressure gradients.

Stage III is defined by a second geostrophic adjustment process occurring in a similar manner but to the south and east of the adjustment which occurs during stage I. This adjustment results from the perturbation of the new mass field created during stage II by the transverse circulation in the right exit region of the newly formed mesojet, and it occurs directly above the observed wave generation region (WGR). The dynamically balanced circulation that develops is oriented primarily along the stream because of the much shorter length scale of the pressure gradient force perturbation accompanying the stage II adjustment process.

A low-level mesoscale jetlet is formed during stage IV in response to the low-level pressure falls that are established during stage III. This low-level jetlet is oriented nearly orthogonal to the Absaroka and Bitterroot Mountain Ranges flanking the WGR and, therefore, acts as an adiabatic lifting mechanism for perturbing the low-level mass structure in proximity to the most significant terrain slope. Hence, a low-level jet is simulated to develop within the wave generation region in response to the splitting of the primary mid-upper tropospheric jet by multiple geostrophic adjustment processes. Subsequent papers (Parts II and III) will describe how the perturbation of this low-level mesoscale jetlet by orographically-induced adiabatic and diabatic physical processes is the likely mechanism responsible for the generation of the first and second episode of observed gravity waves.

1. Introduction

One of the most enduring problems in dynamical meteorology concerns the mechanism by which mesoscale gravity waves are generated in the atmosphere. Reviews of theories of gravity wave initiation provided by Uccellini and Koch (1987) and Koch and Dorian (1988) point to four dominant physical mechanisms that may generate gravity waves: shear instability, convection, geostrophic adjustment, and orographic forcing. Typically, however, either observations have been inadequate or numerical experiments too limited by computational resources or numerical limitations to thoroughly investigate the dynamical mechanisms for wave genesis *in a given case study*.

The recent study by Powers and Reed (1993) of the large amplitude gravity waves accompanying the December 14-15 1987 midwest cyclone is a major advance in the ability to address the issue of mesoscale gravity wave generation by use of mesoscale model simulation results. However, one fundamental limitation with that study (which proposes convection/wave-CISK as the generation mechanism) lies in the nonexistence of mesoscale rawinsonde information both downstream and within the wave generation region (WGR) against which simulation results could be verified. Furthermore, questions can be raised concerning the adequacy of the horizontal resolution of the mesoscale model employed as well as the surface data sets utilized in the wave analyses of the same case study as presented in Schneider (1990). Additionally, the strong emphasis on wave-CISK can be called into question, because removal of moisture from the mesoscale model to examine the importance of convection also affects the meso- α scale dynamics through its effect on the magnitude and wavelength of the upper-tropospheric trough-ridge system (Uccellini and Kocin 1990). This exerts a major control on the resulting imbalance, possibly resulting in geostrophic adjustment processes and inertia-gravity wave generation.

A few other simulation studies have produced theoretically reasonable internal gravity waves, however, with a dearth of observations against which to verify the results. For example, in a two-dimensional model simulation, Tripoli and Cotton (1989) compare

simulated internal gravity waves, launched by differential surface sensible heat fluxes between an elevated plateau and adjacent plains region, to satellite observations of convection accompanying these waves. However, no detailed surface analyses of the observed wave characteristics were attempted in an effort to compare the simulated waves to observations. Additionally, excellent simulation studies by Zhang and Fritsch (1988) and Schmidt and Cotton (1990) which produce coherent internal gravity waves, lack a detailed observational mesoscale data set against which to compare simulated to observed waves and, hence, diagnose the physical mechanism(s) responsible for wave genesis.

Koch and Dorian (1988) and Koch *et al.* (1993) employ both standard and mesoscale rawinsonde observations, Doppler radar retrievals, and linear theory in an effort to diagnose the role played by geostrophic adjustment and shear instability in generating the observed gravity waves during the 11-12 July 1981 CCOPE case study. Their observational/theoretical analyses follow the in-depth gravity wave statistical analyses by Koch and Golus (1988) and the wave-convection interaction study of Koch *et al.* (1988) that utilized the highly detailed mesonetwork and radar data provided by CCOPE. These investigators implicate geostrophic adjustment as the most likely wave generation mechanism since unbalanced flow conditions, diagnosed from the synoptic and CCOPE special rawinsonde data, developed shortly before the initiation of internal gravity waves were observed in nature. The theoretical and Doppler radar comparisons indicate the importance of wave overreflection and critical level processes in maintaining wave coherence. Convection was ruled out as a wave generation mechanism, since many of the waves first appeared over the mountains of western Montana without any accompanying deep convection. Nevertheless, once the gravity waves triggered thunderstorms, strong convective feedback effects were observed to amplify the wave pressure field and to locally alter the wave energetics.

Unfortunately, the asynoptic upper-air data set was confined to the region over the gravity wave observational network, which was downstream of the WGR. If a

comprehensive numerical modeling investigation were to be compared to the detailed observational analyses of the 11-12 July 1981 CCOPE case study, a favorable comparison would indicate high confidence in a model-derived analysis of the dynamics of wave generation than could be achieved with either mesoscale observations, synoptic scale rawinsonde data, or numerical model output *seperately*. This analysis would have model-simulated upper air data, mesoscale rawinsonde and radar data, and detailed mesonet surface analyses for comparison to observed wave development and propagation characteristics. Hence, the 11-12 July 1981 observational-numerical-theoretical case study would represent the most complete mesoscale analysis of an observed gravity wave episode ever compiled. The use of a mesoscale numerical model to diagnose the mechanism(s) for the generation and evolution of the observed dual episode of CCOPE waves represents the purpose of this three-part series of papers.

In this first paper, Part I, we will endeavor to diagnose the genesis of subsynoptic ageostrophic upper and lower-level mesoscale momentum maxima (jetlets) which organized the first of the two gravity wave episodes observed by Koch and Golus (1988). We will employ several mesoscale numerical simulations as well as a synoptic scale simulation in an effort to define the background geostrophic adjustment processes responsible for jet streak initiation aloft as well as within the planetary boundary layer. The generation of the low-level PBL jet streak is critical for the formation of these CCOPE gravity wave episodes (as will be shown in later sections of Part I, as well as in Parts II and III of this paper). This is because simulations indicate a key role played by: terrain-induced cold air damming, adiabatic heating, and elevated sensible heating, as well as latent heating in the initiation and subsequent amplification of individual gravity waves over the WGR which includes the Absaroka and Bitterroot mountain region of southwestern Montana, southeastern Idaho, and northwestern Wyoming. All but the first of these physical processes are the direct or indirect result of the low-level jet formation over the WGR, and all gravity waves are

simulated to occur when the low-level jet impinges upon mass perturbations produced by orographic and/or diabatic forcing.

Section 2 describes the numerical model and the details of the simulation experiments. In section 3 we discuss the observed synoptic scale environment which preceded the generation of internal gravity waves. In section 4 we compare the synoptic scale simulation, produced by the same model as the mesoscale simulations, but with degraded horizontal resolution, to the available synoptic and asynoptic upper-air observations between the WGR and CCOPE, including the jet structure and other key features discussed in section 3. The purpose here is to build confidence in the mesoscale simulation results as well as to improve our understanding of the significance of the observed synoptic scale processes outlined in section 3. Section 5 involves an in-depth analysis of the evolution of the primary mid-upper tropospheric jet streak into multiple mesoscale jetlets by simulated geostrophic adjustment processes which subsequently creates mid-upper level frontogenesis. This process is ultimately responsible for the genesis of the low-level mesoscale jet. The model results indicate that the low-level jet is the critical physical factor for the launching of internal gravity waves at later times as it impinges on orographically-induced thermal perturbations. Sensitivity of the simulated set of geostrophic adjustment processes to a spectrum of terrain configurations will also be addressed. Section 6 concludes with a discussion and summary of the major results.

2. Numerical Model and Experiments

The numerical model to be utilized in the experiments is the GMASS model (Manobianco *et al.*, 1994). This is a modified version of the MASS model which has been employed in a wide variety of simulation studies and has been evaluated in depth (e. g., Kaplan *et al.*, 1982; Koch, 1985; Koch *et al.*, 1985; Zack and Kaplan, 1987; Whitaker *et al.*, 1988; Manobianco *et al.*, 1991, 1992; Kaplan and Karyampudi, 1992a, b). Table 1 describes the details of the model version used in this study. This hydrostatic model

Table 1. Composition of the GMASS mesoscale model used in this study.

Numerics

- 3-D primitive equations for u, v, T, q, and p
 - Terrain-following σ -p vertical coordinate
 - Arakawa "A" grid on a polar stereographic map image plane
 - Fourth-order accurate horizontal spatial differencing
 - Split-explicit time integration employing the Adams-Bashforth and Messinger schemes
 - Fourth-order bi-harmonic diffusion operator
 - One-way interactive grid nesting
 - Time-dependent lateral boundary conditions from NMC analyses
 - Sponge-type upper boundary condition
-

Initialization

- LFM analysis of ten mandatory pressure levels as first guess
 - Re-analysis using Barnes scheme applied to significant level and surface data
 - Interpolation to finer mesh using cubic splines under tension
 - "Static initialization" removes integrated mass divergence (eliminates external gravity wave, but not internal waves)
-

PBL Formulation

- Blackadar high resolution PBL scheme (Zhang and Anthes 1982)
 - Force-restore surface energy budget over land
-

Moisture Physics (although not used in present paper, will be discussed in future papers on the CCOPE simulations)

- Grid-scale condensation based on layer supersaturation
 - Explicit liquid water and ice continuity equations
 - Condensate can evaporate in unsaturated layers
 - Fritsch-Chappell (1980) and Molinari (1982) cumulus parameterization schemes
-

Radiation

- Radiation is considered only in the surface energy budget
-

employs a σ - p vertical coordinate system, a one-way nested-grid with sponge (Perkey-Kreitzberg) lateral boundary conditions, a Blackadar planetary boundary layer formulation with a complete surface energy budget, and an additional artificial sponge layer whose Rayleigh friction coefficient increases with height within the model stratosphere for effective gravity wave absorption. For the experiments to be described in this paper, all of the *cloud condensational heating was suppressed so that physical processes other than stratiform and convective latent heat release could be identified, and determine their role in the geostrophic adjustment processes which occur in this case study.* Consistent with that hypothesis, i. e., that *physical processes other than stratiform and convective latent heating dominate the development of the precursor low-level mesoscale jet in the planetary boundary layer over the WGR*, soil moisture was set to a uniformly low value. The role of simulated diabatic heating (which includes surface sensible heating as well as convective latent heating) on wave generation and evolution will be evaluated in Parts II and III, respectively.

The coarse and nested-grid regions over which the model was integrated as well as key observing station locators are depicted in Fig. 1. The nested grid was centered just downstream from the WGR as specified in Koch and Dorian (1988), which is located over the region bordering Montana, Wyoming, and Idaho (Fig. 2). This places the region between the WGR and CCOPE (Figs. 2b-c) in the middle of the nested-grid computational domain. A matrix of 223x146x30 grid points was employed for both the coarse (16 km) and nested (8 km) grid simulations. These horizontal resolutions, true at 90 N latitude, imply even finer resolution over the region of interest centered at ~47.5 N latitude. The specific horizontal resolutions were selected to fully resolve, with a minimum of 10 grid points, the primary ($\lambda \sim 160$ km) and secondary ($\lambda \sim 70$ km) gravity waves observed by Koch and Golas (1988). The vertical structure of the 30 σ - p surfaces was uniformly spaced between the planetary boundary layer and the model top located at 100 mb.

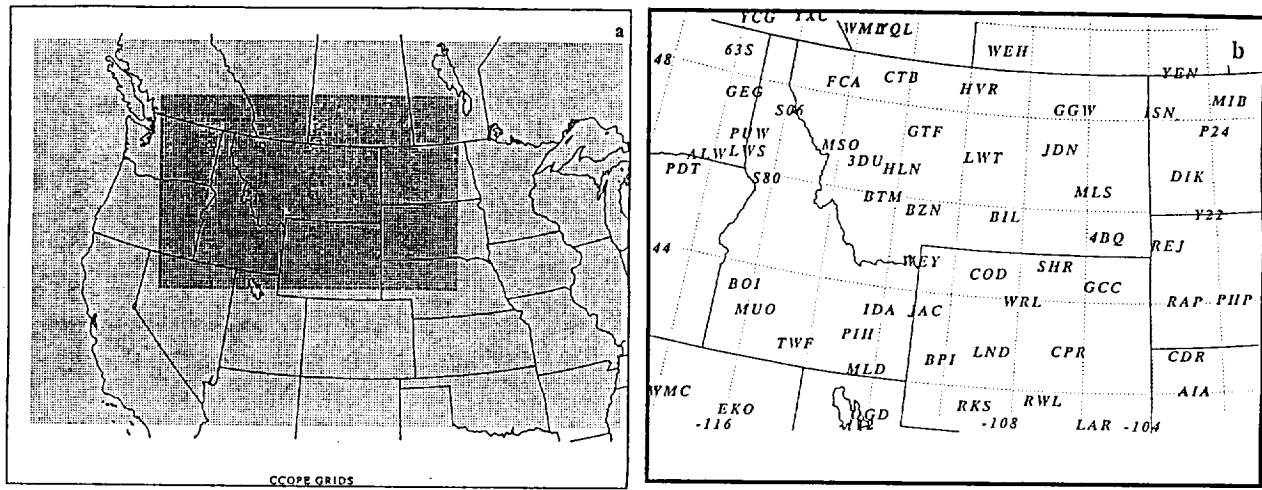


Fig. 1. (a) Region of integration of the numerical model for coarse (16 km) and fine (8 km) resolution simulations with superimposed 223 x 146 grid point matrices. (b) Location of rawinsonde and hourly reporting stations.

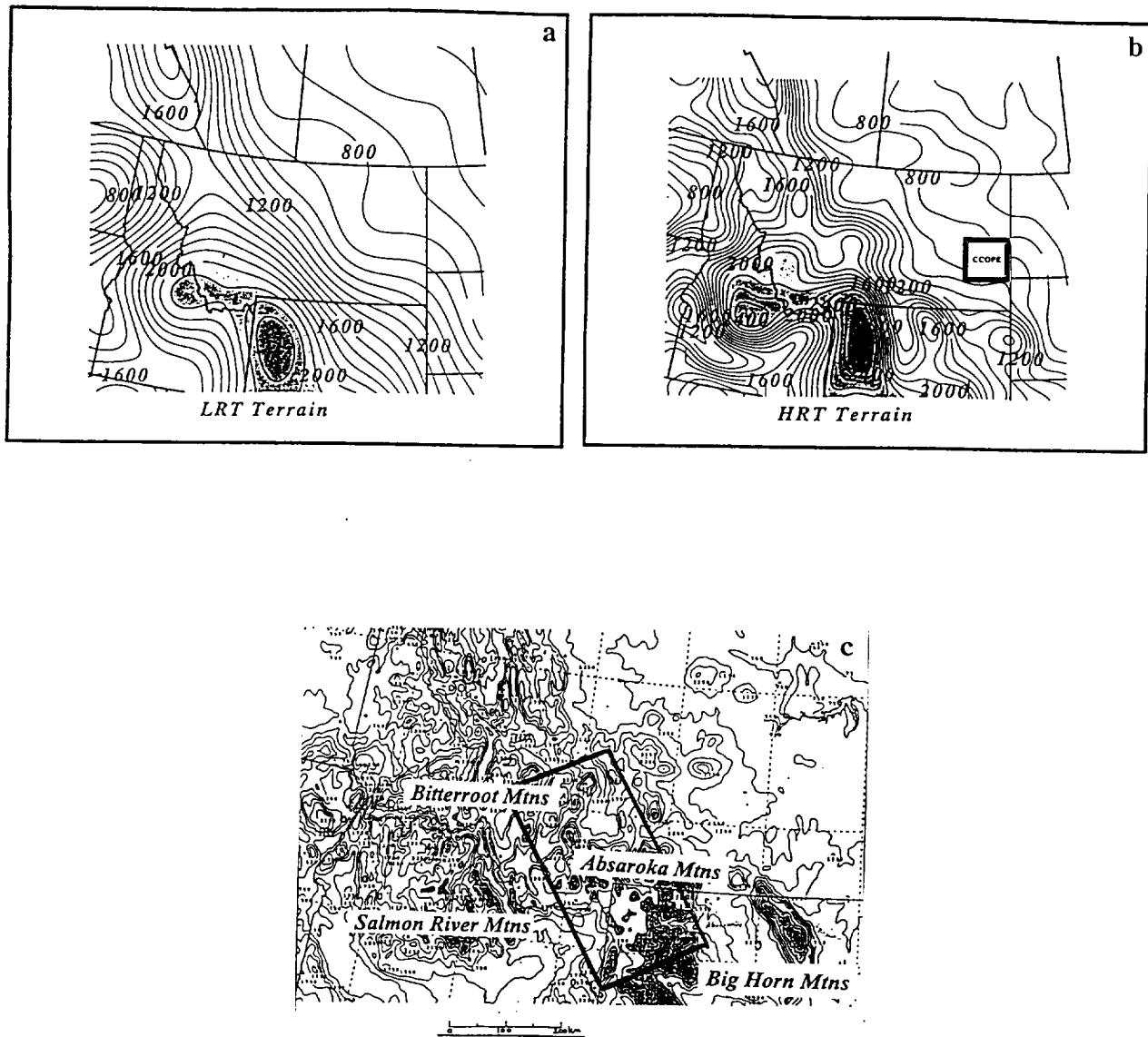


Fig. 2. (a) Low resolution (LRT) simulation, (b) high resolution (HRT) simulation, and (c) observed (8 km) terrain (m) data bases. The rectangle in panel (b) represents the CCOPE region, whereas that in (c) represents the Wave Generation Region (WGR).

Hydrostatic consistency was maintained by choosing x and y grid distances and the vertical separation between σ -p surfaces such that the ratio of the horizontal to vertical grid distances is less than the maximum terrain slope in both the x and y directions.

Three different terrain geometries were used in the four simulations to be described in this first paper. Experiments 1 and 2 employ a uniform terrain (UT) wherein the northern Rockies are effectively removed and replaced by a flat, rigid plate with a horizontally homogeneous surface value of 1500 m. This terrain is used for the uniform terrain mesoscale and synoptic scale simulations, which are referred to hereafter as UT and QG, respectively. Experiment 3 employs an NWS LFM II model low-resolution terrain (Fig. 2a), and is defined and referred to hereafter as the mesoscale simulation LRT. Finally, Experiment 4 employs a high resolution (~ 8 km) terrain (Fig. 2b), which is defined and referred to hereafter as the mesoscale simulation HRT (see Table 2 for a comparison of the simulation characteristics). The high resolution terrain was smoothed in order to prevent terrain instability according to Phillips' (1957) criteria. Fig. 2c depicts the observed terrain derived from the 8 km data base. Results from these four simulations to be compared later will show that upper-level jet streak geostrophic adjustment processes resulting in low-level jetogenesis occur *independent of terrain geometry/configuration*.

Four of the seven numerical experiments described in Table 2 will be discussed in this paper. These four specific experiments were performed in an effort to gauge the effect of orographic forcing as well as model resolution on the initiation of observed CCOPE gravity wave episodes 1 and 2. These involved the uniform (UT), low resolution (LRT), and high resolution (HRT) terrain simulations. Each simulation allowed a complete suite of planetary boundary layer processes, including diurnal surface sensible heat fluxes with both uniform and low soil moisture distributions. Subsequent simulations to be discussed in Parts II and III will deal with the issue of diabatic heating on gravity wave generation through differential surface sensible heat fluxes and convective latent heating. *This first paper will only deal with the issue of the role of geostrophic adjustment responsible for*

Table 2. Summary of model simulation experiments.

Simulation	Horizontal Resolution ¹	Number of Vertical Levels	Terrain Type ²	Model Physics ³
QG	125 km	30	Uniform	PBL/No LH
UT	16/8 km	30	Uniform	PBL/No LH
LRT	16/8 km	30	LFM	PBL/No LH
HRT	16/8 km	30	High	PBL/No LH

¹ N/M = Ratio of coarse/nested fine grid horizontal mesh sizes. QG contains only the coarse grid.

² Uniform terrain is horizontally homogeneous 1500 m high terrain. LFM terrain is that used in the NWS LFM II model. High resolution terrain is an 8 km resolution terrain database.

³ PBL refers to use of full PBL physics. No LH means that stratiform and convective latent heating is totally suppressed although atmosphere is moist.

upper- and lower-level jet streak genesis, the modifications due to terrain configuration, and their combined implications for the initiation of gravity wave episode #1.

The coarse mesh simulations were initialized at 0000 UTC 11 July 1981 and integrated 30 hours through 0600 UTC 12 July 1981, which therefore includes both episodes of observed gravity waves as well as the initiation of the mesoscale convective system (MCS) over the Dakotas as described by Koch *et al.* (1988). The nested-grid simulation was initialized at 0900 UTC 11 July 1981 and integrated for 21 hours through 0600 UTC 12 July 1981. This time for the initialization of the nested-grid simulations was chosen because the first episode of the observed gravity waves develops over the WGR on or about 1100 UTC 11 July 1981 (see Koch *et al.*, 1988). The initial conditions for each coarse mesh simulation were derived from the NWS Limited Fine Mesh (LFM) analyses, North American rawinsonde data, as well as hourly surface data. Lateral boundary conditions were prescribed from LFM six-hourly forecast data as well as observations at 0000 and 1200 UTC. The initial conditions for the nested-grid simulations were derived from cubic spline interpolated coarse mesh fields, and the one-way lateral boundary conditions needed for the nested-grid simulations were derived from interpolated hourly coarse mesh simulated fields.

3. Early Observed Synoptic Conditions

a. Mid-Upper Tropospheric Rawinsonde Data

Fig. 3 depicts the observed NWS rawinsonde-derived 850, 700, 500, and 300 mb analyses valid at 0000 UTC 11 July 1981. In addition to the massive ridge of high pressure over the west central Plains states and the cutoff low pressure area over western Washington, six important features are evident in these synoptic scale analyses:

- 1) a thermal ridge in the 700 and 850 mb temperature fields over the elevated terrain, which acts to quasi-geostrophically enhance the pre-existing background synoptic-scale ridge in the upper tropospheric height field extending from eastern Wyoming to southern Alberta and Saskatchewan.

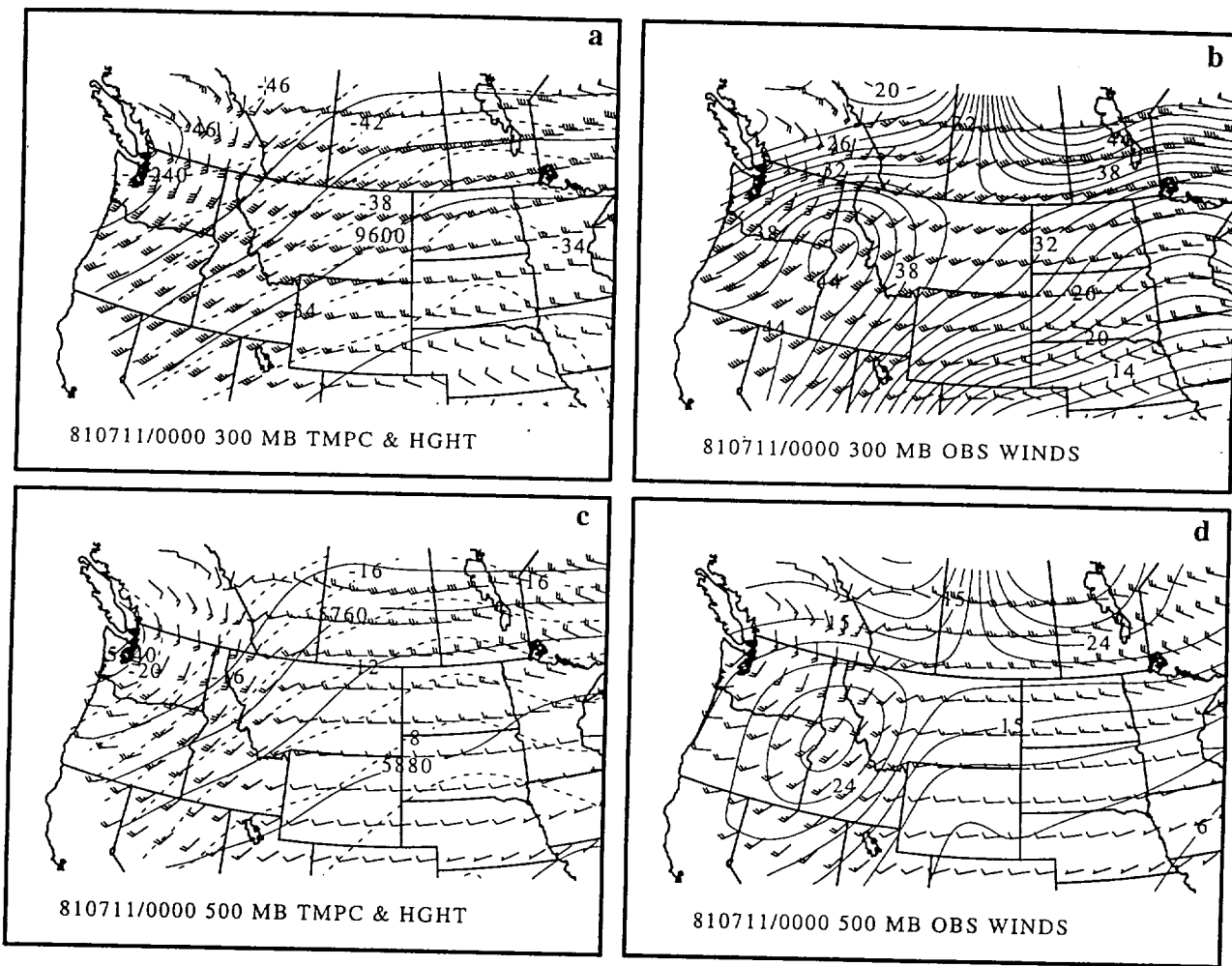
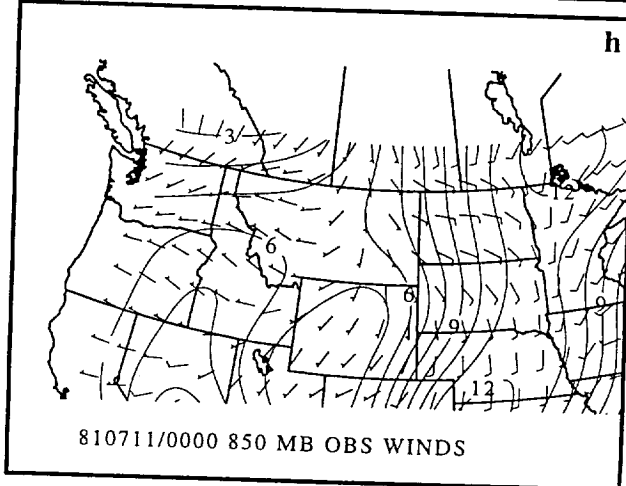
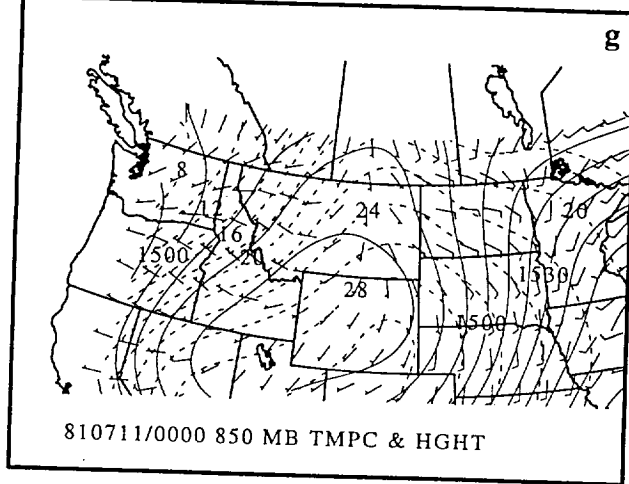
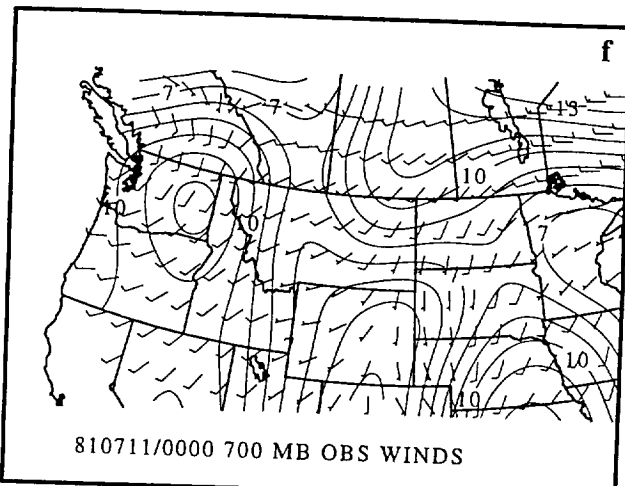
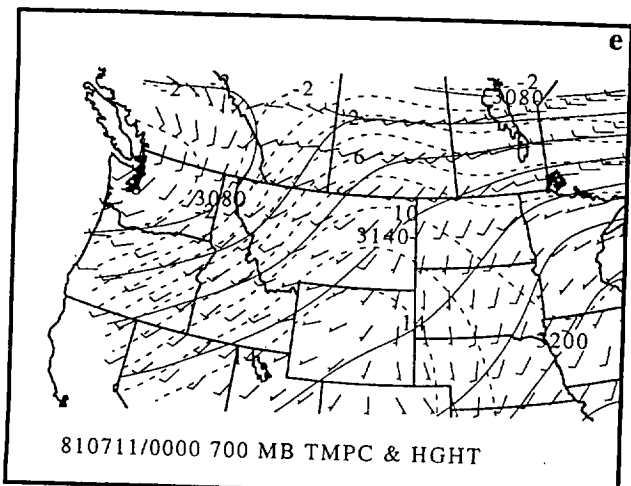


Fig. 3. Barnes objective analyses of rawinsonde data: (a) temperature (C, dashed lines), geopotential height (m, solid lines), and wind vectors at 300 mb; (b) isotachs ($m s^{-1}$) and wind vectors at 300 mb; (c-d) same as in (a-b), except at 500 mb; (e-f) same as in (a-b), except at 700 mb; and (g-h) same as in (a-b), except at 850 mb.



- 2) a trough in the 700 mb height field extending from north central Oregon to south central Nevada.
- 3) the 500-300 mb level polar jet streak extending from just west of the California coast to the northern Rockies, placing its exit region over eastern Idaho and western Montana.
- 4) a weak low-level jet at 700 mb over eastern Washington and Oregon.
- 5) a midtropospheric front over Idaho at 500 mb.
- 6) a strong *midtropospheric* lapse rate over the intermountain region, including the region between the WGR and CCOPE.

Depicted in Fig. 4 is the set of analyses of the 850, 700, 500, and 300 mb height, wind, and temperature fields 12 hr later. While there is little overall change to the synoptic scale flow pattern, the 700 mb trough has propagated northeastwards toward eastern Idaho (where the heights have fallen throughout this region during this time period), the 300 mb jet streak exit region has shifted slightly eastward (although the dominant along-stream shear is still located between central Idaho and southwestern Montana), and the heights and temperatures at 500 mb have decreased near the WGR. Additionally, substantial nocturnal radiational cooling (evident from the 500, 700, and 850 mb temperature fields over the elevated terrain) has contributed to a reduction in the amplitude of the mid-upper tropospheric ridge over the elevated terrain from western Wyoming to southwestern Canada. This leads to the question of whether or not mesoscale temperature and wind perturbations are superimposed upon the synoptic scale 12 hour changes?

An important inference to be discerned from the 1200 UTC 500 mb fields depicted in Figs. 4 and 5, is evidence for the mesoscale pattern of weak cooling over central Idaho and central Montana during the preceding 12 hour period. These midtropospheric temperature changes may be due to adiabatic cooling and/or weak mesoscale cold advection as there is weak, if any, large scale thermal advection in the

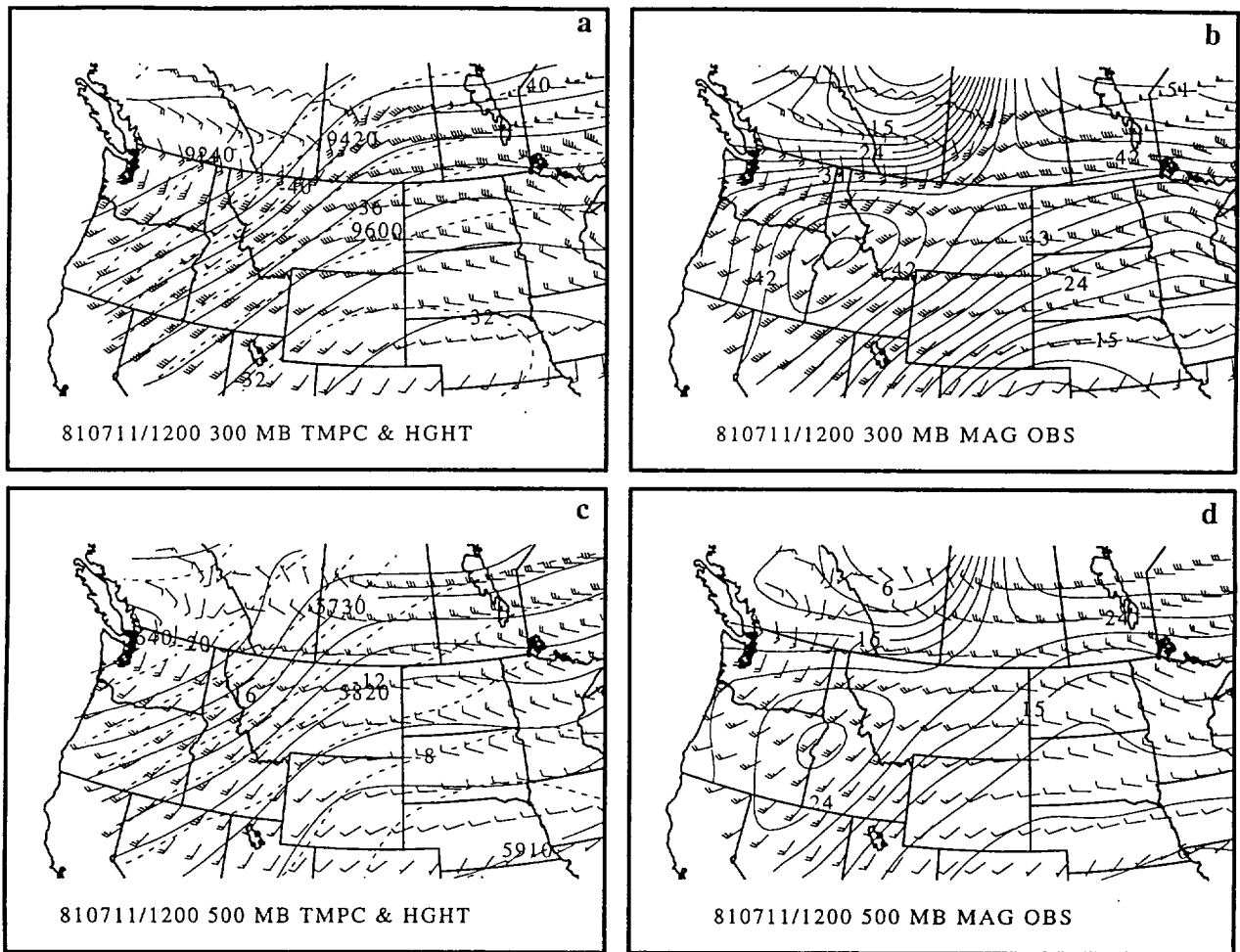
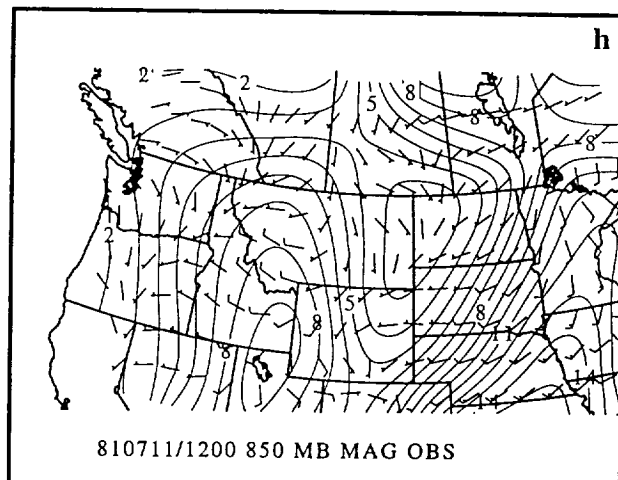
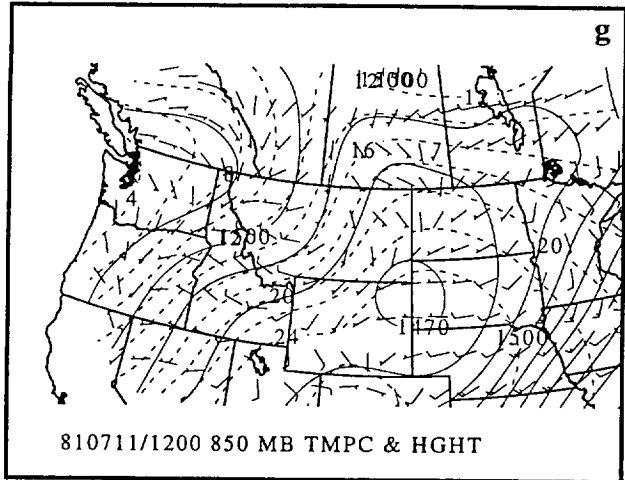
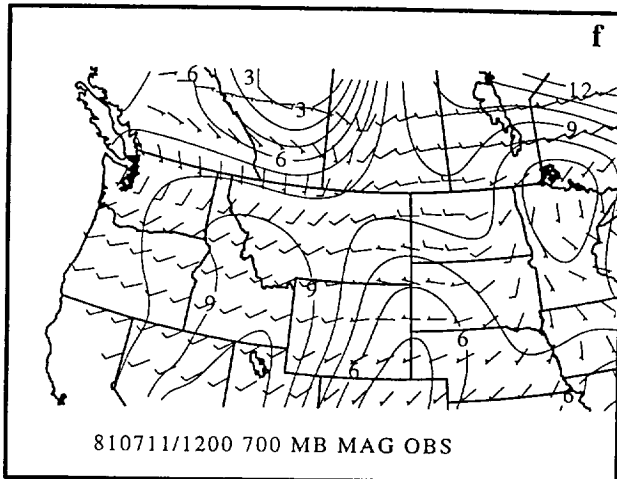
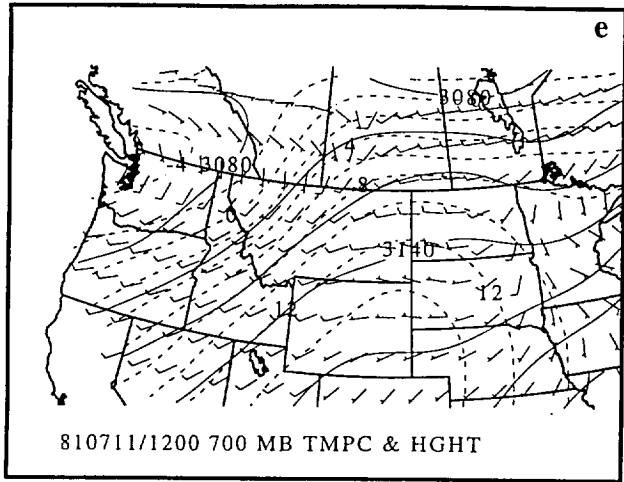


Fig. 4. As in Fig. 3 but at 1200 UTC 11 July 1981.



quasi-stationary, nonamplifying synoptic scale baroclinic wave and because the precipitation/cloud cover is isolated and diminishing in coverage and intensity during the overnight period over Wyoming, Montana, and Idaho. However, they could reflect typical diurnal cooling often observed in rawinsonde data over mountainous regions.

Evidence for the existence of mesoscale ageostrophic circulations includes the persistent ageostrophic cross-stream wind component directed to the left (right) of the primary polar jet streak exit region at Spokane, Washington (GEG) (Glascow, Montana (GGW)). The leftward-directed cross stream ageostrophic flow at GEG observed at 1200 UTC is also observed upstream at Boise, Idaho (BOI) 12 hours earlier. Furthermore, cooling of $\sim 1C$ ($2C$) can be seen at BOI (Great Falls, Montana (GTF)) on the cyclonic side of the jet streak's exit region, while there is $\sim 1C$ warming at Lander, Wyoming (LND) on the anticyclonic side of the jet streak's exit region. Warming of similar magnitude also occurs at GEG northwest of the jet streak exit region (Figs. 4 and 5). *Additionally, colocated with the cooling is an arc of 500 and 300 mb height falls oriented southwest to northeast, i.e., orthogonal to the elevated terrain, while the larger synoptic scale height change pattern indicates relatively weak height rises.*

Consistent with these midtropospheric temperature and height changes are the 12 hourly 700 mb height changes at LND and Salt Lake City, Utah (SLC) which show little or no height change, while BOI and GTF show height falls $\sim 10\text{-}20$ m (Fig. 5). This differential height fall pattern is also consistent with the 1200 UTC development of a weak low-level jet to the southeast of the 0000 UTC 700 mb wind maximum. This new low-level jet results from the formation of a northward or northwestward-directed issalobaric wind component between BOI, GTF, SLC, and LND. This weak low-level jet forms directly under the midtropospheric region wherein observed cooling (warming) to the northwest (southeast) occurs. Note that the northward-directed height difference along the 700 mb surface has increased within the area enclosed by SLC, LND, BOI, and GTF from ~ 35 m at 0000 UTC to ~ 44 m at 1200 UTC. This shift and slight increase in the

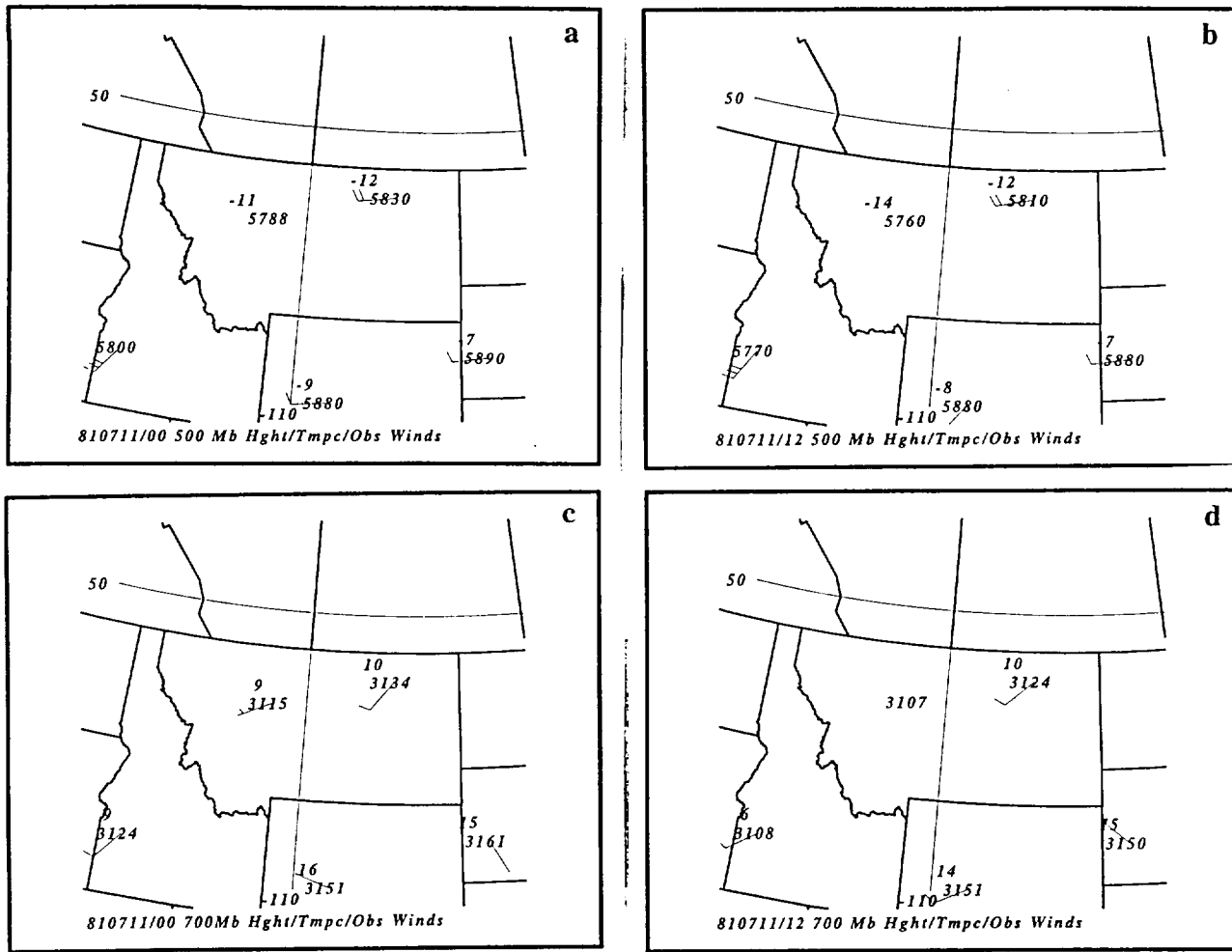


Fig. 5 . Synoptic rawinsonde-observed 12-hourly change fields between 0000 UTC 11 July 1981 (a-c) and 1200 UTC 11 July 1981 (b-d) of (a) 500 mb height (m), temperature (C), and winds ($m s^{-1}$), (b) 500 mb height (m), temperature (C), and winds ($m s^{-1}$), (c) 700 mb height (m), temperature (C), and winds ($m s^{-1}$), and (d) 700 mb height (m), temperature (C), and winds ($m s^{-1}$). Negative values denote decreases over the 12-hr period.

northward-directed pressure gradient force is evident from the wind shift at LND from west-northwest to southwest during this time period. These rawinsonde stations surround the WGR as defined by Koch and Dorian (1988), which is located over the borders of Montana, Idaho, and Wyoming. Furthermore, 850 mb and surface winds over the elevated terrain within southeastern Idaho and western Wyoming reflect this increasing southwesterly flow regime.

b. Lower-Tropospheric/Surface Data

In addition to these upper-air changes near the WGR is the development of a cool wedge of high pressure over western Montana and northwestern Wyoming between 0000 and 1200 UTC 11 July 1981, which is evident in both the 850 mb and mean sea level pressure (MSLP) analyses. Quite evident are the juxtapositioning of substantial cooling and low-level pressure/height rises over southwestern Montana between 0000 and 1200 UTC. Figs. 3g-h, 4g-h, and 5c-d depict the 850 mb pressure fields at these times as well as the twelve hour 850 mb height and temperature changes over Wyoming, Montana, and Idaho. These juxtaposed fields both have a northwest-southeast oriented alignment that is parallel to both the Bitterroot and Absaroka mountain ranges.

Consistent with these pressure changes is the development of a wedge of high pressure over northwestern Montana and the increase in the northwesterly 850 mb flow by 1200 UTC as depicted in Figs. 3g-h and 4g-h. 850 mb heights rise ~26 m at GTF, which is located immediately to the lee of the Bitterroot mountains. This should be contrasted with zero, 12 m, 5 m, and 17 m height rises at GGW, GEG, BOI, and LND, respectively. This elongated northwest-southeast oriented maximum of height rises strongly implies that cold air drainage is occurring to the lee of the northwest-southeast oriented Bitterroot and Absaroka mountain ranges.

These same analyzed features are replicated in both the three-hourly mean sea level pressure data and surface observations depicted in Figs. 6a-c. These figures indicate the presence of a wedge of cold air lying directly to the east of the mountains that is closely

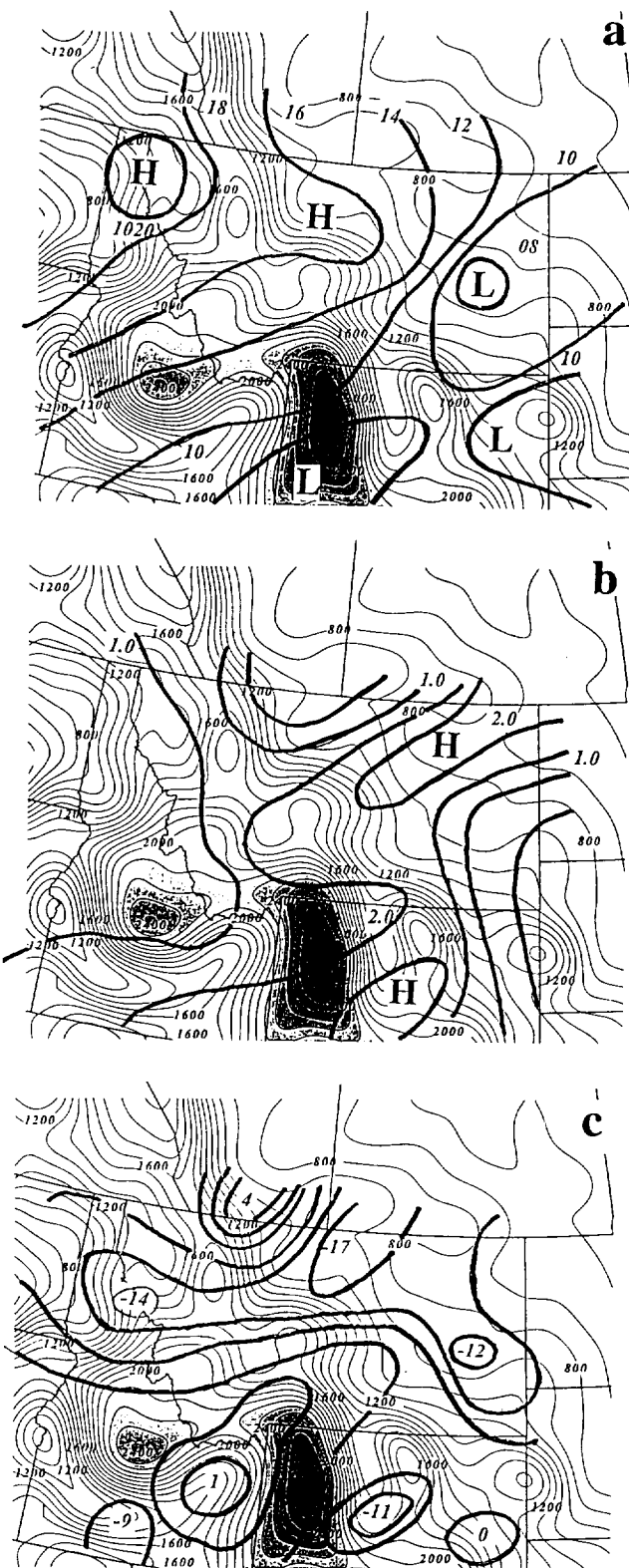


Fig. 6. (a) Observed mean sea level pressure (mb) at 1200 UTC 11 July 1981. (b) Observed three-hourly mean sea level pressure change (mb) analyses at 1200 UTC. (c) Observed six-hourly surface temperature (C) change analyses at 1200 UTC. The background terrain field (m) is from the high resolution terrain simulation.

correlated with the region of southward pressure rises located over central Montana and Wyoming during the 0900-1200 UTC time period. The cooling induces surface pressure rises and reflects the effects of radiative processes, northerly low-level flow, and cold air drainage/damming to the east of the mountains shortly before the formation of the observed weak 700 mb southwesterly low-level jet in the flow over southeastern Idaho and northwestern Wyoming which is depicted in Figs. 4e-f, 5b, and 6a. Most interesting, perhaps, is the fact that the 1200 UTC surface analysis (Fig. 6a) indicates the presence of a mesoridge oriented along a northwest-southeast axis just east of the mountains which is orthogonal to a mesotrough aligned with the mid-upper tropospheric momentum and temperature fields over southcentral Montana and western Wyoming. This suggests the possibility of a misalignment between the lower tropospheric and deep jet streak circulations.

c. Satellite Observations

Fig. 7 depicts infrared satellite imagery valid at 0600, 0900, and 1200 UTC over the northern Rocky Mountain region. A striking feature in this imagery is the development of two cirrus streaks or plumes. The first is located between southwestern Oregon and northern Montana, and defines the cyclonic side of the primary polar jet streak, while the second is located approximately 200-300 km to the southeast and which redevelops in time to the northeast towards the WGR. These cirrus streaks indicate that a secondary upper-level jet streak may be forming during this time period with its exit region passing over the WGR (Note how the first gravity wave observed by Koch and Golus (1988) forms within the second cirrus plume over the WGR, Fig. 7c).

It should be noted, however, that these cloud streaks may also be the result of horizontal velocity confluence zones and moisture advection on the anticyclonic side of the jet streak rather than adiabatic cooling accompanying ascending motions on the cyclonic side of the jet as has been shown by Durran and Weber (1988). These confluence and moisture advection patterns are more consistent with the location of the secondary

a

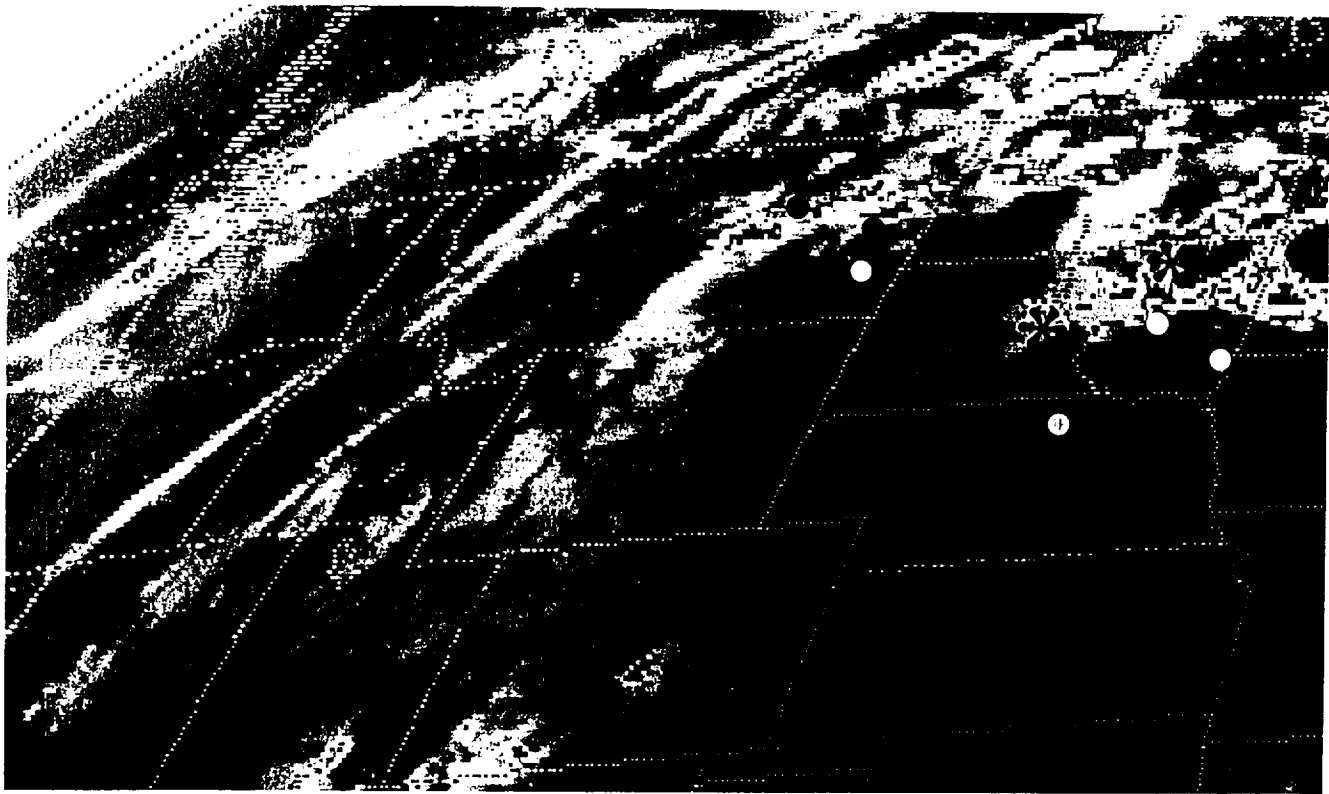
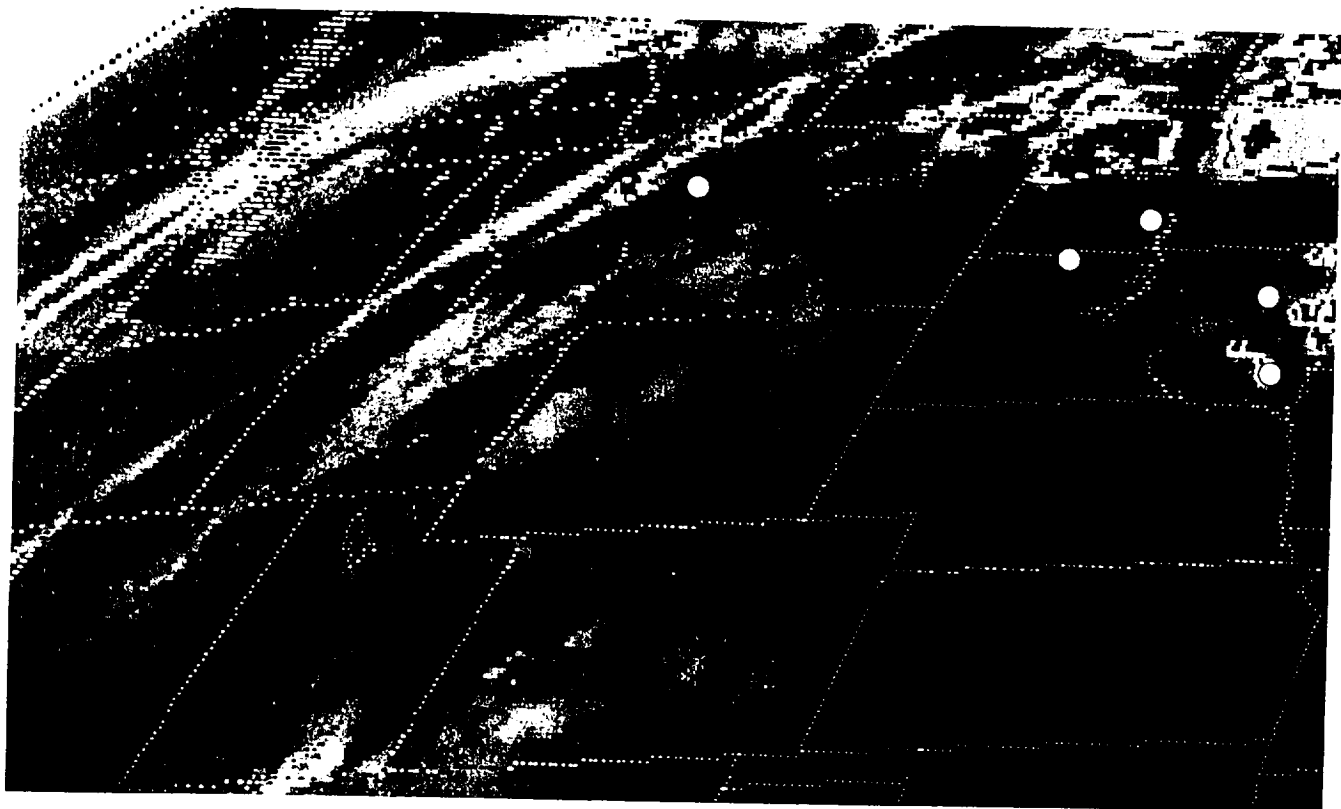
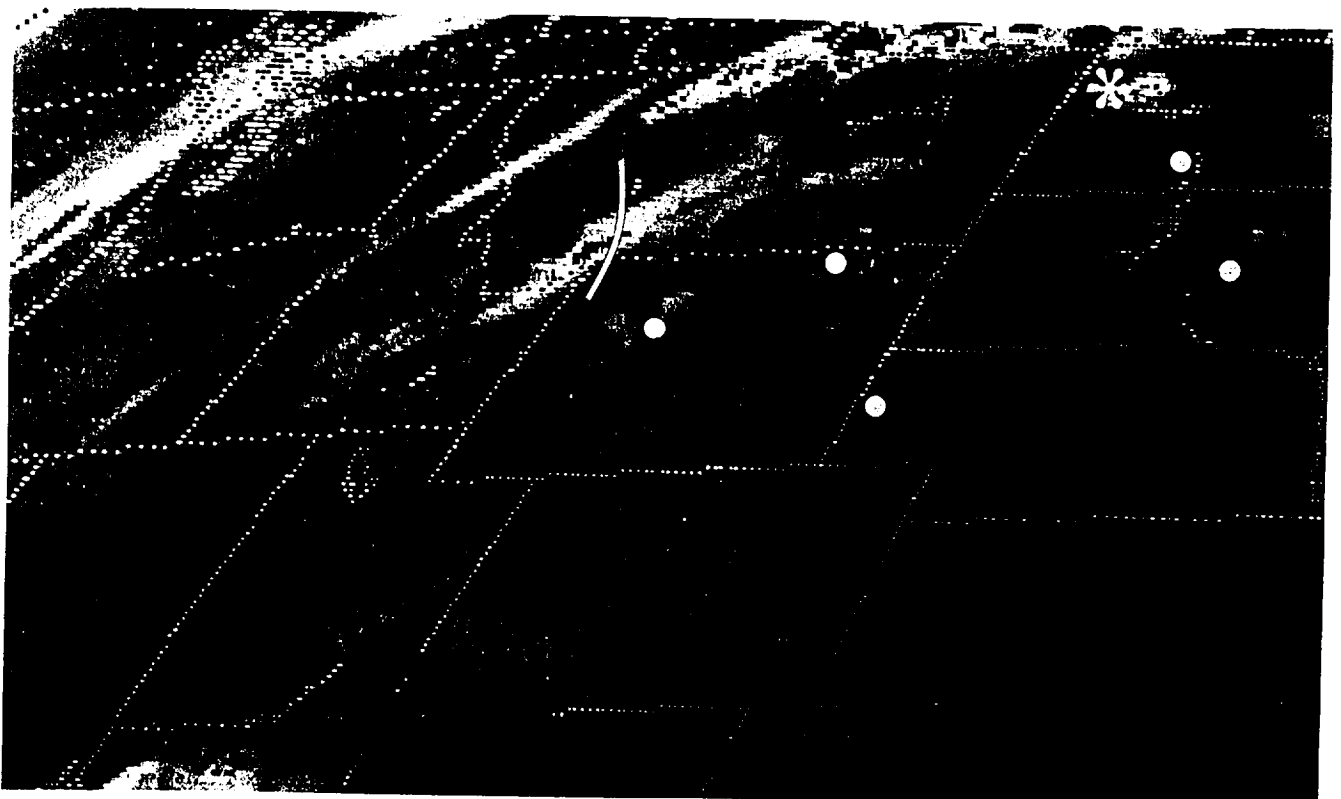


Fig. 7. Infrared satellite imagery over the northwestern U.S. valid at (a) 0600 UTC, (b) 0900 UTC, and (c) 1200 UTC 11 July 1981.

b



c



southeastward-shifted jet streak than is the cooling pattern, which is itself more indicative of the location of the primary jet streak located to the northwest. This conclusion is based on the rawinsonde-derived analyses of the mid-upper tropospheric jet streak position at 1200 UTC 11 July depicted in Figs. 4b and d wherein confluent flow in the right exit region exists on the warm side of the synoptic scale wind maximum.

d. Summary of Synoptic Observations

Rawinsonde observations indicate that: 1) the cross-stream ageostrophic wind components within the mid-upper troposphere, 2) secondary cirrus plume formation, 3) 300 mb height falls, 4) 500 mb temperature rise/fall couplets and height falls, 5) 700 mb height falls and, 6) the 850 mb surface height rises and cold surge may be the most significant evidence for any type of change in the region surrounding the WGR during the 0000-1200 UTC 11 July 1981 time period. While these changes are weak, they infer a region of cooling and lower-middle tropospheric height falls just north and west of the WGR. Such cooling may be the result of standard diurnal forcing or may reflect a mesoscale mass adjustment consistent with the ageostrophic winds observed within the exit region of the jet. This mass adjustment would require a region of ascent surrounded by regions of descent analogous to a thermally direct circulation over northern Idaho and northwestern Montana flanked by a thermally indirect circulation to the southeast of the WGR.

This hypothesized thermally direct circulation at 1200 UTC derived from synoptic scale observations would be consistent with the observed *northwestward-directed* ageostrophic winds over eastern Washington, northern Idaho, and northwestern Montana (Fig. 9c of Koch and Dorian (1988)) as is the thermally indirect circulation which is located further to the southeast over southern Idaho, southwestern Montana, and northwestern Wyoming as diagnosed from the observed *southeastward-directed* ageostrophic winds in the same figure. Their analyses indicate leftward-directed cross-stream ageostrophic flow over southeastern Oregon, most of Idaho, and extreme northwestern Montana, and

rightward-directed cross-stream ageostrophic flow across most of the remainder of Wyoming and Montana at 300 mb and 1200 UTC 11 July 1981.

4. Comparison of Synoptic Scale QG Simulation To Standard Observations

In an effort to diagnose the ability of the numerical model to define the background, pre-existing synoptic scale circulations prior to the development of simulated mesoscale circulations, a coarse (125 km) mesh simulation, QG, whose details are listed in Table 2, was performed. This simulation is important for demonstrating that the model could accurately simulate the observed quasi-geostrophic circulations, *outlined in the previous section*, prior to analyzing the numerical results of the much more complex mesoscale processes to be described in the remainder of this paper and in subsequent papers.

Figs. 5 and 8 depict the 12 hourly 500 mb temperature change fields as well as other key fields discussed in the previous subsection. The comparisons in these figures are diagnosed from rawinsonde observations, the QG simulation, and the coarse mesh UT mesoscale simulation. Within the mid-upper troposphere it is quite evident that both observations and the QG simulation indicate 500 mb cooling oriented in a northeast-southwest arc from northcentral Montana to southwestern Idaho during the 12 hour period. The QG cooling is flanked by warming over northern Idaho and northeastern Washington as well as weaker cooling over western Wyoming. The simulated thermodynamic pattern is qualitatively consistent with the rawinsonde observations for the period between 0000 and 1200 UTC 11 July 1981, with the exception that the QG simulation underestimates the warming which occurs in nature over Wyoming. The southwest-northeast QG height fall and cooling patterns are consistent with weak thermal advection and moderate positive vorticity advection patterns within the exit region of the jet streak as inferred from the observations depicted in Figs. 3 and 4. These simulated QG temperature changes add credence to the hypothesis that the observed 500 mb changes are dynamically forced and

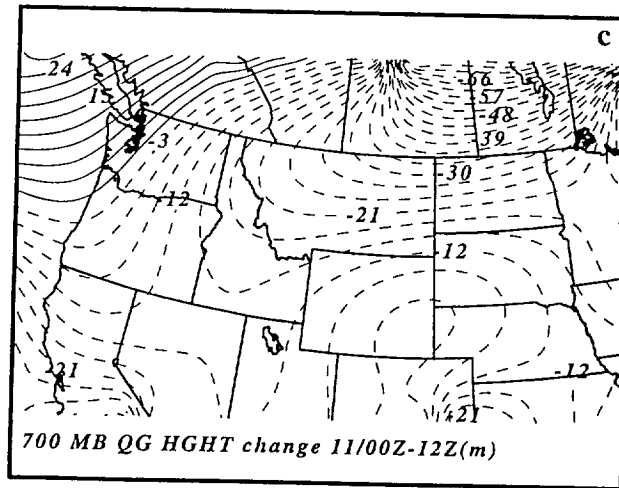
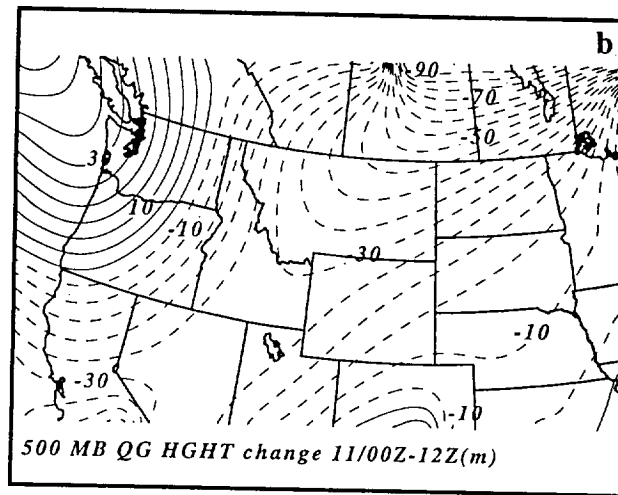
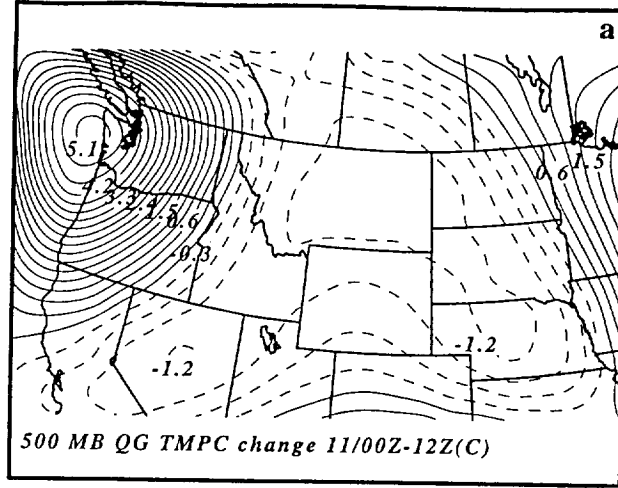
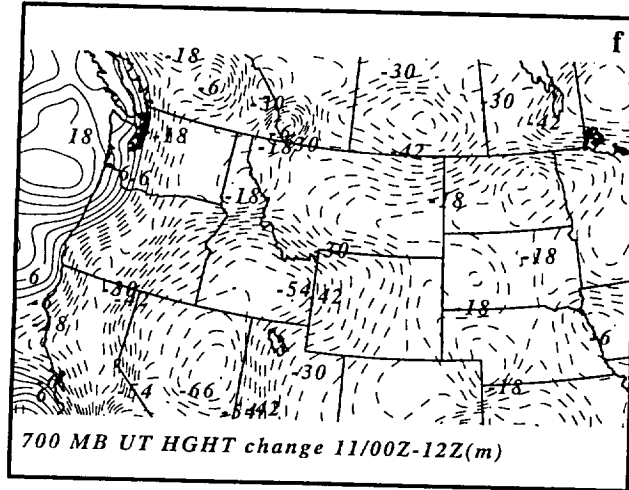
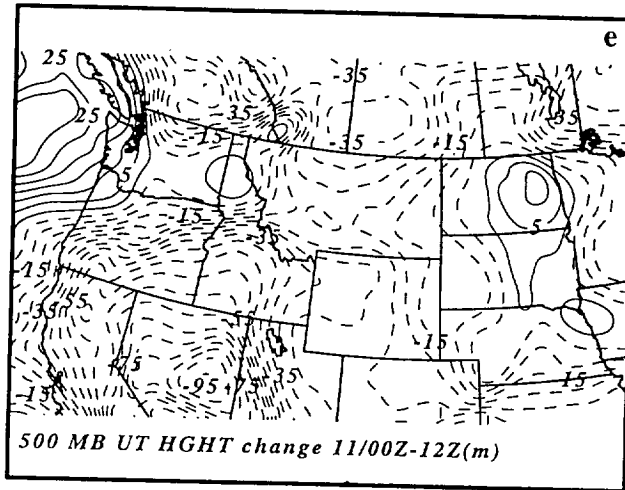
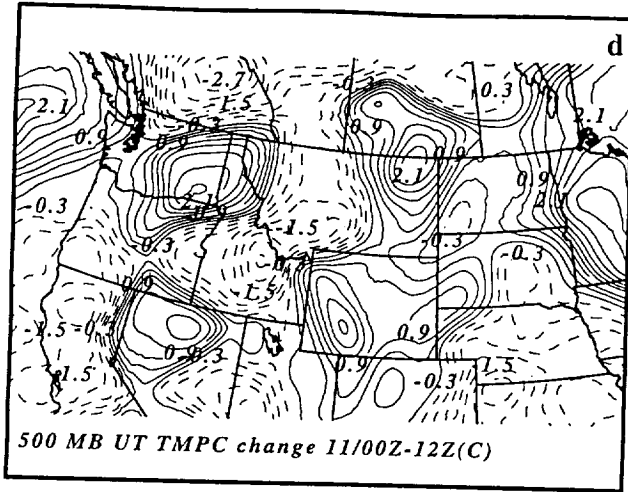


Fig. 8. Synoptic-scale (QG) simulation (a-c) and the coarse mesh UT simulation (d-f) of the same fields as in Figure 5.



not merely the result of standard diurnal changes as suggested in section 3a. Although the pattern of midtropospheric cooling is smoother in the QG simulation, the overall structure over the WGR is not dramatically different from that produced by the UT simulation.

These simulated temperature changes are also consistent with the adiabatic warming and cooling patterns inferred from the simulated QG 6 hour vertical velocity (Fig. 9). This pattern represents persistent rising motion within the region of 12 hour cooling with sinking motions flanking the regions of rising motion. These features act to produce a northwest-southeast oriented midtropospheric thermal boundary lying roughly across central Montana. From these temperature and vertical velocity patterns one can infer that the observed temperature and height changes may very well be associated with a thermally direct circulation which is located well to the northwest of the primary jet streak exit region. Subsidence occurs ahead of the leftward-directed ageostrophic wind component over northern Idaho and northeastern Washington. Southeast of the thermally direct circulation is a thermally indirect circulation centered near or just southeast of the WGR, with the rising branch occurring over central Montana and the sinking branch centered over southern Wyoming. This transverse ageostrophic circulation is roughly colocated with the rightward-directed cross-stream ageostrophic wind which is observed to exist over GGW within the right exit region of the mid-upper tropospheric jet streak as described in the previous subsection. Furthermore, these circulations are consistent with the findings of Koch and Dorian (1988) wherein they analyzed leftward-directed 300 mb cross-stream ageostrophic flow where GMASS simulates subsidence and rightward-directed 300 mb cross-stream ageostrophic flow just downstream from the location where there is simulated rising motion (Figs. 9d and e). The inferred existence of a thermally indirect circulation produced by the QG simulation and the observations is bolstered by the general similarity of the 700 mb height changes and wind fields depicted in Figs. 5, 8, and 9.

Note the development of a weak low-level jet just southwest of the WGR in the QG simulated fields by 1200 UTC. This 700 mb low-level jet is directed towards the thermally

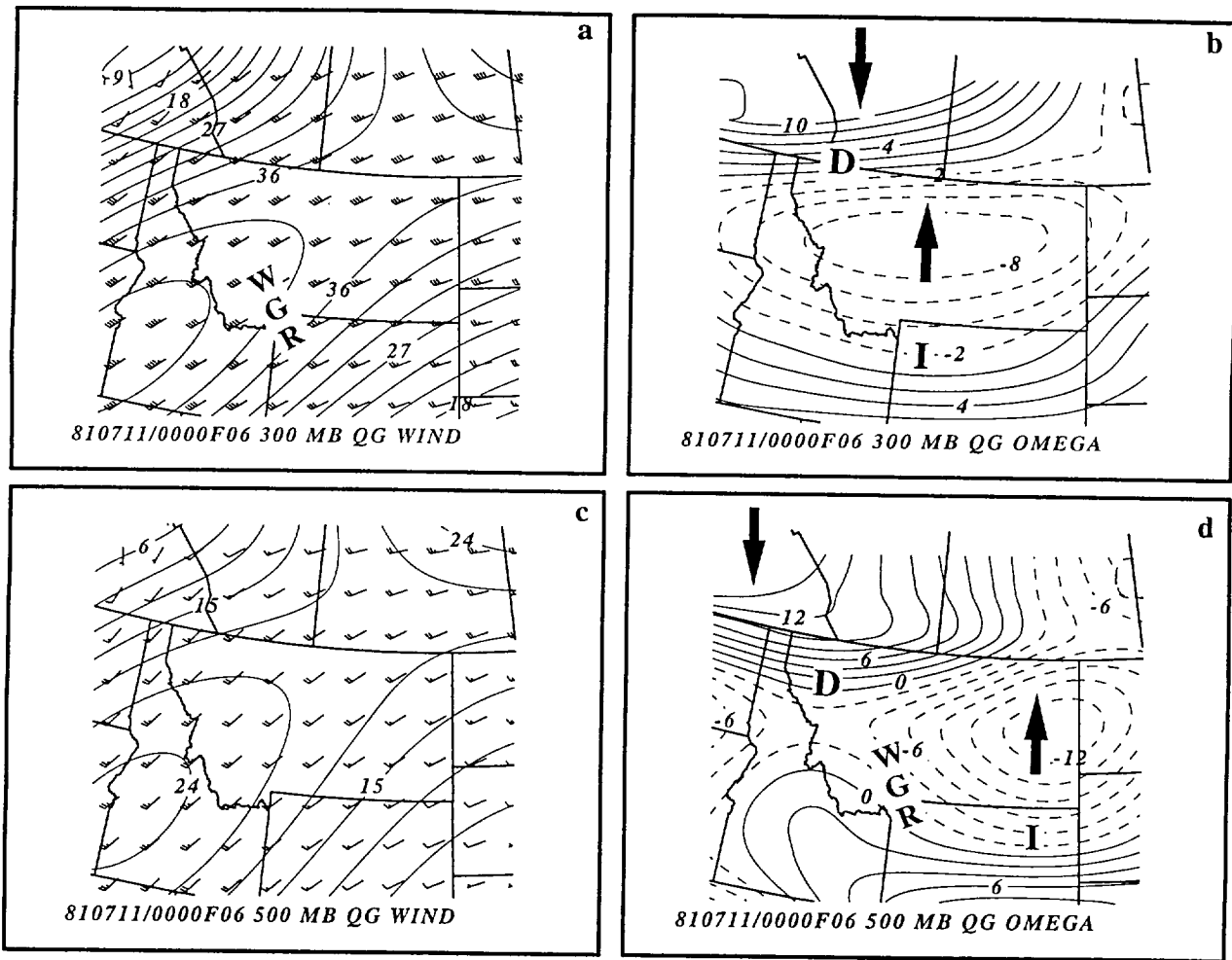
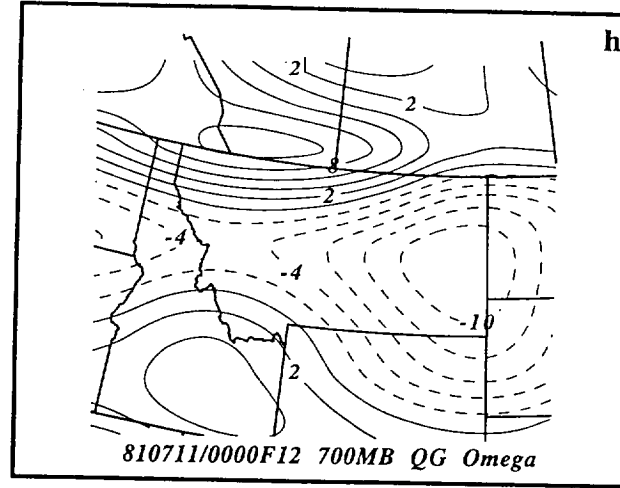
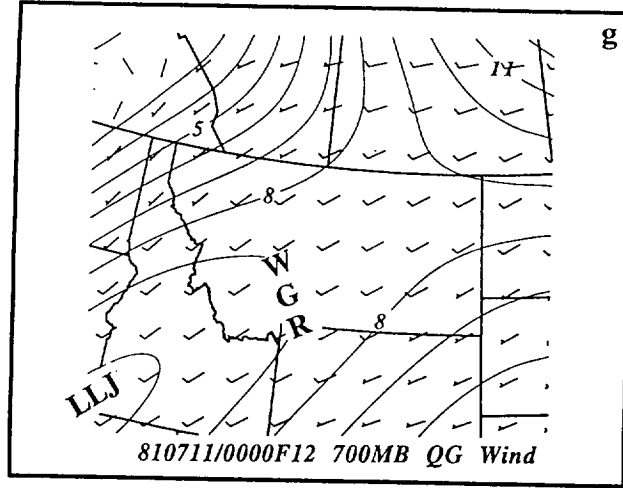
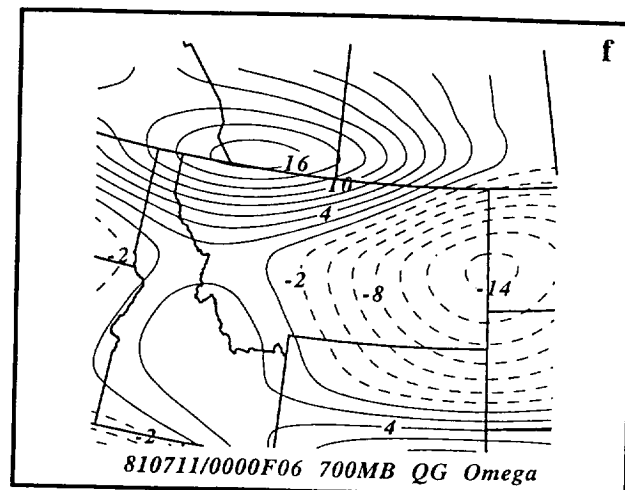
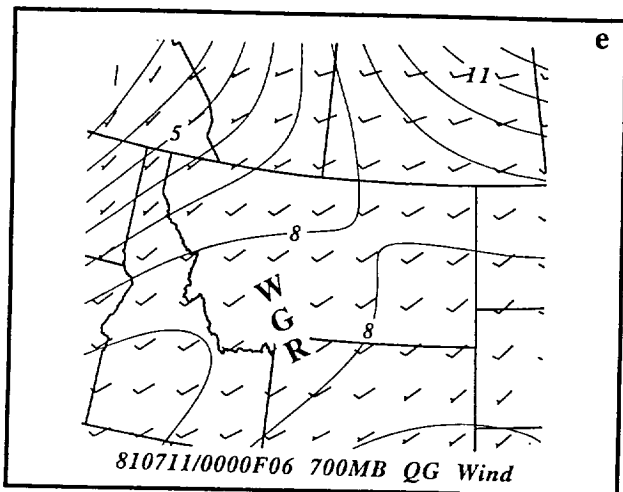


Fig. 9. Synoptic-scale (QG) simulation of (a) 300 mb wind vectors and isotachs (m s^{-1}), (b) 300 mb vertical motion ($\mu\text{b s}^{-1}$), (c) 500 mb wind vectors and isotachs (m s^{-1}), and (d) 500 mb vertical motion ($\mu\text{b s}^{-1}$), as well as (e) 700 mb wind vectors and isotachs (m s^{-1}), and (f) 700 mb vertical motion ($\mu\text{b s}^{-1}$) all valid at 0600 UTC 11 July 1981. (g) Synoptic-scale (QG) simulation of 700 mb wind vectors and isoachs, and (h) 700 mb vertical motion ($\mu\text{b s}^{-1}$) valid at 1200 UTC. Arrows represent the direction of vertical motions. D represents a thermally direct circulation and I represents a thermally indirect circulation. LLJ shows the location of the 700 mb low-level jet. The rectangle represents the Wave Generation Region after Koch and Dorian (1988).



indirect circulation located near the WGR. It is consistent with the observations depicted in Fig. 4 wherein the southwesterly flow increases by 1200 UTC just upstream from the WGR, i.e., the new weak low-level jet which forms to the southeast of the 0000 UTC observed jet. Furthermore, it is oriented nearly orthogonal to the axis of simulated and observed 850 mb cooling located just downstream from the WGR, thus indicating that the QG simulation predicts both lower and mid-upper tropospheric adjustments analogous to the synoptic scale observations. This sequence of adjustments is also predicted by the UT mesoscale simulation (discussed below). The QG simulation reinforces the likelihood that, prior to gravity wave generation, there existed a well-developed thermally indirect circulation within the right exit region of the mid-upper tropospheric jet streak over the WGR coupled with a lower branch return circulation manifested as a 700 mb low-level jet, in addition to a thermally direct circulation located to the northwest of the thermally indirect circulation.

5. Diagnoses of Simulated Mesoscale Background Adjustment Processes

In this section we will analyze the three high resolution nested-grid simulations to relate a complex set of adjustments and their role in the initiation of gravity waves over the WGR. We will define a four-stage process which produces a favorable environment for the initiation of internal gravity waves by orographic and diabatic forcing. The *key developmental process is the genesis of the low-level jet in the planetary boundary layer over the WGR*. This feature develops as a result of deep geostrophic adjustment processes. In an effort to emphasize the geostrophic adjustment processes which occur independent of terrain forcing, we will focus on the uniform terrain (UT) mesoscale simulation to describe the four fundamental stages of background jet streak adjustment processes. We will then compare the UT simulation results to the low resolution terrain (LRT) and high resolution terrain (HRT) simulations to determine if the low-level jet formation normal to the surface terrain occurs in all simulations regardless of terrain

geometry. Furthermore, we will be addressing the following questions: 1) how does geostrophic adjustment organize the low-level jet, 2) does the low-level jet form as a result of predominantly adiabatic *non*orographic processes, 3) are gravity waves excited in the absence of terrain-induced mass perturbations, and 4) is the low-level jet colocated in space and time with the organization of simulated/observed internal gravity waves?

a. Stage I - Primary Mid-Upper Tropospheric Wind Adjustment

Figs. 10 and 11 depict the 500 mb pressure gradient force vectors, vector wind, and isotach fields from the UT simulation valid during the 0000-0500 UTC time period. Depicted in the early part of this time period, i. e., between 0100 and 0300 UTC is the large local velocity increase which parcels undergo to the northwest of MSO (i. e., northeast of the "chimney" of Idaho, and near the border with Alberta and Saskatchewan). This acceleration is evidenced by the northward "bulging" of the isotachs that develops as a mesoscale jetlet J2 emerges within the left exit region of the pre-existing polar jet streak. Here, near station S80, the ageostrophic wind is directed to the northwest as the pressure gradient force vector increases in magnitude and rotates towards the west from its upstream northwestward orientation. This adjustment of the wind to the changing magnitude and direction of the pressure gradient force is consistent with what is found within the inflection point in the height field as noted by Kaplan and Paine (1977), Zack and Kaplan (1987), Uccellini and Koch (1987), and Koch and Dorian (1988). The increased magnitude of the Laplacian of height depicted implicitly in Fig. 10 is indicative of the increased westward-directed pressure gradient force within the inflection point region over western Montana. Parcels which are initially moving northeastward over northcentral Idaho (defined by J1) are accelerated to the north-northwest of their original trajectories resulting in an increase in the meridional velocity component northwest of Missoula, Montana (MSO) near the region surrounding jetlet J2 (Fig. 11). This reorientation of the pressure gradient force near the inflection axis of the synoptic scale baroclinic wave represents both a directional shift as well as a magnitudinal shift, thus

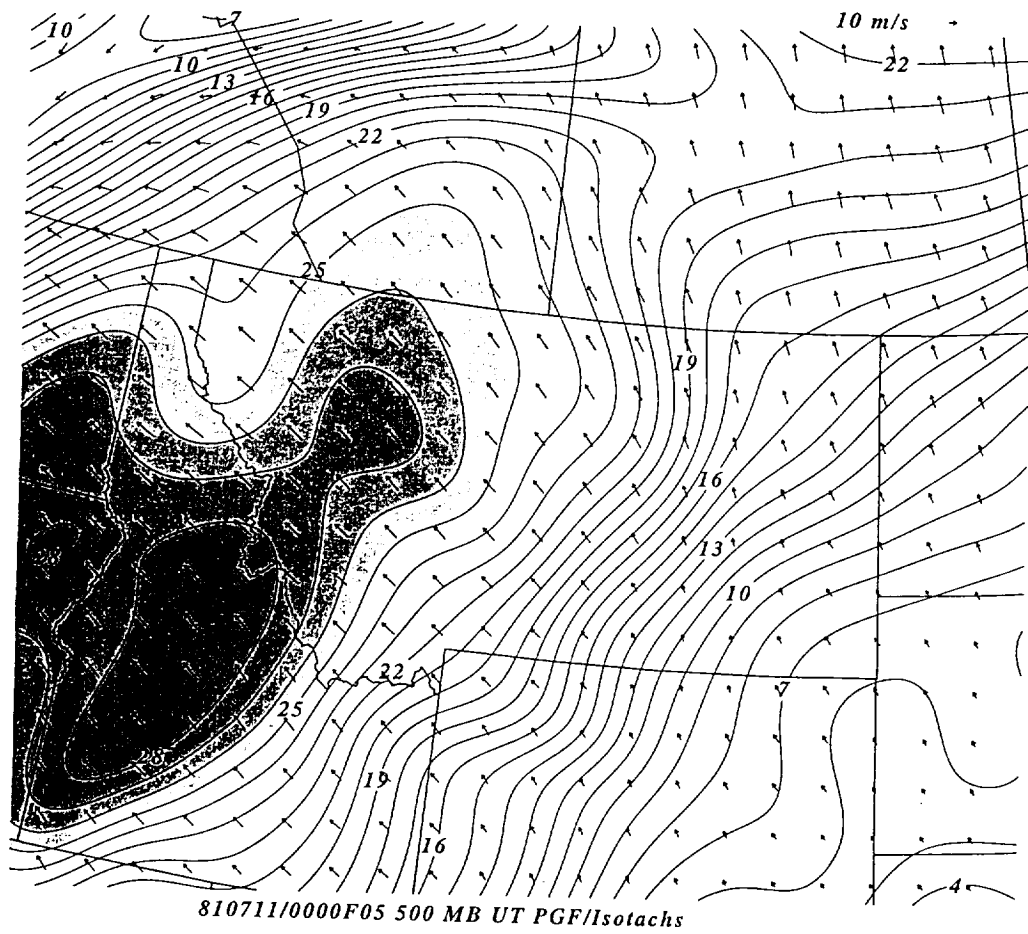


Fig. 10. UT coarse mesh simulation of 500 mb pressure gradient force vectors and wind velocity isotachs (m s^{-1}) valid at 0500 UTC.

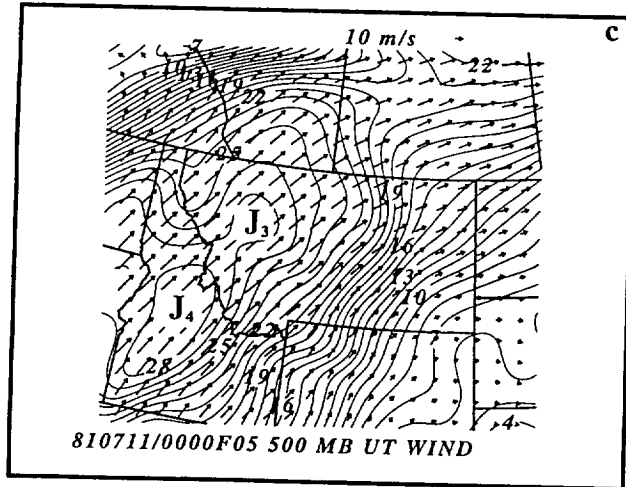
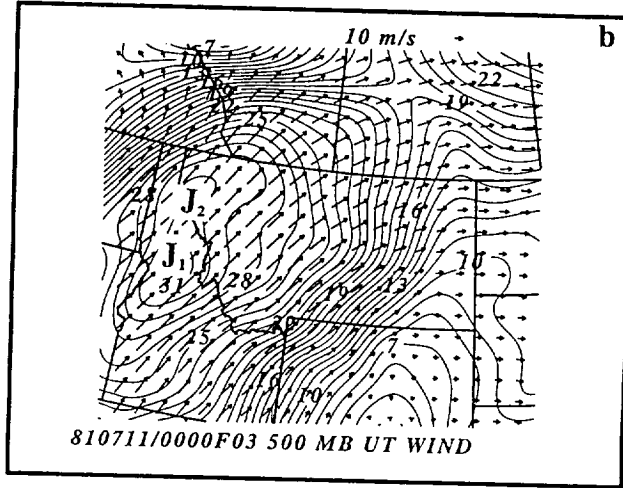
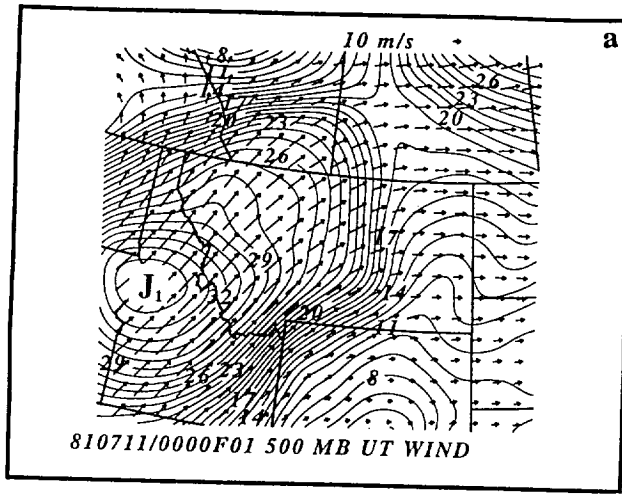
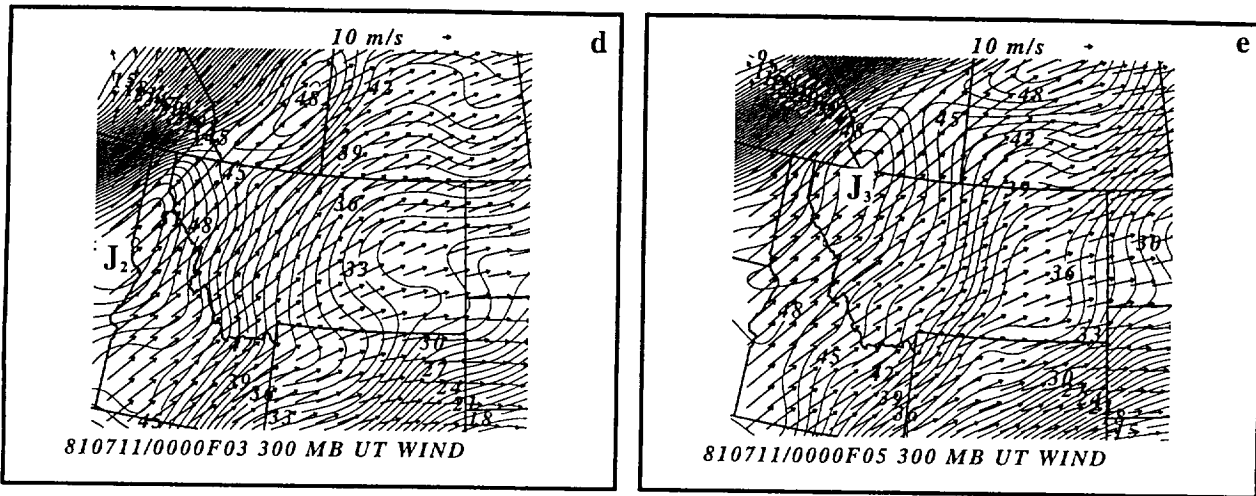


Fig. 11. UT coarse mesh simulation of 500 mb wind vectors and isotachs (m s^{-1}) valid at (a) 0000 UTC, (b) 0300 UTC, and (c) 0500 UTC. Panels (d-e) represent analogous fields at 300 mb. $J_{(x)}$ represent mesoscale momentum maxima (jetlets).



producing a predominantly cross-stream circulation as opposed to an along-stream circulation. The acceleration just east of the chimney of Idaho accompanying the development of J2 increases the cross-stream velocity gradient on the cyclonic side of the jet exit region. This forces mass to accumulate on the left side of the jet exit region which works against the development of ascent in this region which would otherwise act to restore thermal wind balance. This adjustment process is occurring within the left exit region of the pre-existing polar jet streak and represents an increase in the cross-stream unbalanced flow which subsequently increases the streamwise velocity due to the effects of nonlinear inertial-advection acceleration.

Parcels are *unbalanced* (as defined by Koch and Dorian (1988)) over this region which is centered on northern Idaho, northwestern Montana, and southern Alberta. The accelerating flow in this region forces mass to the left of the jet exit region, working against the balancing process which would force it to the right side of the exit region. J2 is short-lived but represents a rapid leftward-shift in the momentum maximum as can be seen in Figs. 11a, b, and d. Therefore, a thermally direct circulation should develop within the polar jet exit region, with descent (ascent) within the cold (warm) air sector of the circulation to the northwest (southeast) of the jet axis. Koch and Dorian (1988) analyze the largest magnitude cross-stream ageostrophic flow to be at 300 mb just south of the "chimney" of Idaho, and the largest Rossby numbers just to the northeast in northwestern Montana by 1200 UTC not unlike what is simulated here.

As can be seen in Fig. 11, by 0500 UTC, the secondary streamwise velocity maximum, J2, which first forms to the northwest of MSO, begins to develop to the right of its original orientation downstream to the northeast of MSO near GTF (J3). The along-stream velocity increase reflects the increase in the inertial-advection terms in the zonal momentum equation north of MSO as the southerly wind component increases near J2 just east of GEG (Note Eqs. (1) and (2)).

$$\frac{\partial u}{\partial t} + u \frac{\partial u}{\partial x} + v \frac{\partial u}{\partial y} + w \frac{\partial u}{\partial z} - f v + \frac{1}{\rho} \frac{\partial p}{\partial x} = 0, \quad (1)$$

$$\frac{\partial v}{\partial t} + u \frac{\partial v}{\partial x} + v \frac{\partial v}{\partial y} + w \frac{\partial v}{\partial z} + f u + \frac{1}{\rho} \frac{\partial p}{\partial y} = 0. \quad (2)$$

These kinematical adjustments result in an increased streamwise "stretching" motion and increased velocity divergence (convergence) northwest (southeast) of the newly perturbed flow (i. e., flanking J3 which grows due to the increasing Coriolis force). Thus, the original jet streak exit region northwest of J1 is transformed by the effects of the westward-directed pressure gradient force, which induces the north-northeasterly directed mesoscale wind maximum/jetlet J2. J3 then develops downstream and to the right of J2 as the streamwise advection of momentum increases. J3 and a new mesoscale jetlet, J4, form as the Coriolis force turns the streamwise wind maxima to the right from southwestern Montana towards southcentral Idaho. J3 and J4 could be viewed as the rapidly adjusted versions of J1 and J2, respectively. In effect, geostrophic adjustment is acting to force the exit region of the geostrophic and ageostrophic jet streaks to become one and the same, i.e., to balance the mass and momentum fields.

By 0500 UTC, the vertical motion fields depicted in Fig. 12 respond by producing three major (and several minor) vertical motion cells. One unbalanced descending cell develops over eastern Washington and southeastern British Columbia under the unbalanced convergent part of the thermally direct circulation, i. e., the region flanking mesoscale jetlet J2. One ascending motion cell develops near and to the northwest of MSO accompanying both the unbalanced flow on the right side of the direct circulation (i. e., flanking J2), and the balanced flow on the left side of the indirect circulation (i. e., flanking J3). The southeastward extension of the ascent accompanying the balanced cell into southwestern Montana is depicted in Fig. 12 near the "I" between J3 and J4. Finally, a descending motion cell develops between GTF and the WGR by 0500 UTC extending

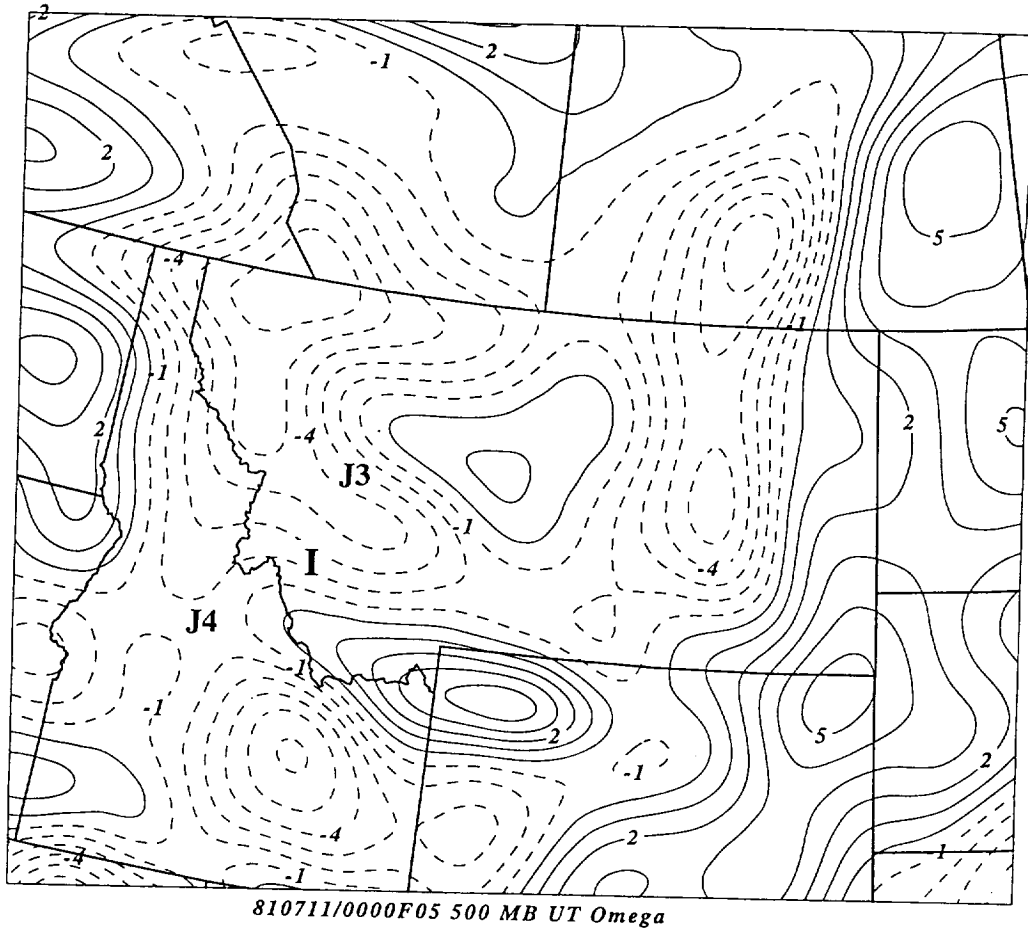


Fig. 12. UT coarse mesh simulation of 500 mb omega ($\mu\text{b s}^{-1}$) valid at 0500 UTC. Thermally indirect circulation is represented by (I) and mesoscale jetlets by J3 and J4.

into northwestern Montana to the right of J3 and J4 as can be seen in Figs. 12 and 13. The latter two cells comprise a thermally indirect circulation (I) with rising (sinking) motion and adiabatic cooling (warming) to the northwest (southeast) with the circulation oriented in a predominantly, but not exclusively, cross-stream manner.

Thus, to the northwest, i. e., near the region connecting British Columbia, eastern Washington, and northern Idaho, where there is velocity convergence accompanying leftward-directed ageostrophic flow, descent accompanying a thermally direct circulation prevails. However, the process of balancing, i. e., the increase in the inertial-advection terms in the equations of motion followed by the Coriolis force, induces multiple mesoscale jetlets J3 and J4 to form to the northeast and southeast of the unbalanced region in addition to a new zone of cooling and warming indicative of a thermally indirect circulation near the WGR (Figs. 11-13). Fig. 13b depicts the balancing thermally-indirect circulation accompanying J3 along a cross section which bisects the WGR. *In effect, the model produces two multicellular transverse ageostrophic circulation patterns during the geostrophic adjustment process, i. e., an unbalanced and a southeastward-colocated-shifted balanced circulation. Without the extraordinary spatial resolution inherent in these numerical simulations, it would be very difficult to define both circulations simultaneously.*

The 300 mb structure of these adjustments is similar as can be seen in Fig. 11. At this level the jet extends downstream and to the right of its original position, placing the strongest sinking lobe of the indirect circulation over the WGR by 0500 UTC.

b. Stage II - Primary Mid-Upper Tropospheric Mass Adjustment and Frontogenesis

The juxtaposed stage I unbalanced thermally direct and balanced thermally indirect circulations which form within the triangle defined by WGR, GEG, and GTF by 0500 UTC have a profound effect on the pre-existing temperature and pressure fields over the same region. Fig. 14 depicts the 500 mb height and temperature, total frontogenesis, and frontogenesis tilting term generated by the UT simulation during the 0200-0800 UTC time period (centered in time at 0500 UTC). Clearly apparent is the tightening of the northwest-

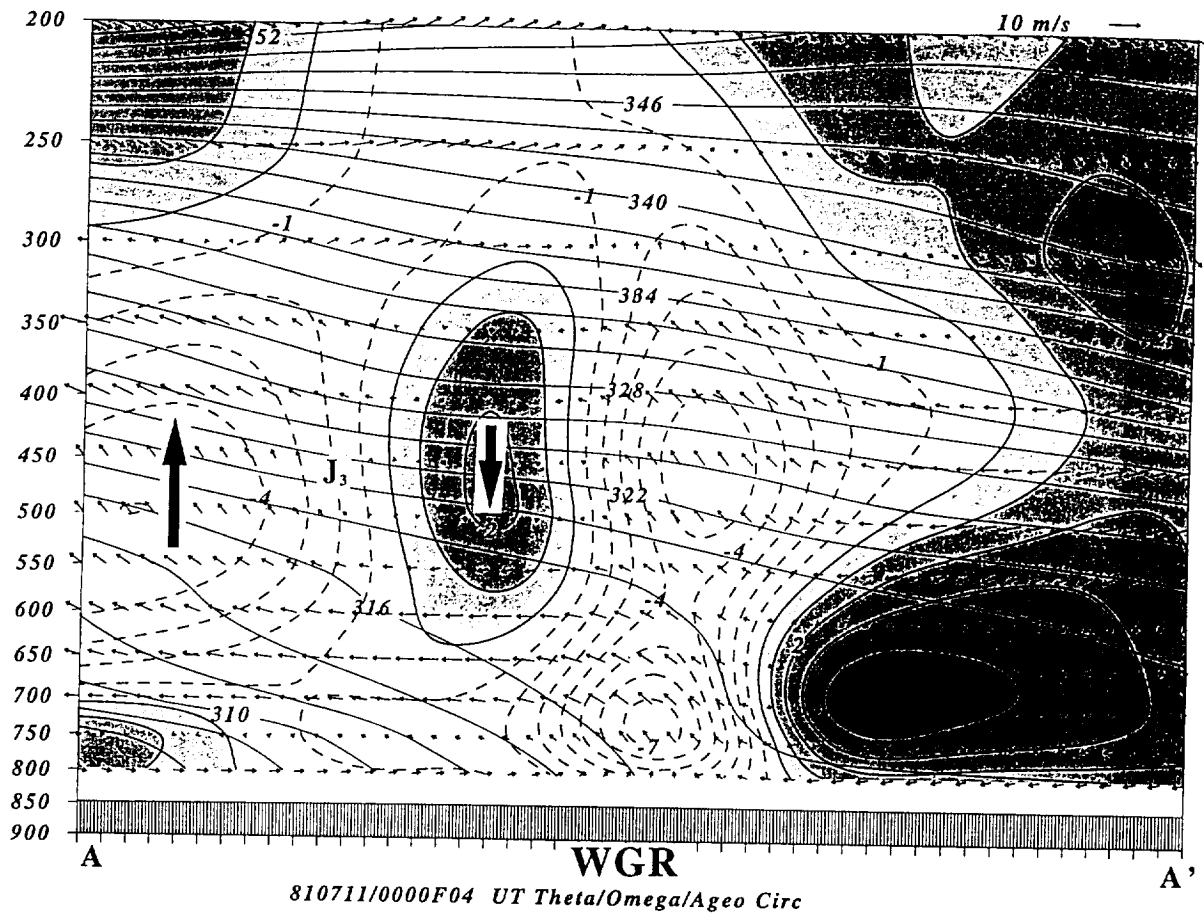


Fig. 13. UT coarse mesh simulation vertical cross section (A-A') of potential temperature (solid in K), transverse ageostrophic circulation vectors (m s^{-1}), and vertical motion ($\mu\text{b s}^{-1}$) valid at 0400 UTC. Thick arrows represent the direction of the thermally indirect circulation, J_3 the mesoscale momentum maximum (jetlet), and WGR shows the location of the Wave Generation Region.

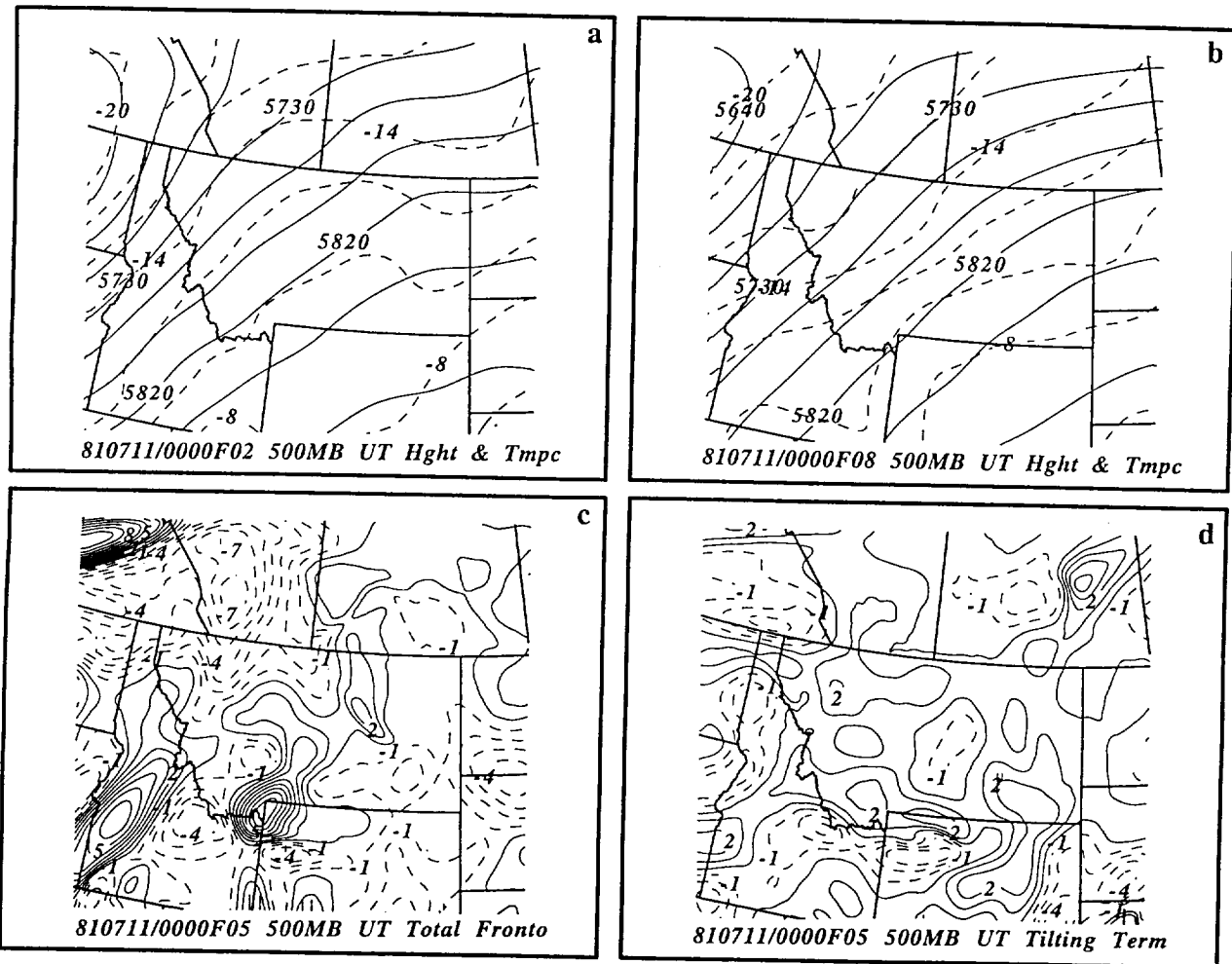


Fig. 14. UT coarse mesh simulation of 500 mb height (m) and temperature (C) valid at (a) 0200 UTC and (b) 0800 UT. Also shown are (c) total frontogenesis ($K m^{-1}s^{-1} \times 10^9$) and (d) frontogenesis tilting term ($K m^{-1}s^{-1} \times 10^9$) valid at 0500 UTC 11 July 1981.

southeast temperature gradient between MSO and the WGR reflecting the $\sim 3C/6$ hour cooling rate northwest of the WGR and $\sim 1C/6$ hour heating rate over the WGR accompanying the cross-stream variation of vertical velocity within the thermally indirect circulation (Figs. 12-15). The frontogenesis is maximized within the region encompassed by the WGR, MSO, and GTF at this time as the dual circulations merge in the cross section depicted in Fig. 15. The primary frontogenetical forcing function is the tilting term, which reflects the importance of the aforementioned thermally indirect circulation (note Eq. (3)).

$$\begin{aligned}
 F = \frac{D}{Dt} |\nabla \theta| = & \frac{1}{|\nabla \theta|} \left\{ \frac{\partial \theta}{\partial x} \left[\frac{1}{C_p} \left(\frac{p_0}{p} \right)^\kappa \frac{\partial}{\partial x} \left(\frac{dQ}{dt} \right) - \frac{\partial u}{\partial x} \frac{\partial \theta}{\partial x} \right. \right. \\
 & \left. \left. - \frac{\partial v}{\partial x} \frac{\partial \theta}{\partial y} - \frac{\partial w}{\partial x} \frac{\partial \theta}{\partial z} \right] + \frac{\partial \theta}{\partial y} \left[\frac{1}{C_p} \left(\frac{p_0}{p} \right)^\kappa \frac{\partial}{\partial y} \left(\frac{dQ}{dt} \right) - \frac{\partial u}{\partial y} \frac{\partial \theta}{\partial x} - \frac{\partial v}{\partial y} \frac{\partial \theta}{\partial y} - \frac{\partial w}{\partial y} \frac{\partial \theta}{\partial z} \right] \right. \\
 & \left. + \frac{\partial \theta}{\partial z} \left[\frac{p_0^\kappa}{C_p} \frac{\partial}{\partial z} \left(p^{-\kappa} \frac{dQ}{dt} \right) - \frac{\partial u}{\partial z} \frac{\partial \theta}{\partial x} - \frac{\partial v}{\partial z} \frac{\partial \theta}{\partial y} - \frac{\partial w}{\partial z} \frac{\partial \theta}{\partial z} \right] \right\}. \quad (3)
 \end{aligned}$$

Consistent with the frontogenesis caused by the differential vertical motions and newly created deformation field, is the shifting of the maximum midtropospheric height gradients oriented across the stream from near and northwest of MSO at 0200 UTC to just northwest of the WGR by 0800 UTC. Hence, the differential vertical motions caused by the predominantly cross-stream ageostrophic wind components accompanying the aforementioned geostrophic adjustment process redistribute the mass within the midtroposphere, thus enhancing the southeast-northwest pressure gradient force (PGF) to the southeast, while the PGF is relaxed within the region where its original maximum is located. This represents a shifting in the cross-stream height gradient within the polar jet streak to the southeast accompanying the balanced circulation which results from the earlier unbalanced circulation. These balanced and unbalanced circulations still exist at 0800 UTC (Fig. 15).

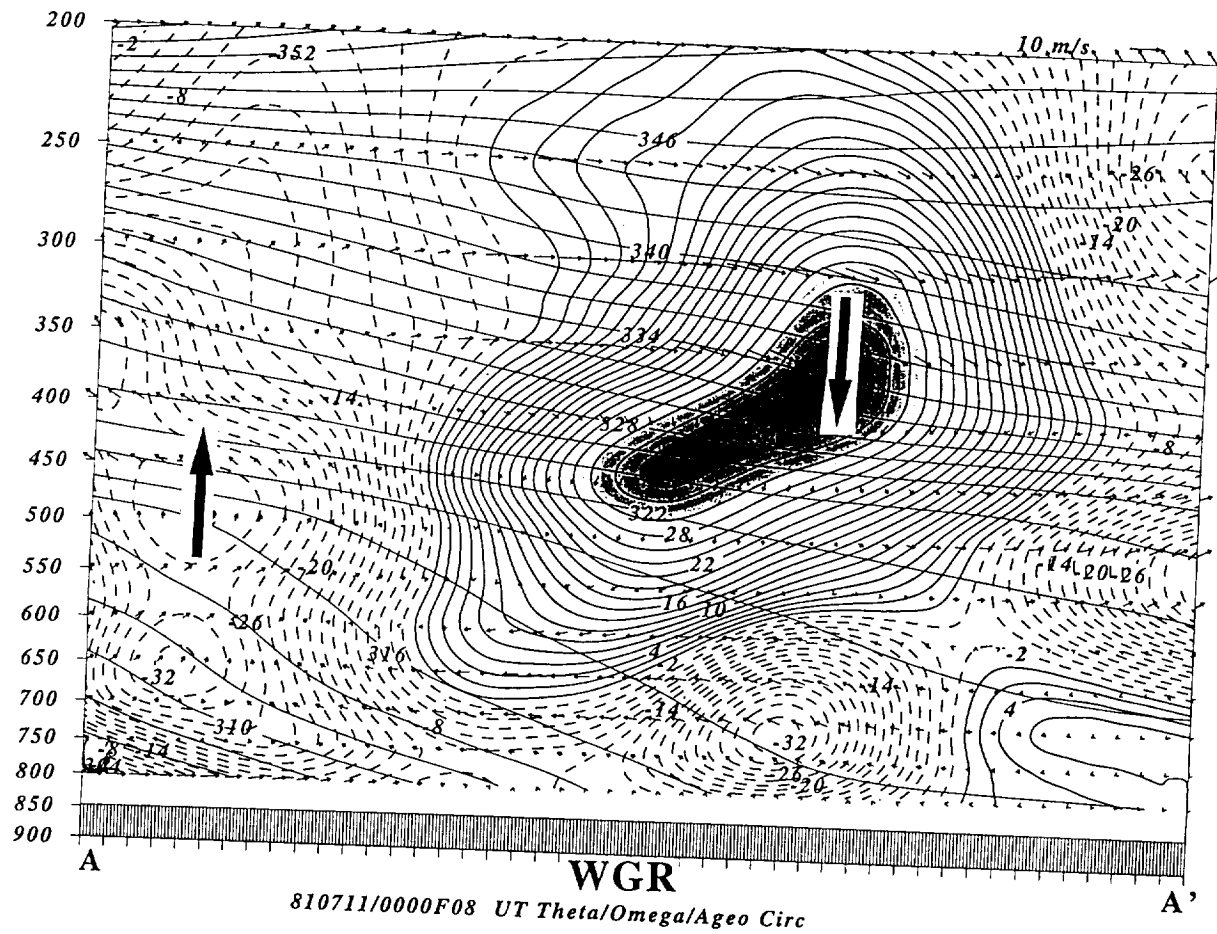


Fig. 15. Vertical cross section (A-A') of potential temperature (solid in K), transverse ageostrophic circulation vectors (m s^{-1}), and vertical motion ($\mu\text{b s}^{-1}$) from UT coarse mesh simulation valid at 0800 UTC 11 July 1981. Nomenclature as in Fig. 13, with the exception that bold arrows represent the direction of the thermally direct circulation.

These simulated temperature and height changes (Fig. 14) are consistent with the observations depicted in Fig. 5 and the QG simulation results shown in Fig. 8. Note the midtropospheric warming (cooling) which is both simulated and observed over eastern Washington, southeastern British Columbia, and southern Alberta (central Idaho and central Montana), and the midtropospheric warming which is both simulated and observed over western and northwestern Wyoming.

c. Stage III - Secondary Mid-Upper Tropospheric Wind Adjustment

The midtropospheric frontogenesis formed during stage II and the accompanying adjustment in the mass field produce another region of simulated geostrophic adjustment nearly directly over and slightly upstream from the WGR (i. e., over southeastern Idaho).

During the 0700-1300 UTC time period, the 500 mb winds and vertical motions depicted in Fig. 16 indicate that a second geostrophic adjustment process occurs in the vicinity of the WGR. The height perturbation accompanying the stage II frontogenesis produces a nonuniform cross-stream realignment of the pressure gradient force which results from the fact that the frontogenesis in the triangle formed by WGR-MSO-GTF is much stronger than it is further to the southwest (Fig. 14). The cross-stream pressure gradient force is weaker upstream over Idaho as well as further northeast over eastern Montana, than it is near the WGR. Hence, parcels traversing this region within the midtroposphere not only must adjust to the changing pressure gradient force within the inflection point in the synoptic scale height field in this region, but they also encounter a marked increase in the magnitude of the cross-stream pressure gradient force. This is evident from Fig. 18 wherein the maximum cross-stream directed pressure gradient force has shifted southeastward to the northwestern periphery of the WGR by 0800 UTC from its earlier location over northern Idaho at 0200 UTC (Fig. 10). Thus, a larger along-stream increase in the cross-stream acceleration will be imposed on parcels as they traverse through this region than would otherwise occur had they been traversing the adjustment region northwest of MSO during stage I. This process therefore represents a secondary

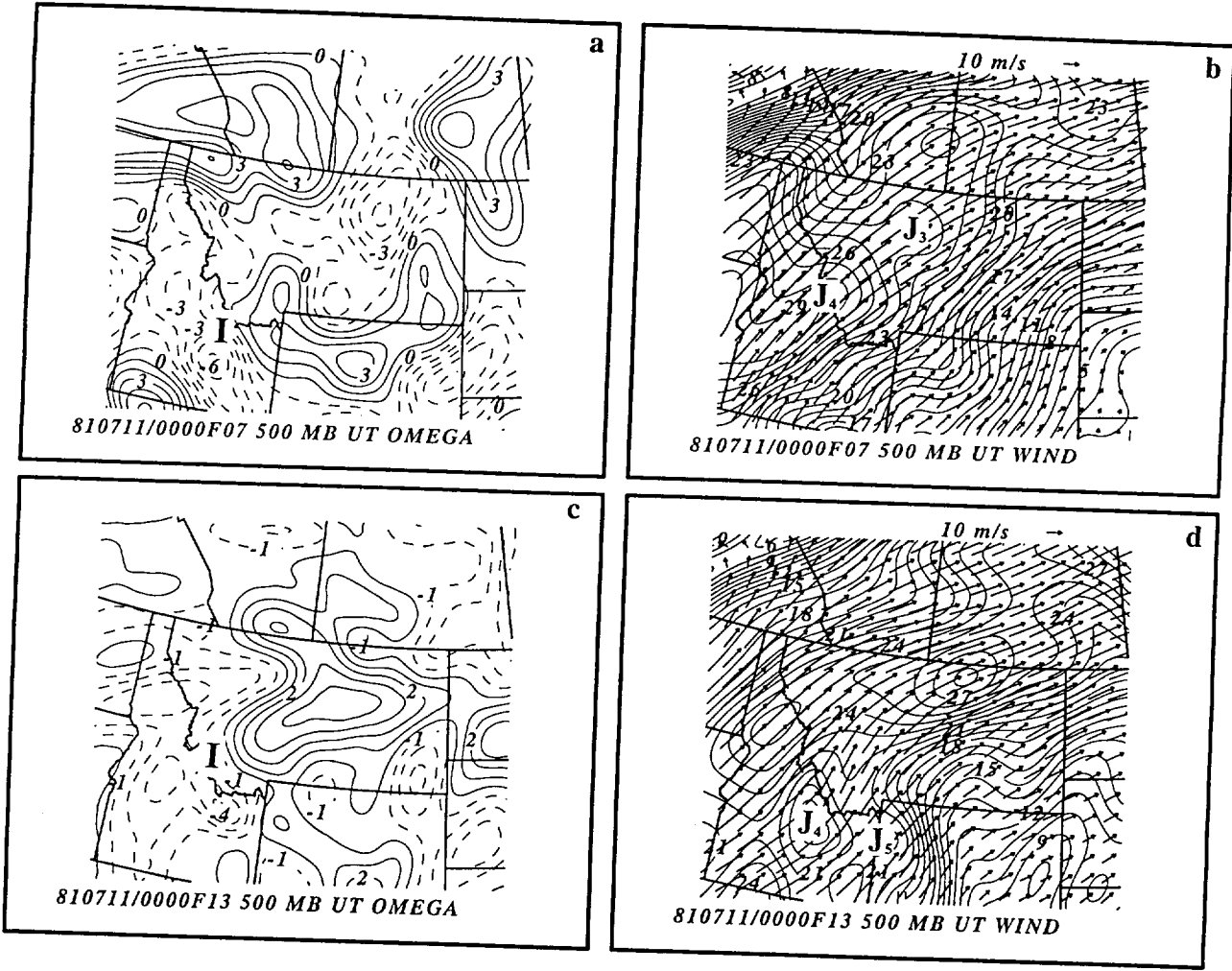


Fig. 16. UT coarse mesh simulation of 500 mb omega ($\mu\text{b s}^{-1}$) as well as 500 mb wind vectors and isotachs (m s^{-1}) valid at (a-b) 0700 UTC and (c-d) 1300 UTC 11 July 1981. $J_{(x)}$ is as in Fig. 11 and I is as in Fig. 12, however, oriented in the along-stream direction.

geostrophic adjustment which is initiated by the newly formed mass and momentum field that developed during the primary geostrophic adjustment defined by stages I and II.

As this secondary geostrophic adjustment occurs, parcels passing over the WGR through the mesoscale jetlet J4 will have their streamwise velocities increased as the inertial-advective terms in the equations of motion, i. e., Eqs. (1) and (2), respond to the increased westward-directed pressure gradient force over the WGR. As the Coriolis force subsequently increases in magnitude, mesoscale jetlet J5 develops (Fig. 16d), thus resulting in the further intensification of the thermally indirect circulation over the WGR (as evident in the vertical cross sections of theta and omega depicted in Fig. 15). While there is clearly a cross-stream component to this intensifying thermally indirect circulation, the horizontal gradient of vertical velocity is actually stronger *along* the stream as opposed to *across* the stream as can be seen in the 500 mb vertical motions (Fig. 16). The magnitude of the ascending motions just southwest of the WGR are sufficiently large such that they produce saturation in the relative humidity fields at 500 mb by 1200 UTC (not shown). Consistent with the fact that the circulation is oriented along the stream is the presence of a bulging lobe of ageostrophic wind southeast of the jet over the WGR at 300 mb (Figs. 17 and 18). As in Stage I, the geostrophic adjustment, i.e., the adjustment of the wind to the mass field, forces a leftward-directed acceleration, but this time it is very concentrated over the WGR.

This adjustment results in the intensification of mesoscale jetlet/wind maxima J5 (Fig. 16) which is the rightward-turning Coriolis response to the streamwise inertial-advective accelerations over the WGR to the east of J4. The exit region of J5 is located nearly directly over the WGR by 1300 UTC (Figs. 16d and 21). This secondary geostrophic adjustment is nearly 300 km to the south-southeast of the primary geostrophic adjustment process which created the mesoscale exit region J3 earlier between MSO and GTF. Thus, J4 evolves out of the mass/momentum perturbations which accompany J3 and

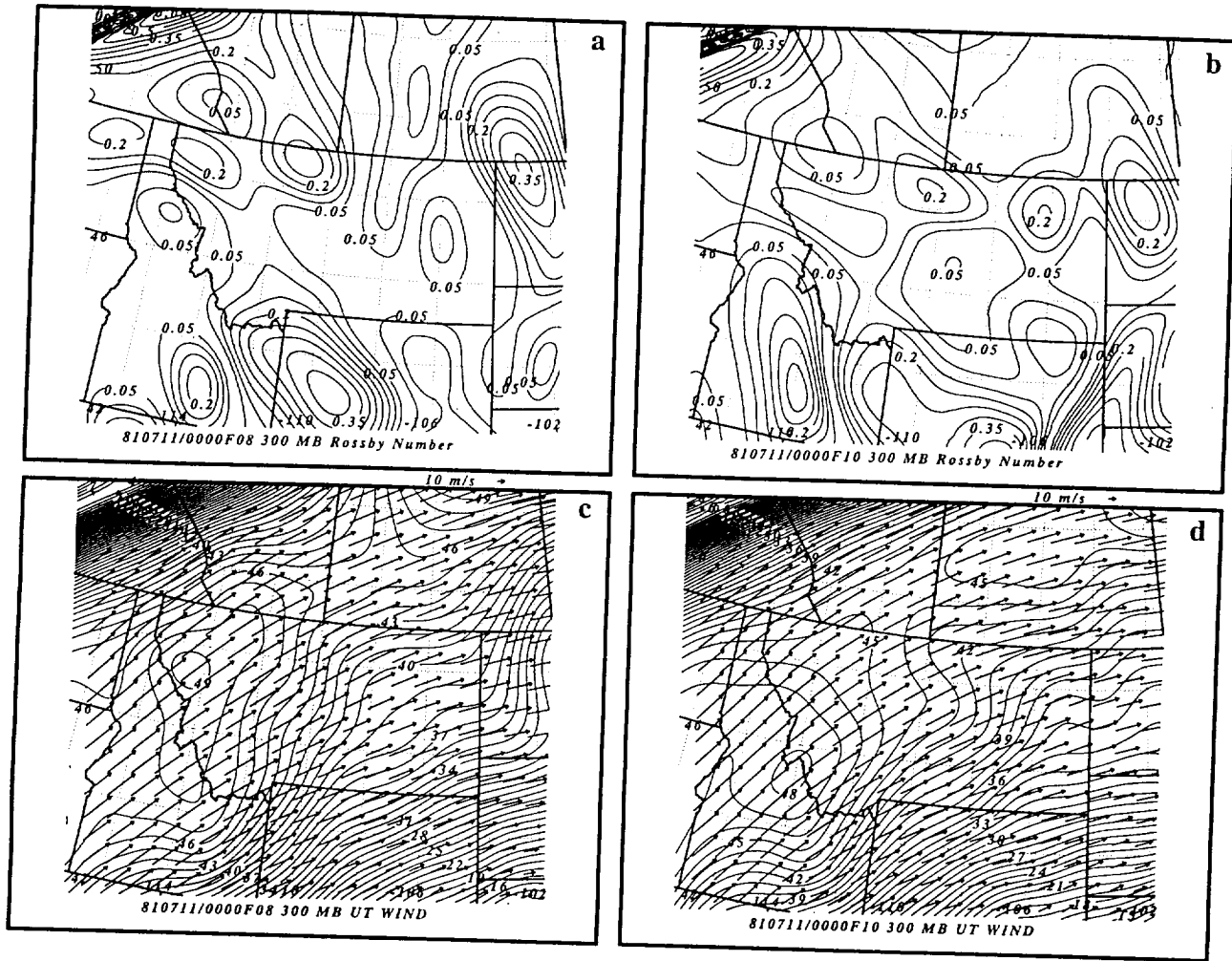


Fig. 17. UT coarse mesh simulation at 300 mb of: (a-b) Eq. (5), i.e., Koch and Dorian (1988) Rossby number and (c-d) wind vectors and isotachs (m s^{-1}) valid at 0800 UTC and 1000 UTC 11 July 1981.

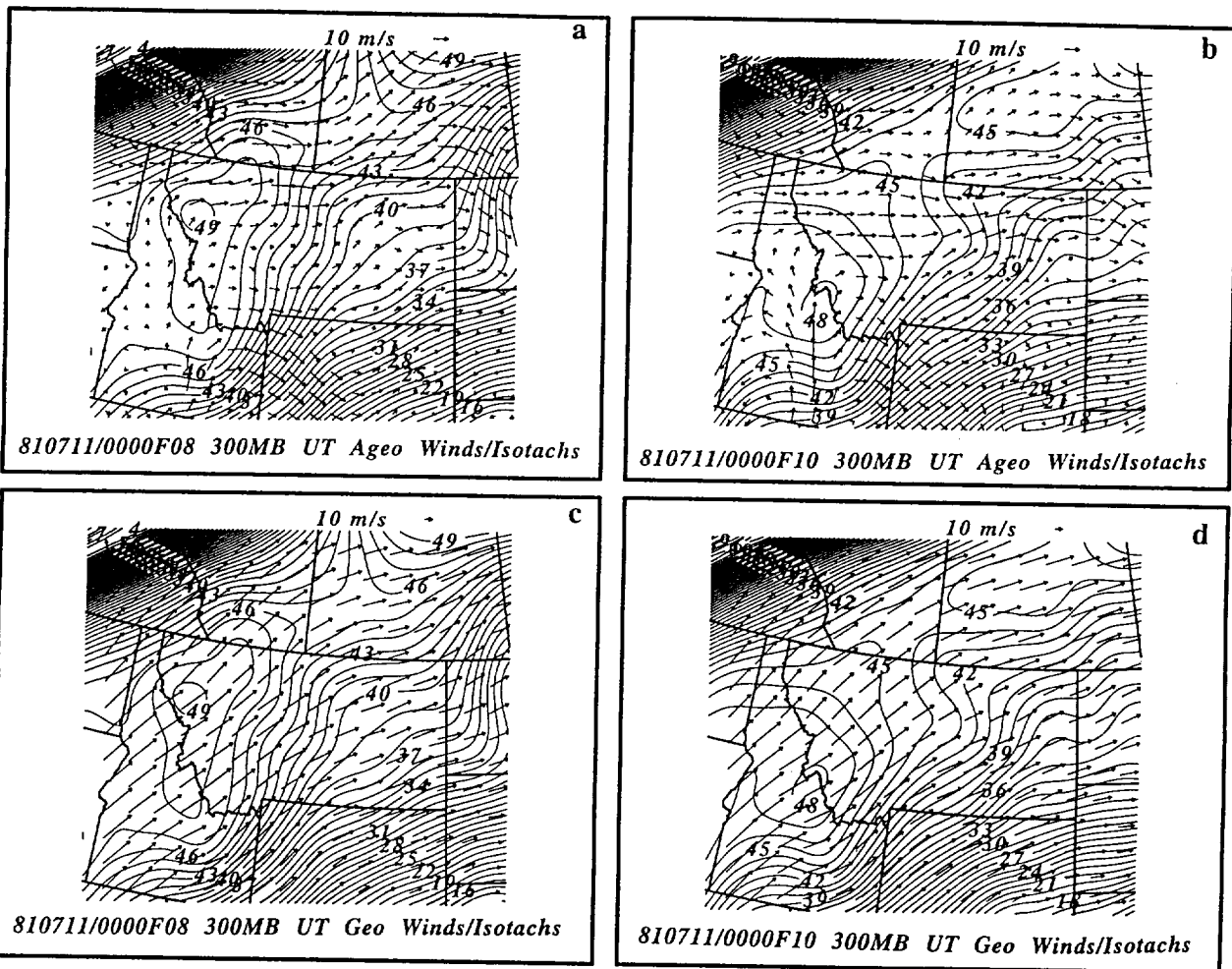


Fig. 18. UT coarse mesh simulation at 300 mb of: (a-b) ageostrophic wind vectors and isotachs (m s^{-1}) and (c-d) geostrophic wind vectors and wind velocity isolachs (m s^{-1}) valid at 0800 UTC and 1000 UTC 11 July 1981.

the parcels adjusting within J4 form a new rotational jet streak wind component, only directly over the WGR.

This second set of adjustments occurs over such a small region that the along-stream unbalanced vertical motions are much larger in magnitude than the balanced vertical motions which are more typical of larger scale semi-geostrophic jet streak adjustments. As can be seen in Figs. 16-18, even in the 16 km UT simulation, the 500 and 300 mb fields indicate a dual geostrophic jet streak structure and a very ageostrophic secondary jet streak structure over the WGR. This cross-stream ageostrophy indicates substantial unbalanced flow and significant increases in parcels' velocity divergence as they enter this region. Fig. 18 depicts the ageostrophic wind vectors consistent with large magnitudes of the Lagrangian divergence tendencies at 500 and 300 mb, which can be defined from the horizontal divergence equation after Kaplan and Paine (1977), Zack and Kaplan (1987), Uccellini and Koch (1987), and Koch and Dorian (1988):

$$\frac{\partial D}{\partial t} + \mathbf{V} \cdot \nabla D + \omega \frac{\partial D}{\partial p} = D^2 - \nabla \omega \cdot \frac{\partial \mathbf{V}}{\partial p} + f \zeta + 2 J(u, v) - \nabla^2 \phi - \beta u . \quad (4)$$

Regions of substantial velocity divergence tendency are nearly synonymous with regions of unbalanced flow accompanying significant cross-stream component of the ageostrophic wind, as defined in terms of a Lagrangian Rossby number (Koch and Dorian 1988):

$$R_o = \frac{|\mathbf{V}_{ag \perp}|}{|\mathbf{V}|} . \quad (5)$$

The ageostrophy and flow imbalance result in substantial increases in total velocity divergence and Lagrangian R_o values >0.5 over the WGR, as can be seen in Fig. 17, and

has a profound effect on the low-level mass field as seen in the adjustment of the low-level wind field during stage IV (discussed below; see Fig. 16).

d. Stage IV - Development of the Secondary Low-Level Mesoscale Jet Over The WGR

As can be seen in Fig. 19, there are two low-level (700 mb) mesoscale jetlets which affect the region near the WGR during the 0900-1300 UTC time period. One jetlet results from the first geostrophic adjustment process over and just northwest of MSO, while a second jetlet forms over the WGR shortly before 1000 UTC. Between 0900 and 1300 UTC the second 700 mb wind maximum intensifies over southeastern Idaho ahead of the low-level trough which had been observed over Oregon and Nevada at 0000 UTC. In time this feature becomes the dominant low-level mesoscale jetlet as a result of the southeastward development of 700 mb height falls ahead of the short wave trough (Fig. 20). The height falls maximize between southeastern Idaho and the WGR under the stage III secondary geostrophic adjustment process. The increase in velocity divergence over the WGR accompanying the stage III circulation produces a rapid increase in the height falls resulting in an increased low-level pressure gradient force which is directed to the north. The low-level flow is clearly directed to the left of the 700 mb geostrophic wind in response to the increasing northward-directed low-level pressure gradient force accompanying *the intensification of the upstream 700 mb trough into a distinct mesotrough near the WGR*. The preexisting isallobaric wind component ahead of the 700 mb trough increases *explosively* in response to the height fall pattern over the WGR caused by the second geostrophic adjustment process.

This low-level convergent flow results in ascending motion at 500 mb accompanying the secondary geostrophic adjustment within the same region at the same time period (Fig. 19d). Another effect of the mesoscale ascent over the WGR is localized moistening (the evolving "bulls eye" evident in the 700 mb relative humidity field depicted over the WGR in Fig. 19e). Not only is the low-level jet highly convergent, but it is also

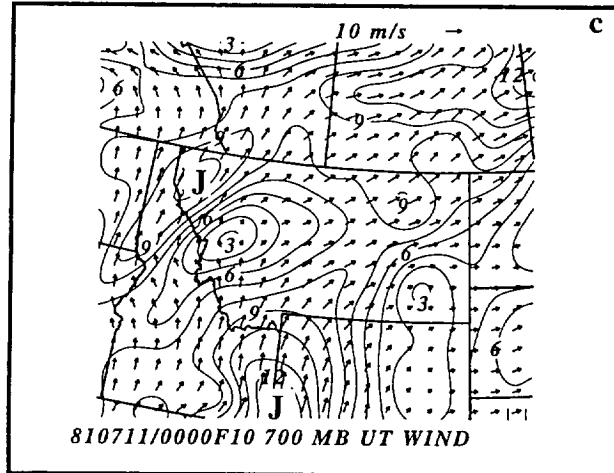
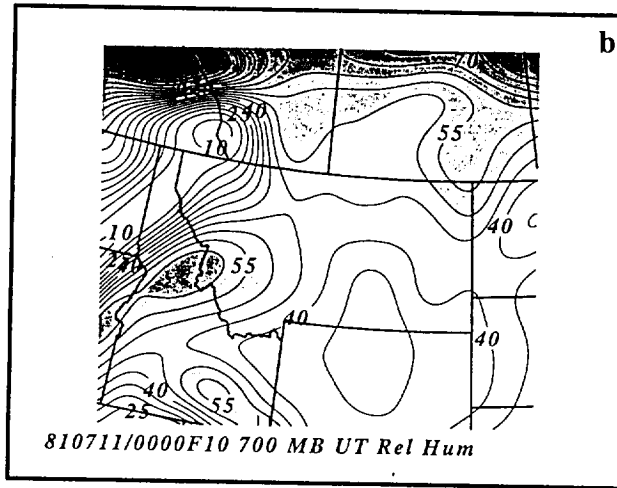
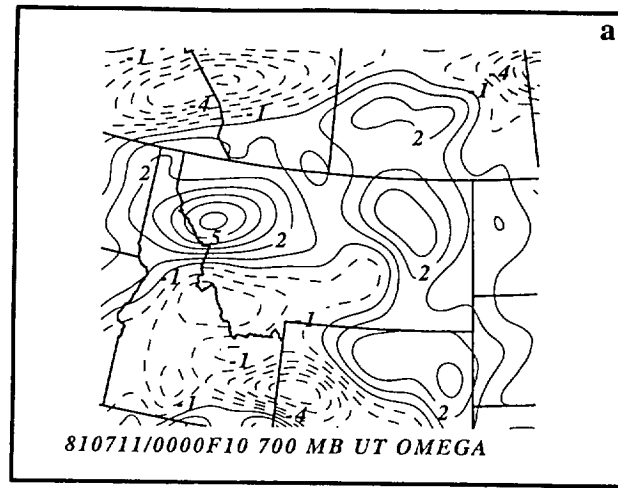
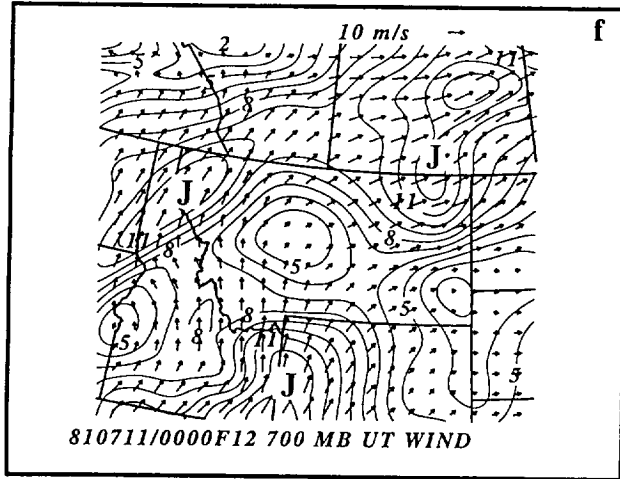
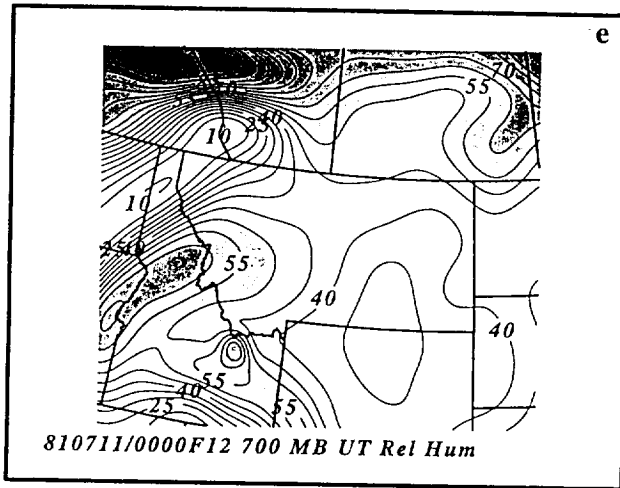
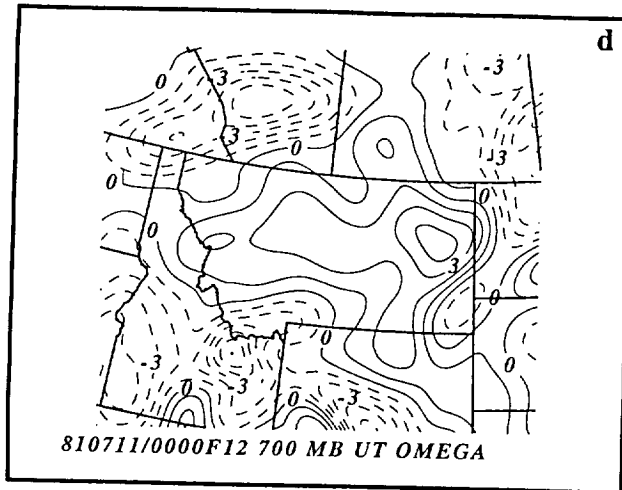


Fig. 19. UT coarse mesh simulation of 700 mb vertical motion ($\mu\text{b s}^{-1}$), relative humidity (%), and wind vectors and isotachs (m s^{-1}) valid at (a-c) 1000 UTC and (d-f) 1200 UTC 11 July 1981. J represents mesoscale low-level momentum maxima (jetlets).



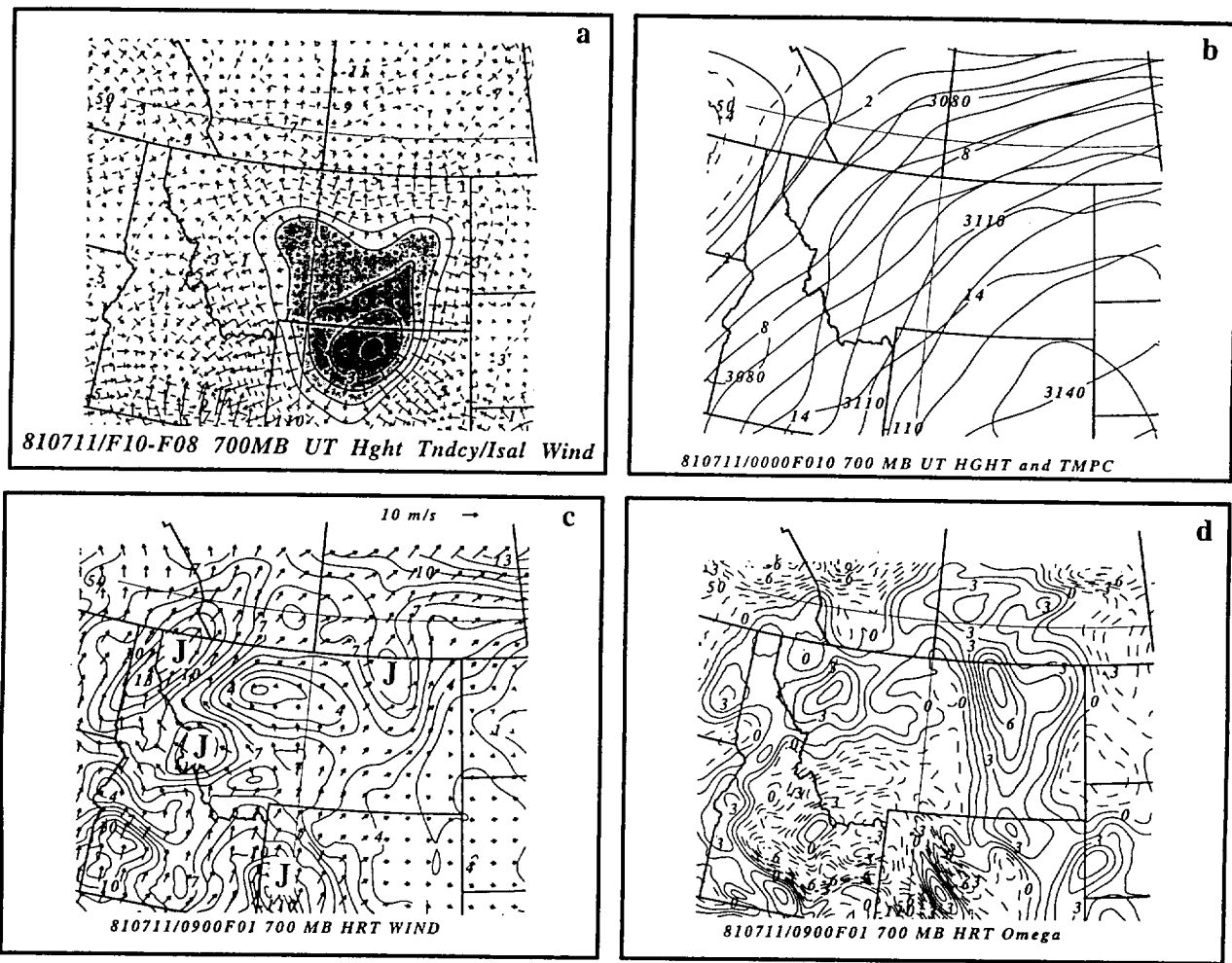


Fig. 20. UT coarse mesh simulation at 700 mb of: (a) height change (m) and isallobaric wind vectors ($m s^{-1}$) valid between 0800 UTC and 1000 UTC 11 July 1981, (b) geopotential height (m) and temperature (C) valid at 1000 UTC 11 July 1981, and HRT nested-grid simulation at 700 mb of (c) wind vectors and isotachs ($m s^{-1}$) and (d) vertical motion ($\mu b s^{-1}$) valid at 1000 UTC 11 July 1981.

aligned nearly perpendicular to the Absaroka mountain range over northwestern Wyoming (hence, it is orthogonal to the WGR). This will have important consequences as the low-level jet encounters orographically-induced mass perturbations in the simulations which include nonhomogeneous terrain. *Most importantly, this secondary ascent/relative humidity maximum occurs very close in space and time to the genesis of the first gravity wave episode observed by Koch and Golas (1988), and accompanies a newly developed cloud mass over the WGR as seen in Fig. 7c.*

e. *Terrain-Induced Thermal Perturbations Diagnosed from the LRT and HRT Simulations*

One of the most obvious and important characteristics of the UT mesoscale simulation is the orientation of the vertical velocity fields which align themselves nearly parallel to the mid-upper tropospheric jet. This alignment is not consistent with the pressure change fields accompanying the gravity waves observed by Koch *et al.* (1988). Even the along-stream component of the vertical velocity perturbations accompanying the secondary geostrophic adjustment process have a wavelength >700 km, which is much larger than the ~160 km primary modes observed by Koch *et al.* (1988). However, by 1000 UTC both the nested-grid and coarse mesh LRT and HRT simulations produce mid-upper tropospheric features in the wind and vertical motion fields, particularly over the WGR, that are aligned orthogonal to the jet and parallel to the terrain axes and have a wavelength which is <200 km (Figs. 21-22). This orientation, position, and wavelength are very similar to the primary gravity waves observed by Koch *et al.* (1988) to develop over the WGR at about 1100 UTC.

The vertical velocity, height, and wind field perturbations at 300, 500, and 700 mb (Figs. 21-22) are a direct result of the pressure perturbations established within the boundary layer to the lee of the Bitterroot and Absaroka mountain ranges within both the LRT and HRT simulations. While these two simulations produce a similar dominant mesoscale low-level jet over the WGR similar to that produced in the UT simulation,

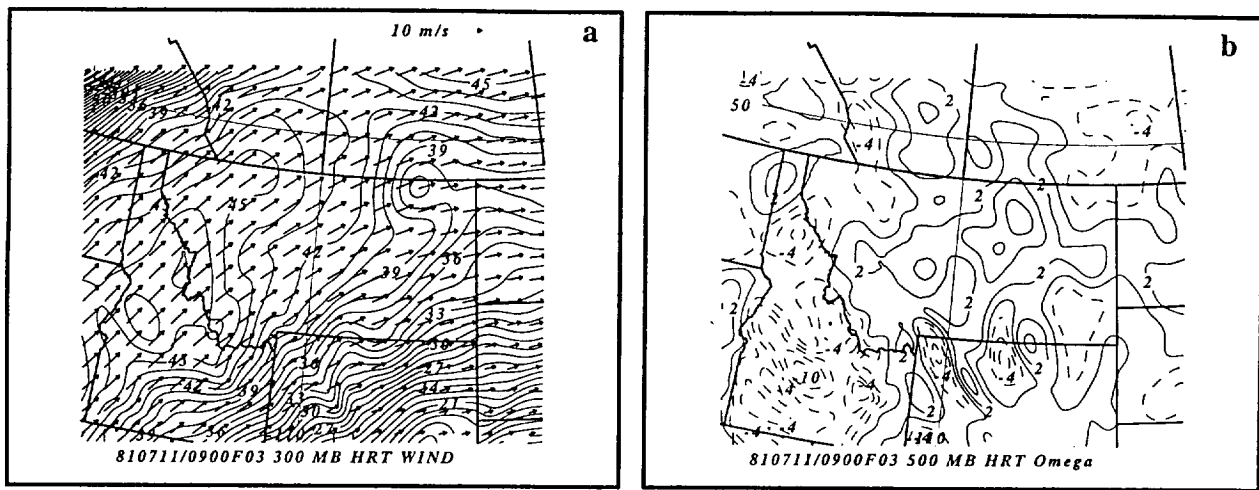


Fig. 21. HRT nested-grid simulation of (a) 300 mb wind vectors and isotachs (m s^{-1}) and (b) 500 mb vertical motion ($\mu\text{b s}^{-1}$) valid at 1200 UTC 11 July 1981.

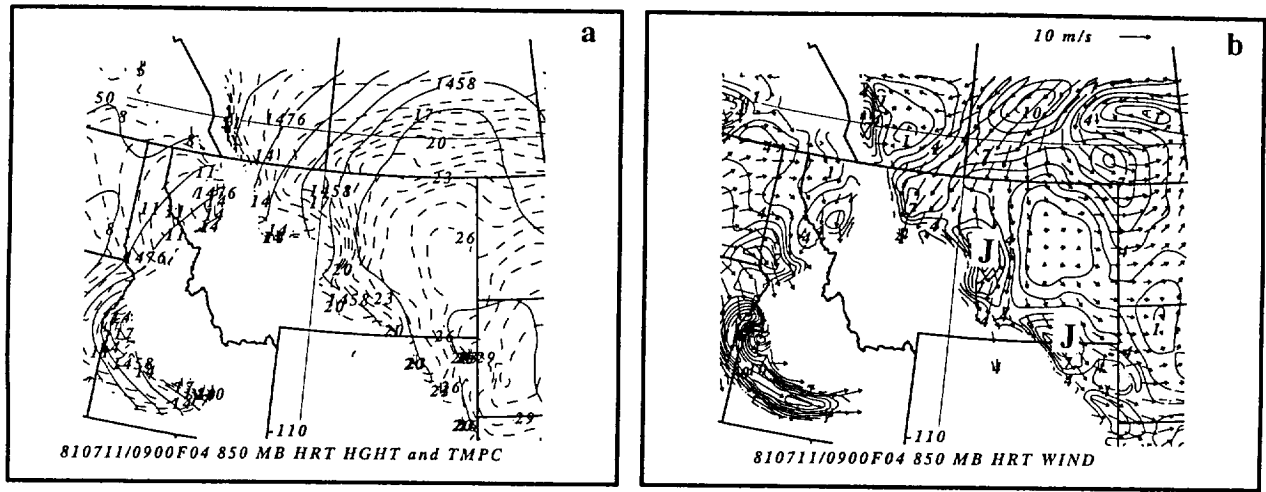
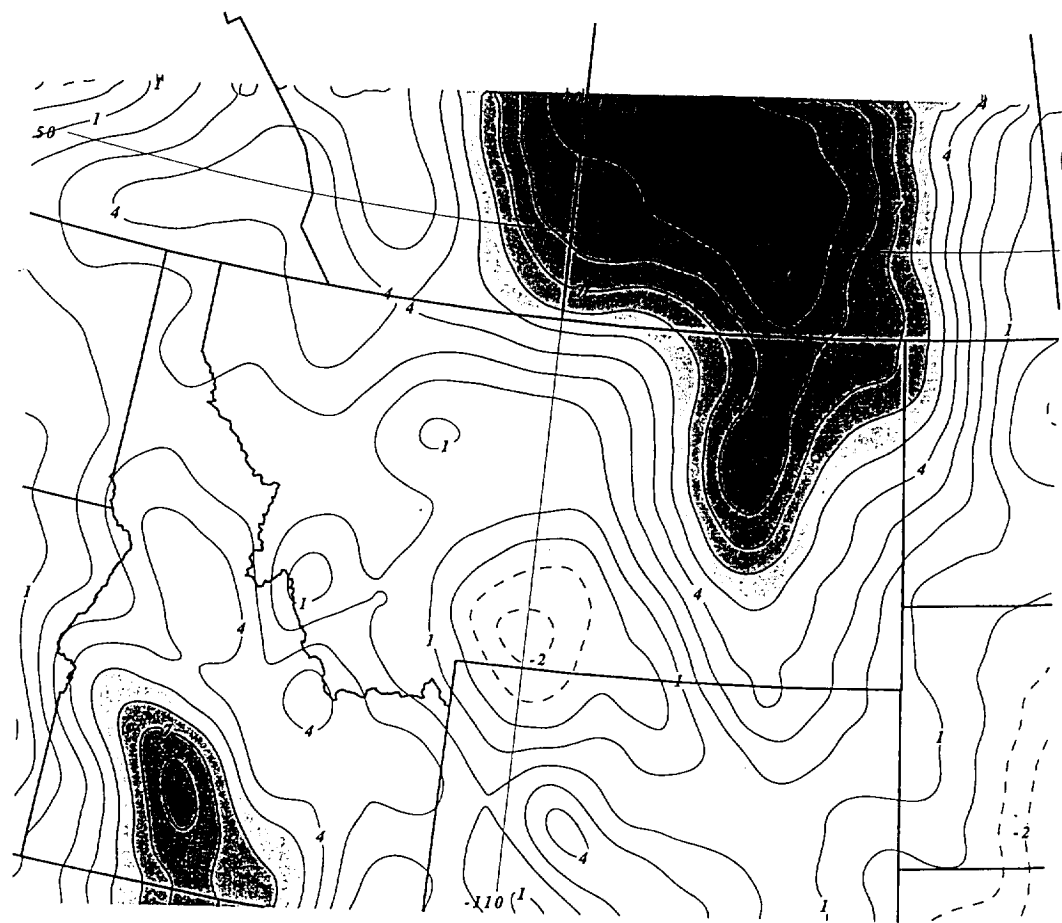


Fig. 22. HRT nested-grid simulation at 850 mb of: (a) height (m) and temperature (C) and (b) wind vectors and isotachs (m s^{-1}) valid at 1300 UTC 11 July 1981.

terrain-induced thermal perturbations result in a reorientation and scale-contraction of the vertical velocity perturbations produced by the LRT and HRT simulations.

In analyzing these mass perturbations we will focus on the HRT simulation results. The HRT simulation produces the largest amplitude and shortest wavelength response of the two simulations, as expected. There are two thermal perturbations which are evident in these simulations that include inhomogeneous terrain which are not present in the UT simulation. The first thermal perturbation can be inferred from the 850 mb temperature fields produced in the nested-grid HRT simulation after 1200 UTC (Fig. 23). Even before the gravity waves are well-organized, a wedge of cool air can be seen reinforcing the pressure rise and northerly wind component just northeast of the WGR over central Montana. The cool air damming/drainage against the mountains is easily distinguishable by comparing the UT 850 mb fields to the HRT 850 mb fields at the same time. As the low-level flow intensifies within the HRT simulation (driven largely by simulated nocturnal radiational cooling and reduced friction within the planetary boundary layer over the adjacent plains region east of the mountains), the cool northeasterly flow travels implicitly up the terrain slope between 850 and 700 mb. As this layer of cool air spreads southeastwards and up the sloping terrain, it produces a weak ridge in the height field *which perturbs the height distribution throughout the column*. Thus, it acts to modify the along-stream pressure gradient force encountered by parcels within the secondary low-level mesoscale wind maximum/jetlet exit region which propagates over the WGR after 0900 UTC.

In addition to this first thermal perturbation, as the secondary low-level mesoscale PBL jet streak passes nearly perpendicular to the Absaroka mountain range (diagnosed from the HRT nested-grid simulation depicted in Fig. 22), the adiabatically cooled convergent upslope flow over southeastern Idaho produces height falls while the downslope adiabatic warming on the lee slope over northwestern Wyoming and southwestern Montana produces height rises accompanying the development of the



810711/0000F12 500MB HRT-UT Hght Tndcy

Fig. 23. 500 mb height differences (m) between the UT and HRT nested-grid simulations valid at 1200 UTC 11 July 1981.

hydrostatic mountain wave. These waves are evident from the vertical velocity and height difference fields depicted over northwestern Wyoming in Figs. 22b and 24, respectively. Hence, a second area of thermally-induced height falls and rises (oriented in a predominantly northwest-southeast fashion) are perturbing the deep height and vertical motion patterns over the WGR simultaneously as the secondary low-level jet propagates over the same region. These differential height changes will modify the along-stream pressure gradient force and enhance the along-stream variation of the ageostrophic winds over short time intervals. There is also a strong impact on the gravity wave energetics, since the vertical structure of the thermal and kinematic perturbations occurring beneath the geostrophic adjustment region aloft will act to modify the Scorer parameter, which affects wave ducting and shear instability.

The consequences of these terrain-induced thermal perturbations on the process of gravity wave generation are significant. The thermal perturbations in the exit region of the unbalanced secondary low-level jet streak produce along-stream variations of the cross-stream component of the pressure gradient force (Fig. 24). These perturbations in the pressure gradient force produce along-stream variations in the horizontal velocity divergence tendencies and unbalanced flow indicated by Eqs. (4) and (5), respectively. These velocity perturbations are quite evident in Figs. 21 and 25a, where the mesoscale ageostrophic wind maxima at 300 mb over the WGR create along-stream mass fluctuations. Hence, the integrated effect of the along-stream height perturbations induced by the terrain (Fig. 24) is to produce vertically integrated divergence tendencies (Fig. 24) which perturb the surface pressure, resulting in the along-stream mean sea level pressure tendencies shown in Fig. 25a for the 1300 through 1400 UTC time period. It is this interaction between the accelerating low-level jet impinging upon the terrain-induced mass perturbations associated with the hydrostatic mountain wave(s) that contract the scale of the velocity divergence, producing along-stream mass perturbations. These features have a wavelength ~ 150 km and the obvious perturbation of the wind, theta, and omega fields

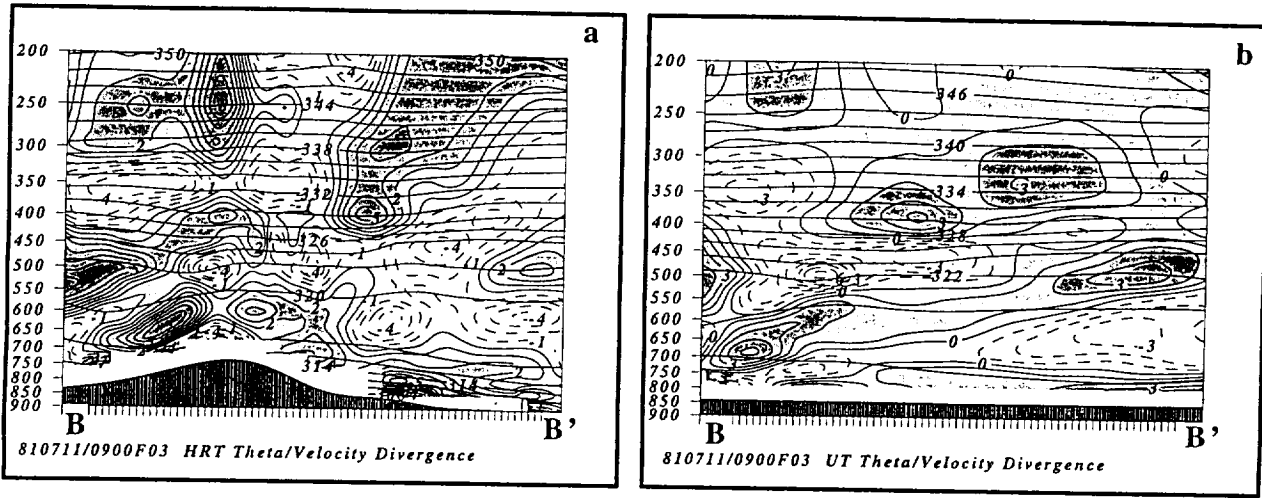


Fig. 24. Vertical cross section (B-B') from: (a) HRT nested-grid simulation and (b) UT nested-grid simulation of potential temperature (light solid lines, in K) and velocity divergence (positive shaded, 10^4 s^{-1}) valid at 1200 UTC 11 July 1981.

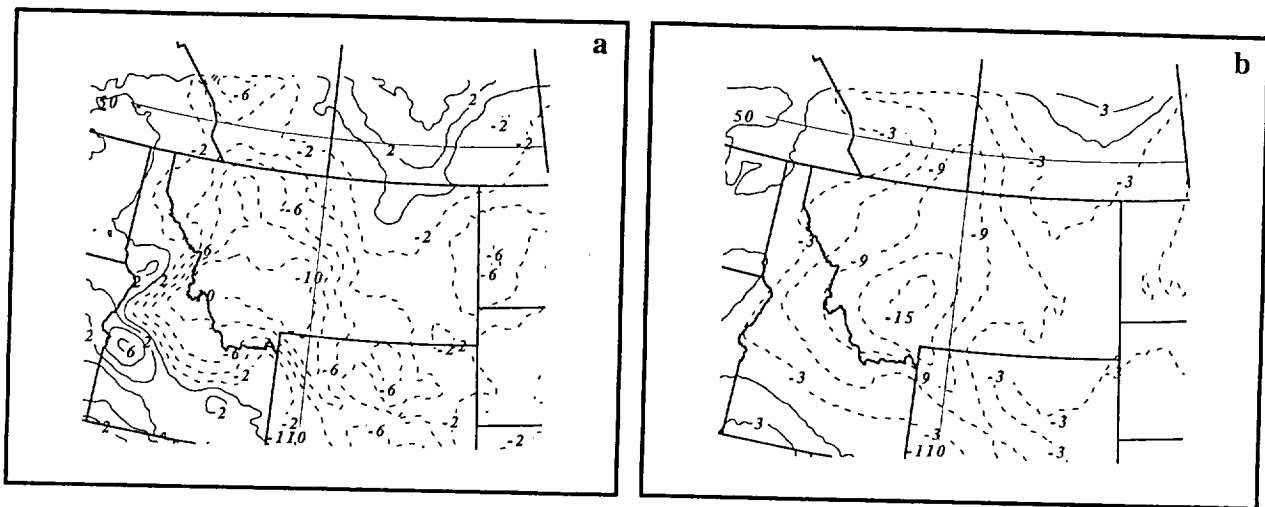


Fig. 25. (a) HRT nested-grid simulation and (b) UT nested-grid simulation of hourly mean sea level pressure change (mb) valid between 1300 UTC and 1400 UTC 11 July 1981.

orthogonal to the flow above the integrated pressure rises and falls are consistent with that characterizing and defining internal gravity waves. These pressure perturbations are clearly absent in the uniform terrain (UT) simulation (Fig. 25b). However, it takes several hours longer for these simulated mass and momentum perturbations to achieve the amplitude of those observed in nature by Koch and Golas (1988). *This indicates that some physical process is absent from these numerical simulations that is important for wave amplification.* Parts II and III will show that this process is, very likely, convective latent heat release.

6. Summary and Conclusions

In the first of a series of papers on the physical mechanisms responsible for the generation of the mesoscale gravity waves observed by Koch and Golas (1988), we have examined how geostrophic adjustment processes produced a mesoscale wind maximum in the planetary boundary layer *close to the location and time of observed wave generation.* Mesoscale numerical simulations employing three different terrain configurations in a moist atmosphere in which convective and stratiform latent heating is totally suppressed all produce the low-level jetlet in approximately the same place and time. However, only the nested-grid simulations employing high resolution terrain (HRT) produce inertia-gravity waves with characteristic wavelengths analogous to the "primary" waves observed by Koch and Golas (1988). This indicates that: 1) the background adiabatic geostrophic adjustment processes are responsible for low-level jet formation independent of terrain geometry, surface sensible, and/or convective latent heating physics, 2) the location of the low-level jet in close proximity to the orography is important in the wave generation process(es), and 3) the fine numerical resolution needed to resolve these waves, e. g., ~8 km for ~150 km wavelength features, points towards nonlinear wave-wave interaction/amplification as critical to wave development. Since the simulations indicate that it is the perturbation of the low-level mesoscale jetlet by the terrain-induced pressure ridges and troughs which results in gravity wave formation, it is very important to understand the

role of geostrophic adjustment processes in mesoscale upper- and low-level jet streak formation.

The simulated four-stage sequence of events responsible for the development of the low-level jetlet (Fig. 26) involves two distinct, but coupled, geostrophic adjustment processes. During stage I, the wind in the exit region of a pre-existing polar jet streak (the “primary jet”) adjusts to an increasing westward-directed pressure gradient force as it propagates towards the inflection point in the geopotential height field located over eastern Idaho. This produces a westward (cross-stream) acceleration followed by a northeastward streamwise inertial-advection adjustment and eventual rightward-turning as the Coriolis force increases. The strong leftward-directed unbalanced adjustment within the left exit region of the existing polar jet streak is analogous to that analyzed from available rawinsonde data by Koch and Dorian (1988). It should be noted that the substantial magnitude of this adjustment is most likely the result of: 1) the proximity of the propagating primary jet streak exit region to the inflection point in the height field and 2) the near superpositioning of the synoptic scale ridge in the height field with the subsynoptic scale thickness ridge accompanying high surface temperatures above the elevated plateau (including the WGR) at the time of model initialization. The midtropospheric descent over northern Idaho and eastern Washington accompanying the “unbalanced” adjustment causes adiabatic compression and warming northwest of the jet streak exit region as well as ascent and adiabatic cooling south of the exit region over central Montana (Fig. 26). The flow is “unbalanced” because the mass flux convergence is occurring on the opposite side of the jet streak exit region from that which would produce adiabatic warming and cooling patterns appropriate to produce thermal wind balance. The result is the establishment of a thermally direct ageostrophic circulation. Eventually, in an effort to balance the flow and maintain thermal wind balance, a thermally indirect circulation develops to the right of the thermally direct circulation reinforcing the cooling over much of central Montana and warming over northwestern Wyoming.

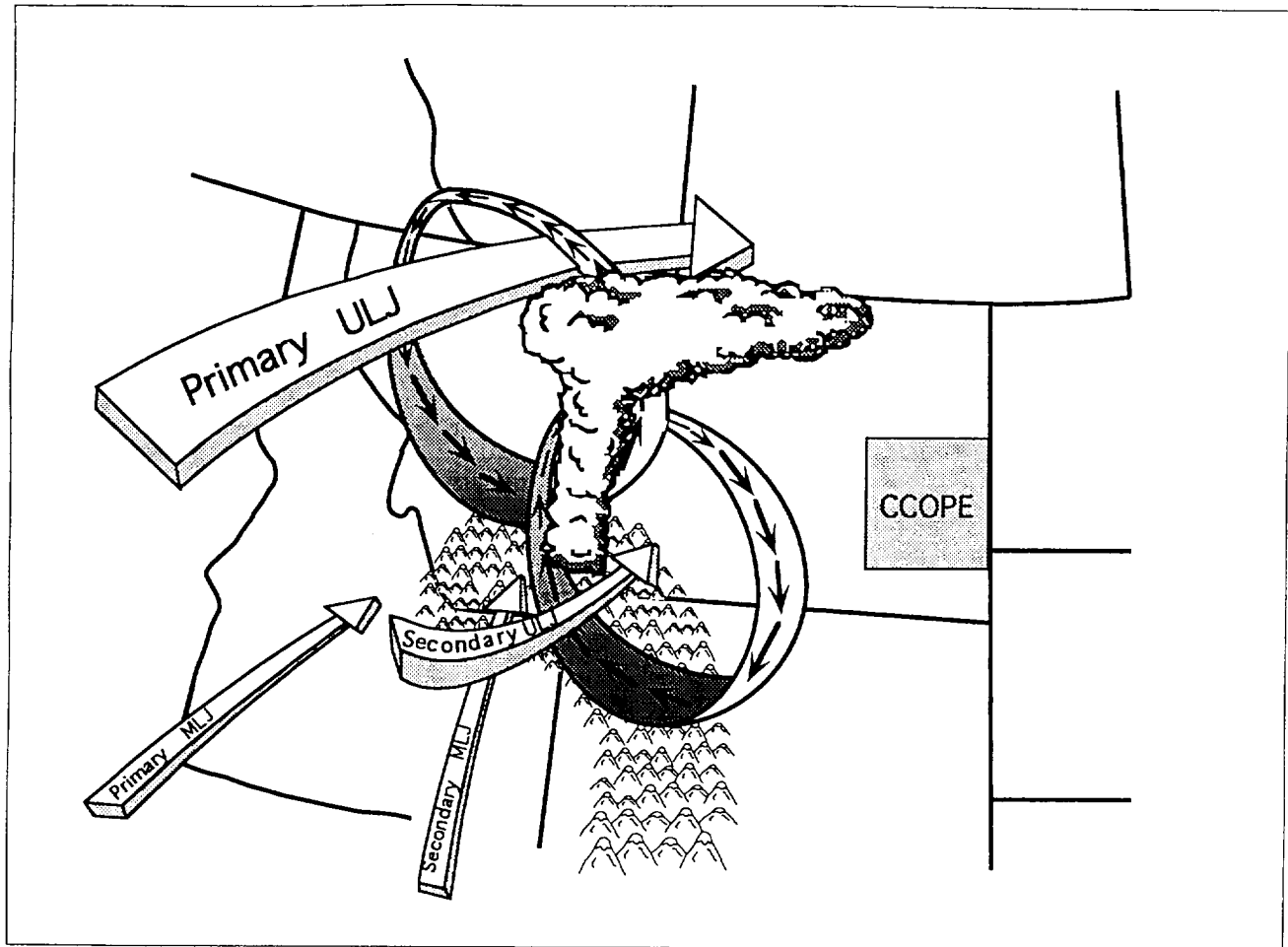


Fig. 26. Schematic depicting many of the components of the four-stage process described in Part I. Included are the primary and secondary upper- and lower- level jets (arrows) relative to the Wave Generation Region after Koch and Dorian (1988). Transverse thermally direct and indirect circulations about the unbalanced and balanced mid-upper tropospheric mesoscale wind maxima (jetlets) are also shown.

Stage II results from the adjustment of the mass field to the new wind field as differential vertical motions accompanying the stage I geostrophic adjustment process enhance the mesoscale cross-stream frontal zone. The differential adiabatic temperature changes produce hydrostatic height perturbations which shift the mass field accompanying the newly formed mesoscale jetlet further southeastwards. Thus, an eastward-shifted mass perturbation forms within the pre-existing jet stream, resulting in a dual jet streak structure (a “secondary jet”).

Stage III occurs when the newly-formed balanced momentum exit region, which was forced by the first (stage I) geostrophic adjustment process, encounters the new mass perturbation (a front) which develops during stage II. A secondary geostrophic adjustment process then occurs, resulting in a new mesoscale jetlet in close proximity to the gravity wave generation region (WGR). Beneath this new jetlet, hydrostatic pressure falls induce an accompanying low-level pressure perturbation.

During stage IV, the low-level wind adjusts isallobarically to the new (stage III) mass field, producing a ~700 mb mesoscale jetlet over the wave generation region (a “secondary low-level jet”). This jetlet is oriented orthogonal to the Absaroka mountain range. As it propagates over this orography, differential thermal forcing due to a combination of cold air drainage to the lee of the mountains and adiabatic expansion and compression associated with the hydrostatic mountain wave result in mass perturbations that eventually contract to a wavelength similar to that of the gravity waves observed during episode I of Koch and Golus (1988). *In effect, it is the nonlinear interaction between: 1) the unbalanced, lower-middle tropospheric, nocturnal, radiationally-driven flow (pressure rises, northerly flow, cold air drainage, etc.) with 2) the balanced return branch of the thermally indirect circulation (the lower-middle tropospheric jetlet), that organizes/excites the inertia-gravity waves during the first wave episode.* This interaction would be expected to occur between 500 and 700 mb over the elevated terrain which is consistent with the findings of Koch *et al.* (1993). These investigators determined the wave source region,

i.e. the critical level, to be within this layer at about 5.5 km MSL. Additionally, it should be noted that the 0009 UTC and 0251 UTC 12 July 1981 Knowlton, Montana (KNO) soundings employed by Koch and Dorian (1988) and Koch *et al.* (1993), respectively, in their theoretical analyses is several hundreds of kilometers and several hours away and later than, respectively, the time of episode I gravity wave generation, which was observed to occur at ~ 1100 UTC 11 July 1981. Hence, the larger along-propagation simulated and observed wind velocity at 1200 UTC 11 July 1981 between 500 and 700 mb may have resulted in a critical level lower than that calculated by Koch and Dorian (1988) and Koch *et al.* (1993), thus adding credence to these conclusions that the layer between the middle and lowert troposphere was key to gravity wave generation.

In Part II we will diagnose the dynamics responsible for wave episode #2 as differential surface sensible heating induces an orographically-forced mountain-plains solenoid, resulting in the formation of additional mesoscale jetlets and internal gravity waves. Finally, in Part III we will diagnose how convective latent heating modifies the numerically simulated terrain-induced episode #1 and #2 internal gravity waves, especially their amplitude and phase velocities, which provides better agreement with those wave characteristics observed in nature.

**Part II. The Role of a Mountain-Plains Solenoidal
Circulation in Jet Streak Geostrophic
Adjustment Processes During CCOPE**

Executive Summary (Part II)

This paper examines a likely mechanism for the organization of the second gravity wave episode observed by Koch *et al.* (1988) over the CCOPE mesonet in eastern Montana. Numerical simulation results as well as lower tropospheric observations indicate that shortly after the mid-upper tropospheric geostrophic adjustment process described in Kaplan *et al.* (1994, Part I), a diurnal circulation was developing upstream over the Rocky Mountains which encompassed the origin location of the second gravity wave episode.

The diurnal circulation represented a classic mountain-plains solenoid, where the early morning solar heating of the elevated plateau over the wave generation region produced a lower-middle tropospheric thermally-direct circulation. The rising branch of this circulation developed in response to the heating of the planetary boundary layer by surface sensible heat flux during the morning. The sinking branch of the circulation extended downstream over the lower plains region as mass processed through the ascending branch sank in the cooler air far from the elevated plateau. The significance of this mountain-plains solenoidal circulation for gravity wave generation lies in the fact that above the inflowing branch of the thermally-direct circulation within the boundary layer is an outflowing jet of air extending downstream. This diabatically-induced outflow jet acts to produce a source of lower-middle tropospheric momentum which impulsively perturbs the mass-momentum balance as well as the vertical Scorer Parameter structure just downstream of the mountains over the wave generation region. Hence, it acts like its predecessor low-level jet, diagnosed from numerical simulation studies in Part I, which was primarily the result of adiabatic geostrophic adjustment processes accompanying the polar jet streak, in that it impulsively perturbs the mesoscale mass field which itself is undergoing differential terrain-induced diabatic heating.

This case study of mountain-plains solenoid development is unique from other published case studies because of this *unseasonably strong background mid-upper*

tropospheric jet streak directly above the mountain-plains region. All other published two and three-dimensional simulation studies of the mountain-plains solenoidal circulation employed background atmospheric states which were largely synoptically calm, i. e., large anticyclonic patterns devoid of strong jet streaks, therefore largely devoid of strong vertical wind shears. The background zonal momentum accompanying the mid-upper tropospheric jet streak in the CCOPE case study acts to increase the magnitude of the outflowing mid-lower tropospheric jet which effectively acts to increase the mass fluxes accompanying the mountain-plains solenoidal circulation. The stronger low-level jet structure simply aids in the impulsive organization of mass perturbations which eventually amplify into internal gravity waves. Thus, a second low-level jet is coupled to a second episode of gravity waves during CCOPE. The upper-level jet implicitly enhances the gravity wave generation process by providing additional momentum to accelerate the nonlinear increase in velocity divergence during the geostrophic adjustment of the wind field to the perturbed mass above the heated elevated plateau.

As was the case in Part I accompanying the first gravity wave episode, this second low-level jet and geostrophic adjustment process establishes the initial slowly propagating wave perturbations which eventually amplify into rapidly-propagating inertia-gravity waves when latent heating perturbs the vertical wave structure.

1. Introduction

Recently, several comprehensive numerical simulation studies have been published which have revealed the detailed characteristics of the mountain-plains solenoidal (MPS) circulation which develops primarily in the western U. S. during the warm season (e. g. Tripoli and Cotton, 1989a,b; Bossert, 1990; Bossert and Cotton, 1994a,b; Wolyn and McGhee, 1992, 1994). Theoretical, synoptic-scale conceptual models of this circulation have been constructed from these studies which describe a multi-stage process which begins with the early morning differential solar heating of the exposed mountain slopes and the adjacent low-lying plains. The decrease in pressure above the heated elevated plateau produces a thermally-direct circulation wherein air evacuated above the heated surface is replaced by upslope flow which transfers cooler surface air from the plains to the mountain slopes. Mass transferred vertically is then removed from the column above the terrain by an increasing outflow jet which extends downstream, producing substantial descent within the cool air. This upper-level branch of the developing thermally-forced ageostrophic circulation is driven by the downstream-oriented pressure gradient force above the elevated plateau.

The excellent numerical simulations which have resulted in the aforementioned theory have all shared a similarity in that the background mid-upper tropospheric jet stream was *very weak or nonexistent*. A question which arises, therefore, is how does the presence of a strong jet stream in which a significant *jet streak* is embedded modify the nature of the simple thermally-direct circulation described above? This question is paramount to the CCOPE case study of gravity wave generation and propagation observed by Koch and Golus (1988), Koch and Dorian (1988), and Koch *et al.* (1988, 1993) over southeastern Montana during the summer of 1981. These researchers document two specific episodes of gravity wave generation to the lee of the northern Rocky Mountain elevated plateau in southwestern Montana and northwestern Wyoming during the warm season when the synoptic scale flow is characterized by the presence of a strong mid-upper tropospheric jet streak.

Kaplan *et al.* (1994, 1995) employed a mesoscale numerical model to simulate the first of the two episodes of gravity waves observed by Koch and Golas (1988). This first episode occurs during the early morning hours prior to the development of significant surface heating, i. e., at and just shortly after 1100 UTC 11 July 1981. Their simulations clearly indicate that geostrophic adjustment processes forced by the nonlinear interaction between the mid-upper tropospheric polar jet streak exit region and high pressure ridge coincident with the elevated plateau resulted in a mid-level mesoscale momentum maximum (jetlet) which subsequently triggered gravity waves as it became perturbed by the leeside baroclinic zone and large amplitude mountain waves. The MPS circulation could only affect this geostrophic adjustment process *indirectly* by modifying the amplitude (i. e., increasing the thickness) of the mesoscale high pressure ridge above the elevated plateau prior to model initialization and the subsequent numerically simulated geostrophic adjustment processes. The second episode of gravity waves observed over CCOPE occurs during the late afternoon, hence, there exists the possibility of *direct* interaction between the MPS and the synoptic scale mid-upper tropospheric jet streak in the generation of internal gravity waves.

The origin of this second episode of gravity waves observed downstream over the CCOPE mesonet in eastern Montana will be investigated in this paper by combining analysis of observed data with mesoscale model results.

2. Terrain Geometry

Fig. 27a depicts the 8km data set employed in constructing the numerical simulations' high resolution terrain (HRT) surface topography (Fig. 27b). The centroid of the mountainous terrain represents the Wave Generation Region (WGR) (Koch and Golas, 1988), wherein the observed gravity waves developed for both wave episodes I and II which is upstream from the CCOPE mesonet. Even the highly smoothed terrain depicted in Fig. 27b indicates the complexity of the northern Rocky Mountains upstream from CCOPE. The dominant terrain feature is the Bitterroot Mountain chain, which extends from western Alberta southeastward into northwestern Wyoming. Additional NW-SE oriented mountain ranges located in Wyoming include the Big Belt Absaroka

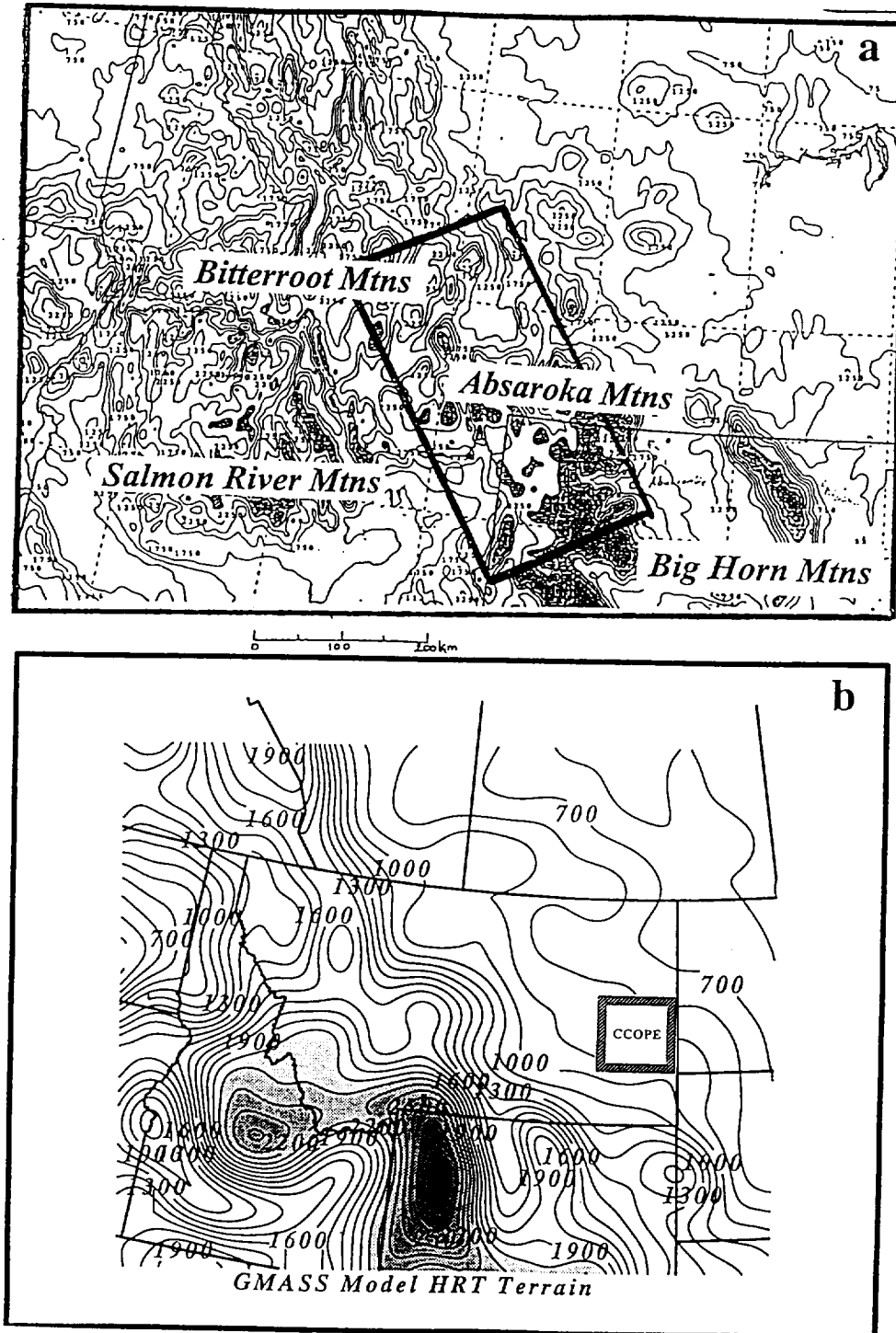


Fig. 27 (a): 8-km resolution terrain employed in creating the model high resolution terrain (HRT) data base. Rectangle represents the Wave Generation Region (WGR) defined by Koch and Gonus (1988). (B) High resolution terrain used in the GMASS model simulation. Elevation above 2 km is shaded.

and Big Horn mountain ranges. There is also a large elevated plateau oriented NE-SW from western Montana into central Idaho, which is comprised primarily of the Pioneer and Salmon River mountain ranges, both of which average over 2km in elevation. Hence, there is a massive region to the west of the CCOPE mesonet which lies 1-2km *above* the ~ 850 m elevation of CCOPE.

3. Observations of a Mountain-Plains Solenoid

Figs. 28-30 depict six hourly surface temperature and three hourly mean sea level pressure changes, as well as mean sea level pressure analyses, respectively, for two key time periods on 11 July 1981, i. e., 0600-1200 UTC and 1500-2100 UTC. It is during the first (second) time period that gravity wave episode I (II) develops over the WGR as described by Koch *et al.* (1988). The extreme difference in surface weather over the elevated plateau and adjacent low-lying plains between these two time periods unambiguously indicates the importance of the MPS. These surface analyses clearly depict a transition from early morning pressure rises and cooling downstream of the mountains to midday warming and pressure falls directly over the mountains. These patterns are clearly associated with and driven by terrain geometry.

During the period from 0600-1200 UTC (0000-0600 MDT) there is a marked pattern of cooling and mean sea level pressure rises surrounding the elevated plateau encompassing the Bitterroot and Absaroka mountain ranges over the WGR. This surface cooling, occurring with primarily clear skies and light winds, likely results from nocturnal radiational cooling as well as the drainage flow of cold air away from the elevated plateau southward and eastward towards central Montana, southcentral Wyoming, and southeastern Idaho. The three-hourly pressure rise pattern depicted in Fig. 29 for the 0900-1200 UTC time period indicates the presence of a S-SW oriented wedge ridge from eastcentral Montana to southeastern Idaho. This low-level meso- β scale pressure rise pattern is oriented nearly orthogonal to the NE-SW oriented meso- α scale pressure trough at 1200 UTC depicted in Fig. 30. At this time, little or no organized convection is

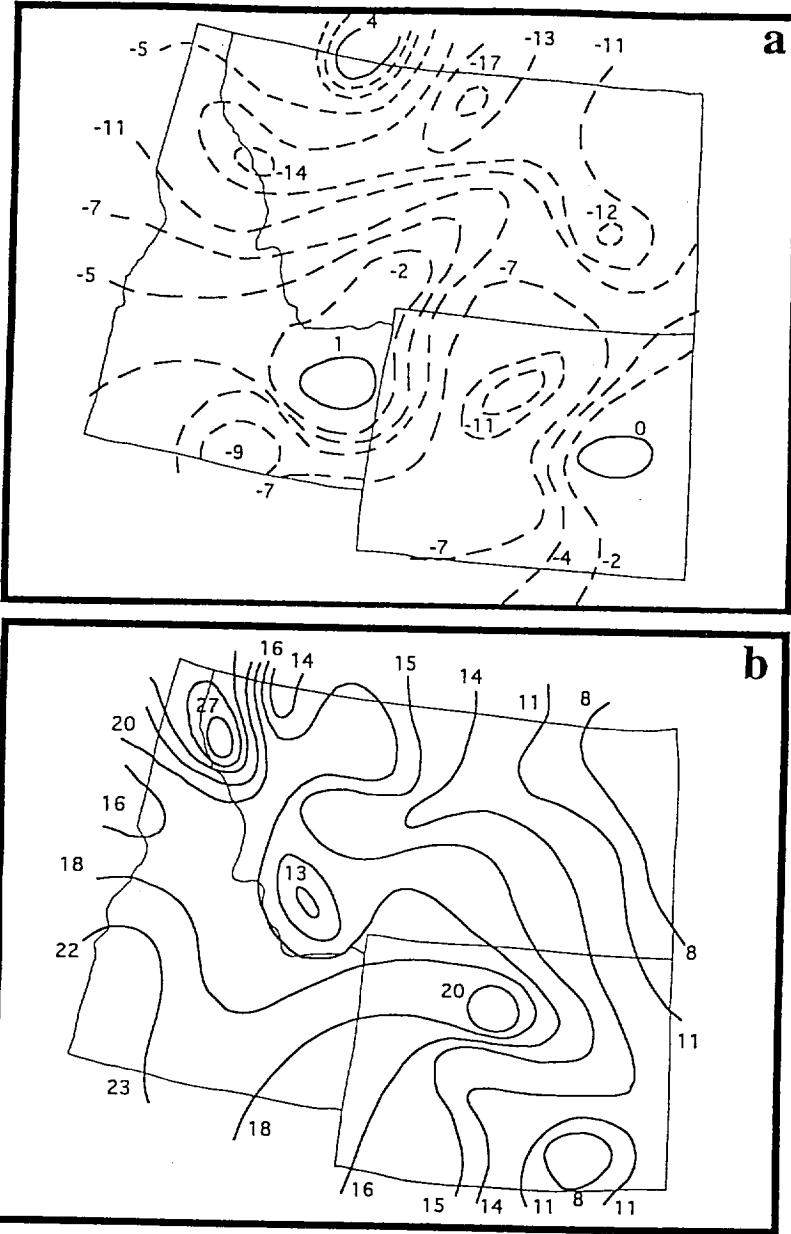


Fig. 28: Observed 6 hour surface temperature change analyses (positive solid) in degrees Celcius valid between (a) 0600 and 1200 UTC and (b) 1500 and 2100 UTC 11 July 1981.

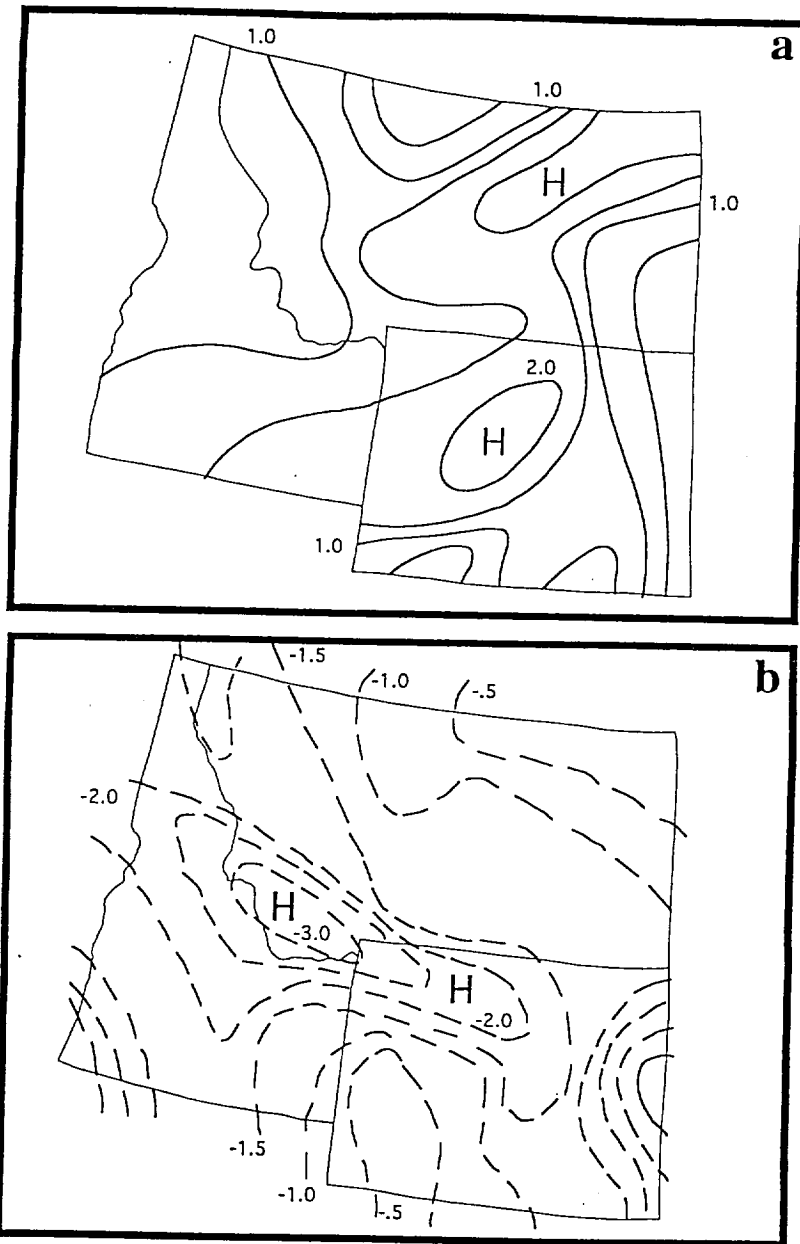


Fig. 29: Observed 3 hour mean sea level pressure change analyses (positive solid) in millibars valid between (a) 0900 and 1200 UTC and (b) 1800 and 2100 UTC 11 July 1981.

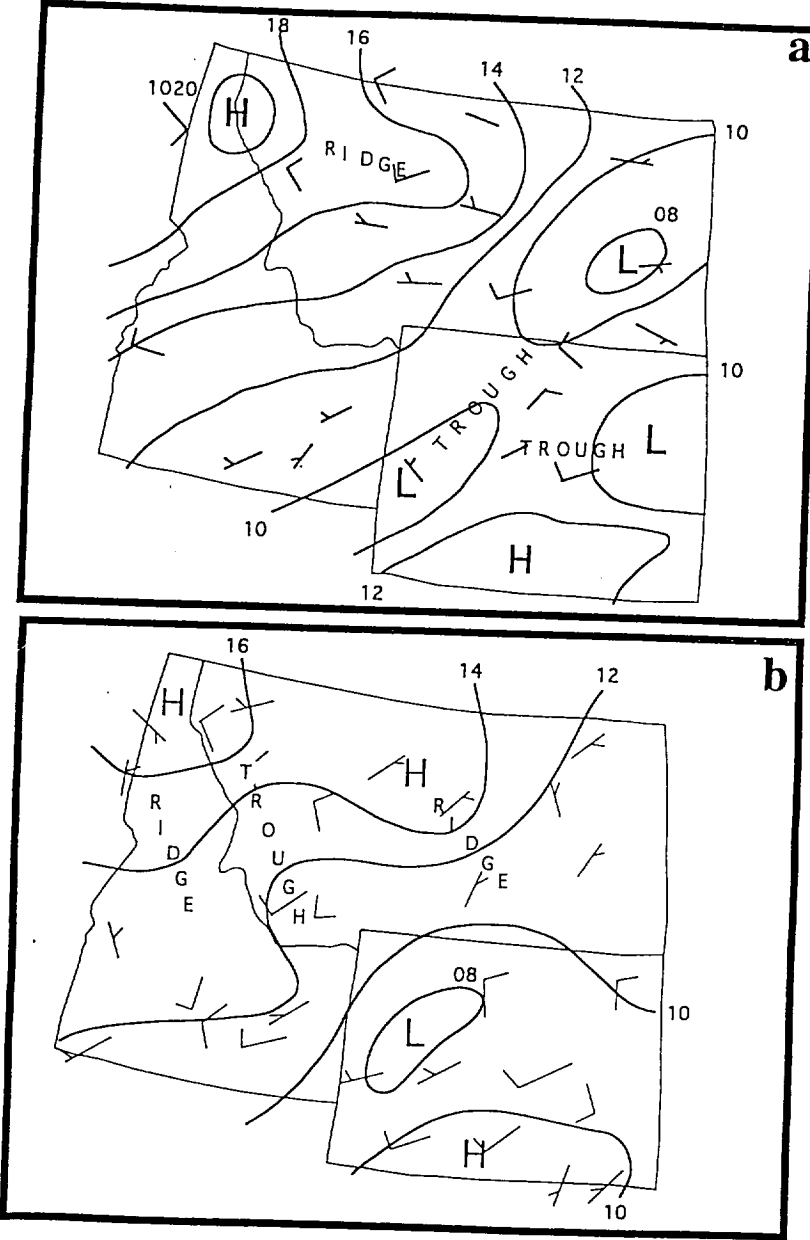


Fig. 30: Observed mean sea level pressure analyses (in millibars) valid at (a) 1200 UTC and (b) 2100 UTC 11 July 1981.

occurring over the WGR with the exception of isolated cloudiness near the origin of the first gravity wave episode as depicted in Koch *et al.* (1988).

During the period from 1500-2100 UTC (0900-1500 MDT) the dynamical pattern reverses completely, as would be expected from a diurnal circulation. Mean sea level pressures fall in a pattern which reflects the dominant NW-SE oriented Bitterroot Mountain chain, with local pressure fall maxima occurring along the spine of both the Bitterroot and Absaroka ranges. The broader pressure fall maxima align closely with the major axes of the mountain ranges (Fig. 29). Within this same region temperatures rise more rapidly than over the lower terrain which is located both upstream and downstream, and take on a similar pattern to the pressure change field (compare Figs. 28 and 28). The heating maxima tend to be slightly skewed towards the eastward facing lee slopes of the mountain ranges. There clearly is a distinct coupling between the heating, pressure falls, and surface terrain geometry (Figs. 27-29). Furthermore, low-level winds (not shown) dramatically change their direction as the afternoon progresses, blowing towards (away from) the terrain during the late afternoon (early morning). There develops a cyclonic pattern to the wind field over the WGR to match the inverted troughing evident in the mean sea level pressure and pressure change patterns along the spine of the Bitterroot and Absaroka mountain ranges between 1800 and 2100 UTC (Figs. 29-30).

These surface changes reflect a 12h diurnal time period wherein low-level early morning (afternoon) thermally-induced anticyclogenesis (cyclogenesis) is taking place. This MPS transports near surface mass away from (towards) the WGR during the early morning (afternoon), thus fueling the mid-lower tropospheric outflow/diffluence inferred from the 0000 UTC 12 July 1981 700 and 500 mb rawinsonde observations over Great Falls, Montana (GTF) and Spokane, Washington (GEG) as well as the low-level inflow at 850 mb over GTF (not shown). Furthermore, radar observations between 1835 and 2135 UTC indicate the *explosive* development of convection just east of the lee slopes of the Bitterroot and Absaroka mountain ranges in response to the upslope flow and intense elevated PBL heating (not shown).

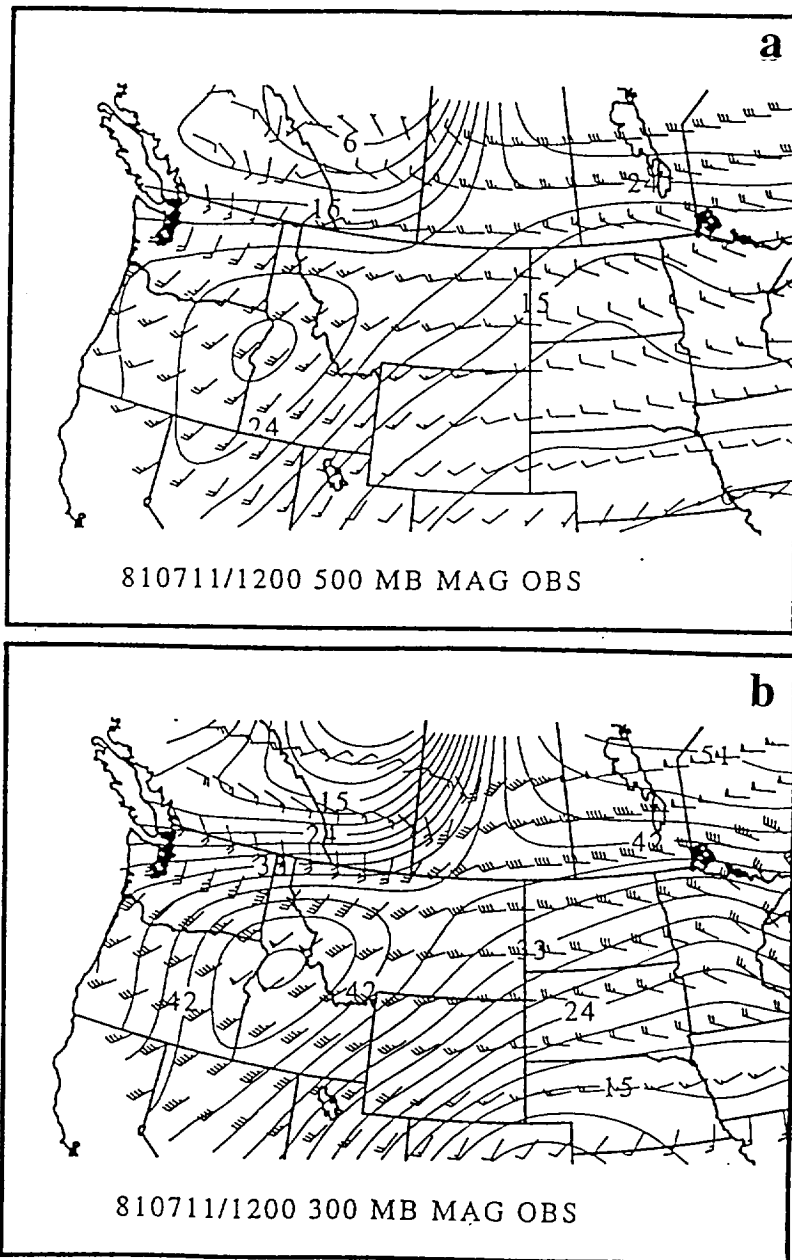


Fig. 31: Observed rawinsonde-derived wind vectors and isotachs ($\text{in } \text{ms}^{-1}$) valid at 1200 UTC 11 July 1981 for (a) 500 mb and (b) 300 mb.

4. Numerical Model and Experiments

The numerical model utilized in this study is the GMASS model (e. g., Manobianco *et al.*, 1994). The coarse and nested grid arrays over which the model was integrated are depicted in Fig. 32. The grids were centered just downstream from the WGR. This places the region between the WGR and CCOPE in the center of the computational domain. A matrix of 223x146x32 grid points was employed for both the coarse (16km) and nested (8km) grid simulations. A high resolution (~8km) terrain (Fig 27b) was employed for the nested grid simulation described in this paper. Although the model atmosphere is moist, both stratiform and convective latent heating was totally suppressed and soil moisture was maintained at a uniformly low value in an effort to *focus specifically on the physics of the jet streak-MPS interaction*. The coarse (nested) mesh simulation was initialized at 0000 (0900) UTC 11 July 1981 and integrated 30 (21) hours through 0600 UTC 12 July 1981. The initial conditions for the coarse mesh simulation were derived from NMC Limited Fine Mesh (LFM) analyses, North American radar data, as well as hourly surface data. Lateral boundary conditions were prescribed from LFM six-hourly forecast data as well as observations at 0000 and 1200 UTC. The initial conditions for the nested grid simulations were derived from cubic spline interpolated coarsh mesh fields. The one-way interactive nested grid lateral boundary conditions were derived from hourly coarse mesh simulated fields.

5. Numerically Simulated MPS Circulation

The simulated MPS circulation and its interaction with the mid-upper tropospheric jet streak will be described in the following paragraphs as a four-stage process.

a) Stage I: Presolenodal Structure

Figs. 33-36 depict cross sections of potential temperature, vertical motion, and ageostrophic circulation vectors from Salmon, Idaho (SMN) to Dickinson, North Dakota (DIK) during the 1100-2000 UTC time period from the high resolution (HRT) nested grid simulation. One can see that at 1100 UTC (0500 MDT) there is a broad area of descending air over the lee

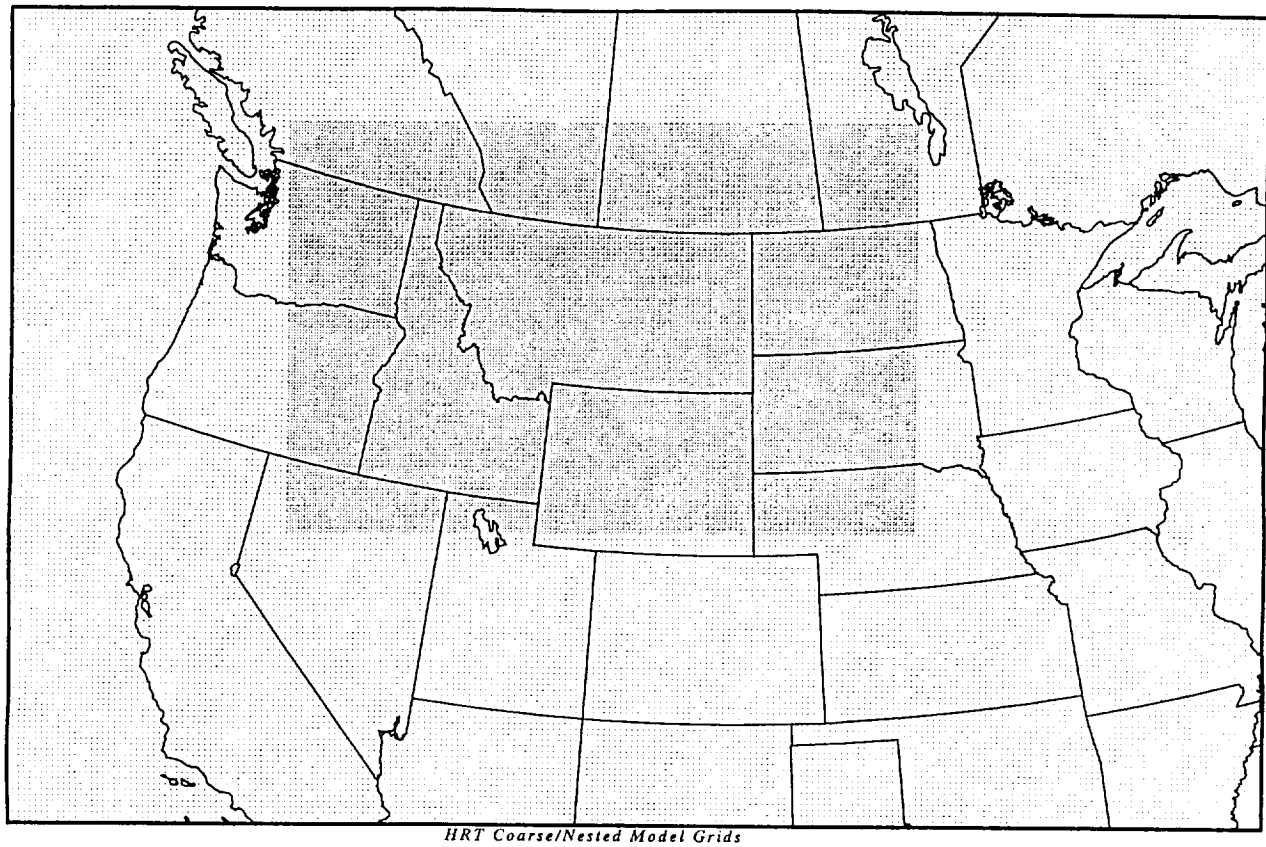


Fig. 32: Coarse and nested-grid array regions employed in the GMASS HRT simulation.

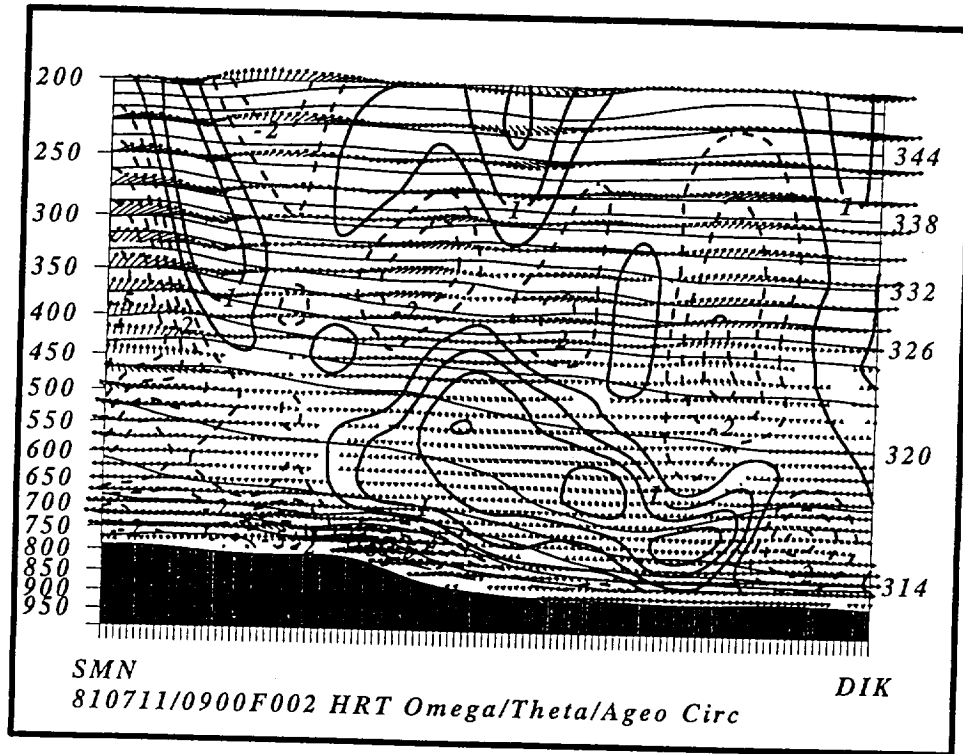


Fig. 33: GMASS HRT simulation vertical cross section from Salmon, Idaho (SMN) to Dickinson, North Dakota (DIK) of potential temperature (K), vertical motion (ascent dashed in $\mu\text{b s}^{-1}$), and ageostrophic circulation vectors valid at 1100 UTC 11 July 1981.

slope of the mountains with shallow flow away from the elevated plateau under the near-surface inversion. The isentropic surfaces over the elevated plateau encompassing northwestern Wyoming, southeastern Idaho, and southwestern Montana show little evidence of any significant perturbation, with the exception of slight downfolding over the sloping terrain. The shallow surface flow is largely downslope towards the southeast on the lee slope of the terrain. The subsidence extends up above 450 mb over most of the region depicted in the cross section. This simulated pattern is *dynamically* consistent with the observed 0600-1200 UTC surface cooling, downslope surface flow, and wedge ridge located to the east of the elevated plateau (Figs. 28-30).

b) Stage II: Development of the MPS

Between 1400 and 1700 UTC (0800 and 1100 MDT) the simulated MPS circulation becomes very evident in Figs. 34 and 35. The 320-316 K isentropic surfaces located between 550 and 700 mb begin to fold down over the elevated plateau, while very little change occurs downstream over the adjacent plains. This downfolding induces a horizontal temperature gradient on pressure surfaces within this layer; hence, solenoids are produced. The developing solenoids induce a circulation which is accompanied by a major areal increase in the very shallow (~50 mb deep) upslope flow/low-level jet directly underneath the newly perturbed isentropic surfaces. This transforms the vertical motion pattern from one of weak descent to weak ascent, whose maximum occurs at ~650 mb near the top of the elevated plateau by 1700 UTC. The ascending flow which is closely coupled to the intensifying upslope jet then propagates slowly upslope under the downfolded isentropic surfaces, remaining just upstream of the newly formed outflow jet. These upslope and outflow jets are simply the result of: (1) the increasing upslope-directed pressure gradient force accompanying the developing near-surface inverted trough, and (2) the downslope-directed pressure gradient force caused by the mesoscale thickness ridge directly above the inverted trough at 700 mb, both of which are depicted in Fig. 37.

The dramatic change from mean sea level pressure rises to mean sea level pressure falls which is observed during the period after 1500 UTC verifies the development of simulated near-

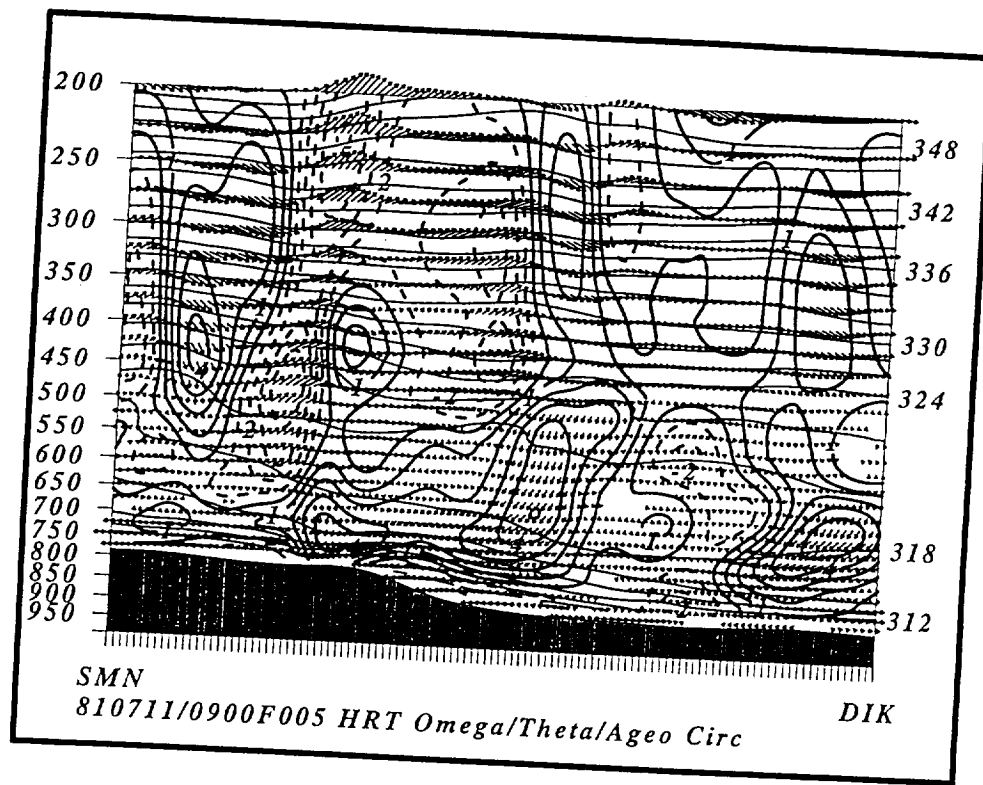


Fig. 34: Same as Fig. 33 but valid at 1400 UTC 11 July 1981.

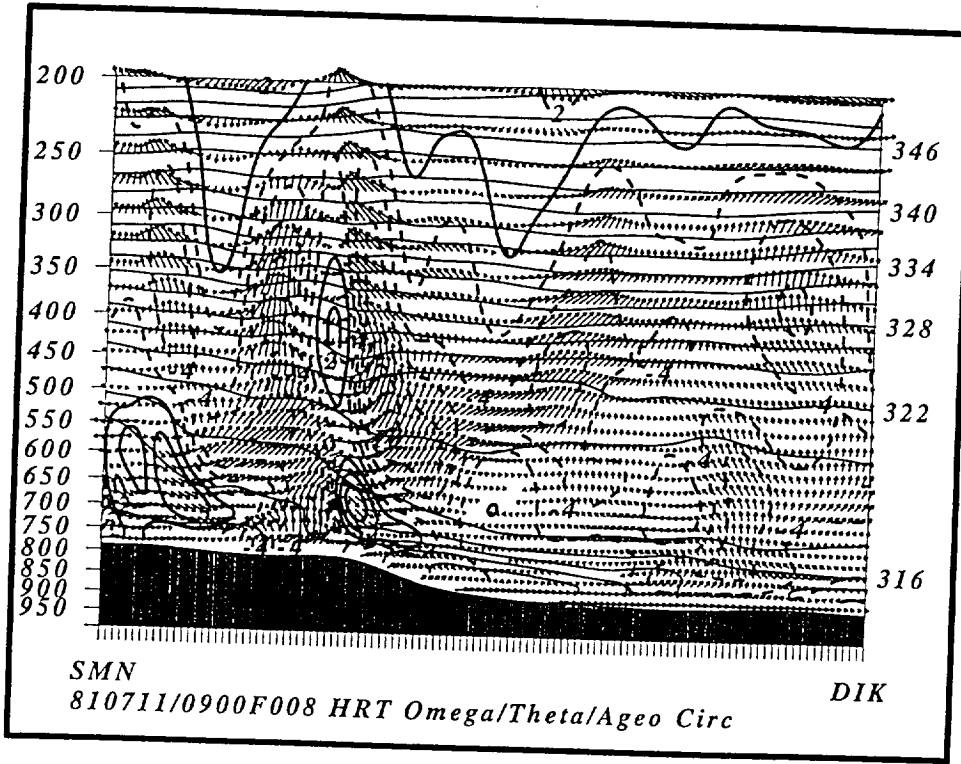


Fig. 35: Same as Fig. 33 but valid at 1700 UTC 11 July 1981.

surface height falls accompanying the low-level PBL heating and upslope flow. It is at this time in the observational data that the trough forms over the elevated plateau accompanying the transition from surface cooling to surface warming (note Figs 28-30).

c) Stage III: Mature MPS Circulation/Jet Streak Interaction

This thermally-forced ageostrophic circulation reaches its maximum intensity between 1800 and 2000 UTC (1200 and 1400 MDT) (Fig. 36). During this time period the PBL between the 320 and 316 K isentropic surfaces over the elevated plateau deepens to in excess of 500 mb. The outflow jet maximum descends to \sim 725 mb where total wind velocities exceed 15 ms^{-1} . Increasing horizontal pressure gradients associated with height rises at 700 mb accelerate the flow towards the E-NE while at 800 mb a mesotrough deepens from southwestern Montana and northwestern Wyoming northwestwards up the Bitterroot mountain range, thus accelerating the near-surface flow towards the W-NW.

A very strong, but relatively shallow couplet of ascending and descending motion develop in conjunction with the outflow jet as well as with the upslope flow. However, shortly after 1800 UTC, directly above the the solenoid accompanying the elevated plateau heating, the mid-upper tropospheric jet becomes *perturbed* resulting in a secondary wind maximum forming nearly directly above the low-level jet (Figs. 36 and 38). *As the deep height rises couple to the upper level jet, the structure of the upper-level jet changes drastically.*

The observations indicate that the mean sea level pressure falls reach their peak magnitude during the 1800-2100 UTC time period which is consistent with the simulation results. The strongest wind component at the surface (which is directed towards the west) develops at this time, consistent with the lowest mean sea level pressures and highest surface temperatures over the elevated plateau. Also, observed convection develops at this time which is consistent with the intense simulated upslope vertical motions along the eastward-facing part of the elevated plateau which exceed $50 \mu\text{b s}^{-1}$ (Fig. 36).

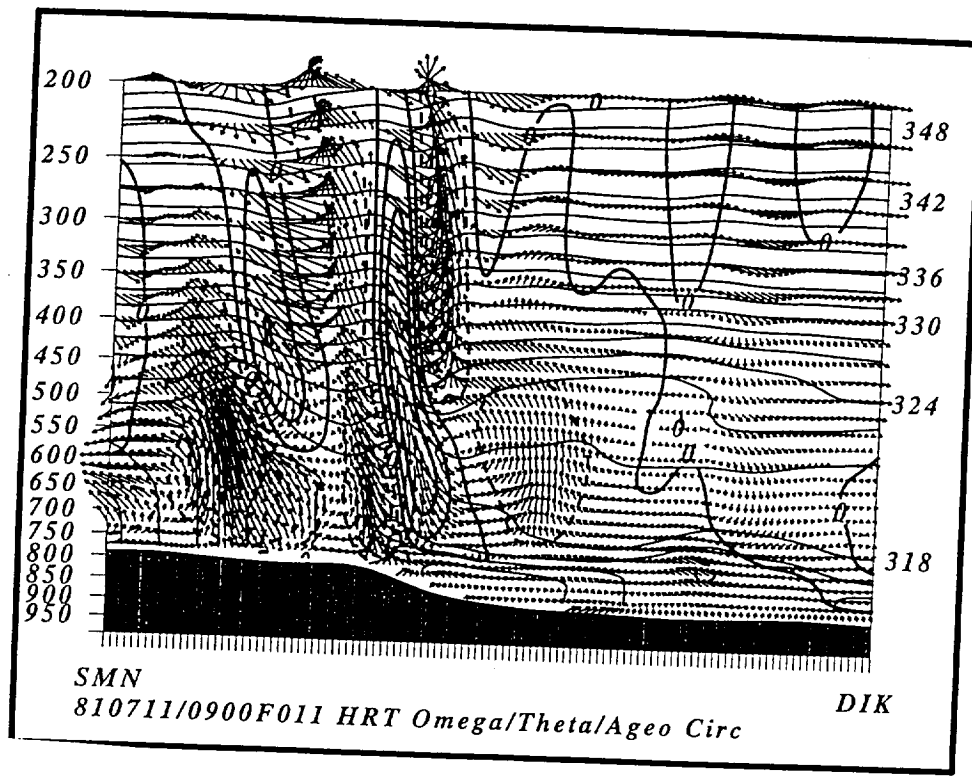


Fig. 36: Same as Fig. 33 but valid at 2000 UTC 11 July 1981.

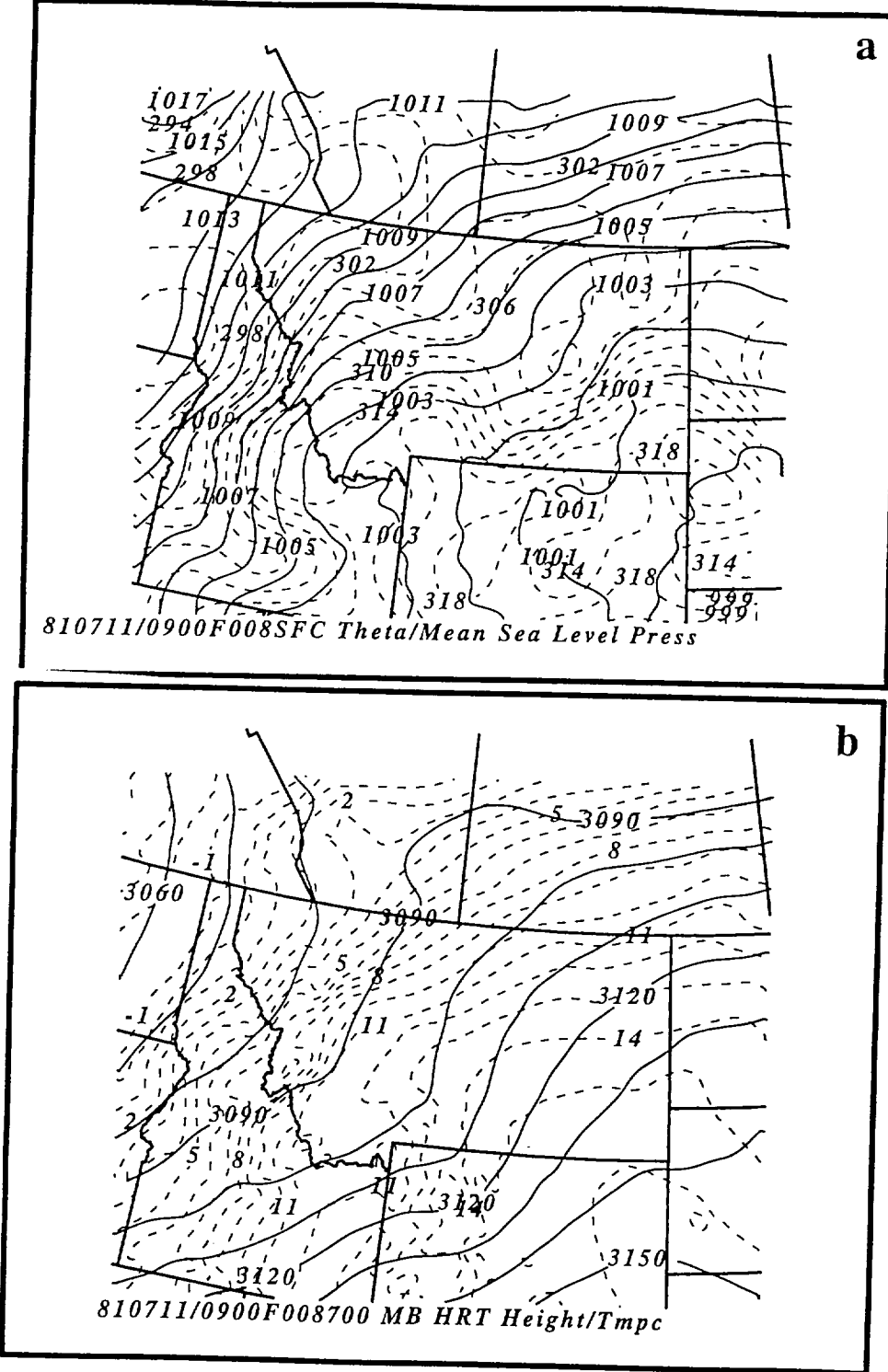


Fig. 37 (a): GMASS HRT simulation mean sea level pressure (solid in mb) and surface potential temperature (dashed in K) valid at 1700 UTC 11 July 1981. (B) GMASS HRT simulation 700 mb height (solid in m) and potential temperature (dashed in K) valid at 1700 UTC 11 July 1981.

e) Stage IV: Geostrophic Adjustment and the Generation of Internal Gravity Waves

During the period after 2000 UTC, the outflow jet and new upper-tropospheric jet maximum propagate downstream away from the original mountain-plains solenoidal circulation. During the period of coupling, the original thermally direct circulation transforms into a thermally indirect circulation followed by the generation of distinct inertia-gravity waves (IGWs) (note Fig. 38). This wave generation process involves the building of the thickness ridge over the elevated plateau at the same time that the low-level outflow jet maximizes in intensity. The wind over a major portion of the vertical column adjusts to the thickness ridge producing the continued acceleration of the low-level jet. At the same time that the outflow jet maximizes, geostrophic adjustment occurs within the mid-upper troposphere due to the hydrostatic height rises above the elevated plateau. This induces a focussing of the low-level pressure falls accompanying a thermally indirect circulation and the development of inertia-gravity waves.

The wavelength of these ‘dry’ gravity waves ($\sim 180\text{km}$) is similar to the primary waves observed by Koch *et al.* (1988); however, their phase speeds are much slower ($\sim 10 \text{ ms}^{-1}$), being approximately half of that observed. As can be seen in Figs. 36 and 38, the ascending and descending motions accompanying the IGWs are in quadrature, however, they are misphased when compared to the standard relationship between a gravity wave crest/trough and the sign of the vertical motions expected for a vertically erect mode as described in Koch *et al.* (1993).

As described by Kaplan *et al.* (1995) concerning the physical mechanisms responsible for the formation of gravity wave episode I, *the simulated gravity waves*, which have a realistic wavelength and genesis location, *are the result of impulsive forcing of a mid-level jet in proximity to a well-developed wave duct and horizontal mass perturbation*. However, these simulated waves are incapable of propagating with the observed phase speed, which is very likely due to the absence of latent heating in the numerical simulations.

It should be noted that Koch *et al.* (1988) observed the development of gravity wave episode II over the WGR during the period from 1800 to 2300 UTC, which corresponds roughly with to the period of simulated development, which is from 1900 through 2100 UTC.

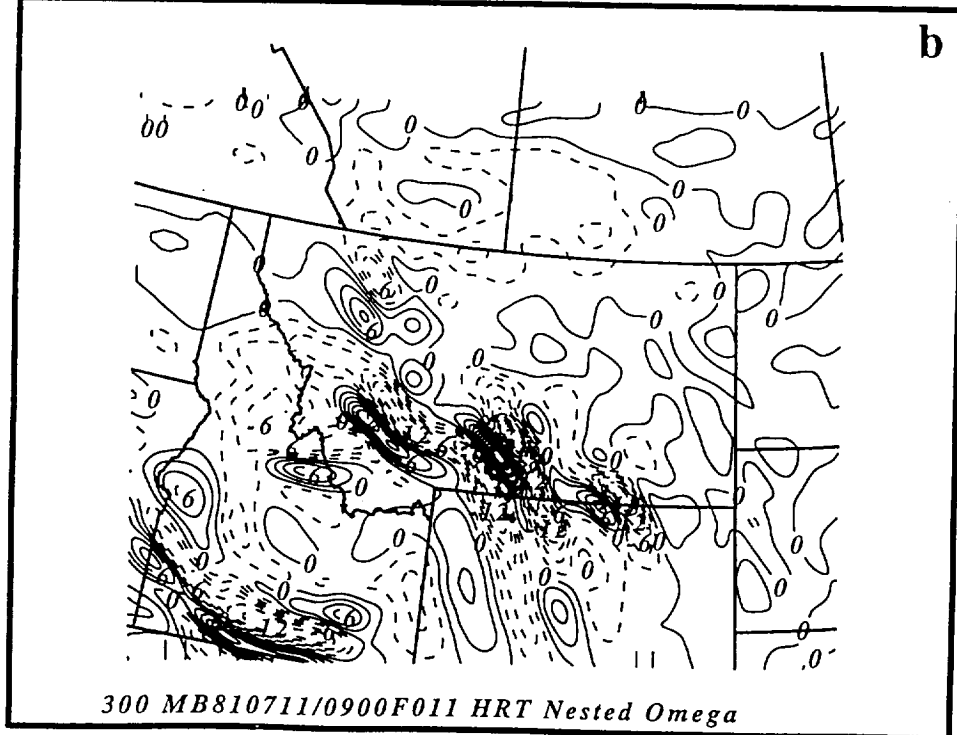
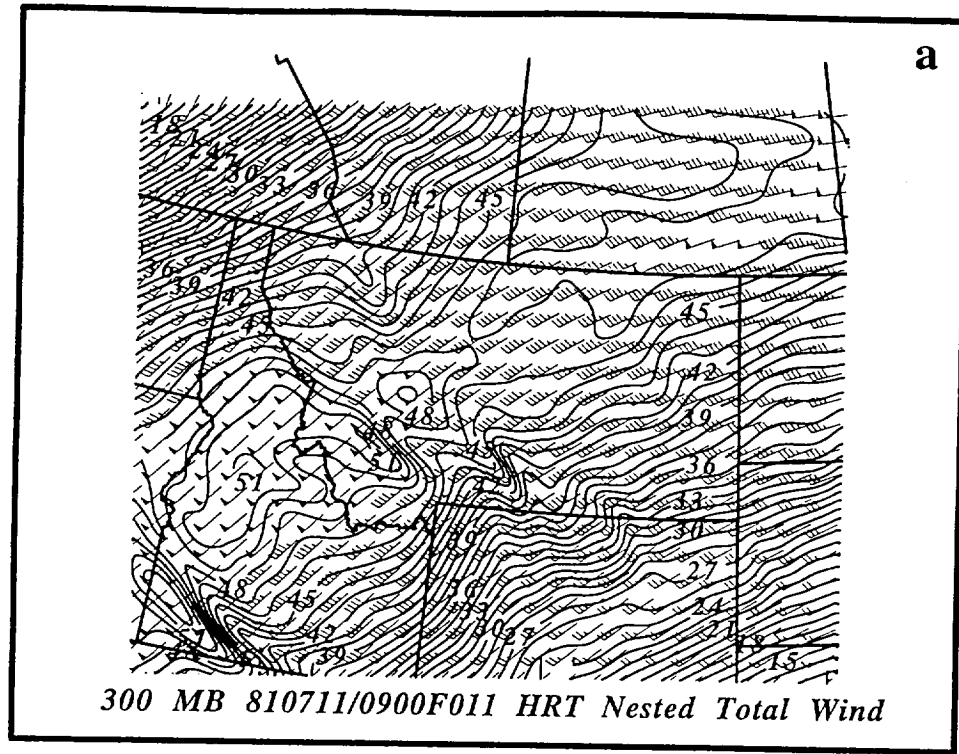


Fig. 38 (a): GMASS HRT simulation 300 mb wind vectors and isotachs (ms^{-1}) valid at 2000 UTC 11 July 1981. (B) GMASS HRT simulation 300 mb vertical motion (ascent dashed in $\mu\text{b s}^{-1}$) valid at 2000 UTC 11 July 1981.

6. Summary and Conclusions

This paper has examined the numerical simulation results of a mountain-plains solenoidal circulation and its role in organizing the second episode of gravity waves observed during the CCOPE case study of 11-12 July 1981. The simulated MPS circulation fundamentally conforms to previous numerical simulation studies by other authors as well as to observations of a diurnal orographically forced thermally direct circulation. During the early morning, prior to sunrise, a shallow near-surface jet is associated with the weak descent above and cool air drainage away from the elevated terrain producing pressure rises over the lower terrain. Once surface heating occurs, the formerly quasi-horizontal isentropic surfaces above the elevated terrain fold down as the planetary boundary layer warms more rapidly in this region as compared to the surrounding lowlands. This modifies the mass field producing an upslope near-surface jet, upward vertical motions above the elevated plateau, and an increasing outflow jet which is directed downstream away from the plateau in response to the growing thickness ridge aloft above the elevated plateau. This circulation intensifies and builds vertically during the midafternoon period, resulting in an inverted surface trough and cyclonic circulation over the elevated plateau.

This simple thermally direct circulation breaks down as it begins to directly perturb the mass/momentum balance of the synoptic scale polar jet streak exit region located between 500 and 200 mb. As the hydrostatic height rises above the elevated plateau eventually reach the jet streak level, a geostrophic adjustment process occurs. The *unbalanced* cross stream ageostrophic flow accompanying the deepening mesoridge aloft triggers a *balanced* inertial-advection adjustment directed to the right of the upper-level jet stream flow. Mid-upper tropospheric mass flux divergence (convergence) on the cyclonic (anticyclonic) side of the jet streak exit region develops in response to the mass/momentum adjustment process. The vertical motion patterns associated with this adjustment process transform the original thermally-direct MPS circulation into a thermally-indirect circulation. This new ageostrophic circulation results in enhanced pressure falls downstream within the preexisting low pressure trough/high pressure ridge complex and low-level

outflow jet accompanying the mature MPS circulation. This accelerates the MPS outflow jet as it impulsively interacts with the low-level MPS trough/ridge in the mass field. Eventually, the alongstream divergence/convergence patterns intensify in response to the impulsive forcing of the low-level jet resulting in the generation of the second episode of gravity waves over the WGR. This complex scale-interactive process is depicted schematically by the conceptual model shown in Fig. 39.

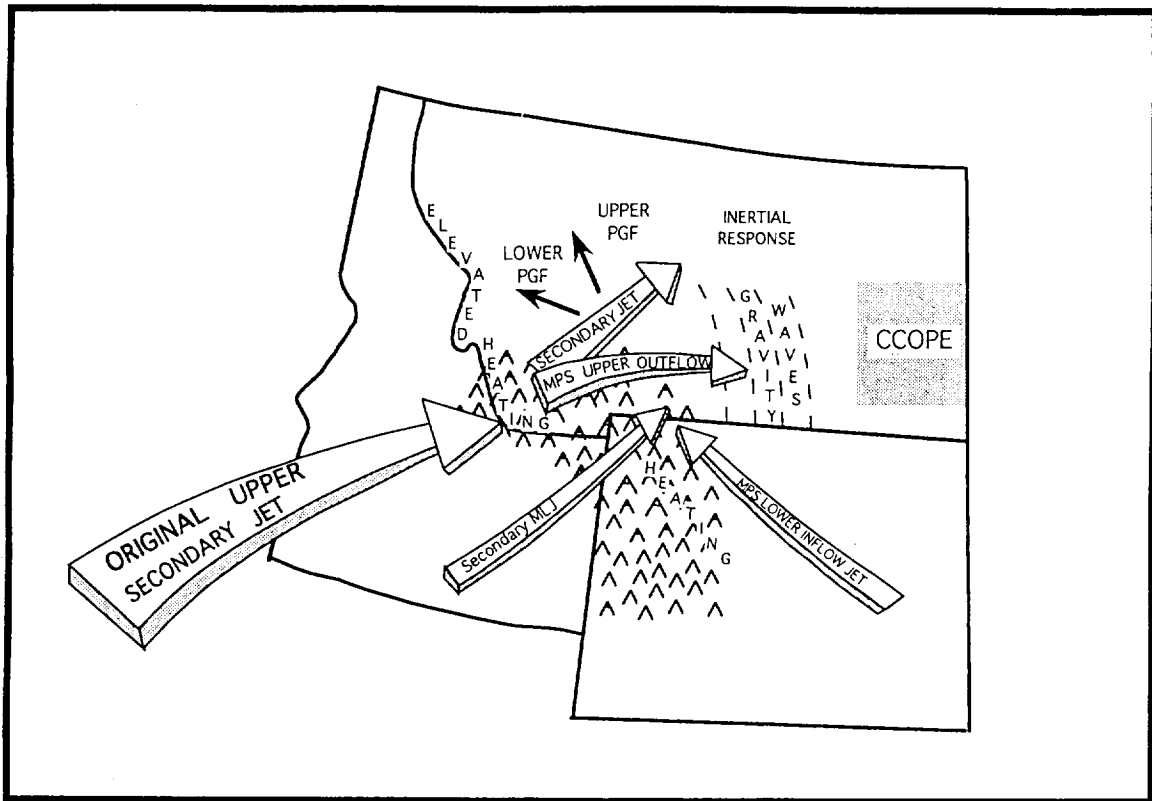


Fig. 39: Conceptual model depicting key synoptic and mesoscale dynamical features during the period of MPS/jet streak interaction of 11 July 1981.

Part III. The Role of Latent Heating in Modifying the Terrain-Induced Jet Streak Mass/Momentum Perturbations

While the aforementioned simulation studies were capable of determining the effect of terrain-induced mass perturbations on the deep jet streak geostrophic adjustment processes, many key phenomena observed by Koch *et al.* (1988) were absent in these ‘dry’ simulations. These phenomena include seven rapidly propagating *observed* inertia-gravity waves and a massive downstream mesoscale convective system (MCS). The gravity waves simulated in the aforementioned GMASS simulations were in poor agreement with those observed, especially when compared to the phase velocity and vertical structure of the waves which occurred in nature. In an effort to diagnose how latent heating modifies the structure of the terrain-induced circulations, two additional computationally demanding numerical simulations were performed with the GMASS mesoscale model. First, the nested-grid (8 km horizontal resolution) experiment was repeated with grid-scale latent heating and the Molinari (1982) cumulus parameterization scheme activated. The second set of experiments employing a complete, explicit microphysical formulation in a more advanced version of the MASS model is presently being attempted on the North Carolina Supercomputing Center’s Cray Y-MP/E. The results from this latter simulation will be described in detail in a forthcoming journal article. However, results from the initial ‘moist’ simulation (i. e., stratiform and convective latent heating *not* suppressed as was done in the earlier ‘dry’ simulations) are sufficiently realistic to indicate two things: (1) it is possible to replicate the observed gravity wave phase velocities, vertical structure, and the MCS development with a significant degree of realism, and (2) the observed gravity waves and MCS likely develop as the result of *diabatically-enhanced terrain-induced geostrophic adjustment processes* which have been discussed in detail in Parts I and II of this report.

A simple statistical comparison between the observed and simulated internal waves indicates that the waves are accurately simulated even with relatively simple moist physics. Seven waves were simulated in the nested-grid simulation and seven waves were observed

by Koch *et al.* (1988) during the period between 0900 UTC 11 July 1981 and 0600 UTC 12 July 1981. All seven numerically simulated gravity waves developed, as observed, within the Wave Generation Region (WGR) near the borders of Wyoming, Idaho, and Montana. The GMASS model replicated nature accurately by producing two distinct episodes of internal gravity waves separated by several hours. The average time of simulated wave genesis was approximately 1330 UTC and 2140 UTC for episodes I and II, respectively, as opposed to approximately 1345 UTC and 2040 UTC for the observed waves. The average wavelength for both episodes of simulated internal gravity waves was approximately 174 km, while the average wavelength for the observed waves was approximately 159 km, yielding an error of slightly less than 10%. The observed mean phase velocity was 16.6 ms^{-1} for all of the observed waves and 18.6 ms^{-1} for all of the simulated waves. Similar comparisons indicate that direction of wave propagation for the simulated (observed) waves was approximately from 253 (258) degrees, while the mean period and frequency for all of the simulated (observed) waves were approximately 161 minutes and $0.00667 \text{ minute}^{-1}$ (153 minutes and $0.00657 \text{ minute}^{-1}$), respectively.

It is interesting to note that while there are some differences in the average characteristics between the simulated and observed waves based on surface characteristics of the observed waves, there is remarkable similarity between the average simulated characteristics and that derived from Doppler radar data reported by Koch *et al.* (1993) for waves observed over the CCOPE mesonet in eastern Montana. For example, Koch *et al.* described a vertically erect mode which was observed whose maximum amplitude was between 500 and 700 mb, had a horizontal wavelength of ~ 168 km, period of 148 minutes, and a phase velocity of propagation equal to 18.6 ms^{-1} . This should be compared to the numerically simulated vertically erect modes which have a horizontal wavelength of 174 km, period of 161 minutes, and a phase velocity of 18.6 ms^{-1} . The simulated waves also had maximum amplitude in the 500-700 mb layer near the critical level. Additionally, the GMASS numerical simulations clearly indicate that gravity wave genesis is closely tied to

the aforementioned low-level mesoscale wind maxima (jetlets) which develop in the planetary boundary layer just before the observed waves develop. This emphasizes the importance of the terrain-induced geostrophic adjustment processes described in Parts I and II of this report.

Furthermore, the model is capable, even with relatively simple moist physical processes, of simulating the development of a massive MCS over the Dakotas close to the time it develops in nature, i. e., just after 0000 UTC 12 July 1981. The moist simulation indicates that it is the juxtapositioning of several low-level mesoscale momentum maxima (jetlets), which form as a result of upstream terrain-induced geostrophic adjustment processes, which produce the lifting and destabilization necessary for the organization of the massive mesoscale convective system. Also, the model indicates that the mass adjustments forced by the MCS act to accelerate the upper tropospheric momentum field to the northwest near the North Dakota/Montana/Canadian border region producing a separate *upper-tropospheric* mesoscale momentum maximum (jetlet) which is observed in the rawinsonde data. However, the simple moist physics parameterization degrades the quality of the numerical simulation during its latter stages because too much latent heat is released too low in the troposphere which results in an overdeepening of the wave-CISK-induced mesolow over the Dakotas as well as an overprediction of the circulation strength of the mesolow over eastern Montana. These late period errors in the simulation will result in the misrepresentation of the characteristics of the latter two internal gravity waves during the second wave episode. That is to say, the phase velocities tend to be significantly reduced as these waves interact with the strong mesolow circulation simulated in eastern Montana. However, the simulated trend indicating that the latter period gravity waves propagate towards the east-southeast as opposed to the earlier 'dry' simulations which predict propagation to the east-northeast for wave episode I is observed to occur in nature. It is anticipated that the second moist simulation with improved microphysics will more

accurately simulate the MCS evolution, thus resulting in a more accurate simulation of episode II CCOPE gravity waves.

Clearly evident from the first simple moist simulation using the GMASS mesoscale model is the fact that latent heating acts to amplify the geostrophic adjustment processes accompanying the jet streak which were originally initiated by PBL surface heating which occurs above the elevated terrain in western Wyoming, Idaho, and Montana. This implicitly transmits the effects of orographic forcing several hundreds of kilometers downstream!

**Part IV. Linear Geostrophic Adjustment and
Jetogenesis Forced by Impulsive and
Propagating Zonal Momentum Sources
in a Stratified Atmosphere**

Executive Summary (Part IV)

We investigate the three-dimensional linear response of a zonally uniform barotropic flow in a vertically unbounded, continuously stratified, Boussinesq atmosphere which is perturbed from geostrophic equilibrium. The methods of perturbation potential vorticity (PV) theory are used to address the initial-value and forced geostrophic adjustment problems imposed by: (i) the introduction of a localized, unbalanced, ageostrophic zonal wind anomaly into the basic state flow, and (ii) a traveling zonal momentum forcing which represents entrance (exit) region acceleration (deceleration) experienced by the basic flow as it passes through an isolated jet streak maximum in the interior of the fluid, respectively.

The transient response shows evidence of dispersive inertia-gravity waves (IGWs) which excite a broader spectrum of modes in the zonal direction as compared to the meridional direction. The dispersive IGWs in all fields are essentially removed in the first 12 h of the response associated with the initial-value problem. The existence of a uniform zonal flow Doppler shifts the phase velocities of the transient IGWs responsible for removing the ageostrophic divergence of the initial state during the adjustment to geostrophic equilibrium. The steady-state response predicted by linear theory which conserves the PV of the initial state is a localized, geostrophic zonal jet with meridionally confluent (diffluent) flow in its entrance (exit) region, which is supported by a couplet of perturbation low (high) pressure north (south) of the zonal jet core. The steady-state linear response characterizes a localized *thermal wind balance* among the baroclinic perturbations defining the primary circulations associated with the geostrophic jet. In the absence of momentum forcing, the secondary circulations predicted by linear theory are trivially zero. In a non-zero basic state flow, the steady-state PV couplet is advected downstream by the uniform zonal flow.

Taking the basic flow to be locally representative of the planetary jet stream in which midlatitude jet streaks are observed to exist, we investigate the response to a

momentum forcing propagating at the speed $c < U$ through the basic state current. The magnitude of the traveling zonal wind anomaly represented by this forcing is taken to be greater than the magnitude of the basic state flow, $|u_{j0}| > |U|$, yielding propagation characteristics very representative of real midlatitude jet streaks.

For a Galilean observer, the response predicted by linear theory at early times is primarily dominated by the prescribed structure of the imposed momentum forcing. Since the length scale of the forced zonal winds are much less than the Rossby deformation radius defined by the total depth of the zonal wind anomaly represented by the forcing ($L_R \sim N^2 d_{jet}/f$), the transient response associated with this particular forced adjustment problem shows the adjustment of the mass fields to the momentum (wind) fields. At later times, the linear response is dominated by the circulations associated with the PV anomaly generated by the meridional gradient of the 'vorticity' of the prescribed forcing, $-\partial F_\zeta / \partial y$.

An isolated zonal jet with meridionally confluent (diffluent) flow in the jet entrance (exit) region eventually becomes established in the vicinity of the forcing center. A dipole couplet of perturbation pressure supports this localized zonal jet. This pressure couplet is related hydrostatically to the perturbation potential temperature field. The forced geostrophic circulations are similar to that predicted for the initial-value problem. The ageostrophic circulations transfer mass from the cyclonic to the anticyclonic (anticyclonic to the cyclonic) side of the jet core in the entrance (exit) region, yielding a well-defined 'four-cell' pattern of vertical motion in the quadrants flanking the jet core. These transverse ageostrophic circulations are similar to those produced in a rotating homogeneous atmosphere of finite depth, but are simply *reversed* from those commonly inferred to be associated with midlatitude jet streaks in the real atmosphere. We define the forced linear response as baroclinic *jetogenesis*.

1. Introduction

Interest in the mechanism of geostrophic adjustment as a probable energy source mechanism of observed meso- α/β scale gravity waves identified by sophisticated observational networks in a variety of synoptic scale environments associated with severe weather events has been renewed recently (Uccellini and Koch, 1987). Other physical mechanisms commonly identified as being responsible for gravity wave generation at these scales include forcing by orography, mesoscale convective systems, and shear instability. One common feature of typical midlatitude synoptic scale environments in which these types of mesoscale gravity waves are observed is a propagating planetary scale wave which may itself be embedded with zonal wind anomalies or *jet streaks*.

Most geostrophic adjustment studies have focused on the adjustment to balanced equilibrium from an initially unbalanced small-amplitude ageostrophic state introduced into a motionless basic state (Blumen, 1972; Gill, 1982, and references therein). In order to distinguish the internal gravity waves due solely to geostrophic adjustment processes from the spectrum of wave modes forced by alternative wave source mechanisms which may exist simultaneously in more realistic atmospheric environments, the first step is to determine the response of a *non-resting* rotating basic state to initial imbalances in the mass and momentum fields. Surprisingly, a thorough review of classical geostrophic adjustment literature shows that little information concerning this problem exists, and even that recently published geostrophic adjustment studies continue to ignore the advective effects of non-resting basic states for atmospheric environments which clearly are not quiescent (Zhu and Holton, 1987; Barwell and Bromley, 1988; Fritts and Luo, 1992; Luo and Fritts, 1993).

However, it appears that some work towards alleviating this deficiency has been done. Schubert *et al.* (1980) uses the two-layer model studied by Paegle (1978) to investigate the response of a basic state flow in gradient wind balance to axisymmetric mass and momentum perturbations with application to the dynamics of tropical cyclones. Duffy (1990) has investigated the effects of vertical wind shear in an idealized two-layer rigid lid

model (Williams, 1965), while Vallis (1992) recently has shown that a state of non-divergent geostrophic equilibrium constitutes the minimum energy state allowable under the constraint of potential vorticity conservation for the shallow water equations linearized about a non-resting basic state.

Under the situation in which an upper-level midlatitude jet streak exists in the developing synoptic scale baroclinic wave and is propagating downstream toward a quasi-stationary ridge in the geopotential height field, Kaplan and Paine (1977) recognized, based on dynamical analysis of the nonlinear balance equation, that the flow in such regions is highly ageostrophic. The divergence tendency of the flow under these conditions cannot be neglected, and is the physical mechanism which is responsible for the excitation of inertia-gravity waves as the atmosphere attempts to re-establish a quasi-nondivergent balance as the jet stream flow passes through the isotach maximum and approaches the ridge axis. The ageostrophic winds in this situation have the effect of transferring mass from the anticyclonic to the cyclonic side of the baroclinic wave in the jet streak exit region. This developing thermally direct circulation converts available potential energy into zonal kinetic energy, causing the flow to accelerate alongstream rather than to decelerate, as it typically would in regions of the baroclinic wave where curvature effects are less pronounced. Strong upper-level geostrophic adjustment mechanisms such as this are a common characteristic of synoptic scale environments conducive to the formation of severe weather events (Uccellini and Koch, 1987), and are currently believed to be responsible for generating observed meso- α/β scale inertia-gravity waves.

It is important to recognize that the geostrophic adjustment processes associated with a propagating jet streak which is *perturbed* from quasi-geostrophic equilibrium due to the physical mechanisms of inertial-advection nonlinearity (Van Tuyl and Young, 1982), orographic forcing (Kaplan *et al.* 1994a), or thermal forcing associated with low- to mid-level latent heat release of nearby mesoscale convective systems (Kaplan *et al.* 1994b), defines an ageostrophic initial value problem for the inertia-gravity wave radiation field and

the asymptotic approach to a *new* geostrophic equilibrium. The classical conceptual models of midlatitude jet streaks and their associated ageostrophic circulations (University of Chicago, 1947; Namias and Clapp, 1949; Riehl *et al.*, 1952; Murray and Daniels, 1953; Reiter, 1969) are based on quasi-geostrophic dynamics whose physical framework neglects the divergence tendency associated with the ageostrophic components of the flow physically responsible for the excitation of inertia-gravity waves. In fact, an unperturbed jet streak is in reality a quasi-balanced entity in the sense that the divergence associated with the alongstream zonal wind gradient is balanced by thermally direct (indirect) ageostrophic circulations in the jet streak's entrance (exit) regions which are driven by the baroclinicity of the midlatitude basic state environment.

Nevertheless, it is important from a fundamental geophysical fluid dynamics standpoint to understand theoretically both the free and forced transient responses and the subsequent adjustment to steady quasi-geostrophic equilibrium rotating homogeneous and continuously stratified *barotropic flows* undergo due to the impulsive and temporally continuous addition of localized momentum. In this regard, ageostrophic zonal wind anomalies and independently propagating zonal momentum forcings are used as a first approach to understanding the fundamental physics of the interaction between the real atmosphere and observed midlatitude jet streaks. This line of inquiry is pursued primarily in order to help fill the gap between the results of classical adjustment theory (Rossby, 1938; Cahn, 1945), which deals with idealized ageostrophic initial states evolving in motionless basic state atmospheres whose mass and momentum fields generally are not very representative of midlatitude jet streaks, and the role played by tropospheric jet streaks as upper-level forcing mechanisms in the nonlinear evolution of complex baroclinic storm producing environments (Uccellini and Johnson, 1979; Zack and Kaplan, 1987; Koch and Dorian, 1988; Kaplan *et al.*, 1994a, b).

The problem is approached from a theoretical perspective by assuming that the physical mechanisms responsible for the initial stages of midlatitude jet streak genesis can

be approximated by a small-amplitude zonal wind anomaly introduced into a uniformly rotating barotropic flow. The well-established methods of linear perturbation theory, which have been so successful in understanding the fundamental physics of orographically (Smith, 1979, 1989) and thermally (Lin, 1994a, b) forced gravity waves are used to derive the appropriate set of *coupled* wave equations based upon potential vorticity theory, and addresses both the initial-value and forced problems governing the geostrophic adjustment dynamics associated with impulsive and traveling zonal momentum sources in a rotating atmosphere.

In this study we investigate the three-dimensional response associated with several linear geostrophic adjustment problems in a barotropic, vertically unbounded (infinite), continuously stratified, Boussinesq atmosphere which is perturbed from geostrophic equilibrium. Section 2 outlines and discusses the linear theory governing the initial value problem imposed by the introduction of a localized ageostrophic zonal wind anomaly into a geostrophically balanced, uniform zonal flow. Section 3 outlines and discusses the linear theory governing the forced problem which is imposed by the introduction of a uniformly propagating zonal momentum forcing traveling at the speed $c < U$ through the basic state current. This problem is formulated in order to investigate the basic dynamics associated with entrance (exit) region acceleration (deceleration) experienced by the basic state flow as it passes through the slower moving isotach maximum. Section 4 summarizes the major findings and offers directions for future research.

2. Linear Theory for the Initial Value Problem

The set of linearized equations expressing the conservation of zonal, meridional, and vertical momentum, mass, and thermodynamic energy governing the response of small-amplitude, hydrostatic, baroclinic perturbations in a barotropic, continuously stratified, uniform Boussinesq flow on a planetary f -plane in the presence of external momentum and thermal forcing may be written as:

$$\frac{Du'}{Dt} - f v' + \frac{1}{\rho_0} \frac{\partial p'}{\partial x} = F_x, \quad (1)$$

$$\frac{Dv'}{Dt} + f u' + \frac{1}{\rho_0} \frac{\partial p'}{\partial y} = F_y, \quad (2)$$

$$\frac{1}{\rho_0} \frac{\partial p'}{\partial z} - \frac{g}{\theta_0} \theta' = 0, \quad (3)$$

$$\frac{\partial u'}{\partial x} + \frac{\partial v'}{\partial y} + \frac{\partial w'}{\partial z} = 0, \quad (4)$$

$$\frac{D\theta'}{Dt} + \frac{N^2 \theta_0}{g} w' = \frac{\theta_0}{c_p T_0} Q, \quad (5)$$

where $D/Dt = \partial/\partial t + U \partial/\partial x + V \partial/\partial y$, F_x and F_y [ms^{-2}] are zonal and meridional momentum forcings, respectively, and Q is the diabatic forcing [$\text{J kg}^{-1}\text{s}^{-1}$]. Other symbols have their conventional meanings.

For a quiescent atmosphere in the absence of orographic and thermal forcings, our theoretical model reduces to the one employed by Zhu and Holton (1987). If we further assume that only a zonal component of external momentum forcing exists, then the model further reduces to the forced geostrophic adjustment model for a quiescent atmosphere employed by Luo and Fritts (1993). The inclusion of a non-zero basic state flow allows for a more complete description of the adjustment to geostrophic equilibrium and subsequent motions in a rotating atmosphere. Note that the presence of a non-zero basic state flow allows our theory to incorporate the *commonly ignored* physical mechanisms of geostrophic vorticity advection, $-\mathbf{U} \cdot \nabla \zeta_g'$, and horizontal temperature advection, $-\mathbf{U} \cdot \nabla \theta'$. This is important for more realistic problems than we are addressing here, and which may include: (i) a pre-existing PV anomaly which can interact with the isolated PV couplet considered here through advection by the basic state flow, (ii) the presence of external

forcings in addition to an initial PV distribution, and (iii) self-advection due to nonlinear processes. For example, these physical mechanisms are known to play an essential role in the development of midlatitude synoptic scale systems when the zonal wind anomaly is viewed as an upper-level forcing mechanism interacting with low-level diabatically and orographically forced PV anomalies (Hoskins *et al.*, 1985).

The appropriate form of the potential vorticity equation which governs the forced inertia-gravity wave response may be derived from Eqs. (1)-(5), and is given by:

$$\frac{Dq'}{Dt} = F_\zeta + \frac{fg}{N^2 c_p T_0} \frac{\partial Q}{\partial z}. \quad (6)$$

In Eq. (6), the perturbation potential vorticity is defined as:

$$q' = \zeta' + \frac{f}{\rho_0 N^2} \frac{\partial^2 p'}{\partial z^2}, \quad (7)$$

which, in general, has contributions from both the induced relative vorticity and the perturbation stratification ($\partial\theta'/\partial z$, see Eq. (3)). $F_\zeta = \partial F_y / \partial x - \partial F_x / \partial y$ is the 'vorticity' associated with the external momentum forcing (Zhu and Holton, 1987). In the absence of external forcing, the perturbation PV is conserved following the motion of the basic state barotropic flow. The linearized wave equations governing the baroclinic perturbations $\mathbf{u}' = (u', v', w')$, p' , and θ' may be written collectively as:

$$L\phi'(\mathbf{r},t) = S(\mathbf{r},t), \quad (8)$$

where $\mathbf{r} = (x, y, z)$, $\phi' = q'$, \mathbf{u}' , p' , or θ' , L is a differential operator defined as:

$$L = \left\{ \left[\left(\frac{\partial}{\partial t} + U \frac{\partial}{\partial x} + V \frac{\partial}{\partial y} \right)^2 + f^2 \right] \frac{\partial^2}{\partial z^2} + N^2 \left(\frac{\partial^2}{\partial x^2} + \frac{\partial^2}{\partial y^2} \right), \text{ if } \phi' = (\mathbf{u}', p', \text{ or } \theta') \right\}, \quad (9)$$

and $S(\mathbf{r},t)$ is an inhomogeneous source term which describes the evolution of the initial PV distribution characterizing the perturbed state of the atmosphere:

$$S(\mathbf{r},t) = \begin{cases} -N^2 \frac{\partial q'}{\partial y} + \frac{\partial^2}{\partial z^2} \left(\frac{DF_x}{Dt} + f F_y \right) - \frac{g}{c_p T_0} \frac{\partial^2 Q}{\partial z \partial x}, & \text{if } \phi' = u' \\ N^2 \frac{\partial q'}{\partial x} + \frac{\partial^2}{\partial z^2} \left(\frac{DF_y}{Dt} - f F_x \right) - \frac{g}{c_p T_0} \frac{\partial^2 Q}{\partial z \partial y}, & \text{if } \phi' = v' \\ -\frac{\partial}{\partial z} \left(\frac{DF_\delta}{Dt} + f F_\zeta \right) + \frac{g}{c_p T_0} \nabla_H^2 Q, & \text{if } \phi' = w' \\ \rho_0 \left[N^2 (f q' + F_\delta) + \frac{g}{c_p T_0} \frac{D}{Dt} \frac{\partial Q}{\partial z} \right], & \text{if } \phi' = p' \\ \frac{N^2 \theta_0}{g} \left(f \frac{\partial q'}{\partial z} + \frac{\partial F_\delta}{\partial z} \right) + \frac{\theta_0}{c_p T_0} \frac{D}{Dt} \frac{\partial^2 Q}{\partial z^2}, & \text{if } \phi' = \theta' \end{cases}. \quad (10)$$

Note that a mathematically closed system consists of the potential vorticity equation, Eq. (6), and any one of the wave equations represented by Eq. (8). This system requires the specification of the three initial conditions ϕ'_i , $\partial\phi'_i/\partial t$, and q'_i . This formulation shows that in order to investigate the geostrophic adjustment dynamics of a non-resting continuously stratified atmosphere, the physical degeneracy of the *f*-plane equations (Gill, 1982) must first be lifted by determining the spatial distribution of the linearized PV as a function of time by solving Eq. (6). Once this distribution is obtained, it can be incorporated into the r.h.s. of the linearized wave equations from which the respective dynamical fields \mathbf{u}' , p' , and θ' can be obtained.

For a vertically unbounded Boussinesq atmosphere, we can define the three-dimensional Fourier transform of any field variable and its inverse by the integral pair

$$\hat{\phi}(\mathbf{k},t) = \frac{1}{8\pi^3} \int_{-\infty}^{\infty} \int_{-\infty}^{\infty} \int_{-\infty}^{\infty} \phi'(\mathbf{r},t) e^{-i \mathbf{k} \cdot \mathbf{r}} d\mathbf{r}, \quad (11)$$

$$\phi'(\mathbf{r},t) = \int_{-\infty}^{\infty} \int_{-\infty}^{\infty} \int_{-\infty}^{\infty} \hat{\phi}(\mathbf{k},t) e^{+i \mathbf{k} \cdot \mathbf{r}} d\mathbf{k}, \quad (12)$$

where $\mathbf{k} = (k, l, m)$. Taking the Fourier transform of the potential vorticity equation in the absence of any imposed forcing yields

$$\frac{\partial \hat{q}}{\partial t} + i(kU + lV) \hat{q} = 0. \quad (13)$$

Equation (13) has the following general solution

$$\hat{q}(\mathbf{k}, t) = \hat{q}_i(\mathbf{k}) e^{-i\Omega t}, \quad (14)$$

where $\Omega = kU + lV$ is the intrinsic wave frequency and \hat{q}_i is the initial perturbation potential vorticity distribution. With the addition of a non-zero basic state flow, the PV associated with the initial disturbance is advected downstream from the initial source location by the uniform barotropic current where, in the real atmosphere, it may interact with other pre-existing PV anomalies associated with orographically and/or diabatically forced circulations. Making the Fourier transform of the initial potential vorticity anomaly, Eq. (7), gives:

$$\hat{q}_i(\mathbf{k}) = i [k \hat{v}_i(\mathbf{k}) - l \hat{u}_i(\mathbf{k})] - \frac{m^2 f}{\rho_0 N^2} \hat{p}_i(\mathbf{k}), \quad (15)$$

where the subscript i denotes the initial wind and pressure perturbations associated with the disturbance.

Expanding the material derivative and taking the Fourier transform of the inhomogeneous wave equations, Eqs. (9) and (10), we obtain:

$$\frac{\partial^2 \hat{\phi}}{\partial t^2} + 2i\Omega \frac{\partial \hat{\phi}}{\partial t} + \left[\frac{N^2 k^2}{m^2} + f^2 - \Omega^2 \right] \hat{\phi} = R(\mathbf{k}) e^{-i\Omega t}, \quad (16)$$

where

$$R(\mathbf{k}) = \begin{cases} \frac{i l N^2}{m^2} \hat{q}_i(\mathbf{k}), & \text{if } \phi' = u' \\ -\frac{i k N^2}{m^2} \hat{q}_i(\mathbf{k}), & \text{if } \phi' = v' \\ 0, & \text{if } \phi' = w' \\ -\frac{\rho_0 N^2 f}{m^2} \hat{q}_i(\mathbf{k}), & \text{if } \phi' = p' \\ -\frac{i N^2 \theta_0 f}{g m} \hat{q}_i(\mathbf{k}), & \text{if } \phi' = \theta' \end{cases}. \quad (17)$$

In Eq. (16), $\kappa^2 = k^2 + l^2$. Primary contributions to the complete Fourier spectrum of zonal, meridional, and vertical wave numbers, defined here as $k = 2\pi/a_x$, $l = 2\pi/a_y$, and $m = 2\pi/a_z$, respectively, will come from an initial disturbance whose zonal, meridional, and vertical scales are a_x , a_y , a_z . The general solution to the perturbation potential vorticity equation, Eq. (14), has been incorporated into the inhomogeneous source terms on the r.h.s. of Eq. (16). The wave equations have a general solution of the form

$$\hat{\phi}(\mathbf{k}, t) = A_\phi(\mathbf{k}) e^{+i\omega_+ t} + B_\phi(\mathbf{k}) e^{-i\omega_+ t} + \frac{m^2 R(\mathbf{k})}{(N^2 \kappa^2 + m^2 f^2)} e^{-i\Omega t}. \quad (18)$$

The first two terms on the r.h.s. correspond physically to the transient inertia-gravity waves excited by the non-zero divergence tendency of the wind field associated with the initial PV anomaly. The third term corresponds to the linear, geostrophically balanced, steady-state equilibrium that the initial ageostrophic potential vorticity state asymptotically adjusts to, and by being advected downstream by the uniform basic state flow, gives rise to the physical mechanisms of geostrophic vorticity advection, $-\mathbf{U} \cdot \nabla \zeta'_g$, and horizontal temperature advection, $-\mathbf{U} \cdot \nabla \theta'$, associated with the traveling PV anomaly.

The dispersion relationship for these three-dimensional inertia-gravity waves may be written as:

$$\omega_{\pm} = f \sqrt{1 + \frac{N^2 \kappa^2}{m^2 f^2}} \pm \Omega, \quad (19)$$

which indicates that there exists an *infinite* number of natural length scales or Rossby deformation radii, $L_{R,m} = N/(fm)$, *one for each internal baroclinic mode of vertical wavenumber m*. Defining $m = 2\pi/L_z$, where L_z is the vertical wavelength of the transient inertia-gravity waves, we see that the Rossby deformation radius can be rewritten as $L_{R,m} = NL_z/(2\pi f)$. Each of these internal gravity waves can be defined by the phase speed $c_m = N/m = NL_z/2\pi$, and therefore can be related to the phase speed of short waves excited in a rotating homogeneous atmosphere if one defines an *equivalent depth*

$$H_e = \frac{N^2 L_z^2}{4 \pi^2 g}, \quad (20)$$

for each baroclinic mode (Gill, 1982). Since $c_m = N/m$, Eq. (16) implies that the horizontal structure of each internal mode in this system evolves exactly as that predicted by linear shallow water theory, if the undisturbed depth H of that system is replaced by the appropriate equivalent depth H_e for the specific vertical mode $m = 2\pi/L_z$.

Also from Eq. (19), we see that there exists two extreme regimes in the angular frequency of the inertia-gravity wave radiation field in a continuously stratified atmosphere. *Regime I:* $N^2\kappa^2/(m^2f^2) \ll 1$. Here we define $\kappa = 2\pi/a$, where a may be considered to be the length scale of the initial disturbance. In this regime, $a \gg L_{R,m}$, and therefore longwave components (with respect to the deformation radius) comprising the total Fourier spectrum of modes characterizing the initial state will have frequencies $\omega = f \pm \Omega$, which approach the inertial frequency as the magnitude of the basic state flow approaches zero. *Regime II:* $N^2\kappa^2/(m^2f^2) \gg 1$. In this regime, $a \ll L_{R,m}$, and shortwave components of the initial disturbance are characterized by waves of frequency $\omega = (N\kappa/m) \pm \Omega$. These waves are called *pure internal gravity waves*, and are not influenced by the effects of rotation. Note that the downstream advection of the balanced equilibrium state does not excite any further inertia-gravity wave modes, since it does not possess a propagation speed which is different from the basic state barotropic current.

The remaining unknown coefficients represented by $A_\phi(\mathbf{k})$ and $B_\phi(\mathbf{k})$ are determined by imposing the appropriate initial conditions u'_i , p'_i , θ'_i , $\partial u'_i / \partial t$, $\partial p'_i / \partial t$, and $\partial \theta'_i / \partial t$. Recall that each system consisting of one wave equation, Eq. (8), and the potential vorticity equation, Eq. (6), requires the three initial conditions ϕ'_i , $\partial \phi'_i / \partial t$, and q'_i for a unique solution. Since we are interested in the adjustment to geostrophic equilibrium from the unbalanced initial state characterized by an ageostrophic zonal wind anomaly, we define our set of *dependent* initial conditions to be:

$$u'_i(\mathbf{r}) = u_{\text{jet}}(\mathbf{r}) = u_{j0} (x^2/a^2 + y^2/b^2 + 1)^{-3/2} e^{-z^2/d_{\text{jet}}^2}, \quad (21)$$

$$v'_i(\mathbf{r}) = p'_i(\mathbf{r}) = \theta'_i(\mathbf{r}) = 0, \quad (22)$$

$$w'_i(\mathbf{r}) = \int_{-\infty}^z -\frac{\partial u_{\text{jet}}(\mathbf{r})}{\partial x} dz, \quad (23)$$

$$\frac{\partial u'_i}{\partial t}(\mathbf{r}) = - (U \frac{\partial}{\partial x} + V \frac{\partial}{\partial y}) u_{\text{jet}}(\mathbf{r}), \quad (24)$$

$$\frac{\partial v'_i}{\partial t}(\mathbf{r}) = - f u_{\text{jet}}(\mathbf{r}), \quad (25)$$

$$\frac{\partial w'_i}{\partial t}(\mathbf{r}) = \int_{-\infty}^z [\frac{\partial}{\partial x} (U \frac{\partial}{\partial x} + V \frac{\partial}{\partial y}) u_{\text{jet}}(\mathbf{r}) + f \frac{\partial u_{\text{jet}}(\mathbf{r})}{\partial y}] dz, \quad (26)$$

$$\frac{\partial \theta'_i}{\partial t}(\mathbf{r}) = - \frac{N^2 \theta_0}{g} w'_i(\mathbf{r}), \quad (27)$$

$$\frac{\partial p'_i}{\partial t}(\mathbf{r}) = \int_{-\infty}^z -\rho_0 N^2 w'_i(\mathbf{r}) dz. \quad (28)$$

For the particular problem addressed here, note that an unbalanced zonal wind anomaly in a rotating continuously stratified atmosphere is equivalent to a PV anomaly given by the meridional gradient of the ageostrophic jet,

$$q'_i(\mathbf{r}) = - \frac{\partial u_{jet}}{\partial y}(\mathbf{r}), \quad (29)$$

and defines the appropriate initial condition on the perturbation potential vorticity which is required for a unique solution. Note that Eq. (21) and the definition of q' from Eq. (7) have been used to derive Eq. (29).

The Fourier transform of Eq. (29) is used in Eq. (17), which determines the coefficient for the last term on the r.h.s. of the general solution given by Eq. (18). The other coefficients are determined to be:

$$A_\phi(\mathbf{k}) = \frac{\hat{u}_{jet}(\mathbf{k})}{2} \left\{ \begin{array}{l} \frac{(N^2 k^2 + m^2 f^2)}{(N^2 \kappa^2 + m^2 f^2)}, \text{ if } \phi' = u' \\ \frac{k l N^2}{(N^2 \kappa^2 + m^2 f^2)} + \frac{i f m}{\sqrt{N^2 \kappa^2 + f^2 m^2}}, \text{ if } \phi' = v' \\ - \frac{1}{m} \left(k + \frac{i l f m}{\sqrt{N^2 \kappa^2 + f^2 m^2}} \right), \text{ if } \phi' = w' \\ - \rho_0 N^2 \left[\frac{i l f}{(N^2 \kappa^2 + m^2 f^2)} + \frac{k}{m \sqrt{N^2 \kappa^2 + f^2 m^2}} \right], \text{ if } \phi' = p' \\ \frac{\theta_0 N^2}{g} \left[\frac{l m f}{(N^2 \kappa^2 + m^2 f^2)} - \frac{i k}{\sqrt{N^2 \kappa^2 + f^2 m^2}} \right], \text{ if } \phi' = \theta' \end{array} \right\}, \quad (30)$$

$$B_\phi(\mathbf{k}) = \left\{ \frac{\left[\left(\sqrt{\frac{N^2 \kappa^2}{m^2} + f^2} - \Omega \right) A_\phi(\mathbf{k}) + \lambda \hat{u}_{jet}(\mathbf{k}) \right]}{\left[\sqrt{\frac{N^2 \kappa^2}{m^2} + f^2} + \Omega \right]} \right\}, \quad (31)$$

$$\text{where } \lambda = \begin{cases} \Omega \frac{(N^2 k^2 + m^2 f^2)}{(N^2 \kappa^2 + m^2 f^2)}, & \text{if } \phi' = u' \\ [-i f + \frac{k l N^2 \Omega}{(N^2 \kappa^2 + m^2 f^2)}], & \text{if } \phi' = v' \\ i \left[\frac{(i k \Omega + l f)}{m} \right], & \text{if } \phi' = w' \\ \rho_0 N^2 \left[\frac{k}{m^2} - \frac{i l f \Omega}{(N^2 \kappa^2 + m^2 f^2)} \right], & \text{if } \phi' = p' \\ \frac{\theta_0 N^2}{g} \left[\frac{i k}{m} + \frac{l f m \Omega}{(N^2 \kappa^2 + m^2 f^2)} \right], & \text{if } \phi' = \theta' \end{cases}. \quad (32)$$

The solution in physical space is then obtained by integrating Eq. (12) numerically through the use of a Fast Fourier transform (FFT) algorithm.

Figures 40–46 show the response predicted by the linear theory during the first 12 h after the ageostrophic zonal wind anomaly given by Eq. (21) is introduced into a quiescent, vertically unbounded, continuously stratified atmosphere. We discuss the response in a motionless basic state first to clearly illustrate the evolution of both the *geostrophic* and *ageostrophic* perturbation winds in the absence of linear advection by the basic state flow. Although this type of partitioning is seldom done in geostrophic adjustment studies, it is necessary here because: (i) unlike the perturbations of classical adjustment theory (Rossby, 1938; Cahn, 1945; Blumen, 1972), we are dealing with mass and momentum fields which are more representative of midlatitude jet streaks, and (ii) the *ageostrophic* motions associated with these meso- α scale disturbances in the jet stream are fundamentally important to the development of severe weather (Uccellini and Johnson, 1979; Uccellini and Koch, 1987; Zack and Kaplan, 1987; Kaplan *et al.*, 1994a, b) and therefore their *genesis* and subsequent evolution needs to be clearly identified. The basic state flow parameters are taken to be $N = 0.01 \text{ s}^{-1}$, $f = 10^{-4} \text{ s}^{-1}$, $\rho_0 = 1 \text{ kg m}^{-3}$, and $\theta_0 = 273 \text{ K}$. The magnitude of the initial ageostrophic zonal wind anomaly is taken to be $u_{j0} = 20 \text{ ms}^{-1}$, and its zonal and meridional half-widths and vertical *e*-folding scale are specified to be $a = b = 500 \text{ km}$, and $d = 12.5 \text{ km}$, respectively.

Although there exist an infinite number of Rossby deformation radii in a continuously stratified atmosphere, they will be dominated by $L_R = NH/f$, where H is the total depth of the initial disturbance. Taking $H = 2d_{jet} = 25$ km yields a Rossby deformation radius of 2500 km. If a and b are taken to be 500 km ($=L_R/5$), an initial disturbance in the wind field of this horizontal and vertical scale in a continuously stratified atmosphere will tend to evoke a response in which the mass (potential temperature) field adjusts to the initial ageostrophic perturbation in the wind field.

Figures 40a and 40b show the horizontal cross sections at $z = 0$ of the total zonal wind perturbation ($u' = u'_g + u'_a$) at $t = 3$ and 12 h. Linear theory predicts that the magnitude of the ageostrophic zonal wind anomaly has dropped from its initial value of 20 ms^{-1} to approximately 13 ms^{-1} during the first hour of adjustment (not shown), a reduction of roughly 35%. At $t = 3$ h, two oppositely propagating inertia-gravity waves (IGWs) can be detected, which propagate away from the jet core, whose centers are located approximately 1600 km east and west of the main jet core located at $\mathbf{r} = (0,0,0)$ (Fig. 40a). The zonal phase speed of these transient waves is estimated to be approximately $c_{px} = 148 \text{ ms}^{-1}$. The jet core magnitude at this time is roughly 8 ms^{-1} , which corresponds to a decrease of $\sim 5 \text{ ms}^{-1}$ from its value at $t = 1$ h. Also at this time two weak compensating zonal counter currents ($u' < 0$) of $\sim 1.3 \text{ ms}^{-1}$ exist, whose centers are located roughly 800 km north and south of the main jet core. These counter currents are actually portions of perturbation return flow around the evolving high-low dipole couplet in the perturbation pressure field (Fig. 44a), which is becoming established to support the nondivergent portion of the zonal wind.

By $t = 6$ h the centers of the transient IGWs have now propagated beyond $|x| \sim 3200$ km (not shown). Another set of propagating modes whose centers are located at $|x| \sim 1600$ km at this time are present (not shown) and are associated with longer wavelengths (and hence, smaller c_{gx}) comprising the total Fourier spectrum of modes defining the fully isolated three-dimensional initial state. Assuming this second set of IGWs to have

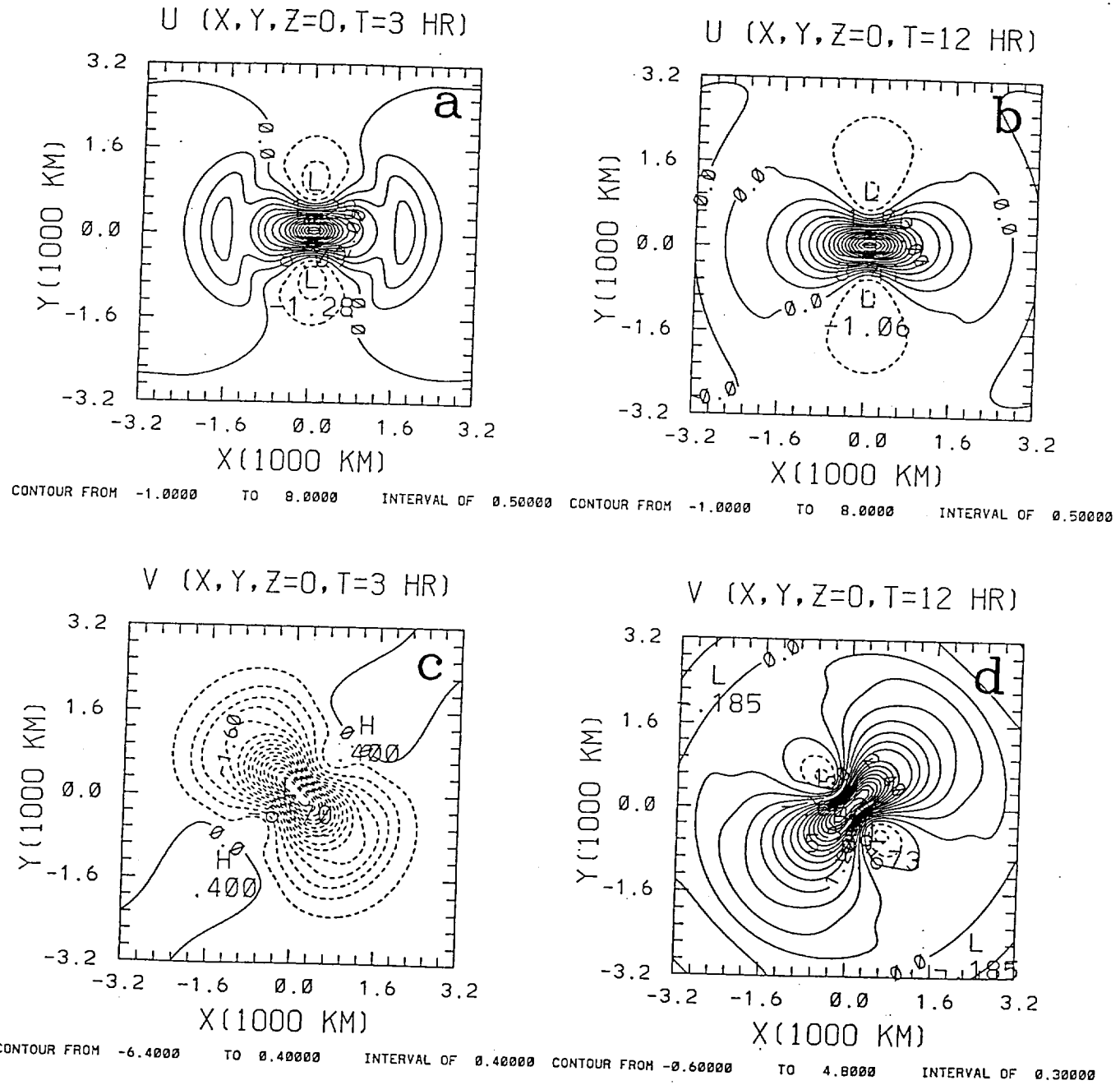
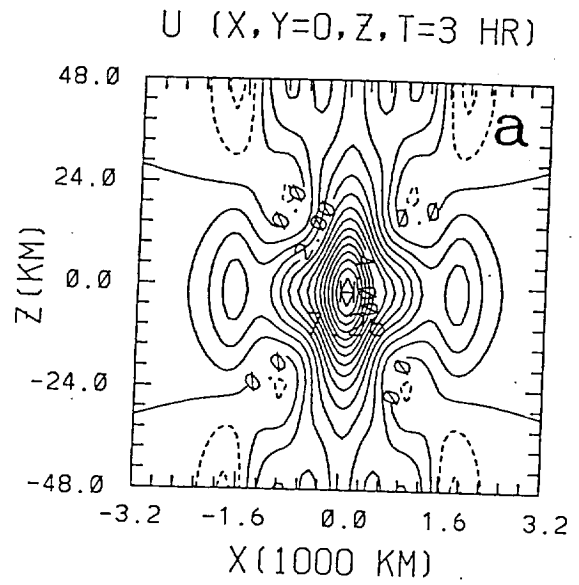


Fig. 40: Linear theoretical solution at $z = 0$ for u' at a) $t = 3$ h, b) $t = 12$ h, and v' at c) $t = 3$ h, and d) $t = 12$ h produced by the impulsive addition of zonally localized momentum from an unbalanced jet given by Eq. (21) to a quiescent, rotating, laterally and vertically unbounded, continuously stratified Boussinesq atmosphere. The magnitude, zonal, meridional, and vertical half-widths of the ageostrophic jet are 20 ms^{-1} , $a = b = 500 \text{ km}$, and $d_{\text{jet}} = 12.5 \text{ km}$, respectively. N and f are 10^{-2} s^{-1} and 10^{-4} s^{-1} , respectively.

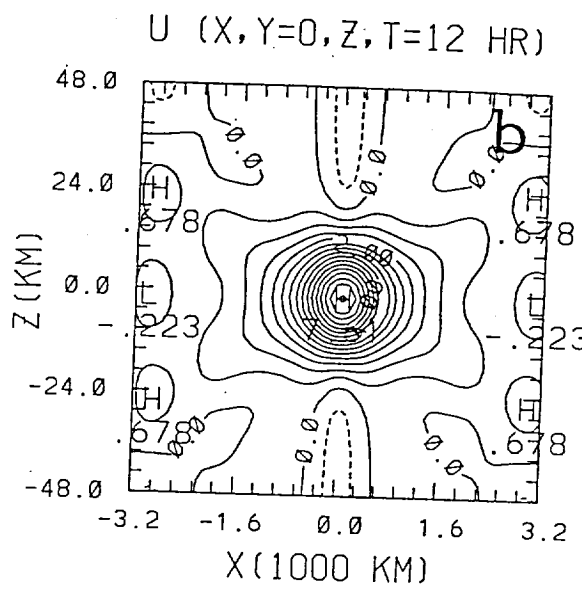
originated at the origin at $t = 0$ yields an estimate of $c_{px} \sim 74 \text{ ms}^{-1}$ for their zonal phase speed. The magnitude of the jet core at this time is $\sim 5.6 \text{ ms}^{-1}$, and the zonal counter currents have increased to $\sim -3 \text{ ms}^{-1}$ due to the strengthening perturbation pressure field. Six hours later at $t = 12 \text{ h}$ (Fig. 40b), the jet core has strengthened to $\sim 8.4 \text{ ms}^{-1}$, while the zonal counter currents have been reduced to $\sim 1.06 \text{ ms}^{-1}$ from their value of $\sim 1.28 \text{ ms}^{-1}$ at $t = 3 \text{ h}$. This temporal oscillation of the zonal wind perturbation (see Figs. 48a and 49a) is consistent with classical adjustment theory (Rossby, 1938; Cahn, 1945; Blumen, 1972), and indicates the removal of the ageostrophic portion of the evolving zonal wind perturbation by transient dispersive IGWs, and the asymptotic approach to a nondivergent balanced equilibrium state which is consistent with the conservation of perturbation potential vorticity (Gill, 1982).

Figures 40c and 40d show the horizontal cross sections at $z = 0$ of the total meridional wind perturbation ($v' = v'_g + v'_a$) at $t = 3$ and 12 h . At $t = 1 \text{ h}$, an isolated northwesterly to southeasterly oriented jet of $\sim -5 \text{ ms}^{-1}$ is induced by the Coriolis force acting on the initially unbalanced, ageostrophic zonal wind anomaly (not shown), which slightly strengthens to $\sim -6.7 \text{ ms}^{-1}$ by $t = 3 \text{ h}$ (Fig. 40c). Three hours later at $t = 6 \text{ h}$, the isolated cells of southerly meridional wind located in the southwest and northeast quadrants of the zonal jet (Fig. 40c) have significantly strengthened to $\sim 1.3 \text{ ms}^{-1}$, and are primarily the geostrophic component of the meridional wind defined by the east-west gradient of the evolving perturbation pressure couplet (not shown). By $t = 12 \text{ h}$, the entrance (exit) region confluence (diffluence) evident six hours prior no longer exists (Fig. 40d), because the northwesterly to southeasterly oriented jet has become a southwesterly to northeasterly oriented jet. This indicates that the meridional wind component at the origin is primarily dominated by its ageostrophic component at this time.

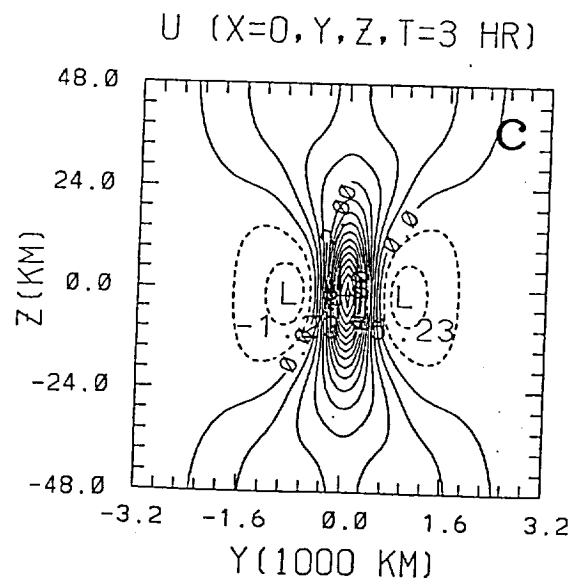
Figures 41a and b show the east-west vertical cross section through $y = 0$ of u' at $t = 3$ and 12 h . Early in the adjustment at $t = 1 \text{ h}$ (not shown), the wind anomaly is primarily confined to within an e -folding distance of $\mathbf{r} = (0, 0, 0)$, indicating that not much wave



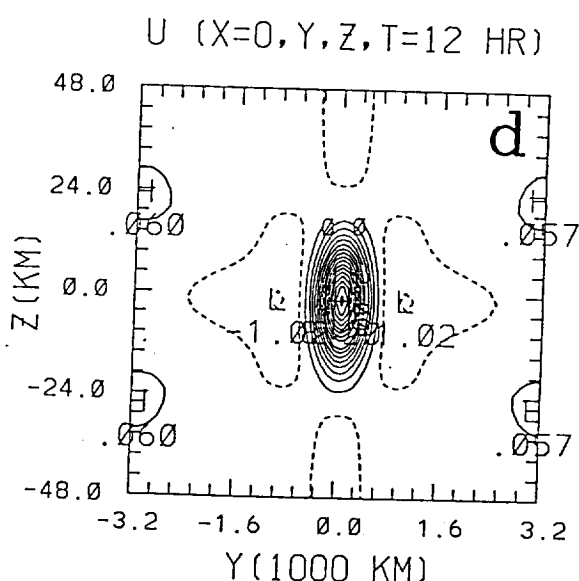
CONTOUR FROM -1.0000 TO 7.0000 INTERVAL OF 0.50000



TOUR FROM -0.50000 TO 7.5000 INTERVAL OF 0.50000



CONTOUR FROM -1.0000 TO 7.5000 INTERVAL OF 0.50



TO 8.0000 INTERVAL OF 0.50000

Fig. 41: East-west (a, b) and north-south (c, d) vertical cross sections of u' predicted by linear theory at t = a) 3 h, b) 12 h, c) 3 h, and d) 12 h for an infinite Boussinesq atmosphere.

energy associated with vertically propagating internal gravity waves has yet occurred. Two hours later at $t = 3$ h (Fig. 41a), notice that horizontally propagating modes whose centers are located at $|x| \sim 1600$ km are still primarily dominant on this vertical plane, and correspond with those shown earlier (Fig. 40a). By $t = 6$ h, however, significant vertical propagation of IGWs both above and below the jet core located at $z = 0$ is evident on the $y = 0$ plane (not shown). At $t = 12$ h, most of the significant transient IGW activity at this location has virtually ceased, yielding a well-defined, vertically isolated zonal wind maximum of $\sim 7.6 \text{ ms}^{-1}$ magnitude (Fig. 41b).

Figures 41c and d show the north-south vertical cross section through $x = 0$ of the total zonal wind perturbation at $t = 3$ and 12 h. Similar to the x - z vertical cross section, the y - z cross section at $t = 1$ h shows that the zonal wind anomaly is vertically confined to within an e -folding distance of the origin (not shown). Two hours later at $t = 3$ h, the zonal counter currents have already formed (Fig. 41c), whose centers are located roughly 800 km north and south of the zonal jet core. The magnitude of the zonal counter currents have strengthened almost by a factor of three by $t = 6$ h, while the magnitude of the primary zonal jet core has been reduced by $\sim 2 \text{ ms}^{-1}$ (not shown). During the subsequent six hour period, the magnitude of the zonal wind anomaly strengthens by $\sim 3 \text{ ms}^{-1}$ (Fig. 41d), while the counter currents decrease in magnitude, indicating that u' is still asymptotically adjusting to its final equilibrium value which conserves the PV associated with the initial disturbance.

Figure 42 shows horizontal cross sections of the vertical velocity field w' at 6 km below the level of maximum zonal perturbation wind at $t = 1, 3, 6$, and 12 h. At early times during the adjustment process, note that within the vicinity of the jet entrance (exit) region, descending (ascending) motion is occurring, beyond which transient dispersive IGWs are clearly evident (Figs. 40a-b). The dominant cell of ascending (descending) vertical motion is associated with convergence (divergence) induced in these regions (Eq. 23). At 1 h, the centers of oppositely propagating IGWs are located at approximately $|x| \sim$

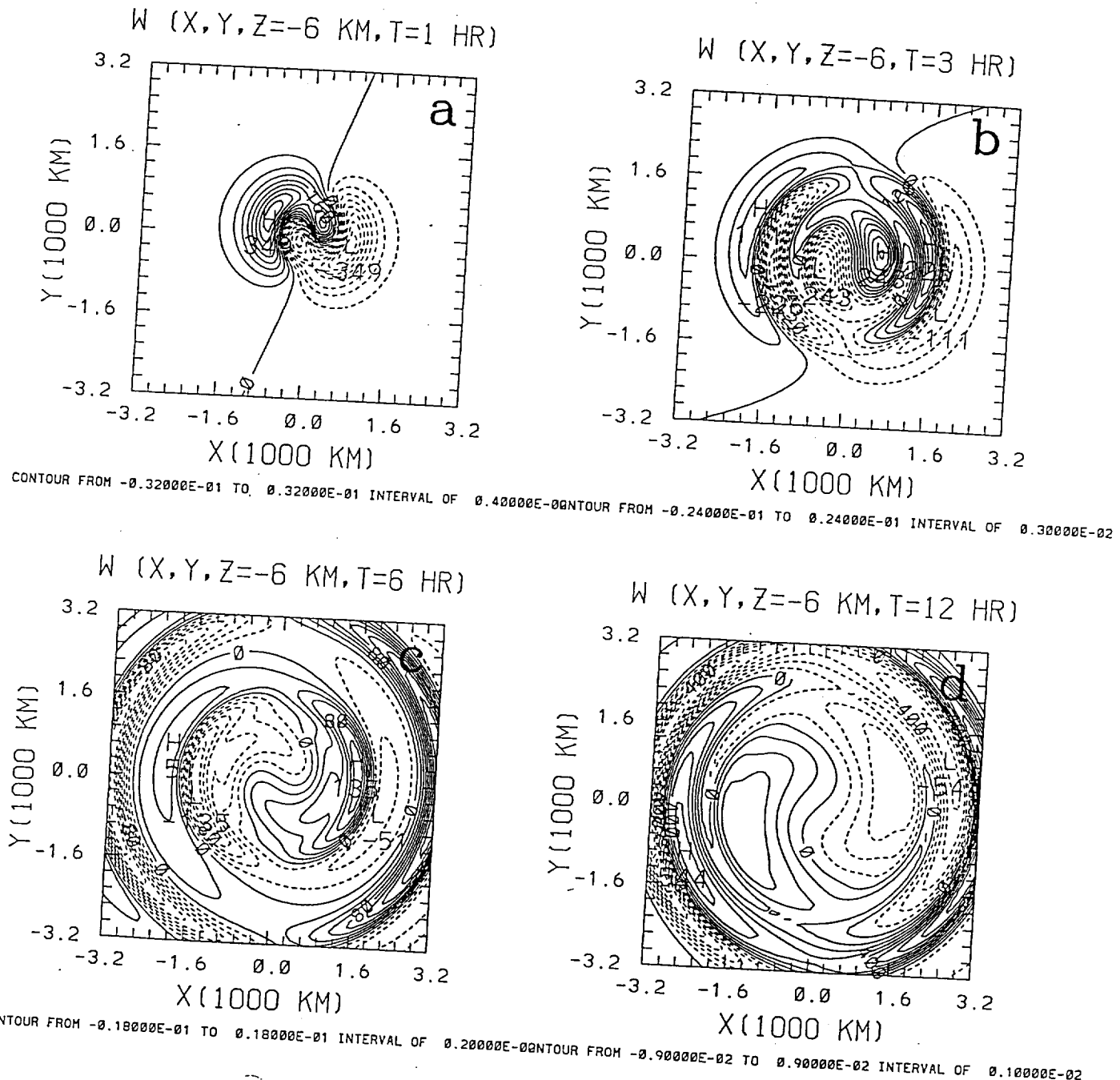


Fig. 42: Horizontal cross sections of w' at $z = -6 \text{ km}$ predicted by linear theory due to the impulsive addition of ageostrophic zonal momentum at $t =$ a) 1 h, b) 3 h, c) 6 h, and d) 12 h.

800 km, yielding an estimate of $c_{px} \sim 222 \text{ ms}^{-1}$ (Fig. 3a). Two hours later these propagating IGWs have traveled to $|x| \sim 1600 \text{ km}$, and are immediately flanked by IGW modes of the opposite sign, whose centers are located at approximately 1200 km (Fig. 42b).

The IGWs have propagated to $|x| \sim 3200 \text{ km}$ by $t = 6 \text{ h}$, behind which slower propagating, longer wavelength modes are also radially propagating (Fig. 42c). Six hours later note that significant transient IGW activity is still occurring on the $z = -6 \text{ km}$ plane (Fig. 42d). Since the linearized PV associated with the initially unbalanced zonal wind anomaly makes no direct contribution to the vertical velocity field (see Eqs. (16)-(18)), this perturbation field consists solely of transient, dispersive, ageostrophic IGWs.

Figure 43 shows horizontal cross sections of the evolving perturbation pressure p' and potential temperature θ' fields at $z = 0$ and -12 km , respectively. The linear theory presented here predicts that the mass fields (whose vertical structures are hydrostatically related) quickly adjust to the disturbance in the wind field for an initial perturbation characterized by the chosen parameters, leaving couplets of low (high) perturbation pressure (Figs. 43a and b) and cold (warm) air (Figs. 43c and d) north (south) of the origin at all levels below the level of maximum zonal perturbation wind (Figs. 50c and d). These fields are reversed at all levels above $z = 0$, (Figs. 50c, d) and in the absence of any vertical motions (i.e. as $t \rightarrow \infty$), therefore defines a *local thermal wind balance* between the three-dimensional baroclinic perturbations.

Figure 44 shows horizontal cross sections at $z = 0$ of the evolving geostrophic components u'_g and v'_g of the perturbation winds at $t = 3$ and 12 h . Notice that transient IGWs are clearly evident in both the zonal (Fig. 44a) and meridional (Fig. 44c) geostrophic wind perturbations at $t = 3 \text{ h}$, and are a result of the evolving perturbation pressure field at this time (Fig. 43a). A well-defined isolated zonal geostrophic jet core of $\sim 8.7 \text{ ms}^{-1}$ exists at this time in the vicinity of the origin (Fig. 44a), while a 'four-cell' pattern indicative of meridionally confluent (diffluent) flow is attempting to become established in the vicinity of

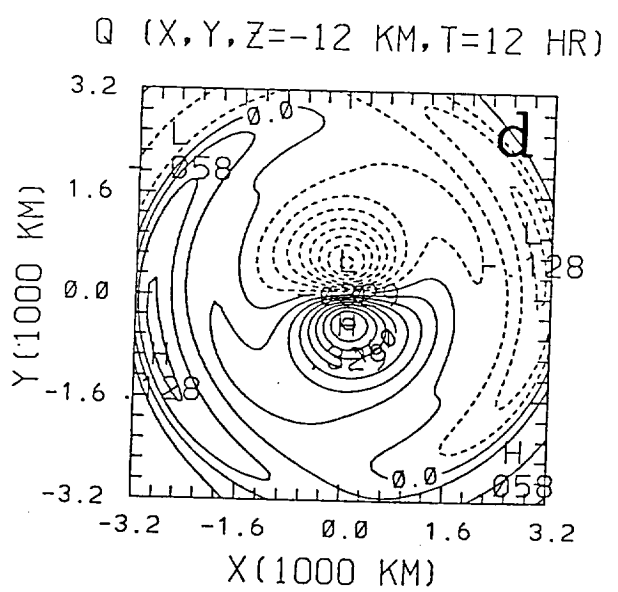
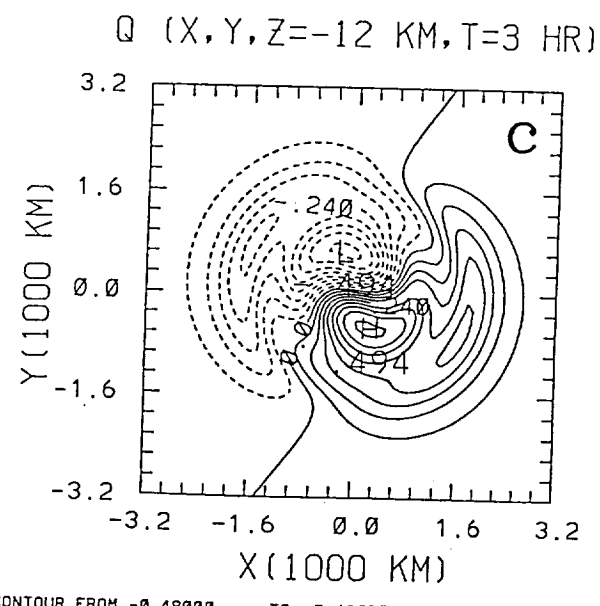
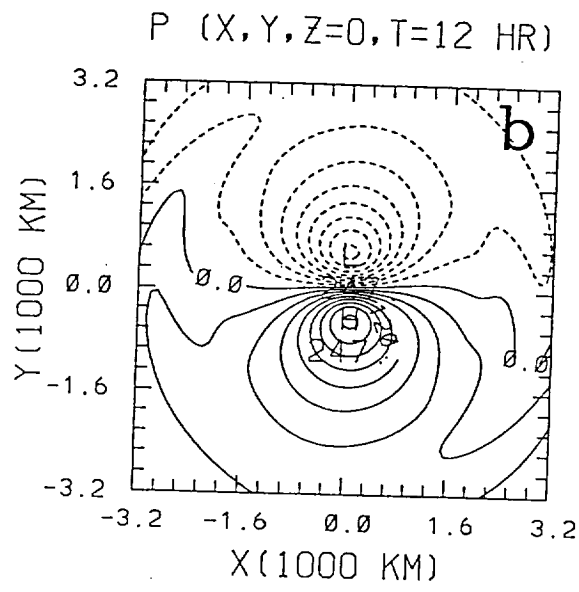
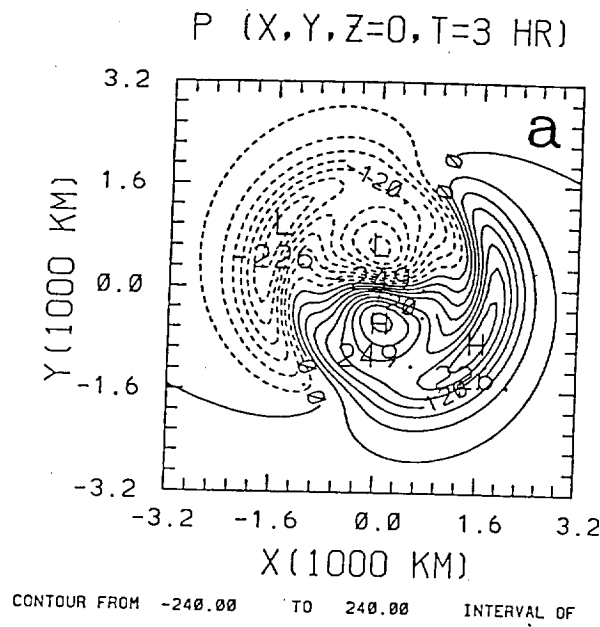


Fig. 43: Same as Fig. 40 except that p' at $z = 0$ and θ' at $z = -12$ km are shown.

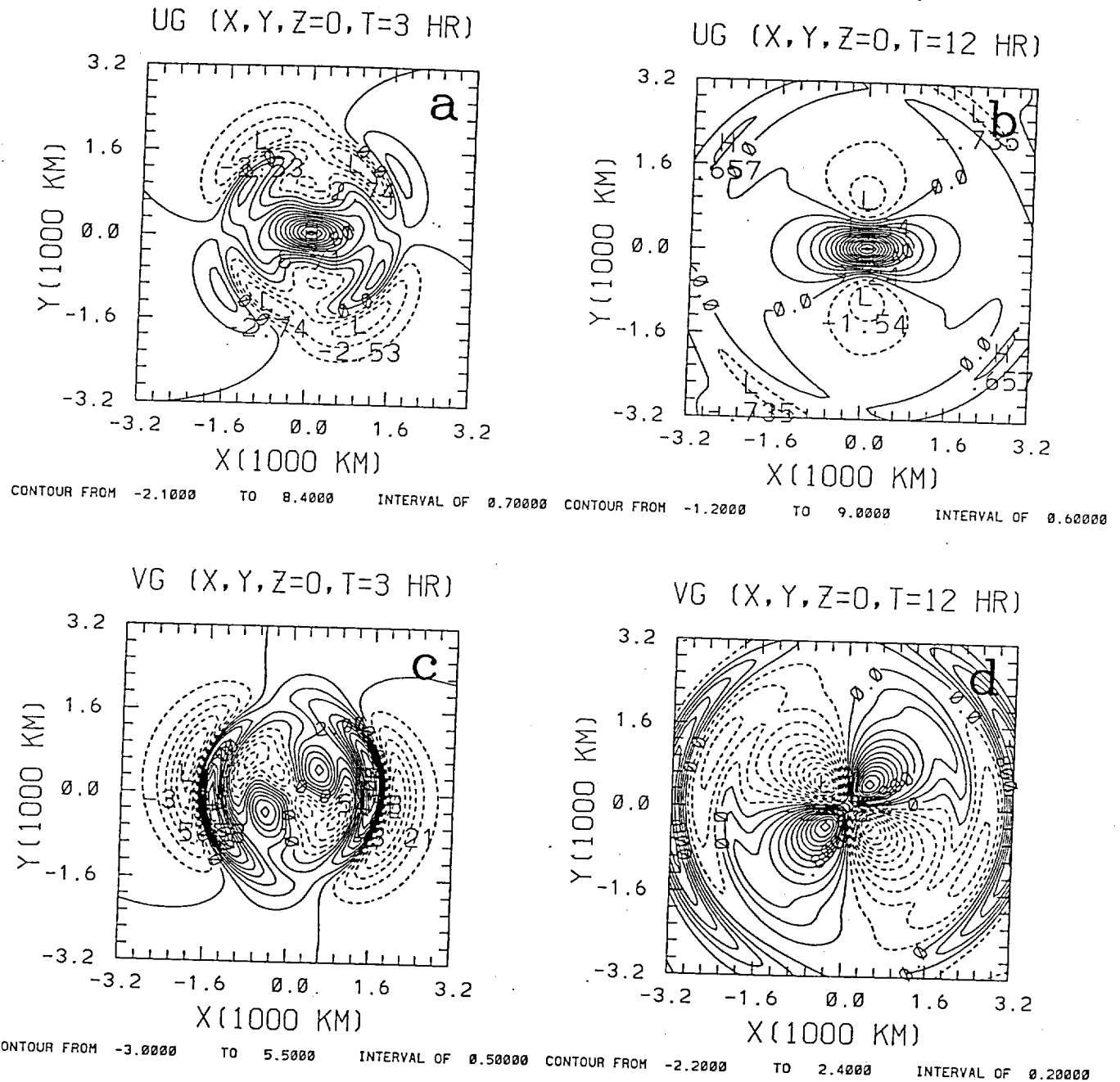


Fig. 44: Same as Fig. 40 except that u'_g and v'_g are shown.

$|x| \sim 800$ km in the entrance (exit) region of the geostrophic zonal jet (Fig. 44c). By $t = 12$ h, although transient IGW activity is still clearly evident in the geostrophic perturbation winds (Figs. 44b and d), clearly these flow components are dominated at this time by an isolated geostrophic zonal jet of $\sim 9.24 \text{ ms}^{-1}$, flanked by isolated zonal counter currents of $\sim -1.5 \text{ ms}^{-1}$, whose centers are located at $|y| \sim 800$ km north and south of the geostrophic jet core, and a well-defined pattern of confluent (diffluent) flow of $\sim \pm 2.4 \text{ ms}^{-1}$ in the jet entrance (exit) region.

Figure 45 shows the horizontal cross sections at $z = 0$ of the ageostrophic components $u'_a = u' - u'_g$ and $v'_a = v' - v'_g$ at $t = 3$ and 12 h. Note that the response in these perturbation fields at these times is dominated primarily by transient dispersive IGWs (Figs. 45a-d). By $t = 12$ h, although significant IGW activity is still present, note that the magnitude of u'_a is relatively small compared to the magnitude of u'_g , especially at the origin (compare Fig. 45b with Fig. 44b), indicating that the total zonal wind component u' is becoming dominated by its geostrophic component. However, note that a well-defined, isolated meridional ageostrophic wind component of $\sim 5 \text{ ms}^{-1}$ magnitude exists at the origin at this time (Fig. 45d). Comparing the geostrophic component (Fig. 44d) with the ageostrophic component (Fig. 45d) of the total meridional wind perturbation, we can see that v' at $\mathbf{r} = (0,0,0)$ will for all times be dominated by v'_a , and therefore this point in the fluid will be dominated by an inertial oscillation, which will asymptotically decay as the energy contained in the slow moving long wavelength components are eventually dispersed to a larger and larger volume of fluid.

Figure 46 shows the vertical cross sections of the total meridional perturbation wind v' , vertical velocity w' , perturbation pressure p' , and perturbation potential temperature θ' at $t = 12$ h. Six hundred kilometers to the west of the main jet core, an isolated cell of positive meridional wind of $\sim 3.2 \text{ ms}^{-1}$ exists on the south side in the jet entrance region (Figs. 40c and 46a). Above and below the level of maximum zonal wind, north of $y = 0$, vertically propagating IGWs are clearly evident as the meridional wind adjusts to the

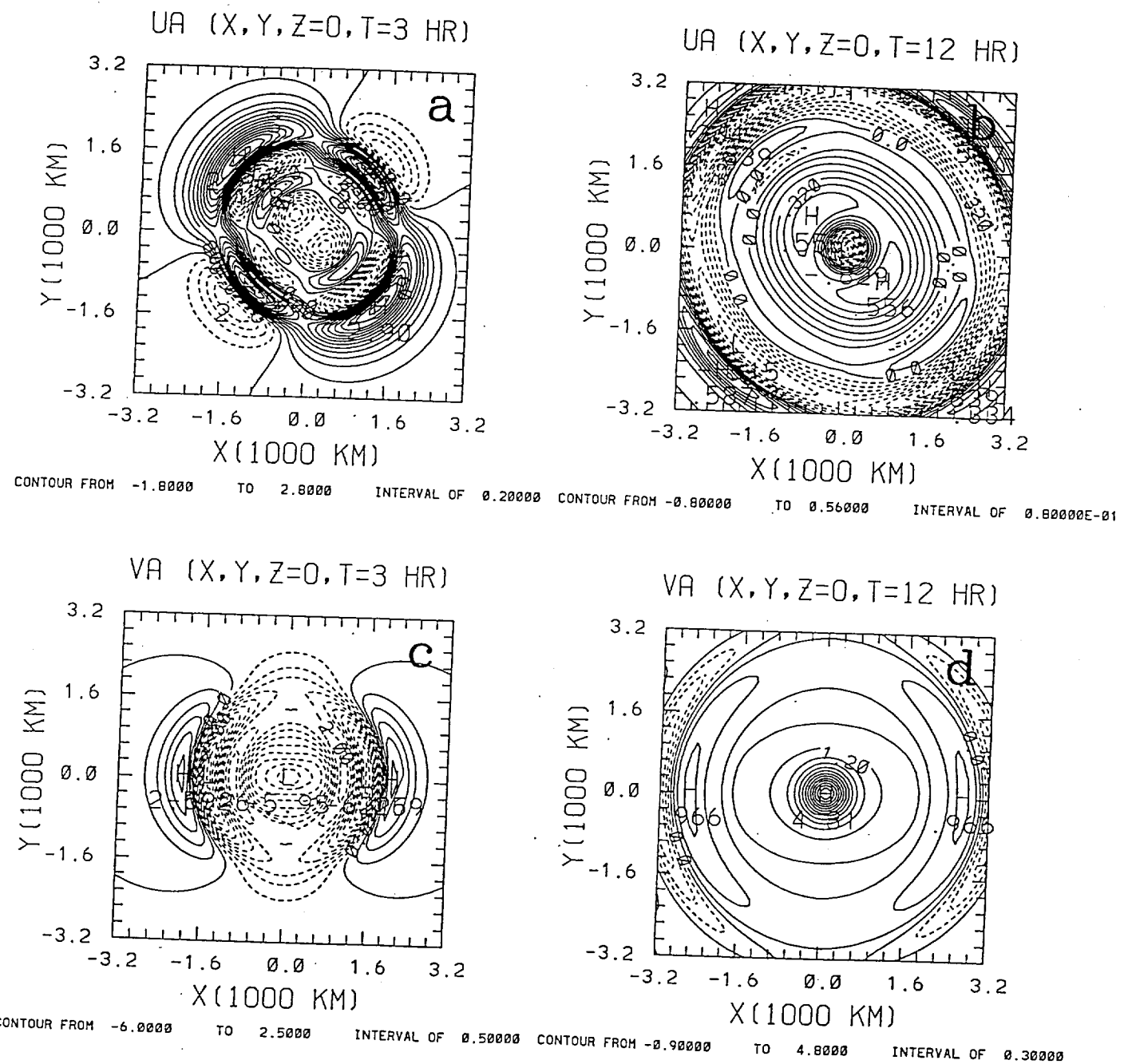


Fig. 45: Same as Fig. 44 except that u'_a and v'_a are shown.

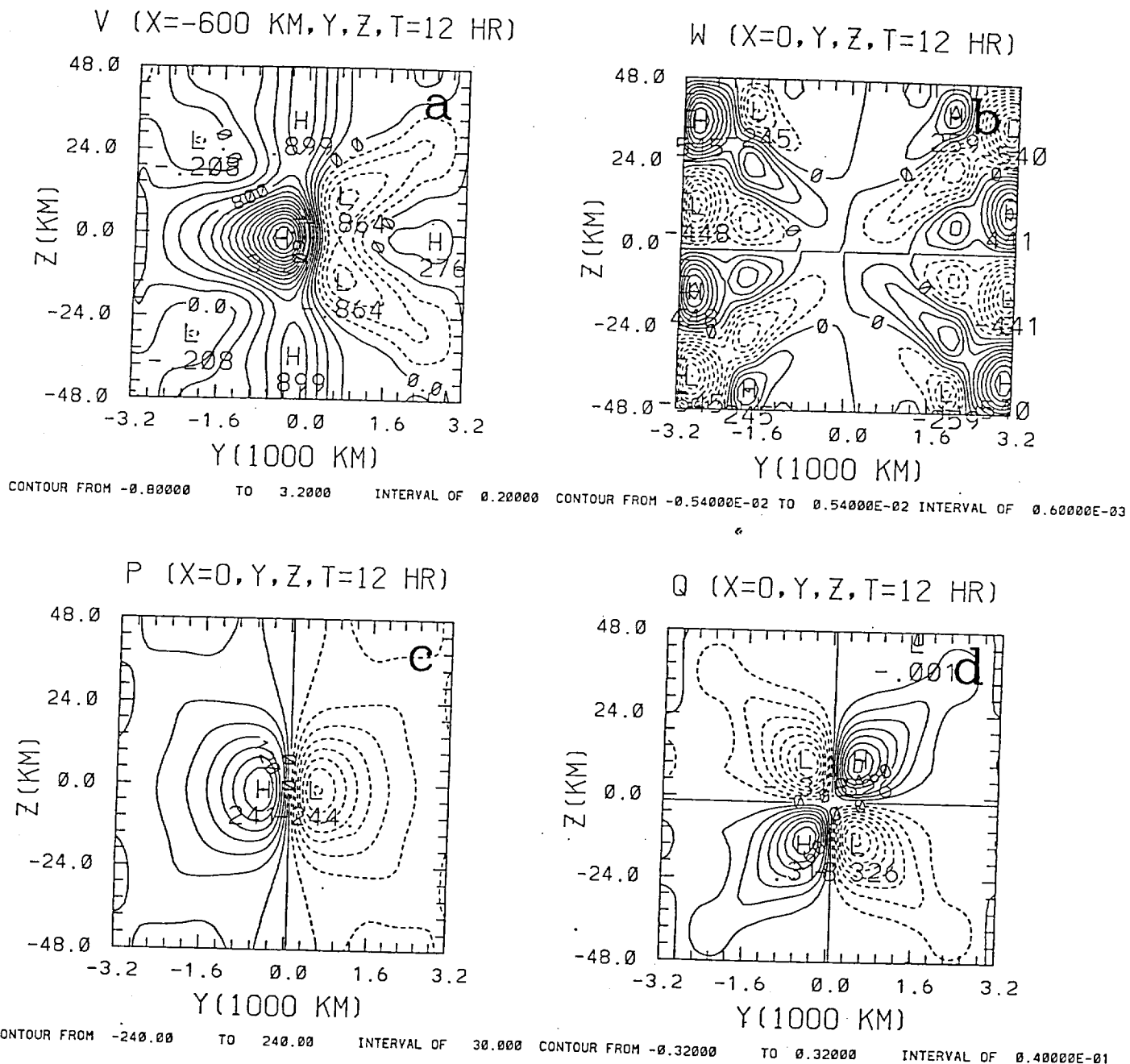


Fig. 46: North-south vertical cross sections of a) v' at 600 km west of the main jet core, b) w' , c) p' , and d) θ' at $t = 12$ h.

evolving perturbation pressure field. On the $x = 0$ plane, above and below $z = 0$, transient, vertically propagating IGWs most evident in the vertical velocity field are dispersing ageostrophic wave energy into the surrounding quiescent atmosphere as the fluid approaches a new balanced equilibrium state (Fig. 46b). Figs. 46c and d show that isolated couplets of perturbation high (low) pressure are colocated with warm (cold) air on the south (north) side of the zonal jet below the level of maximum zonal wind. This pattern is reversed above $z = 0$, as required by the hydrostatic balance.

Figures 47 and 48 show the temporal evolution in total u' , p' , w' , and θ' at $(x, 0, 0)$ and $(0, y, 0)$, respectively, predicted by linear theory during the first 48 h of adjustment to a non-divergent, geostrophically balanced equilibrium. Figs. 47a and 48a show that u' decreases steadily during the early stages of adjustment, reaching a minimum of $\sim 6 \text{ ms}^{-1}$ at $t \sim 7.5 \text{ h}$, after which it begins to increase and approaches another maximum of approximately 11.2 ms^{-1} at $t \sim 17 \text{ h}$ (Fig. 47a). Notice that u' continues to oscillate about its final equilibrium value with slowly decreasing amplitude for all time after this. Fig. 48a indicates that the zonal counter currents flanking the jet core begin forming at $t \sim 3 \text{ h}$, and continue to evolve with the maxima forming at $|y| \sim 800 \text{ km}$ approximately at $t \sim 6 \text{ h}$. Note that this portion of the perturbation return flow occurs at approximately the same time as the high-low pressure perturbation couplet reaches its maximum value (Fig. 48b). The zonal wind anomaly with its compensating counter currents continually oscillate about their equilibrium values for $t > 12 \text{ h}$ (Fig. 48a). Fig. 47b shows that most of the transient IGW activity propagating in the zonal direction associated with the evolving p' field occurs during the first 12 hours of the adjustment. These IGWs propagate a distance of $|x| \sim 6400 \text{ km}$, yielding a zonal phase speed of $c_{px} \sim 148 \text{ ms}^{-1}$.

The temporal evolution of the vertical velocity w' (Fig. 47c) and potential temperature (Fig. 47d) fields indicate that a broader spectrum of wave modes are excited in the zonal direction during the first 12 h of adjustment, in which there are at least three primary modes evident in w' (not shown). The first mode originates at $t = 0$, and

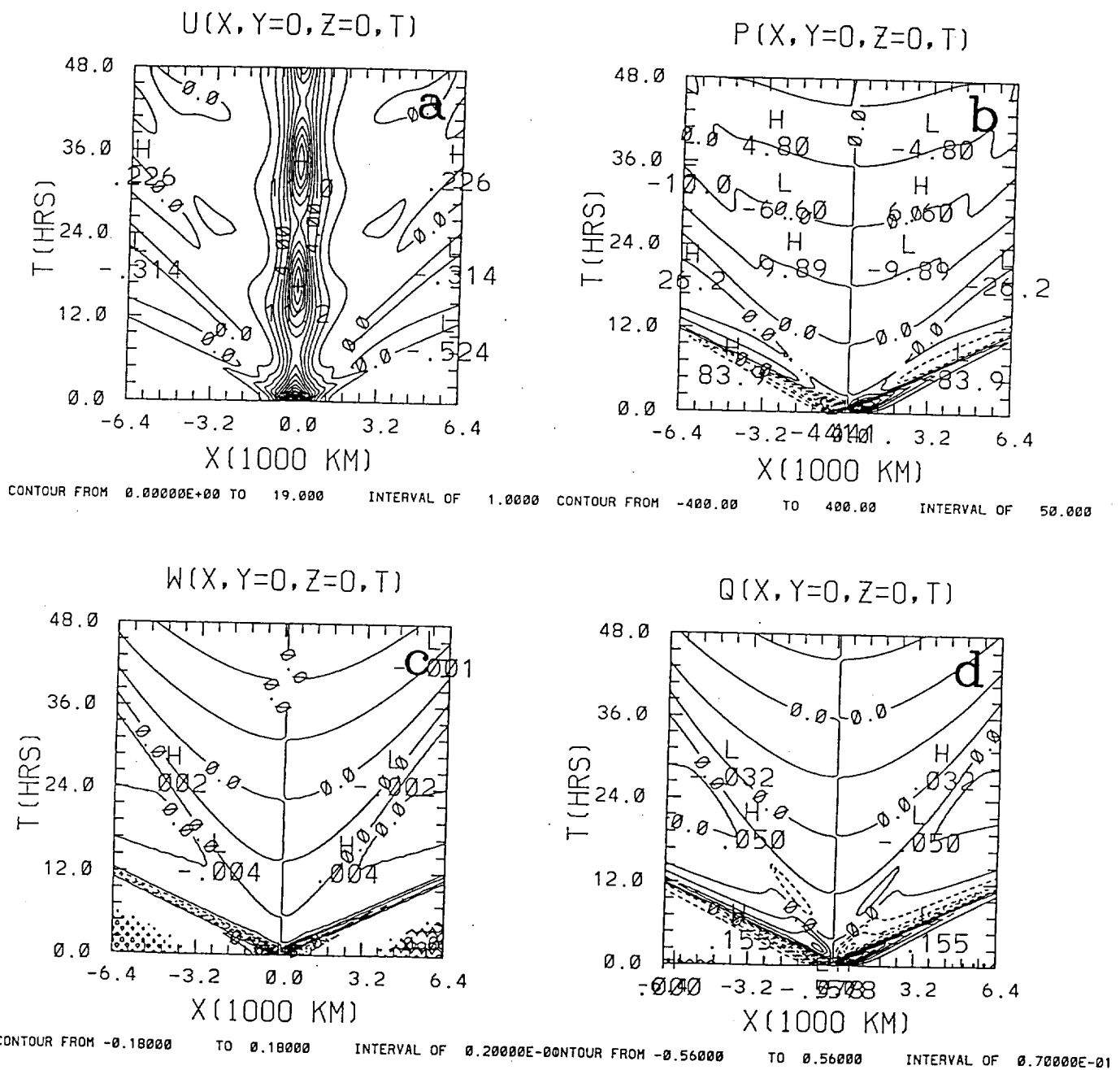


Fig. 47: Temporal evolution of a) u' , b) p' , c) w' , and d) θ' along the zonal direction ($y = 0$) during the first 48 h after the quiescent Boussinesq atmosphere is perturbed from geostrophic equilibrium.

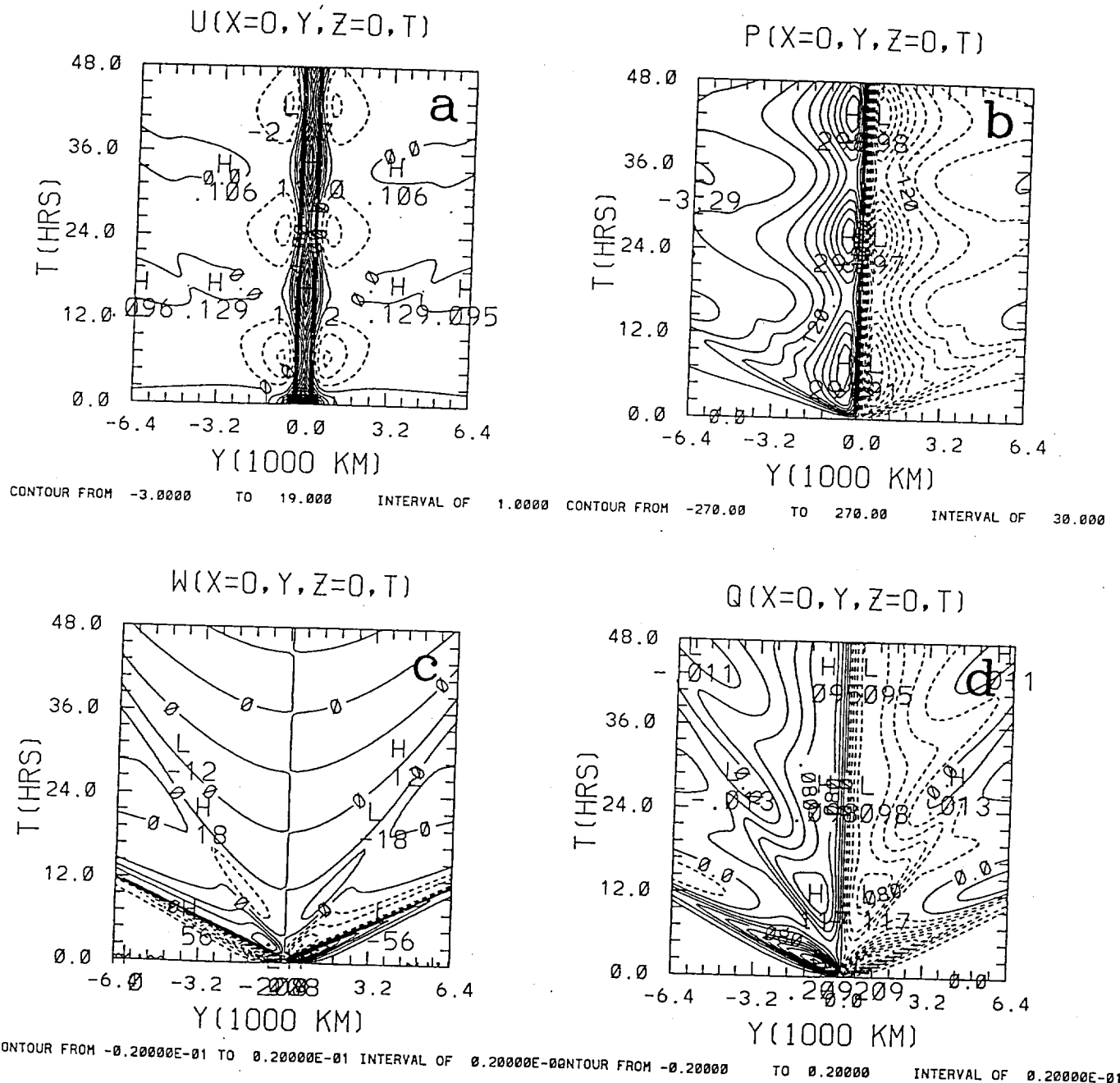


Fig. 48: Same as Fig. 47 except that the temporal evolution in the meridional direction ($x = 0$) is shown.

propagates a distance of $|x| \sim 1600$ km in the first 3 h, therefore implying a zonal propagation speed of $c_{px} \sim 148 \text{ ms}^{-1}$. The second and third modes appear to originate at $t \sim 1.2$ h. The second mode propagates a distance of $|x| \sim 3200$ km in approximately 4.8 h, implying $c_{px} \sim 185 \text{ ms}^{-1}$, while the third mode takes roughly 10.8 h to propagate the same distance, whose zonal phase speed is therefore $c_{px} \sim 82.3 \text{ ms}^{-1}$. Fig. 47c shows that most of the transient zonal IGW activity associated with w' is essentially dispersed during the first 12 h. Detailed analysis indicates that there are two primary IGW modes embedded within the positive (negative) perturbation potential temperature modes east (west) of the origin (not shown). The first mode propagates a distance of $|x| \sim 3200$ km in approximately 6 h, while a slower propagating mode takes ~ 11 h to travel the same distance. This yields estimates of $c_{px} \sim 148 \text{ ms}^{-1}$ and 80.8 ms^{-1} , respectively for these two modes. Fig. 47d also shows that the transient zonal IGW activity associated with θ' is also dispersed during the first 12 h.

Fig. 48 indicates that significant meridional IGW activity is excited during the first 12 h for all perturbation fields except the zonal wind perturbation u' , which tends to exhibit oscillation about its final equilibrium value (Fig. 48a). Fig. 48b indicates that for $t \leq 12$ h, the response in p' is associated with transient IGWs, while for $t > 12$ h, a high-low couplet in p' which supports the zonal wind anomaly also oscillates about its equilibrium value. Although significant IGW radiation is apparent in w' for $t \leq 12$ h, note that weaker amplitude modes continue to be excited for $t > 12$ h, with two modes excited at $t \sim 9$ h taking approximately 27 h to propagate 6400 km (Fig. 48c). Therefore the phase speed associated with these modes is estimated to be $c_{py} \sim 49.38 \text{ ms}^{-1}$. Fig. 48d also indicates that although the majority of significant transient meridional IGW activity in θ' is dispersed for $t \leq 12$ h, slower propagating modes continue to be excited for times greater than this, due to the slow dispersion of longer Fourier modes comprising the ageostrophic initial state.

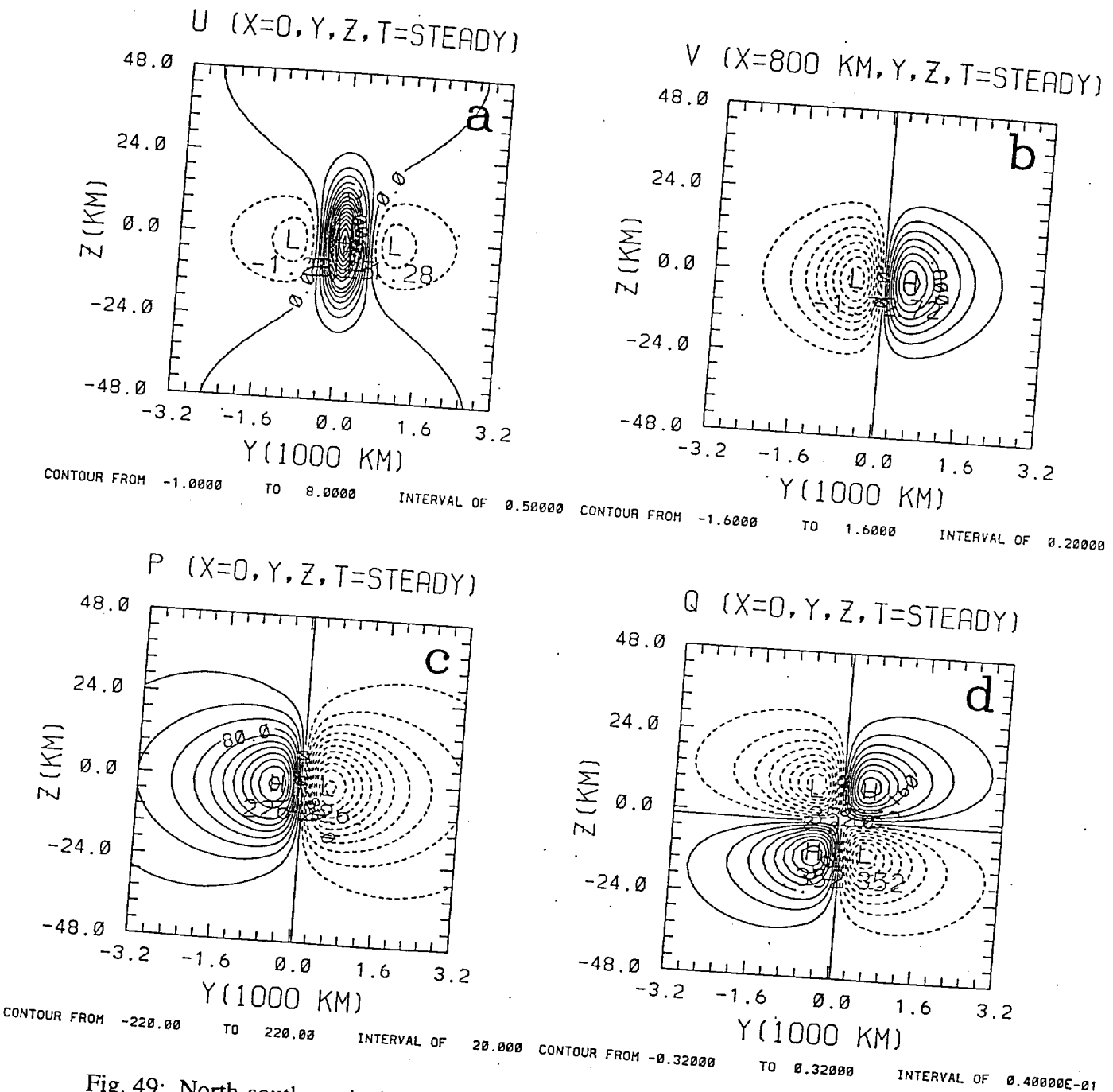


Fig. 49: North-south vertical cross sections of a) u' , b) v' at 800 km east of the jet core in the exit region, c) p' , and d) θ' defining the linear, steady-state response to the impulsive addition of localized ageostrophic momentum to a continuously stratified Boussinesq atmosphere. With the addition of a uniform zonal flow, the physical mechanisms of linearized geostrophic vorticity advection, $-\mathbf{U} \cdot \nabla \zeta_g'$, and horizontal temperature advection, $-\mathbf{U} \cdot \nabla \theta'$ are established.

Figure 49 shows the north-south vertical cross sections of u' , v' , p' , and θ' associated with the steady-state part of the total solution predicted by the linear theory (last term on the r.h.s. of Eq. (18)) due to the impulsive addition of localized ageostrophic zonal momentum into a quiescent, vertically unbounded Boussinesq atmosphere. This asymptotic balanced equilibrium on the x - y plane can be inferred from the earlier figures. This cross section clearly shows the existence of an isolated geostrophic jet (Fig. 49a) with meridional confluent (diffluent) flow in its entrance (exit) region (Fig. 49b), in hydrostatic balance with the thermodynamic fields (Figs. 49c and d). This steady-state therefore defines a localized three-dimensional *thermal wind balance* among the baroclinic perturbations, which is devoid of any steady-state ageostrophic circulations. With the addition of a non-zero basic state flow, the response is essentially the same as that outlined above, except that the transient IGWs are Doppler shifted by the basic state flow (not shown), and the geostrophically balanced zonal jet is advected downstream at the speed U , thereby establishing the physically important mechanisms of geostrophic vorticity advection, $-\mathbf{U} \cdot \nabla \zeta_g'$, and horizontal temperature advection, $-\mathbf{U} \cdot \nabla \theta'$, associated with the traveling PV couplet.

Therefore, although linear theory can correctly predict the *primary* (geostrophic) circulations commonly inferred to be associated with midlatitude jet streaks, the important *secondary* (ageostrophic) circulations responsible for *maintaining* the steady-state thermal wind balance are predicted to be trivially zero in the absence of prescribed forcing. This deficiency of the linear model is addressed by investigating the dynamically important jet streak mechanism of entrance (exit) region acceleration (deceleration) in the next section.

3. Linear Theory for the Forced Problem

In this section we formulate a theoretical model of an *independently propagating* zonal wind anomaly in a uniform, continuously stratified basic state zonal flow. The zonal propagation model is formulated by including a prescribed external momentum forcing term

in the linearized zonal momentum equation, Eq. (1). Here we shall restrict our investigation to the following type of imposed momentum forcing:

$$F_x(r,t) = U^* \frac{\partial}{\partial x} [u_{j0} \{ \frac{(x - c t)^2}{a^2} + \frac{y^2}{b^2} + 1 \}^{-3/2}] e^{-z^2/d_{jet}^2}. \quad (33)$$

Equation (33) represents, in a highly idealized way, *the nonlinear inertial-advection entrance (exit) region acceleration (deceleration) which the basic state barotropic flow experiences as it passes through the slower moving ($c < U$) isotach maximum.* In Eq. (33), u_{j0} is the magnitude of the zonal wind anomaly, a , b , and d_{jet} are the zonal and meridional half-widths and vertical e -folding depth, respectively, and c is the independent propagation speed. The relative velocity of the basic state flow as seen by a Galilean observer in a frame of reference translating at the speed c is $U^* = U - c$. Note that for mathematical convenience we have assumed uniform propagation in the zonal direction.

The governing equations appropriate to this forced adjustment problem are given by (1)-(5) with $F_y(r,t) = Q(r,t) = 0$. In order to make this linear problem mathematically tractable, we introduce the Galilean transformation

$$\xi = x - c t, \quad y' = y, z' = z, \quad t' = t. \quad (34)$$

Note that in this frame of reference that the imposed momentum forcing is stationary.

After the transformation, the potential vorticity and wave field equations may be written collectively as:

$$L_\xi \phi'(\xi, y, z, t) = G_\xi(q', F_\xi), \quad (35)$$

where

$$L_\xi = \left\{ \begin{array}{l} \frac{\partial}{\partial t} + (U - c) \frac{\partial}{\partial \xi} + V \frac{\partial}{\partial y}, \text{ if } \phi' = q' \\ [\{ \frac{\partial}{\partial t} + (U - c) \frac{\partial}{\partial \xi} + V \frac{\partial}{\partial y} \}^2 + f^2] \frac{\partial^2}{\partial z^2} + N^2 \nabla_\xi^2, \text{ if } \phi' = (\mathbf{u}', p', \text{ or } \theta') \end{array} \right\},$$

(36)

and

$$G_\xi(q', F_\xi) = \left\{ \begin{array}{l} -\frac{\partial F_\xi(r_\xi, t)}{\partial y}, \text{ if } \phi' = q' \\ -N^2 \frac{\partial q'(r_\xi, t)}{\partial y} + \frac{\partial^2}{\partial z^2} \left[\left\{ \frac{\partial}{\partial t} + (U - c) \frac{\partial}{\partial \xi} + V \frac{\partial}{\partial y} \right\} F_\xi(r_\xi, t) \right], \text{ if } \phi' = u' \\ + N^2 \frac{\partial q'(r_\xi, t)}{\partial \xi} - f \frac{\partial^2 F_\xi(r_\xi, t)}{\partial z^2}, \text{ if } \phi' = v' \\ - \frac{\partial}{\partial z} \left[\left\{ \frac{\partial}{\partial t} + (U - c) \frac{\partial}{\partial \xi} + V \frac{\partial}{\partial y} \right\} \frac{\partial F_\xi(r_\xi, t)}{\partial \xi} - f \frac{\partial F_\xi(r_\xi, t)}{\partial y} \right], \text{ if } \phi' = w' \\ \rho_0 N^2 \left[f q'(r_\xi, t) + \frac{\partial F_\xi(r_\xi, t)}{\partial \xi} \right], \text{ if } \phi' = p' \\ \theta_0 N^2 \frac{\partial}{\partial z} \left[f q'(r_\xi, t) + \frac{\partial F_\xi(r_\xi, t)}{\partial \xi} \right], \text{ if } \phi' = \theta' \end{array} \right\}, \quad (37)$$

where $r_\xi = (\xi, y, z)$. Assuming that the particular form of applied momentum forcing is known, note that similar to the linear initial value problem of the preceding section, a mathematically closed system for the forced geostrophic adjustment problem consists of the potential vorticity equation and any one of the linearized wave equations, both of which are written collectively here as Eq. (35). This system also requires the specification of the initial conditions ϕ'_i , $\partial\phi'_i/\partial t$, and q'_i for a unique solution. Although the 'vorticity' of the prescribed momentum forcing (Zhu and Holton, 1987) plays the dominant role as the driving mechanism for the *total* zonal (u') and meridional (v') winds, a partitioning into geostrophic and ageostrophic components ($u' = u'_g + u'_a$, $v' = v'_g + v'_a$) shows that the zonal and meridional gradients of the quantity F_δ/f associated with the 'divergence' of the momentum forcing (Zhu and Holton, 1987) play a dominate role in determining the evolution of the *geostrophic* wind perturbations. Details can be found in Weglarz (1994).

The general solution to the perturbation potential vorticity equation is given by:

$$\hat{q}(\mathbf{k},t) = [\hat{q}_i(\mathbf{k}) + \frac{1}{\Omega} \hat{F}_\xi(\mathbf{k},t)] e^{-i\Omega t} - \frac{1}{\Omega} \hat{F}_\xi(\mathbf{k},t), \quad (38)$$

where $\Omega = k(U-c) + IV$ is the intrinsic wave frequency. The first term on the r.h.s. of Eq. (38) shows that not only does any *pre-existing* PV anomaly get advected downstream at the relative velocity $U-c$, but that an additional *PV anomaly generated by the meridional gradient of the vorticity associated with the prescribed momentum forcing* is advected downstream as well. If this forcing is chosen such that its Fourier transform is given by

$$\hat{F}_\xi(\mathbf{k},t) = -\frac{\Omega}{l} \hat{q}_i(\mathbf{k}), \quad (39)$$

then any pre-existing initial PV anomaly is *destroyed*. The last term on the r.h.s. of Eq. (38) is the steady-state contribution to the perturbation potential vorticity field due to the momentum forcing which represents the independently propagating zonal wind anomaly. An observer in a non-translating reference frame will see this steady-state PV anomaly propagate downstream through the basic state flow at the uniform speed c . The forced circulations associated with *this* anomaly will be those identified by this observer as those characteristic of the independently propagating zonal jet, and for a proper choice of prescribed forcing, will be representative of those found with midlatitude jet streaks in the real atmosphere.

The general solutions to the Fourier transformed wave equations may be written as:

$$\hat{\phi}(\mathbf{k},t) = A_\phi(\mathbf{k}) e^{+i\omega_+ t} + B_\phi(\mathbf{k}) e^{-i\omega_+ t} + C_\phi(\mathbf{k}) e^{-i\Omega t} + D_\phi(\mathbf{k}), \quad (40)$$

where

$$C_\phi(\mathbf{k}) = \begin{pmatrix} -i l^2 N^2 \\ -i k_1 l N^2 \\ 0 \\ -\rho_0 l f N^2 \\ -\frac{\theta_0 i m l f N^2}{g} \end{pmatrix} \frac{\hat{F}_\xi(\mathbf{k},t)}{\Omega (N^2 \kappa^2 + m^2 f^2)}, \text{ if } \phi' = \begin{pmatrix} u' \\ v' \\ w' \\ p' \\ \theta' \end{pmatrix}, \quad (41)$$

and

$$D_\phi(\mathbf{k}) = \begin{pmatrix} i(m^2\Omega^2 - l^2N^2) \\ (iklN^2 - m^2\Omega f) \\ \Omega m(lf - ik\Omega) \\ \rho_0 N^2(lf - ik\Omega) \\ -\frac{im\theta_0 N^2(ik\Omega - lf)}{g} \end{pmatrix} \frac{\hat{F}_\xi(\mathbf{k}, t)}{\Omega(N^2\kappa^2 + m^2\{f^2 - \Omega^2\})}, \text{ if } \phi' = \begin{pmatrix} u' \\ v' \\ w' \\ p' \\ \theta' \end{pmatrix}. \quad (42)$$

The dependent initial conditions (ϕ'_i , $\partial\phi'_i/\partial t$) which determine the remaining unknown coefficients $A_\phi(\mathbf{k})$ and $B_\phi(\mathbf{k})$ are taken to be:

$$\hat{u}_i(\mathbf{k}) = \hat{v}_i(\mathbf{k}) = \hat{w}_i(\mathbf{k}) = \hat{p}_i(\mathbf{k}) = \hat{\theta}_i(\mathbf{k}) = 0, \quad (43)$$

$$\frac{\partial \hat{v}_i}{\partial t}(\mathbf{k}) = \frac{\partial \hat{p}_i}{\partial t}(\mathbf{k}) = \frac{\partial \hat{\theta}_i}{\partial t}(\mathbf{k}) = 0, \quad (44)$$

$$\frac{\partial \hat{u}_i}{\partial t}(\mathbf{k}) = \hat{F}_\xi(\mathbf{k}), \quad \frac{\partial \hat{w}_i}{\partial t}(\mathbf{k}) = -\frac{k}{m}\hat{F}_\xi(\mathbf{k}), \quad (45)$$

which yields the coefficients

$$A_\phi(\mathbf{k}) = -\frac{C_\phi(\mathbf{k})}{2} - \frac{D_\phi(\mathbf{k})}{2} \left(1 + \frac{m\Omega}{\sqrt{N^2\kappa^2 + f^2m^2}} \right) - \lambda \frac{i m \hat{F}_\xi}{2\sqrt{N^2\kappa^2 + f^2m^2}}, \quad (46)$$

$$B_\phi(\mathbf{k}) = \frac{[(\sqrt{N^2\kappa^2 + f^2m^2} - m\Omega) A_\phi(\mathbf{k}) - m\Omega C_\phi(\mathbf{k}) + i m \lambda \hat{F}_\xi(\mathbf{k})]}{(\sqrt{N^2\kappa^2 + f^2m^2} + m\Omega)}, \quad (47)$$

$$A_w(\mathbf{k}) = -\frac{m(lf - ik\Omega)}{2[N^2\kappa^2 + m^2(f^2 - \Omega^2)]} \left(1 + \frac{m\Omega}{\sqrt{N^2\kappa^2 + f^2m^2}} \right) \hat{F}_\xi + \frac{ik\hat{F}_\xi}{2\sqrt{N^2\kappa^2 + f^2m^2}}, \quad (48)$$

$$B_w(\mathbf{k}) = \frac{[(\sqrt{N^2\kappa^2 + f^2m^2} - m\Omega) A_w(\mathbf{k}) - ik\hat{F}_\xi(\mathbf{k})]}{(\sqrt{N^2\kappa^2 + f^2m^2} + m\Omega)}, \quad (49)$$

for $\phi' = u', v', p', \theta'$, and where $\lambda = 1$ when $\phi' = u'$, otherwise $\lambda = 0$. Note also that for this particular choice of initial conditions, $q'_i = 0$. The solution in physical space is obtained through inverse FFT of Eq. (12).

Figures 50-58 show the horizontal and vertical cross sections of the forced baroclinic response as seen by a Galilean observer moving at the zonal speed $c = 10 \text{ ms}^{-1}$ in a vertically unbounded, continuously stratified Boussinesq atmosphere. The flow parameters characterizing the stably stratified basic state flow are taken to be $N = 0.01 \text{ s}^{-1}$, $f = 10^{-4} \text{ s}^{-1}$, $\rho_0 = 1 \text{ kg m}^{-3}$, $\theta_0 = 273 \text{ K}$, and $\mathbf{U} = (20, 0) \text{ ms}^{-1}$. The magnitude of the localized zonal wind anomaly is taken to be $u_{j0} = 30 \text{ ms}^{-1}$, its zonal and meridional half-widths are taken to be $a = b = 500 \text{ km}$, and its *e*-folding half-depth $d = 12.5 \text{ km}$. Note that $|u_{j0}| > |U|$, but that $|c| < |U|$, characteristics representative of midlatitude jet streaks (Bluestein, 1993a, b).

Figure 50 shows the horizontal cross sections at $z = 0$ of total u' at $t = 3, 12, 72$, and 144 h . During the early stages of forced adjustment at $t = 3 \text{ h}$ (Fig. 50a), the zonal wind perturbation at the level of maximum forcing acquires a horizontal structure similar to that of the forcing itself due to the initial condition imposed by the l.h.s. of Eq. (45), which forces acceleration (deceleration) in the jet entrance (exit) region. At this time, regions of positive (negative) zonal winds $u' > 0$ ($u' < 0$) exist for $x < 0, |y| \leq 800 \text{ km}$ ($x > 0, |y| \leq 800 \text{ km}$). At $t = 3 \text{ h}$ the magnitude is approximately twice the value it had two hours prior. By $t = 12 \text{ h}$, compensating zonal counter currents have become established north and south of the positive (negative) zonal wind anomaly in the entrance (exit) region of the prescribed momentum forcing (Fig. 50b). Since the magnitudes of the localized zonal jet (counter current) in the forcing entrance (exit) region continue to increase from 6 to 12 h, this indicates that the response in the zonal wind perturbation is primarily dominated by the structure of the prescribed forcing during the first 12 h of forced adjustment.

By $t = 72 \text{ h}$, it is clear that the wind field associated with the PV anomaly generated by the momentum forcing consisting of a zonal jet (zonal counter current, $u' < 0$) in the

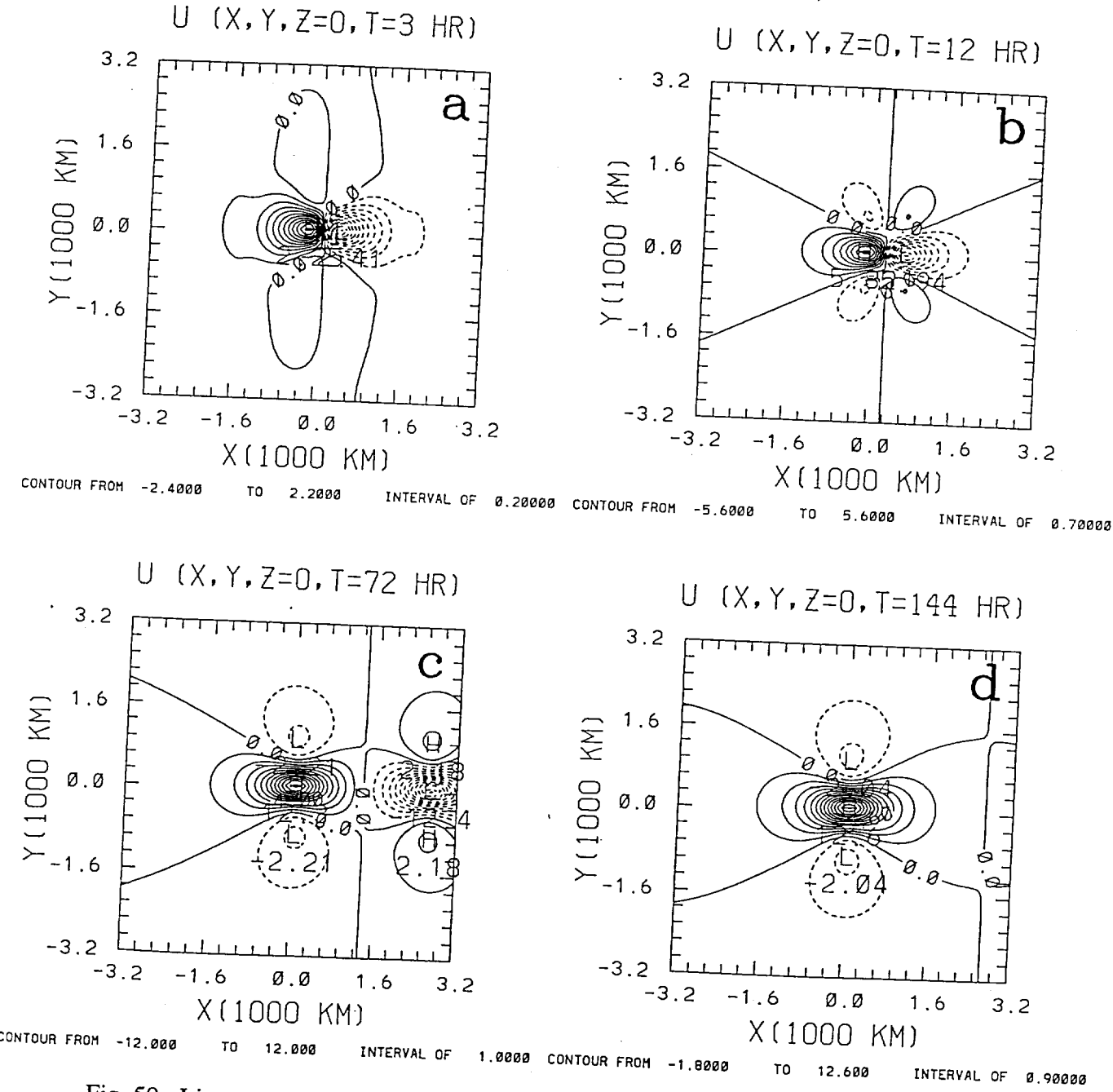


Fig. 50: Linear response of u' at $z = 0$ at $t =$ a) 3 h, b) 12 h, c) 72 h, and d) 144 h for a Galilean observer traveling at the speed $c = 10 \text{ ms}^{-1}$ due to the imposed momentum forcing given by Eq. (33), which represents entrance (exit) region acceleration (deceleration) of the basic state flow as it passes through the slower moving ($c < U$) isotach maximum. $U = 20 \text{ ms}^{-1}$, $u_{j0} = 30 \text{ ms}^{-1}$. Other flow parameters are the same as in Fig. 1.

forcing's entrance (exit) region has strengthened considerably, and is being advected downstream at the relative flow speed $U-c$ (Fig. 50c). At $t = 144$ h, the zonal counter current continues to be advected downstream at later times leaving, within the vicinity of the forcing region, a well-defined, localized zonal jet of $\sim 12.6 \text{ ms}^{-1}$ with compensating zonal counter currents of $\sim 2 \text{ ms}^{-1}$ whose centers are located approximately $|y| \sim 800 \text{ km}$ north and south of the main jet core (Fig. 50d).

Figure 51 shows the vertical cross sections of total u' through $y = 0$ at $t = 3, 12, 72$, and 144 h. Early during the adjustment at $t = 3$ h, although there is evidence of slight IGW propagation above and below $z = 0$ (Fig. 51a), most of the response is confined to within a distance $\sim O(2d_{jet})$. By $t = 12$ h, well-defined, isolated couplets of positive (negative) zonal wind exist west (east) of the forcing center (Fig. 51b). At later times, the response is dominated by the PV anomaly generated by the meridional vorticity gradient of the momentum forcing, which produces a zonal counter current which is advected downstream (Fig. 51c), eventually establishing an isolated zonal wind anomaly of $\sim 11.4 \text{ ms}^{-1}$ within the vicinity of the forcing region (Fig. 51d).

The horizontal structure of v' on the $z = 0$ plane at $t = 3$ h shows northerly (southerly) winds in the forcing entrance (exit) region (Fig. 52a), which are associated with the Coriolis force acting on the positive (negative) zonal wind perturbations which exist in these regions. The magnitude of v' slowly continues to increase from $t = 3$ to 12 h. At $t = 12$ h, v' at the level of maximum applied forcing is dominated primarily by a two-cell pattern with northerly (southerly) directed meridional winds north (south) of $y = 0$ (Fig. 52b). This structure can be explained by the zonal gradient of the perturbation pressure (Fig. 53b) dominating the response in v' at this time. A couplet of diffluent (confluent) flow which is advected downstream from the forcing region for $t \geq 48$ h associated with the meridional wind field is becoming established in the entrance (exit) region of the zonal counter jet (Fig. 52c), leaving in the vicinity of the origin by $t = 144$ h, confluent (diffluent) flow in the zonal jet entrance (exit) region (Fig. 52d).

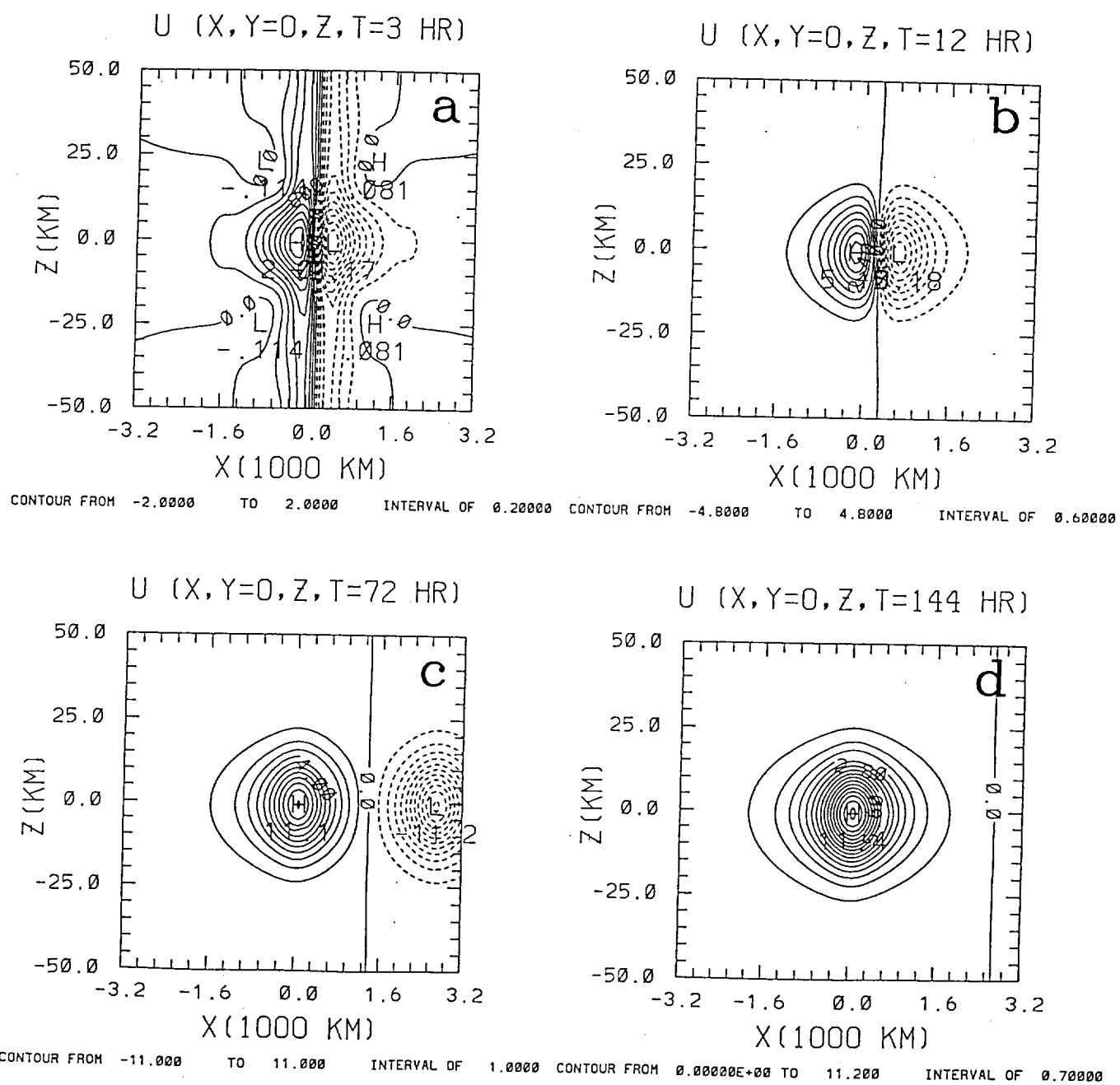


Fig. 51: Same as Fig. 41 except for the forced response at $t =$ a) 3 h, b) 12 h, c) 72 h, and d) 144 h.

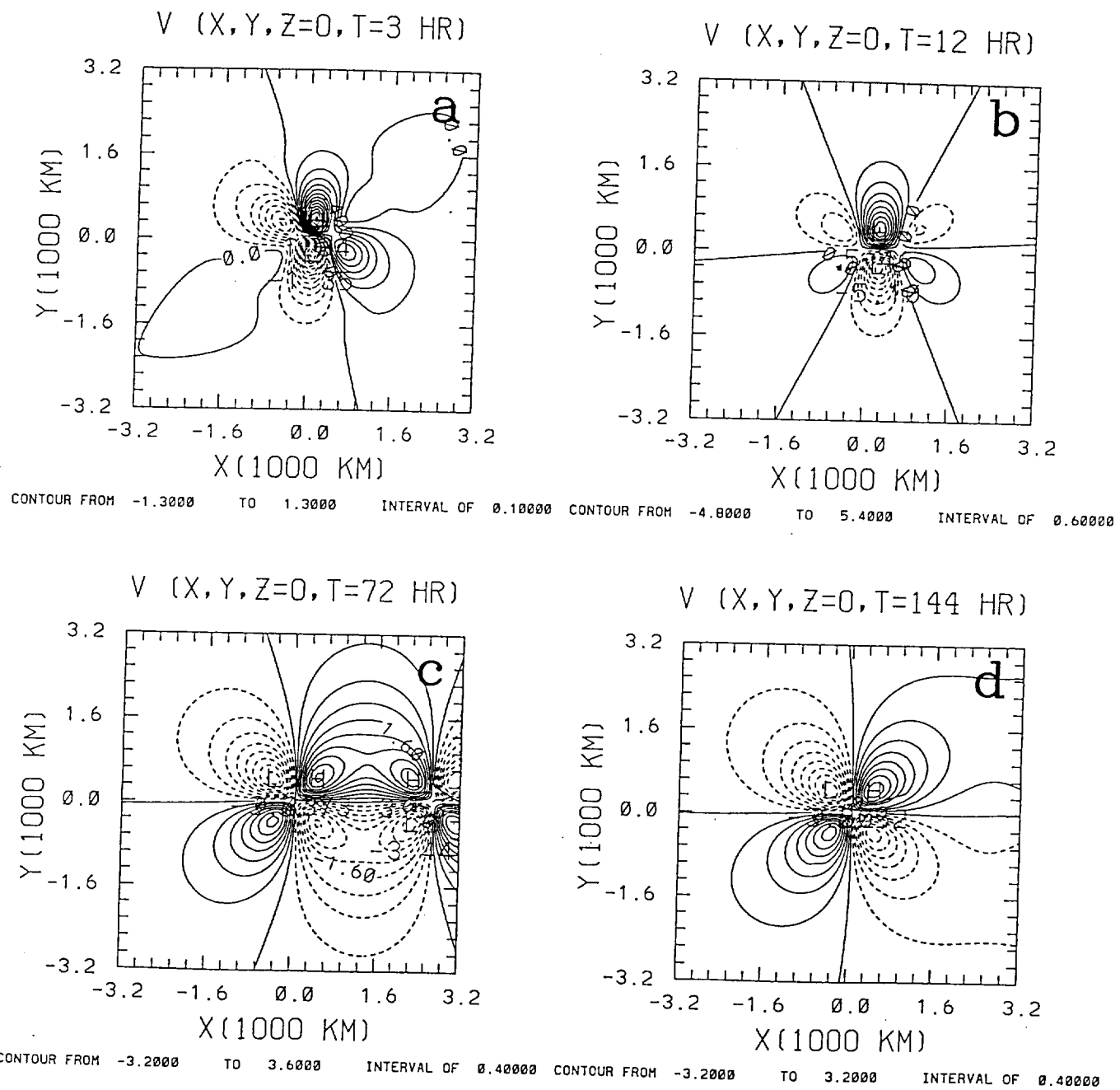


Fig. 52: Same as Fig. 50 except that the meridional wind perturbation v' is shown.

Figure 53 shows the north-south vertical cross sections of total v' through $x = 0$ during the early stages of forced adjustment (Figs. 53a and b) and 800 km west of the forcing center in the jet exit region during the later stages once the PV anomaly has been generated and is traveling downstream (Figs. 53c and d). These cross sections show that the meridional component of the jet exit region flow is confined vertically to a layer $\sim O(2d_{jet})$, and is well established by the time the zonal wind anomaly has propagated to the center of the forcing region at $t = 144$ h (Fig. 51d).

Figure 54 shows the forced vertical velocity field on the $z = -3$ km plane at $t = 1, 3, 6$, and 12 h. At $t = 1$ h, the response is dominated by the zonal gradient of the 'vorticity' associated with the prescribed momentum forcing through the initial condition imposed by the r.h.s. of Eq. (45), yielding an isolated region of subsidence at the center of the forcing region (Fig. 54a). By $t = 3$ h, at least four centers of outwardly propagating IGWs both east and west of $\mathbf{r} = (0,0,0)$ can be identified (Fig. 54b). Two cells of rising motion are located at approximately $|x| = 1920$ km. Assuming these modes originated at $t = 0$, their zonal phase speed is estimated to be $c_{px} \sim 177.8 \text{ ms}^{-1}$. The next pair of IGWs closest to the origin are associated with sinking motion, and have centers located at approximately $|x| = 1280$ km, yielding a zonal propagation phase speed of $c_{px} = 1280 \text{ km}/10800\text{s} \sim 118.5 \text{ ms}^{-1}$. Isolated cells of rising motion are located adjacent to those centers of downward motion which are located at $|x| = 800$ km, yielding $c_{px} = 800 \text{ km}/10800\text{s} \sim 74 \text{ ms}^{-1}$. Finally, cells of sinking motion straddle the origin at $|x| = 320$ km. The zonal phase speed associated with these modes is therefore estimated to be $\sim 29.6 \text{ ms}^{-1}$. The vertical wavelength associated with each of these baroclinic modes can be estimated from $c_{px} \sim N/m \sim NL_z/2\pi$, yielding values of 111.7 km, 74.5 km, 46.5 km, and 18.6 km, respectively.

By $t = 6$ h, note that the centers of rising motion located at $|x| \sim 1920$ km at $t = 3$ h have propagated beyond $|x| \sim 3200$ km, with the downstream propagating mode having traveled somewhat farther than the upstream propagating mode due to advection of the basic state flow (Fig. 54c). Note also that the centers of rising motion which had been

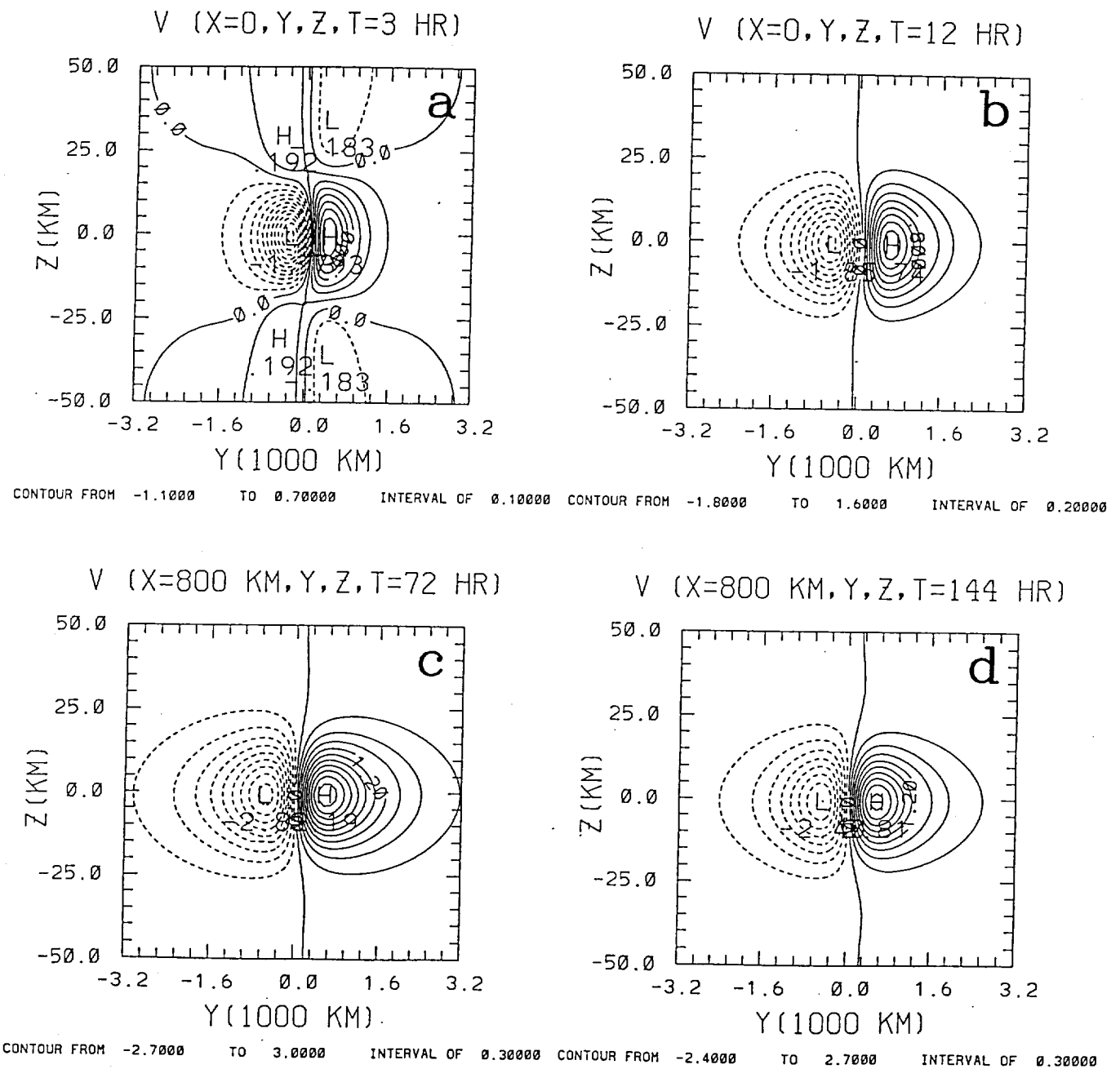
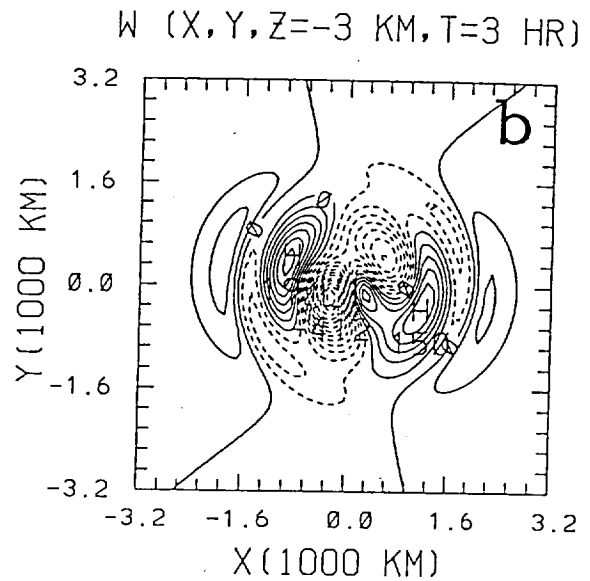
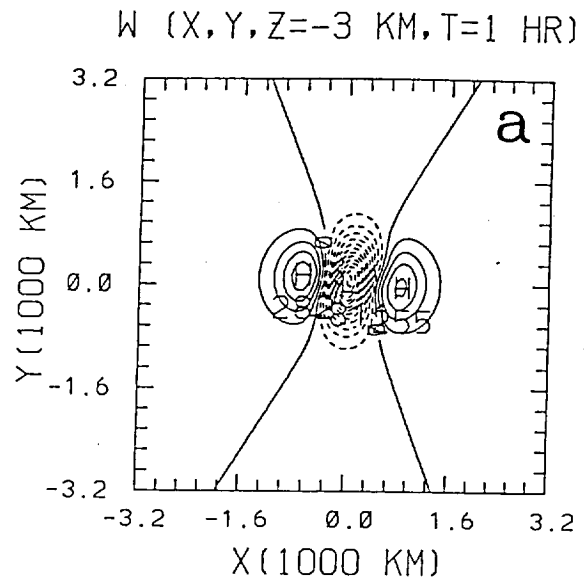
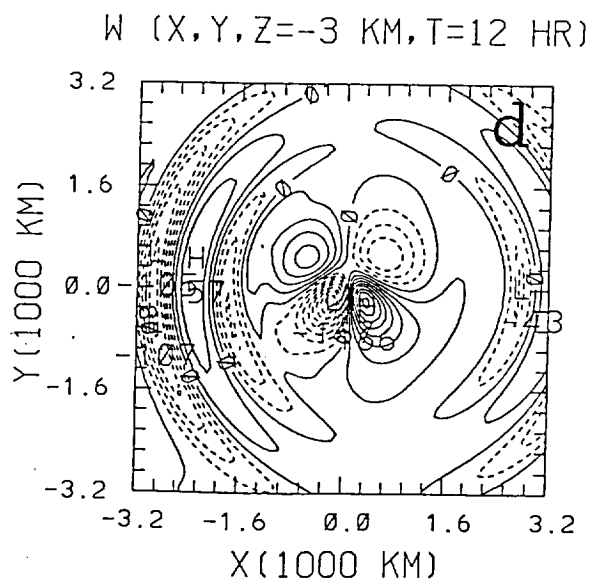
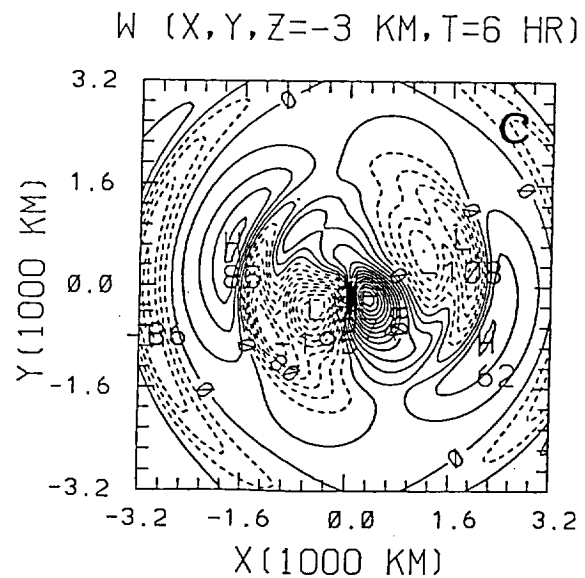


Fig. 53: Same as Fig. 51 except that the meridional wind perturbation v' is shown.



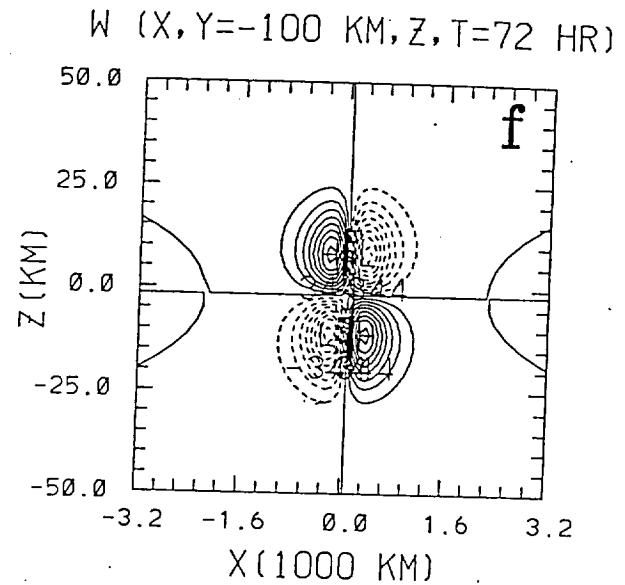
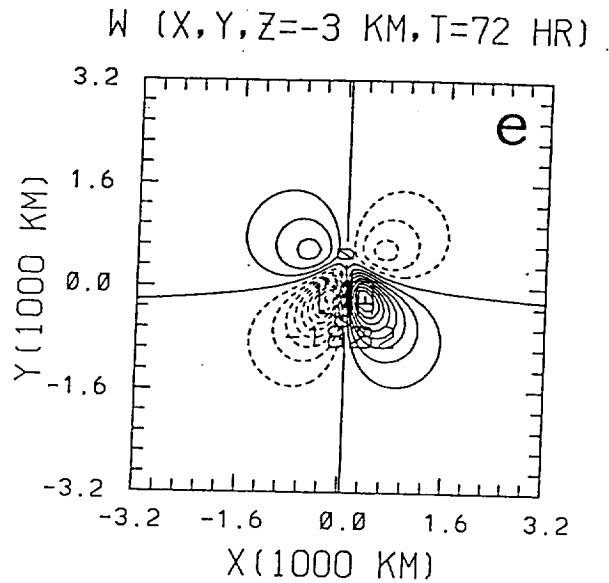
CONTOUR FROM -0.78000E-02 TO 0.24000E-02 INTERVAL OF 0.60000E-03



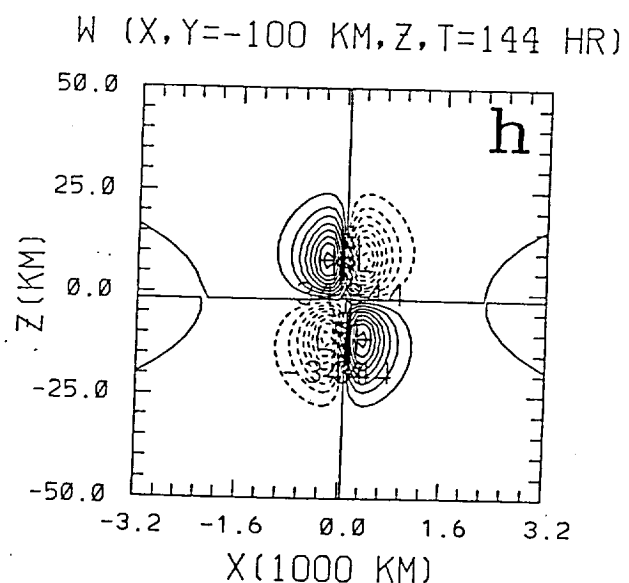
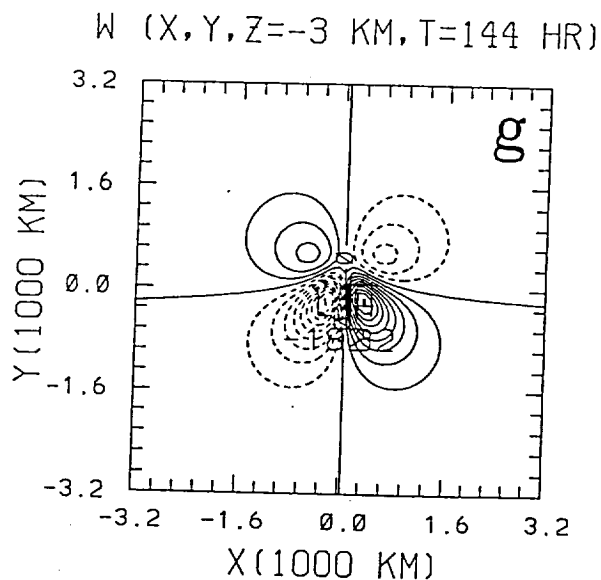
CONTOUR FROM -0.18000E-02 TO 0.26000E-02 INTERVAL OF 0.20000E-03

CONTOUR FROM -0.16000E-02 TO 0.16000E-02 INTERVAL OF 0.20000E-03

Fig. 54: Same as Fig. 42 except that the vertical velocity at $z = -3$ km for the forced response is shown. Note the development of the 'four-cell' pattern of vertical motion in the quadrants flanking the forcing center associated with the transfer of mass by the evolving ageostrophic winds from the cyclonic to the anticyclonic (anticyclonic to the cyclonic) side of the jet in the entrance (exit) region.



CONTOUR FROM -0.18000E-02 TO 0.18000E-02 INTERVAL OF 0.20000E-00 CONTOUR FROM -0.32000E-02 TO 0.32000E-02 INTERVAL OF 0.40000E-03



CONTOUR FROM -0.18000E-02 TO 0.18000E-02 INTERVAL OF 0.20000E-00 CONTOUR FROM -0.32000E-02 TO 0.32000E-02 INTERVAL OF 0.40000E-03

Fig. 54: (continued)

located at $|x| \sim 800$ km at $t = 3$ h have propagated to $|x| \sim 1920$ km. During the subsequent six hours, although transient IGWs still radially propagate from the origin, note that a well-defined 'four-cell' pattern of vertical motion is becoming established at the center of the external momentum forcing (Fig. 54d). At later times after the transient IGWs are dispersed far from the region disturbed from geostrophic equilibrium, a well-defined four-cell pattern of vertical motion exists in the vicinity of the forcing center (Figs. 54e and g). The vertical cross sections 100 km to the south of the forcing center at $t = 72$ (Fig. 54f) and 144 h (Fig. 54h) imply that vertical motion pattern above the level of maximum zonal wind ($z = 0$) has a similar horizontal structure as that below the jet core (not shown), except that the pattern of ascent and descent is simply reversed from that which exists at these times below the jet core. The development of this vertical velocity field is related to the transfer of mass by the meridional component of the ageostrophic wind perturbation v'^a from the cyclonic (anticyclonic) to the anticyclonic (cyclonic) side of the jet core in the entrance (exit) region (discussed below).

Figure 55 shows the horizontal cross sections of perturbation pressure p' at $z = 0$ at $t = 3, 12, 72$, and 144 h. The pressure perturbation at the level of maximum zonal winds at $t = 3$ h (Fig. 55a) is associated with the divergence produced by the alongstream gradient of the perturbation zonal wind couplet on the $z = 0$ plane. At this time, there are two oppositely propagating IGWs whose centers are located roughly at $|x| \sim 1920$ km east and west of the center of external forcing (Fig. 55a). The zonal propagation phase speed associated with these internal modes is therefore approximately $c_{px} \sim 177.8 \text{ ms}^{-1}$. These modes are relatively weak, being only ~ 0.25 mb in magnitude, or approximately one-fifth the magnitude of the pressure perturbation colocated with the center of applied forcing. Three hours later at $t = 6$ h (not shown), the mass (p' , θ') fields are still adjusting to the forced zonal winds. Six hours later at $t = 12$ h, the existence of a well-defined 'four-cell' pattern in the perturbation pressure field (Fig. 16b) is evident on the $z = 0$ plane at the level of maximum applied forcing. The transfer of mass from the cyclonic to the anticyclonic

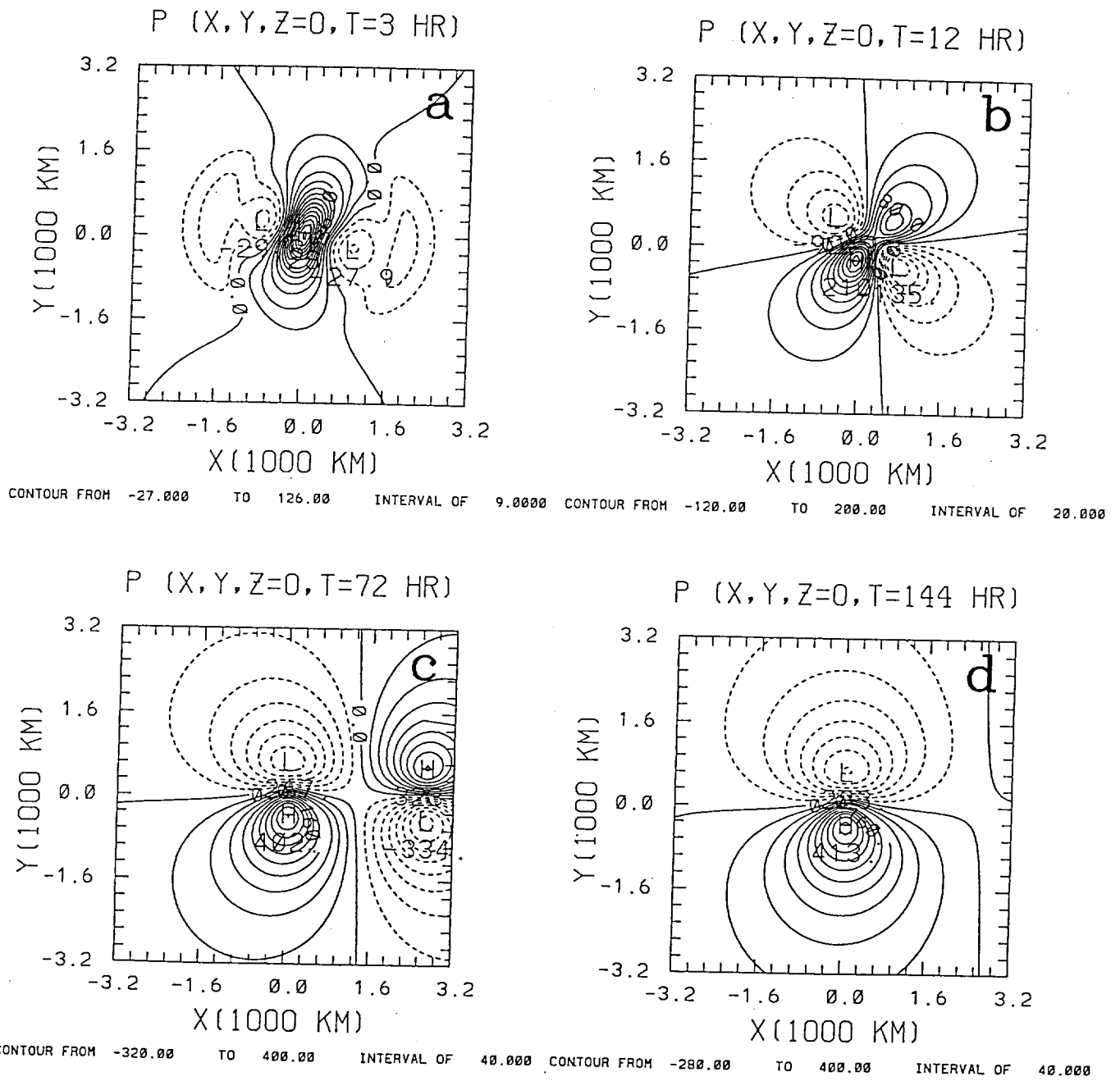


Fig. 55: Same as Fig. 50 except that the perturbation pressure p' at $z = 0$ at $t =$ a) 3 h, b) 12 h, c) 72 h, and d) 144 h is shown.

(anticyclonic to the cyclonic) side in the entrance (exit) region of the propagating jet streak effectively lowers (raises) the perturbation pressure in the northwest and southeast (southwest and northeast) quadrants flanking the jet core as the pressure field adjusts to support the positive (negative) zonal wind anomaly in the entrance (exit) region of the external momentum forcing (Fig. 50b).

At later times during the forced adjustment, a perturbation couplet of high (low) pressure north (south) of $y = 0$ exists in the jet exit region which is advected downstream at the relative velocity $U - c$ (Fig. 55c). This couplet in p' geostrophically supports the zonal counter current (Figs. 50c, 51c) generated by the vorticity of the external momentum forcing as it travels downstream. By $t = 144$ h, an isolated dipole couplet of p' exists in the vicinity of the forcing center which geostrophically supports the positive zonal wind anomaly in this region at this time (Fig. 55d).

Figure 56 shows the east-west (a) and north-south (b-d) vertical cross sections of p' at $t = 3, 12, 72$, and 144 h as the mass fields adjust to support the forced zonal wind perturbations in the entrance and exit regions of the prescribed momentum forcing. At $t = 3$ h, confluence towards the forcing center by the zonal wind perturbations induces a localized region of perturbation high pressure of ~ 1.3 mb at the origin, from which localized IGWs are propagating outward from the forcing center in the zonal direction (Fig. 56a). Fig. 56b shows that by $t = 12$ h, a well-defined couplet of perturbation high (low) pressure exists north (south) of $y = 0$ and 800 km to the west of the forcing center in the jet exit region as the mass field adjusts to the zonal counter current which exists there (Fig. 50b). After this dipole couplet in p' has been advected downstream at the relative velocity $U - c$, isolated cells of low (high) perturbation pressure exist north (south) of $y = 0$ at $t = 72$ h (Fig. 56c) which slowly continues to increase by $t = 144$ h (Fig. 56d) exist which geostrophically support the forced zonal (Figs. 50d, 51d) and meridional (Figs. 52d, 53d) wind perturbations u' and v' within the vicinity of the forcing center at this time.

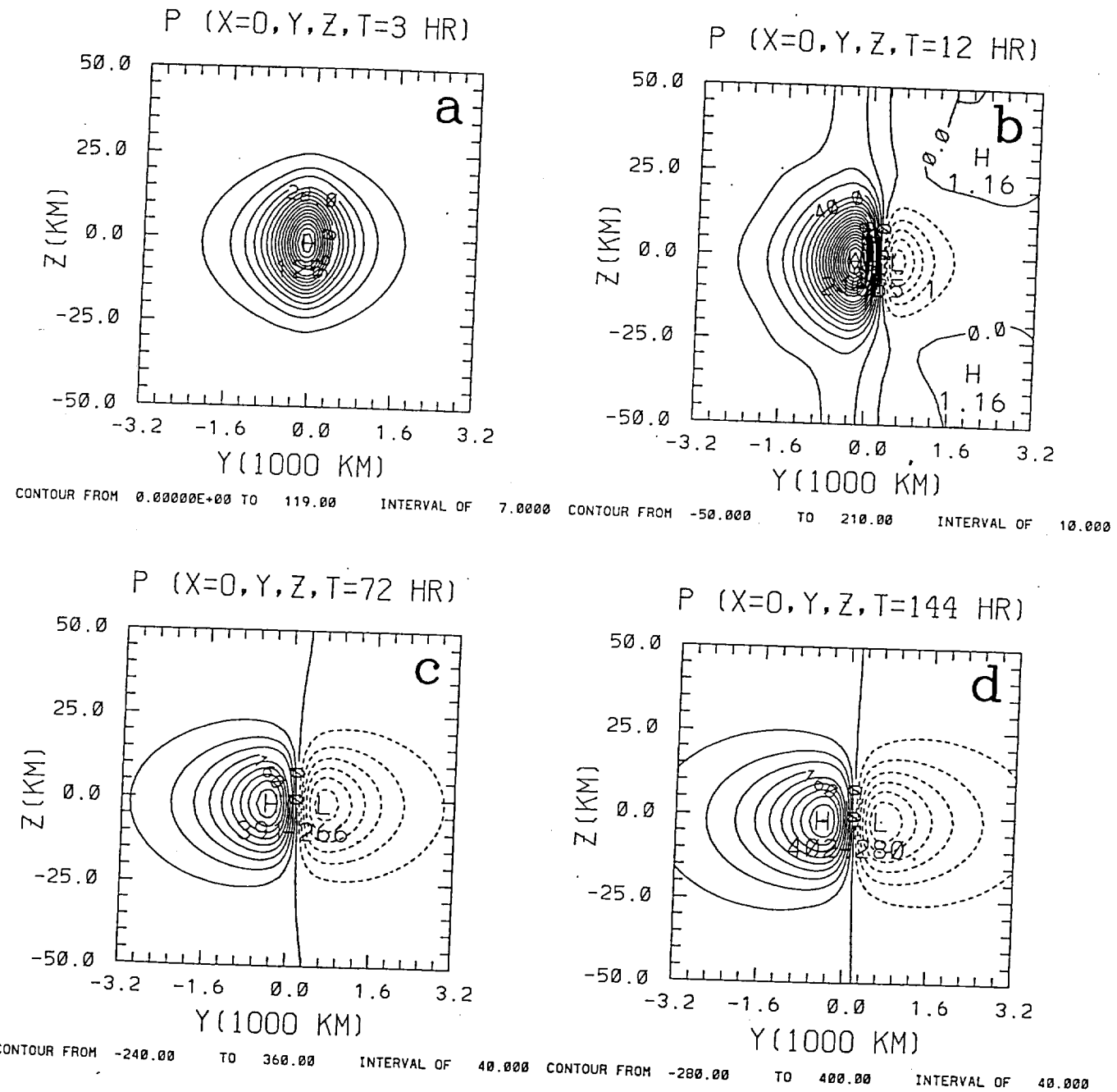


Fig. 56: North-south vertical cross sections of p' associated with the forced geostrophic adjustment at $t =$ a) 3 h, b) 12 h, c) 72 h, and d) 144 h.

Figure 57 shows the horizontal cross sections of perturbation potential temperature θ' 15 km below the forcing center at $t = 3, 12, 72$, and 144 h. At $t = 3$ h, an isolated region of warm air of ~ 0.26 K is colocated with the center of the momentum forcing, and is flanked by isolated regions of cold air to its immediate east and west. The warm region is produced adiabatically by the vertical motion induced by the convergence of the perturbation zonal winds towards the center of the forcing region (Figs. 50a, 51a). By $t = 12$ h (Fig. 57b), the horizontal structure in θ' is similar to p' (Fig. 55b), and shows that a 'four-cell' pattern of adiabatically warm (cold) air exists in the southwest and northeast (northwest and southeast) quadrants of the jet entrance and exit region. This pattern is associated with the transfer of mass from the cyclonic to the anticyclonic (anticyclonic to cyclonic) side of the jet entrance (exit) region, which effectively lowers (increases) the perturbation pressure, and hence induces a four-cell pattern of vertical motion which adiabatically drives the θ' field. Dipole couplets of warm (cold) air (Fig. 57c) located north (south) of $y = 0$, which form the externally forced thermodynamic jet exit region response can be seen to be advected downstream by the basic state relative flow at $t = 72$ h, leaving localized regions of cold (warm) air north (south) of the zonal jet by $t = 144$ h (Fig. 57d) whose centers are colocated with the isolated cells of perturbation low (high) perturbation pressure (Fig. 55d).

Figure 58 shows the east-west (a) and north-south (b-d) vertical cross sections of θ' at $t = 3, 12, 72$ and 144 h. Note that the isolated regions of perturbation cold (warm) air above (below) the $z = 0$ plane (Fig. 58a) are the hydrostatic response to the localized region of high p' centered at $z = 0$ (Fig. 56a) due to the convergence of the forced zonal wind perturbations. which confirm that the externally forced primary (i.e. geostrophic) jet streak circulations establish a localized thermal wind balance between the three-dimensional baroclinic perturbations. By $t = 12$ h (Fig. 58b), isolated couplets of warm (cold) air exist north (south) of $y = 0$ 800 km to the west of the forcing center in the jet exit region at all levels below the level of maximum zonal wind. Note that above $z = 0$, the potential

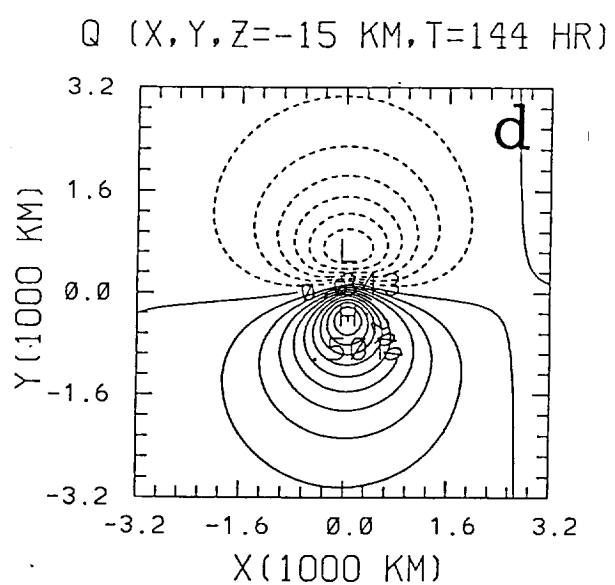
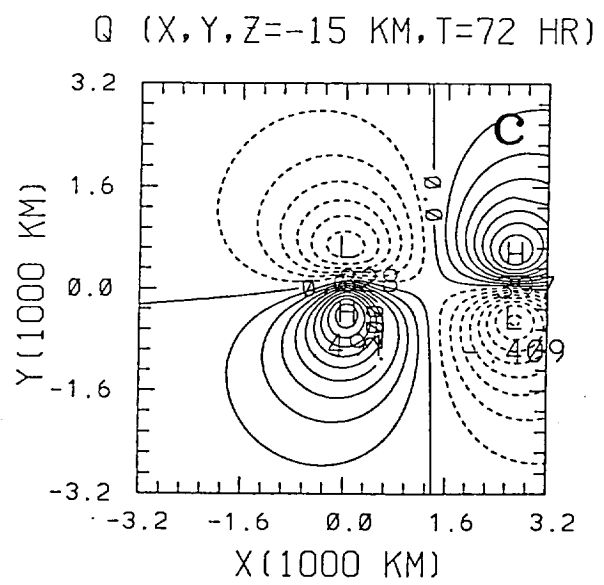
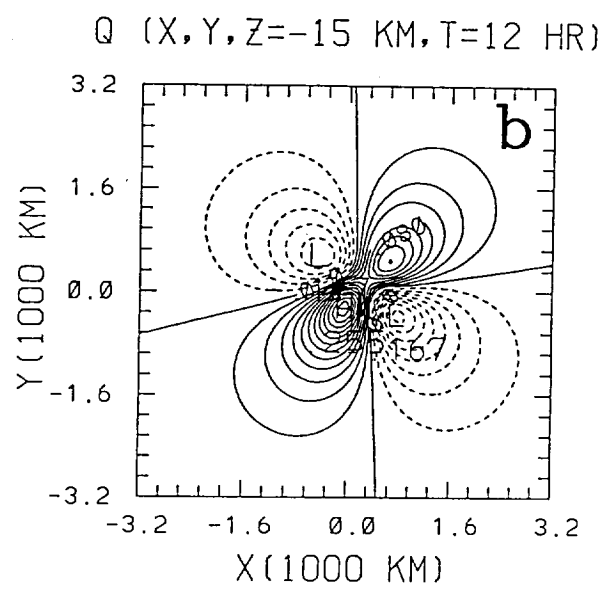
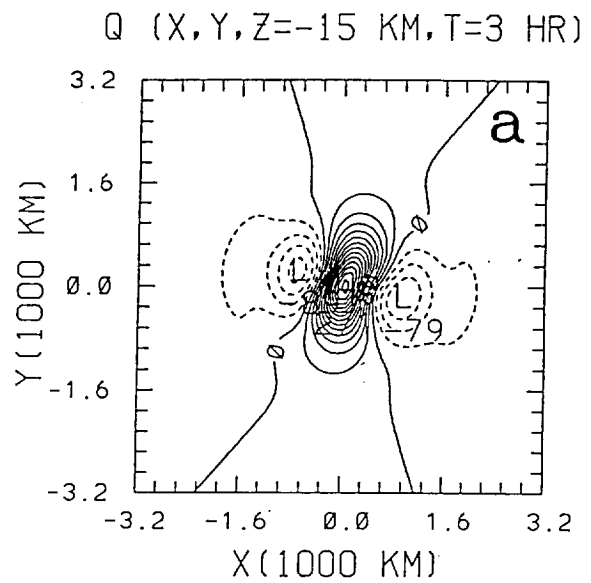


Fig. 57: Same as Fig. 55 except for θ' .

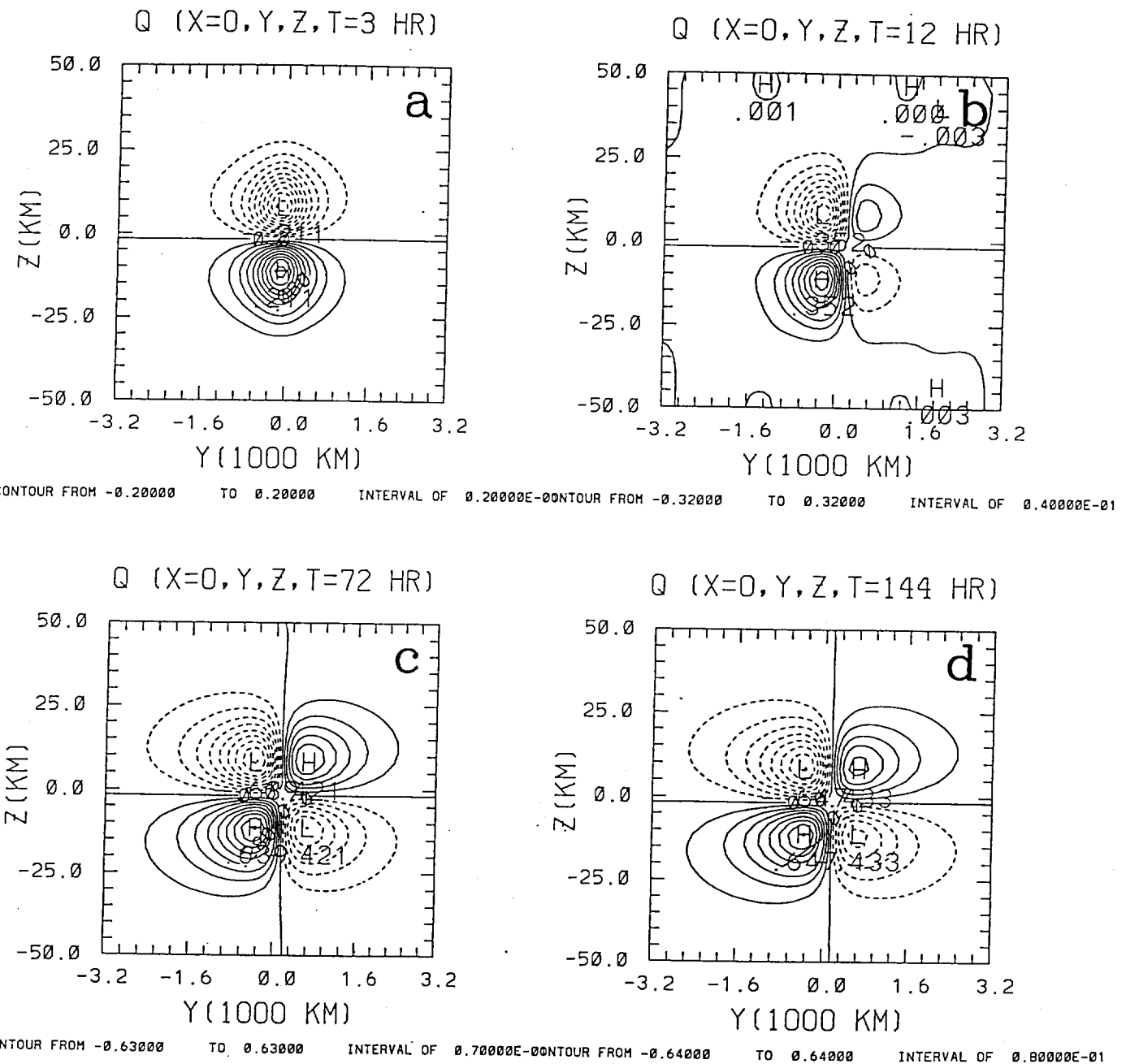


Fig. 58: Same as Fig. 56 except for θ' .

temperature perturbation is reversed from that which exists below $z = 0$ in order to satisfy the hydrostatic balance (Fig. 56b). By $t = 72$ h, a well-defined couplet of cold (warm) air north (south) of $y = 0$ at all levels below the forcing center has become established to hydrostatically balance the perturbation pressure p' (Fig. 56c) which geostrophically supports the externally forced zonal and meridional winds. This vertical structure in θ' remains essentially unchanged (Fig. 58d) once the primary jet streak circulations (Figs. 50d, 52d, and 54d) within the vicinity of the forcing center become established at $t = 144$ h.

Figure 59 shows the horizontal cross sections of u'_g at $t = 3, 12, 72$, and 144 h. This component of the forced zonal wind perturbation is defined by the evolving meridional gradient of the perturbation pressure field (Fig. 55) as the mass field adjusts to the externally forced zonal and meridional wind perturbations. The structure during the early stages of forced adjustment at $t = 3$ (Fig. 59a) and 12 h (Fig. 59b) shows remarkable similarity to the same components produced in a rotating homogeneous atmosphere (Weglarz, 1994). The development of a geostrophic zonal jet (counter current) in the entrance (exit) region of the imposed momentum forcing is associated with the development of a low-high (high-low) couplet in p' in these regions. By $t = 72$ h (Fig. 59c), note that the geostrophic counter current ($u'_g < 0$) is being advected downstream by the basic state flow at the relative velocity $U-c$. Eventually, by $t = 144$ h, an isolated geostrophic zonal jet of $\sim 12.8 \text{ ms}^{-1}$ has become established in the vicinity of the forcing center (Fig. 59d). This geostrophic zonal jet is flanked by isolated geostrophic zonal counter currents, whose centers are located approximately 800 km north and south of $y = 0$.

Figure 60 shows the horizontal cross sections of v'_g at $t = 3, 12, 72$, and 144 h defined by the zonal gradient of the evolving p' field (Fig. 55) at these same times. As the mass field adjusts to the externally forced wind fields, note that the southerly (northerly) character of v'_g (Fig. 60a) initially associated with the localized region of perturbation high pressure (Fig. 55a) forced by confluence towards the forcing center due to the formation of

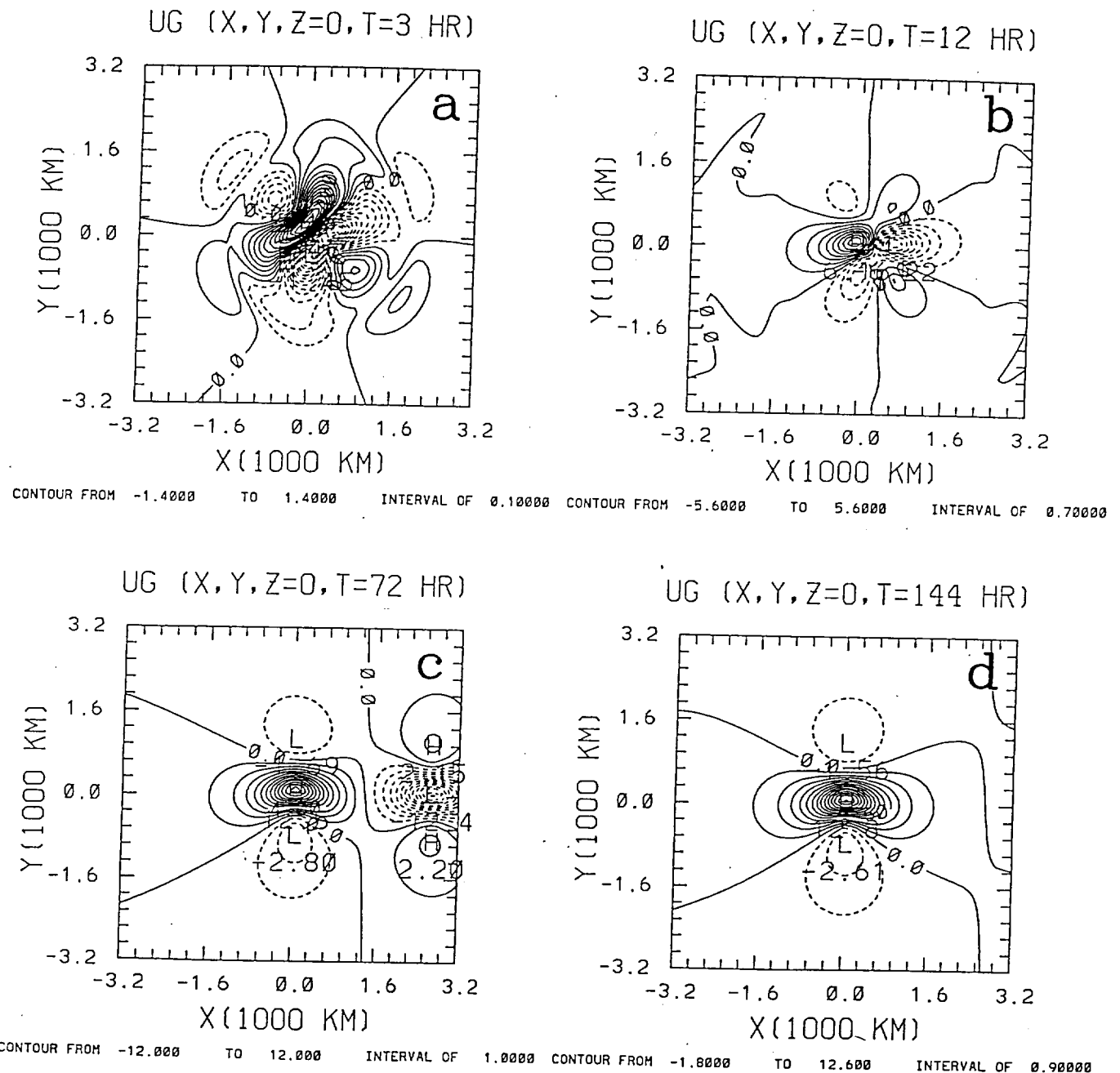


Fig. 59: Horizontal cross sections of u'_g associated with the forced linear response as seen by a Galilean observer at $t =$ a) 3 h, b) 12 h, c) 72 h, and d) 144 h.

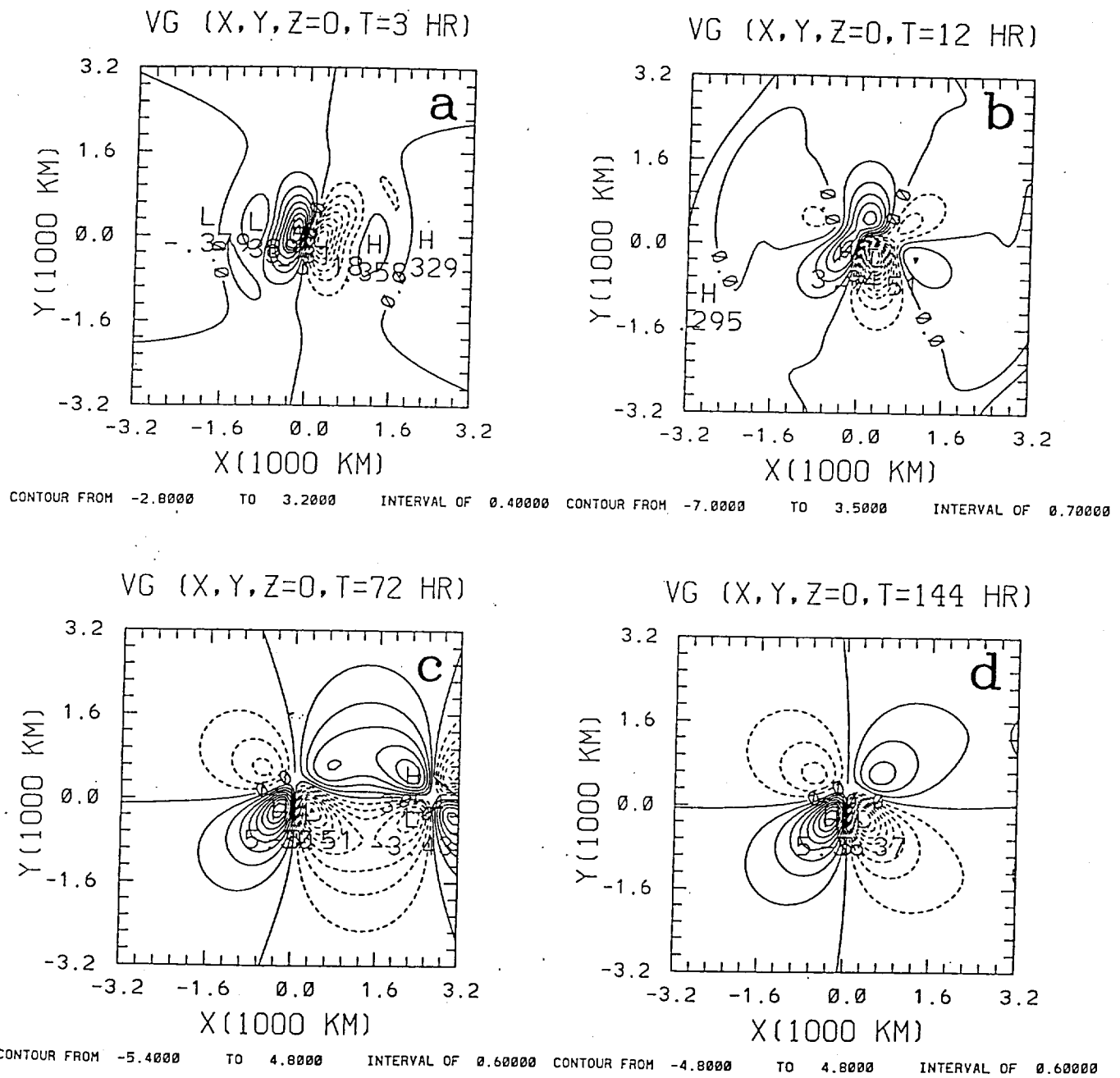


Fig. 60: Same as Fig. 59 except for v'_g .

the zonal jet (counter current) (Fig. 50a) in the forcing entrance (exit) region gradually evolves (Fig. 60b) into two distinct circulations by $t = 72$ h (Fig. 60c), one defining confluence (diffluence) in the entrance (exit) region of the geostrophic zonal jet located in the vicinity of the forcing center (Fig. 59c), while the other defines diffluence (confluence) in the entrance (exit) region of the geostrophic zonal counter current which is being advected downstream (Fig. 50c). By $t = 144$ h, a well-defined four-cell pattern of v'_g exists within the vicinity of the forcing center, establishing a confluent (diffluent) jet entrance (exit) region.

Figures 61 and 62 show the horizontal cross sections of $u'_a = u' - u'_g$ and $v'_a = v' - v'_g$ at $t = 3, 12, 72$, and 144 h. Note that unlike traditional QG jet streak theory, in which the ageostrophic components (u'_a, v'_a) are essentially driven by the advection of the geostrophic components (u'_g, v'_g) by the basic state flow (in a linear sense)

$$u'_a = -\frac{1}{f} \frac{Dv'_g}{Dt}, \quad (50)$$

$$v'_a = \frac{1}{f} \frac{Du'_g}{Dt}, \quad (51)$$

the ageostrophic components are here driven by the structure of the applied momentum forcing through

$$[(\frac{D^2}{Dt^2} + f^2) \frac{\partial^2}{\partial z^2} + N^2 \nabla_H^2] u'_a(\mathbf{r}, t) = [\frac{D}{Dt} \frac{\partial^2}{\partial z^2} + \frac{N^2}{f} \frac{\partial^2}{\partial y \partial x}] F_x(\mathbf{r}, t), \quad (52)$$

$$[(\frac{D^2}{Dt^2} + f^2) \frac{\partial^2}{\partial z^2} + N^2 \nabla_H^2] v'_a(\mathbf{r}, t) = -[f \frac{\partial^2}{\partial z^2} + \frac{N^2}{f} \frac{\partial^2}{\partial x^2}] F_x(\mathbf{r}, t). \quad (53)$$

During the early stages of forced adjustment at $t = 3$ h (Fig. 22a), the ageostrophic zonal wind exhibits confluence towards the forcing center. Six hours later at $t = 12$ h (Fig. 61b), this component of the forced zonal wind perturbation shows evidence of the formation of

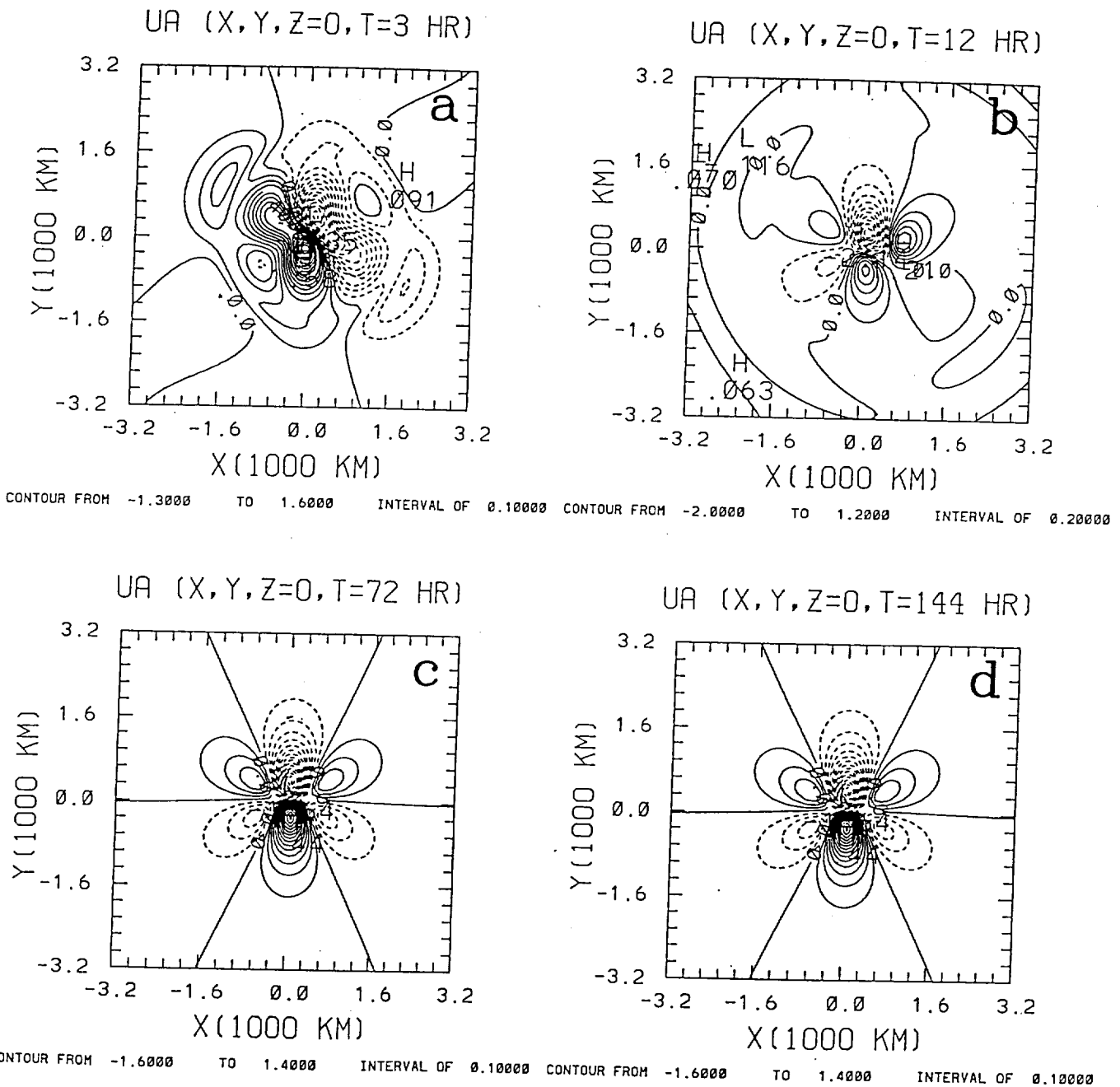


Fig. 61: Same as Fig. 59 except for u'_a .

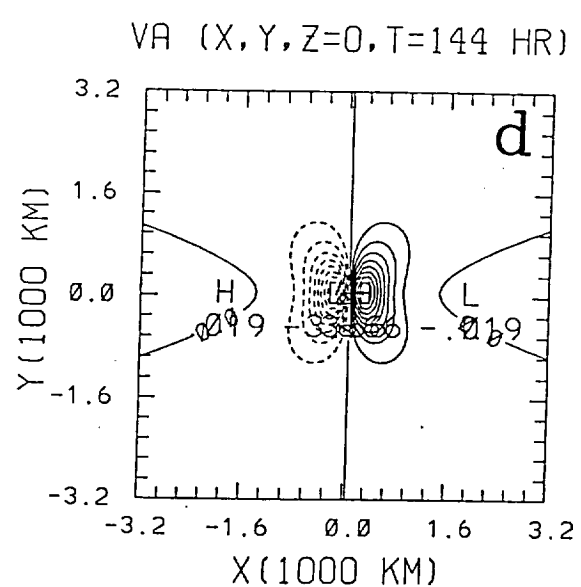
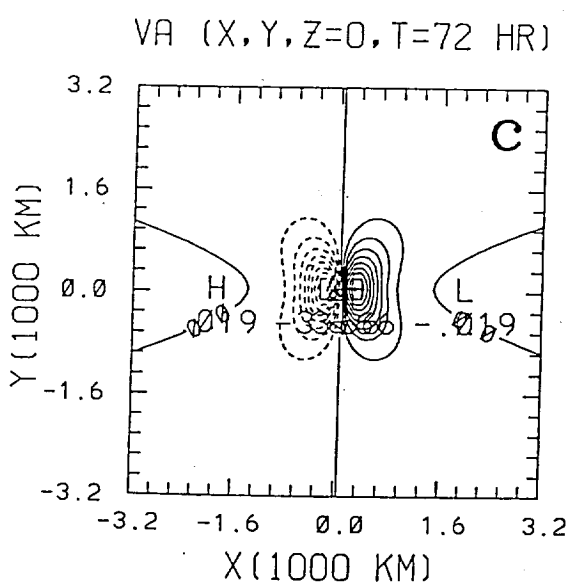
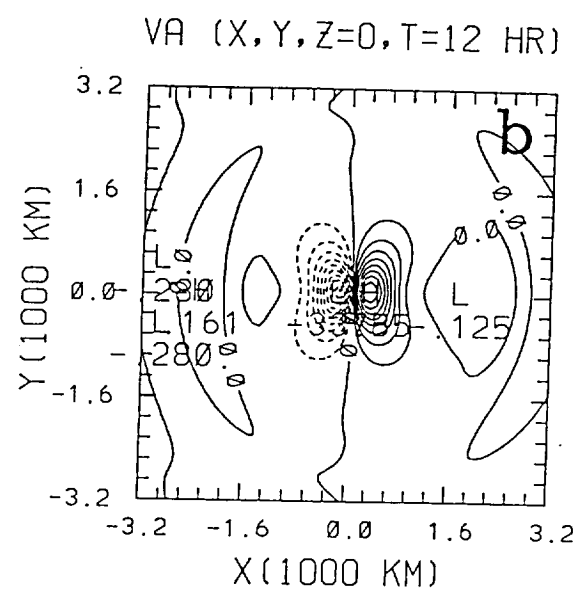
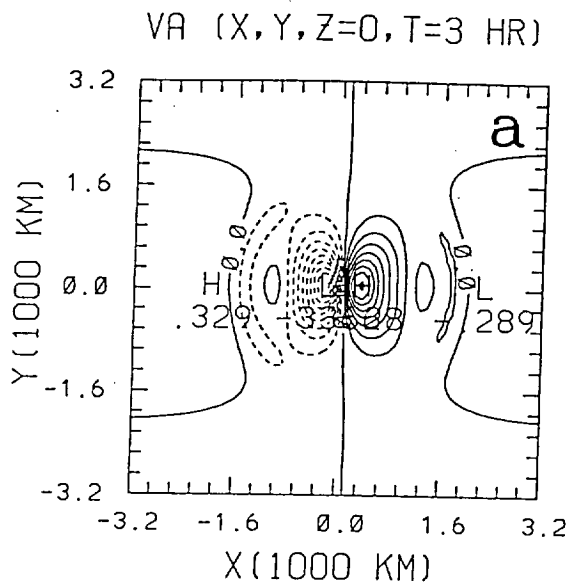


Fig. 62: Same as Fig. 59 except for v'_a .

predominantly two-cell pattern of positive (negative) flow south (north) of the forcing center. The isolated regions of positive and negative u'_a are established relatively early ($t \sim 12$ h), and gradually increase in magnitude over time (Figs. 61c and d), and are flanked by isolated components of zonal flow in the opposite sense to their immediate east and west.

Although transient IGW activity is predicted by the linear theory at $t = 3$ and 12 h (Figs. 62a and b) in the evolving v'_a field, note that for the particular choice of external momentum forcing chosen here, that these components are just reversed from that commonly inferred to exist with real midlatitude jet streaks based on QG theory in the absence of external forcing (Eq. (51)). The development of these ageostrophic meridional wind perturbations early in the response (by $t \sim 3$ h), and which gradually strengthen over time (Figs. 62c and d) have the effect of transferring mass from the cyclonic to the anticyclonic (anticyclonic to the cyclonic side) of the jet in the entrance (exit) region of the external momentum forcing, and is primarily the reason for the reversed pattern of vertical motion (Fig. 54) which develops in the vicinity of the forcing center. The pattern of northerly (southerly) v'_a flow in the forcing entrance (exit) region, coupled with the regions of positive (negative) u'_a to the south (north) of $y = 0$ indicates that the perturbation ageostrophic flow is primarily dominated by an isolated cyclonic circulation whose center is colocated with the center of the prescribed momentum forcing (not shown).

Figure 63 shows the time evolution of u' , v' , p' , and θ' as a function of east-west (Fig. 63a) and north-south (Figs. 63b-d) distance from the forcing center at various locations during the first 144 h of forced adjustment. Fig. 63a shows that the total zonal wind perturbation during the early stages before the formation of the PV anomaly is primarily dominated by confluence toward the forcing center, with a gradual increase in amplitude of both the zonal jet (counter current) in the entrance (exit) region of the external momentum forcing over time. The downstream advection of the zonal counter current is clearly evident for $t \geq 36$ h, leaving, within the vicinity of the forcing center, an isolated positive zonal wind anomaly of $\sim 12 \text{ ms}^{-1}$. On the southern (northern) side of the forcing

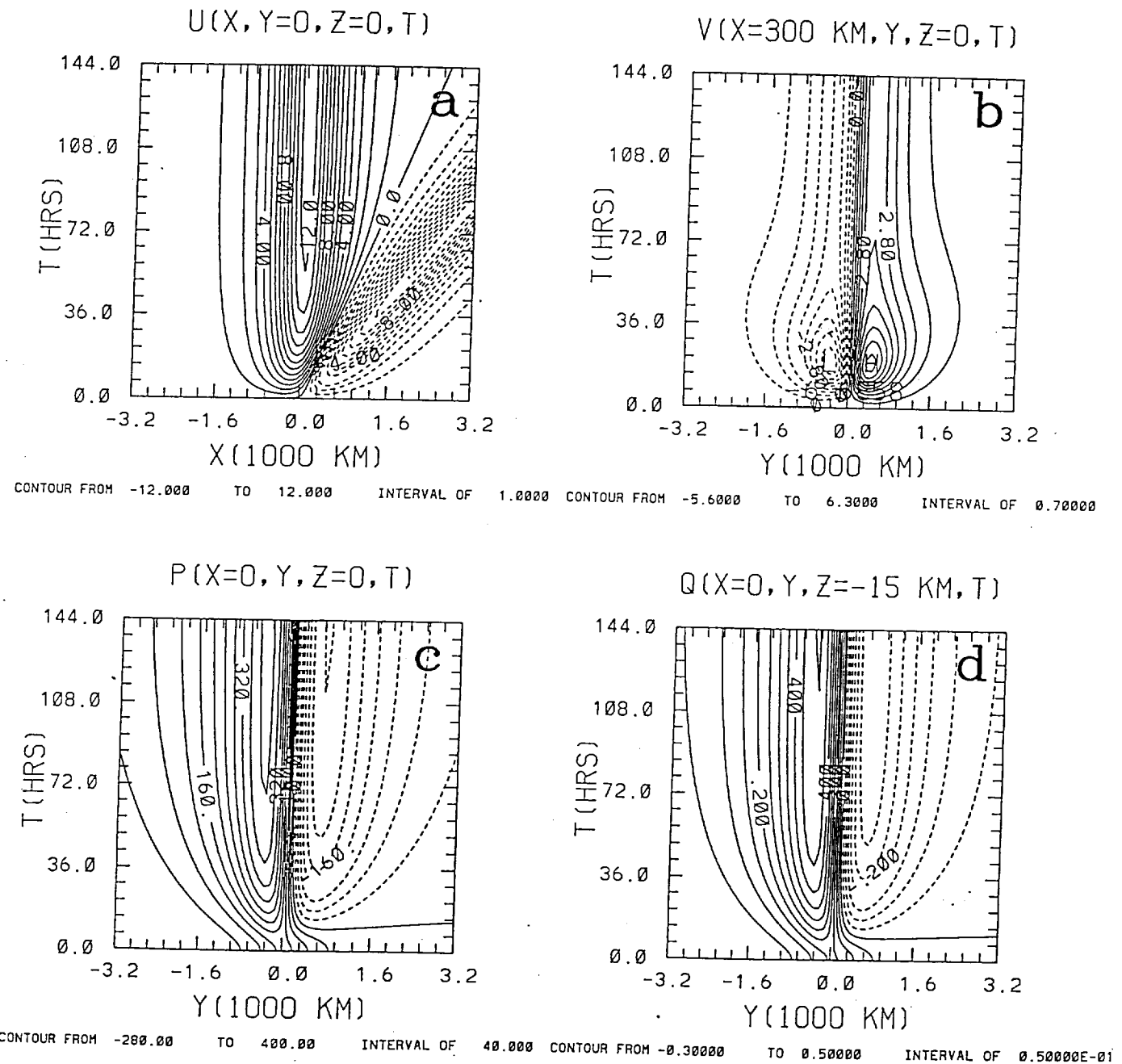


Fig. 63: Temporal evolution of the linear response in a) total u' , b) total v' , c) p' , and d) q' as a function of x at various y locations during the first 144 hours of forced adjustment associated with the traveling momentum forcing given by Eq. (33).

center, 300 km west the origin in the forcing exit region, Fig. 63b shows that the total meridional wind perturbation v' during the first 36 h of forced adjustment is primarily dominated by an isolated region of $v' < 0$ ($v' > 0$). Notice that the dominant, localized regions of v' north and south of $y = 0$ indicate the evolution of diffluent flow in the exit region of the momentum forcing which gradually reach their steady-state asymptotic values for $t \geq 36$ h (Fig. 63b).

Fig. 63c shows that the meridional evolution in p' at the forcing center for $t \leq 12$ h is primarily dominated by an isolated region of perturbation high pressure due to the convergence towards the forcing center driven by the forced zonal wind perturbation (Fig. 63a). As the relatively weak regions of perturbation low pressure which exist east (west) of the region where $p' > 0$, gradually increase (decrease) over time as the mass field adjusts to the externally forced wind field, the pressure perturbation field gradually evolves into a high-low couplet on the southern side of the forcing center (Fig. 55b). The high-low p' couplet in the exit region at this time geostrophically supports the zonal counter current which gets advected downstream (Figs. 55c and 50c), leaving within the vicinity of the origin, a low-high couplet of p' (Fig. 63c) for $t \geq 12$ h which supports the positive zonal wind anomaly which exists there (Fig. 50d). Fig. 63d shows that θ' 15 km below the forcing center during the first 12 h of forced adjustment has a similar structure to p' due to the constraint imposed by the hydrostatic balance. By $t \sim 12$ h, θ' has also gradually evolved into a two-cell pattern of cold (warm) air (east) west of the forcing center on the $z = -15$ km plane (Fig. 57b). This couplet in θ' then is advected downstream over time at the relative velocity $U-c$, leaving at the forcing center, a couplet of cold (warm) air (Fig. 63d) for $z < 0$, whose centers are colocated with those of p' (Fig. 57d). For $z > 0$, this structure in θ' is reversed from that which exists for $z < 0$.

Figure 64 shows the asymptotic steady-state part of the linear forced response (last term on the r.h.s. of Eq. (40)) in a uniform, vertically unbounded, continuously stratified barotropic flow due to the independently propagating prescribed momentum forcing given

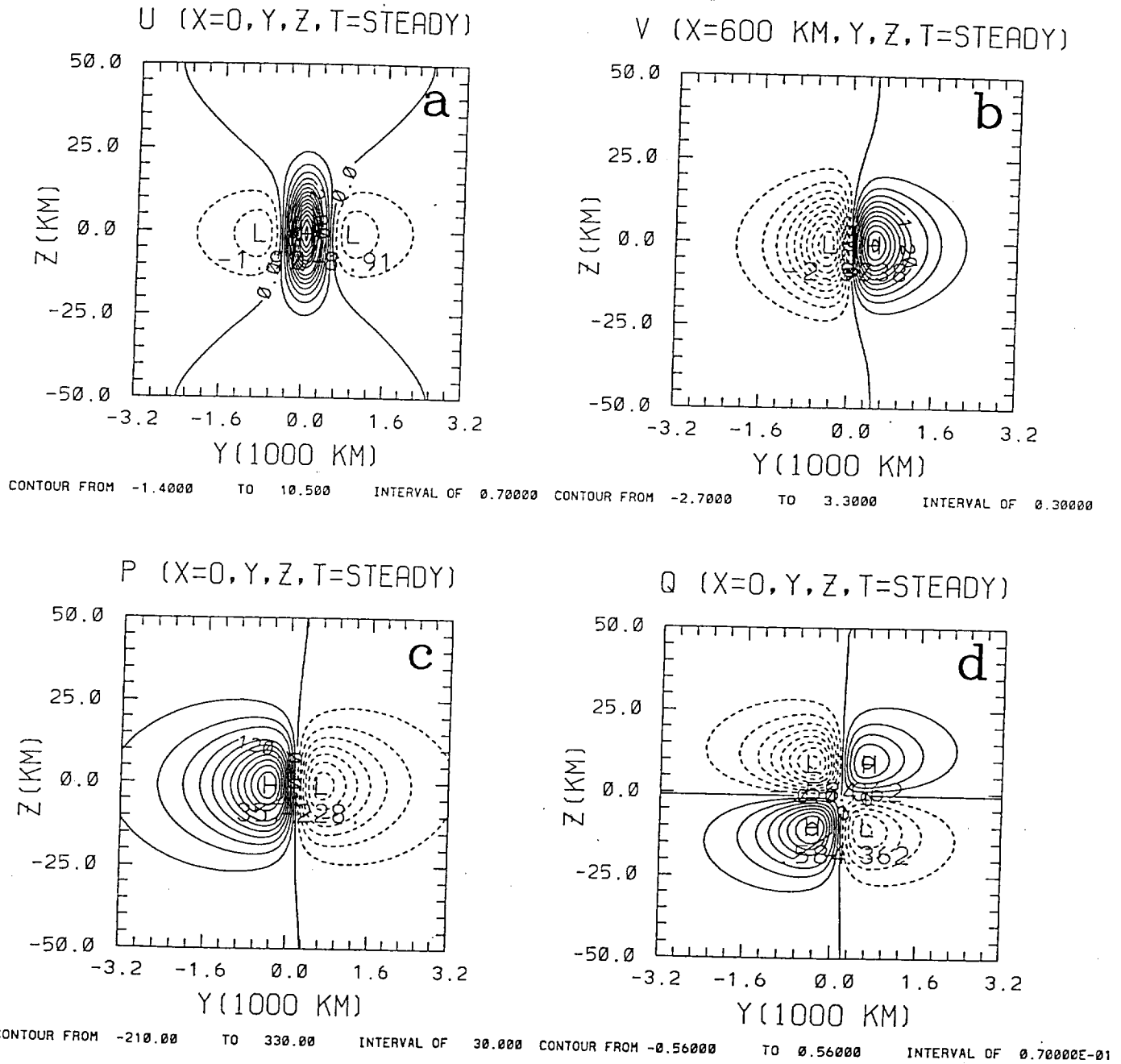


Fig. 64: North-south cross sections of the linear steady-state response as seen by a Galilean observer traveling at the uniform zonal speed $c < U$ produced by the propagating momentum forcing given by Eq. (33) in an unbounded Boussinesq atmosphere. This response is defined to be forced quasi-geostrophic *jetogenesis*.

by Eq. (33). Recall that it is *this* steady-state response that will be seen to propagate downstream at the uniform speed c to a non-translating observer, and therefore will be identified as the mesoscale circulations associated with a mature, quasi-steady, midlatitude jet streak. The horizontal structure of this asymptotic solution on the x - y plane can be inferred from the earlier figures. The linear theory presented here predicts the existence of an isolated region of maximum zonal winds of approximately 11 ms^{-1} , with compensating zonal counter currents of roughly -2 ms^{-1} located to the north and south of the main jet core (Fig. 64a). The vertical cross section of the meridional wind perturbation 600 km to the west of the zonal jet core in the jet entrance region (Fig. 64b) shows that the confluent flow on the anticyclonic and cyclonic sides of the main jet core is primarily confined to a layer of depth $\sim O(2d_{jet})$.

Figures 64c and d show the linear steady-state meridional cross sections of p' and θ' which consist of hydrostatically-related couplets of low (high) perturbation pressure and cold (warm) air north (south) of the zonal jet core. Associated with the centers of perturbation low (high) pressure are centers of cyclonic (anticyclonic) relative vorticity (not shown), indicative of isolated regions of cyclonic (anticyclonic) flow located to the north (south) of the main zonal jet core. Therefore, we may classify the steady-state response of a uniform, vertically unbounded, continuously stratified zonal flow to the propagating external momentum forcing given by Eq. (33) and as seen by a Galilean observer moving with the zonal speed c as *linear quasi-geostrophic jetogenesis*, since the response is typical of a balanced jet streak, with the exception that the secondary ageostrophic circulations in the entrance and exit are simply *reversed* with those implied from quasi-geostrophic theory to be associated with mature, quasi-steady jet streaks in the real atmosphere.

4. Summary and Conclusions

We have investigated the three-dimensional free and forced linear, baroclinic response of a vertically unbounded, continuously stratified, Boussinesq atmosphere to both

the impulsive and temporarily continuous addition of localized zonal momentum. The methods of perturbation potential vorticity theory are used to address the initial-value and forced geostrophic adjustment problems imposed by: (i) the introduction of an unbalanced zonal wind anomaly, and (ii) the entrance (exit) region acceleration (deceleration) experienced by the basic state flow as it passes through the slower moving isotach maximum. The zonal and meridional wind perturbations are partitioned into both geostrophic and ageostrophic components in order to identify the genesis and subsequent evolution of the primary (geostrophic) and secondary (ageostrophic) mesoscirculations associated with the development of jet streak genesis in this simple model atmosphere.

Consistent with classical adjustment theory, the horizontal structure in the evolution of the baroclinic perturbations is the same as predicted by linear shallow water theory if the undisturbed depth H of that geophysical fluid system is replaced by the equivalent depth H_e for each internal mode defined by the vertical wavenumber $m = 2\pi/L_z$. The transient response shows evidence of dispersive IGWs which tend to excite a wider spectrum of modes which can persist for a longer period of time in the zonal direction as compared to the meridional direction. The IGWs in the meridional direction in all fields except the vertical velocity are essentially removed in the first 6 h of the response associated with the initial-value problem. The existence of a uniform zonal flow essentially Doppler shifts the phase velocities of the transient IGWs responsible for removing the ageostrophic divergence of the initial state during the adjustment to geostrophic equilibrium. The steady-state response predicted by linear theory which conserves the PV of the initial state is a localized, geostrophic zonal jet with meridionally confluent (diffluent) flow in its entrance (exit) region, which is supported by a couplet of perturbation low (high) pressure north (south) of the zonal jet core. At all levels below (above) the level of maximum zonal wind, a couplet of cold/warm (warm/cold) air is colocated with the centers of low/high pressure on the cyclonic (anticyclonic) side of the isolated zonal jet. The three-dimensional steady-state linear response characterizes a localized *thermal wind balance* among the baroclinic

perturbations defining the primary (geostrophic) circulations associated with the geostrophic jet. In the absence of prescribed forcing, the secondary (ageostrophic) circulations predicted by linear theory are trivially zero. In a non-zero basic state flow, the steady-state PV couplet is advected downstream, thereby establishing the physical mechanisms of geostrophic vorticity advection $-U \cdot \nabla \zeta_g'$, and horizontal temperature advection, $-U \cdot \nabla \theta'$ accompanying the traveling PV anomaly.

In order to address the effects of entrance (exit) region acceleration (deceleration) experienced by the basic state flow, which is itself taken to be locally representative of the planetary jet stream in which midlatitude jet streaks are observed to exist, we investigate the response of a vertically unbounded, continuously stratified, uniform zonal flow to a prescribed momentum forcing propagating at the speed $c < U$ through the basic state current. The magnitude of the traveling zonal wind anomaly represented by this forcing is taken to be greater than the magnitude of the basic state flow, $|u_{j0}| > |U|$, yielding propagation characteristics very representative of real midlatitude jet streaks.

For a Galilean observer, the response predicted by linear theory is primarily dominated by the structure of the imposed momentum forcing for $t \leq 48$ h (more generally, for $t \leq$ the advective time scale, which is defined as $\tau = 2a/(U-c)$). During this early stage of forced adjustment, a zonal jet (zonal counter current) exists in the forcing entrance (exit) region. Since the length scale of the forced zonal winds are much less than the Rossby deformation radius defined by the total depth of the zonal wind anomaly represented by the prescribed forcing ($L_R \sim N^2 d_{jet}/f$), the transient response shows the adjustment of the mass (p' , θ') fields to the forced momentum (u' , v') fields. For $t \geq 48$ h, after significant transient IGW activity has been dispersed, the linear response is dominated by the circulations associated with the PV anomaly generated by the meridional gradient of the 'vorticity' associated with the applied momentum forcing. An isolated zonal counter current is advected downstream at the relative velocity $U-c$, with meridionally diffluent (confluent) perturbation flow in its entrance (exit) region. A dipole couplet of high (low)

pressure (which is related hydrostatically to the perturbation potential temperature field) supports this localized zonal counter current as it is advected downstream of the forcing exit region by the uniform zonal flow.

Concurrently, an isolated zonal jet with meridionally confluent (diffluent) flow in the jet entrance (exit) region becomes established in the vicinity of the forcing center. The perturbation pressure which supports this localized zonal jet consists of a localized regions of low (high) perturbation pressure north (south) of $y = 0$. This pressure couplet is related hydrostatically to the perturbation potential temperature field, and shows primary (geostrophic) circulations similar to that predicted by linear theory for the initial-value problem. The secondary (ageostrophic) circulations transfer mass from the cyclonic to the anticyclonic (anticyclonic to the cyclonic) side of the jet core in the entrance (exit) region, yielding a well-defined 'four-cell' pattern of vertical motion in the quadrants flanking the jet core. These transverse ageostrophic circulations are similar to those produced in a rotating homogeneous atmosphere of finite depth H (Weglarz, 1994), but are just *reversed* from those commonly inferred to be associated with midlatitude jet streaks in the real atmosphere. Since the primary circulations are correct and the secondary circulations show the correct horizontal and vertical structure, we define the forced linear response as baroclinic *jetogenesis*.

This type of work should be extended to a semi-infinite continuously stratified flow, and focus on the dynamically important nonlinear effects associated with the geostrophic dynamics and subsequent response to balanced equilibrium for both the initial-value and forced problems presented here. Specific emphasis may be placed on the genesis of the transverse ageostrophic entrance and exit region circulations and the accompanying vertical motion which preserves the thermal wind balance, in addition to investigating the three-dimensional quasi-geostrophic frontogenesis, $\mathbf{Q}' \cdot \nabla \theta'$, which is associated with baroclinic jetogenesis in this simple model atmosphere.

References

- Barwell, B. R., and R. A. Bromley, 1988: The adjustment of numerical weather prediction models to local perturbations. *Quart. J. Roy. Meteor. Soc.*, **114**, 665-689.
- Bluestein, H. B., 1993a: *Synoptic-Dynamic Meteorology in Midlatitudes. Volume I: Principles of Kinematics and Dynamics*. Oxford Univ. Press, New York, 431pp.
- , 1993b: *Synoptic-Dynamic Meteorology in Midlatitudes. Volume II: Observations and Theory of Weather Systems*. Oxford Univ. Press, New York, 594pp.
- Blumen, W., 1972: Geostrophic adjustment. *Rev. Geophys. Space Phys.*, **10**, 485-528.
- Bossert, J. E., 1990: Regional scale flows in complex terrain: An observational and numerical investigation. *Ph.D. dissertation*, Colorado State University, 254pp. [Available from University Microfilms, Ann Arbor, MI 48106].
- , and W. R. Cotton, 1994a: Regional scale flows in mountainous terrain. Part I: A numerical and observational comparison. *Mon. Wea. Rev.*, **122**, 1449-1471.
- , and -----, 1994b: Regional scale flows in mountainous terrain. Part II: Simplified numerical experiments. *Mon. Wea. Rev.*, **122**, 1472-1489.
- Cahn, A., 1945: An investigation of the free oscillations of a simple current system. *J. Meteor.*, **2**, 113-119.
- Durran, D. R., and D. B. Weber, 1988: An investigation of the poleward edges of cirrus clouds associated with midlatitude jet streams. *Mon. Wea. Rev.*, **116**, 702-714.
- Fritsch, J. M., and C. F. Chappell, 1980: Numerical prediction of convectively driven mesoscale pressure systems. Part I: Convective parameterization. *J. Atmos. Sci.*, **37**, 1722-1733.
- Fritts, D. C., and Z. Luo, 1992: Gravity wave excitation by geostrophic adjustment of the jet stream. Part I: Two-dimensional forcing. *J. Atmos. Sci.*, **49**, 681-697.
- Gill, A. E., 1982: *Atmosphere-Ocean Dynamics*. Academic Press, 662 pp.
- Hoskins, B. J., M. E. McIntyre, and A. W. Robertson, 1985: On the use and significance of isentropic potential vorticity maps. *Quart. J. Roy. Meteor. Soc.*, **111**, 877-946.
- Kaplan, M. L., and D. A. Paine, 1977: The observed divergence of the horizontal velocity field and pressure gradient force at the mesoscale. Its implications for the parameterization of three-dimensional momentum transport in synoptic-scale numerical models. *Beitr. Phys. Atmos.*, **50**, 321-330.
- , J. W. Zack, V. C. Wong, and J. J. Tuccillo, 1982: Initial results from a mesoscale atmospheric simulation system and comparisons with the AVE-SESAME I data set. *Mon. Wea. Rev.*, **110**, 1564-1590.

- , and V. M. Karyampudi, 1992a: Meso-beta scale numerical simulations of terrain drag-induced along-stream circulations. Part I: Midtropospheric frontogenesis. *Meteor. Atmos. Phys.*, **49**, 133-156.
- , and -----, 1992b: Meso-beta scale numerical simulations of terrain drag-induced along-stream circulations. Part II: Concentration of potential vorticity within dryline bulges. *Meteor. Atmos. Phys.*, **49**, 157-185.
- , S. E. Koch, Y.-L. Lin, R. P. Weglarz, and R. A. Rozumalski, 1994a: The numerical simulation of meso- β scale geostrophic adjustment processes resulting in secondary upper/lower-level jet formation and internal gravity waves during CCOPE. *Sixth Conf. on Mesoscale Processes*, Amer. Meteor. Soc., July 18-22, Portland, OR, 382-384.
- , R. A. Rozumalski, R. P. Weglarz, Y.-L. Lin, and S. E. Koch, 1994b: Numerical simulation studies of the role of convectively-driven ageostrophic jet streak adjustments in creating a favorable environment for the development of an isolated tornado outbreak. *Sixth Conf. on Mesoscale Processes*, Amer. Meteor. Soc., July 18-22, Portland, OR, 144-146.
- , S. E. Koch, R. P. Weglarz, Y.-L. Lin, and R. A. Rozumalski, 1995: Numerical simulations of a gravity wave event over CCOPE. Part I: The role of upper-tropospheric geostrophic adjustment processes in the generation of internal gravity waves. In preparation for submission to *Mon. Wea. Rev.*
- Koch, S. E., 1985: Ability of a regional-scale model to predict the genesis of intense mesoscale convective systems. *Mon. Wea. Rev.*, **113**, 1693-1713.
- , W. C. Skillman, P. J. Kocin, P. J. Wetzel, K. F. Brill, D. A. Keyser, and M. C. McCumber, 1985: Synoptic scale forecast skill and systematic errors in the MASS 2.0 model. *Mon. Wea. Rev.*, **113**, 1714-1737.
- , and R. E. Golus, 1988: A mesoscale gravity wave event observed during CCOPE. Part I: Multiscale statistical analyses of wave characteristics. *Mon. Wea. Rev.*, **116**, 2527-2544.
- , -----, and P. B. Dorian, 1988: A mesoscale gravity wave event observed during CCOPE. Part II: Interactions between mesoscale convective systems and the antecedent waves. *Mon. Wea. Rev.*, **116**, 2545-2569.
- , and P. B. Dorian, 1988: A mesoscale gravity wave event observed over CCOPE. Part III: Wave environment and probable source mechanisms. *Mon. Wea. Rev.*, **116**, 2570-2592.
- , F. Einaudi, P. B. Dorian, S. Lang, and G. M. Heymsfield, 1993: A mesoscale gravity wave event observed during CCOPE. Part IV: Stability analysis and doppler-derived wave vertical structure. *Mon. Wea. Rev.*, **121**, 2483-2510.
- Lin, Y.-L., 1994a: Airflow over mesoscale heat sources. Part I: Responses in a uniform flow. *Proc. NSC*, **18**, 1-32.

- , 1994b: Airflow over mesoscale heat sources. Part II: Responses in a shear flow. *Proc. NSC*, **18**, 119-150.
- Luo, Z., and D. C. Fritts, 1993: Gravity-wave excitation by geostrophic adjustment of the jet stream. Part II: Three-dimensional forcing. *J. Atmos. Sci.*, **50**, 104-115.
- Manobianco, J., L. W. Uccellini, K. F. Brill, and P. J. Kocin, 1991: Contrasting the impact of dynamic data assimilation on the numerical simulation of cyclogenesis during GALE IOP 10 and IOP 1. *Meteor. Atmos. Phys.*, **45**, 41-63.
- , -----, -----, and Y.-H. Kuo, 1992: The impact of dynamic data assimilation on the numerical simulation of the QE II cyclone and an analysis of the jet streak influencing the precyclogenetic environment. *Mon. Wea. Rev.*, **120**, 1973-1996.
- , S. E. Koch, V. M. Karyampudi, and A. J. Negri, 1994: The impact of assimilating satellite-derived precipitation rates on numerical simulations of the ERICA IOP 4 cyclone. *Mon. Wea. Rev.*, **122**, 341-365.
- Molinari, J., 1982: A method for calculating the effects of deep cumulus convection in numerical models. *Mon. Wea. Rev.*, **110**, 1527-1534.
- Murray, R., and S. M. Daniels, 1953: Transverse flow at entrance and exit to jet streams. *Quart. J. Roy. Meteor. Soc.*, **79**, 236-241.
- Namias, J., and P. F. Clapp, 1949: Confluence theory of the high tropospheric jet stream. *J. Meteor.*, **6**, 330-336.
- Paegle, J., 1978: The transient mass-flow adjustment of heated atmospheric circulations. *J. Atmos. Sci.*, **35**, 1678-1688.
- Phillips, N. A., 1957: A coordinate system having some special advantages for numerical forecasting. *J. Meteor.*, **14**, 184-185.
- Powers, J. G., and R. J. Reed, 1993: Numerical simulation of the large-amplitude mesoscale gravity wave event of 15 December 1987 in the Central United States. *Mon. Wea. Rev.*, **121**, 2285-2308.
- Reiter, E. R., 1969: *Jet-Stream Meteorology*. The University of Chicago Press.
- Riehl, H. *et al.*, 1952: *Forecasting in the Middle Latitudes*. Meteor. Monogr., No. 5, Amer. Meteor. Soc., 80 pp.
- Rossby, C. G., 1938: On the mutual adjustment of pressure and velocity distributions in simple current systems, 2. *J. Mar. Res.*, **1**, 239-263.
- Schmidt, J. M., and W. R. Cotton, 1990: Interactions between upper and lower tropospheric gravity waves on squall line structure and maintenance. *J. Atmos. Sci.*, **47**, 1205-1222.
- Schneider, R. S., 1990: Large-amplitude gravity wave disturbances within the intense midwest extratropical cyclone of 15 December 1987. *Wea. and Forecasting*, **5**, 533-558.

- Schubert, W. H., J. J. Hack, P. L. Silva Dias, and S. R. Fulton, 1980: Geostrophic adjustment in an axisymmetric vortex. *J. Atmos. Sci.*, **37**, 1464-1484.
- Smith, R. B., 1979: The influence of mountains on the atmosphere. *Adv. in Geophys.*, **21**, 87-230.
- , 1989: Hydrostatic airflow over mountains. *Adv. in Geophys.*, **31**, 1-41.
- Tripoli, G. J., and W. R. Cotton, 1989a: A numerical study of an observed orogenic mesoscale convective system. Part I: Simulated genesis and comparison with observations. *Mon. Wea. Rev.*, **117**, 273-304.
- , and -----, 1989b: A numerical study of an observed orogenic mesoscale convective system. Part II: Analysis of governing dynamics. *Mon. Wea. Rev.*, **117**, 305-328.
- Uccellini, L. W., and D. R. Johnson, 1979: The coupling of upper and lower tropospheric jet streaks and implications for the development of severe convective storms. *Mon. Wea. Rev.*, **107**, 682-703.
- , and S. E. Koch, 1987: The synoptic setting and possible energy sources for mesoscale wave disturbances. *Mon. Wea. Rev.*, **115**, 721-729.
- , and P. J. Kocin, 1987: The interaction of jet streak circulations during heavy snow events along the east coast of the United States. *Wea. and Forecasting*, **2**, 289-308.
- University of Chicago, 1947: On the general circulation of the atmosphere in middle latitudes. *Bull. Amer. Meteor. Soc.*, **28**, 255-280.
- Vallis, G. K., 1992: Mechanisms and parameterizations of geostrophic adjustment and a variational approach to balanced flow. *J. Atmos. Sci.*, **49**, 1144-1160.
- Van Tuyl, A. H., and J. A. Young, 1982: Numerical simulation of nonlinear jet streak adjustment. *Mon. Wea. Rev.*, **110**, 2038-2054.
- Weglarz, R. P., 1994: Three-dimensional geostrophic adjustment of homogeneous and continuously stratified atmospheres with application to the dynamics of midlatitude jet streaks. *Ph.D. dissertation*, North Carolina State University, 414pp.
- Whitaker, J. S., L. W. Uccellini, and K. F. Brill, 1988: A model-based diagnostic study of the rapid development phase of the Presidents' Day cyclone. *Mon. Wea. Rev.*, **116**, 2337-2365.
- Williams, R. T., 1965: Nonlinear, non-geostrophic effects in a baroclinic atmosphere. *J. Atmos. Sci.*, **22**, 388-401.
- Wolyn, P. G., and T. B. McGhee, 1992: Modeling and observational study of the daytime evolution east of the crest of the Colorado Rockies. Atmospheric Science Paper No. 496, Colorado State University, 225pp.
- , and -----, 1994: The mountain-plains circulation east of a 2km-high north-south barrier. *Mon. Wea. Rev.*, **122**, 1490-1508.

- Zack, J. W., and M. L. Kaplan, 1987: Numerical simulations of the subsynoptic features associated with the AVE-SESAME I Case. Part I: The preconvective environment. *Mon. Wea. Rev.*, **115**, 2367-2393.
- Zhang, D.-L., and R. A. Anthes, 1982: A high-resolution model of the planetary boundary layer--sensitivity tests and comparisons with SESAME-79 data. *J. Appl. Meteor.*, **21**, 1594-1609.
- , and J. M. Fritsch, 1988: Numerical simulation of the meso-beta scale structure and evolution of the 1977 Johnstown flood. Part III: Internal gravity waves and the squall line. *J. Atmos. Sci.*, **45**, 1252-1268.
- Zhu, X., and J. R. Holton, 1987: Mean fields induced by gravity-wave forcing in the middle atmosphere. *J. Atmos. Sci.*, **44**, 620-630.